

Preparation and Characterization of CNT-Based Hierarchically  
Structured Electrodes for Application in a Fuel Cell

# Dissertation

zur Erlangung des Doktorgrades der Naturwissenschaften  
(Dr. rer. nat.)

der

Naturwissenschaftlichen Fakultät II  
Chemie, Physik und Mathematik

der Martin-Luther-Universität  
Halle-Wittenberg

vorgelegt von

Frau Pei Wang

geb. am 14.03.1984 in Shandong

Gutachter:

Prof. Dr. Michael Bron

Prof. Dr. Martin Muhler

Tag der Verteidigung: 06.07.2021



# Acknowledgements

---

Here, I would like to express my appreciation to everyone, who has accompanied and supported me in my PhD study period.

Especially, I would like to express my deep appreciation and gratitude to my 'Doktorvater', namely my research supervisor Prof. Dr. Michael Bron, who gave me the opportunity to join his great working group and start my PhD research work, as well as to acquire extensive knowledge in electrochemistry, nanomaterials and renewable energy. I am greatly thankful to him for his guidance, support and encouragement during my research. He always supported me to discuss, try and prove novel ideas for my research, whereby I have learnt how to plan my work and achieve results. It will benefit my further work and life.

My sincere gratitude goes also to Prof. Dr. Christine Roth at University Bayreuth, who gave me an opportunity to join the project as well as to learn and make experiments of MEA tests in her group. Honest thanks to Dr. Benedikt Peter for his collaboration. During the collaboration, he provided polyaniline for our layer by layer MEAs and performed the MEA tests with me. Their insightful and valuable discussions and advice improved our project and benefited my research work.

I would like to express my special thanks to the former and current colleagues in our group. Dr. Katarzyna Kulp and Dr. Christian Kulp were of great help to me, for example with discussions concerning electrochemistry in the beginning of my research and made me acquire broad electrochemical techniques for my further studies. Dr. Daniela Zambelli Mezalira provided me with helpful discussions about CNT growth, CVD technique and the set up. My deepest thanks to Dr. Tintula Kottakkat for her great help in the preparation of graphene oxide, her kind cooperation and support without any hesitation. They all made me expand my concepts of research. My thanks are also given to Annett Quetschke and Eik Koslowski for SEM, TGA, Raman, XRD measurements and laboratory equipment, Dr. Sabine Schimpf for TEM measurements, our group secretary Anke Hassi for her administrative support, Ronald Schlosser from the mechanical workshop for his help with the furnace system, teflon components and mechanical fabrication support. As

well, I would like to give my appreciation to Matthias Steimecke, Alexander Hartmann, Mark Hartmann, Titus Linderberg, Stefan Rümmler, Heba El Deeb, Alice Schätz, Thomas Eler and Gerda Seiffarth for their help and valuable advice in my daily work. With them all, I have worked and learned in a positive atmosphere and I am happy to have gotten to know them in my PhD studies.

My thanks are also sent to Frank Syrowatka from the Interdisziplinäres Zentrum für Materialwissenschaften of Martin Luther University Halle-Wittenberg for his help with SEM measurements. I have learnt and build up my knowledge of SEM from him.

Additionally, my deep gratitude goes to the German Research Foundation (Deutsche Forschungsgemeinschaft, under contract BR2244/7–1) for financial support so that I could perform my studies and research.

Finally, I would like to give my special and deepest thanks to my family: my parents, my parents-in-law and my husband Alex for their consistent encouragement and support, especially Alex for his patience, company, motivation and understanding in the harsh moments. I am also very grateful to all my good friends for their company, support and help in my daily life.

I would like to express my honest gratitude and appreciation to everyone once more again, who has helped, accompanied and supported me in my PhD study period. It has been a pleasant experience for me.

# Declaration

---

I hereby declare that my dissertation is based on my own work and results as well as is completed by independently writing, where the sources used were mentioned and noted as citations. The contributions of my co-operators are acknowledged in this submission. Moreover, this thesis has not been submitted to any other educational institution for other graduation.

Halle (Saale), December 2020

Signature:

Pei Wang



# Contents

<b>ABSTRACT.....</b>	<b>1</b>
English Version .....	1
German Version .....	3
<b>MOTIVATION AND AIM.....</b>	<b>5</b>
<b>BASIC CONCEPTS.....</b>	<b>9</b>
2.1. Fuel Cells.....	9
2.1.1. Working Principle .....	9
2.1.2. Types of Fuel Cells and their Applications Cells .....	10
2.2. Basic Concept of PEMFCs and DMFCs.....	12
2.2.1. Design of Cells .....	12
2.2.2. Basic Reactions of PEMFCs and DMFCs.....	14
2.2.3. Mechanism of Oxygen Reduction Reaction .....	14
2.2.4. Mechanism of Methanol Oxidation Reaction.....	16
2.3. Catalysts in PEMFCs and DMFCs .....	17
2.3.1. Catalysts for Hydrogen Oxidation Reaction .....	17
2.3.2. Catalysts for Oxygen Reduction reaction.....	18
2.3.3. Catalysts for Methanol Oxidation Reaction .....	20
2.4. Catalysts Supports for Oxygen Reduction Reaction and Methanol Oxidation Reaction .....	21
2.4.1. Carbon Nanotubes and their Growth Mechanism by Thermal Chemical Vapor Deposition .....	23
2.4.2. Graphene and its Synthesis Mechanism.....	27
<b>RESULTS AND DISCUSSION .....</b>	<b>29</b>
3.1. Hierarchically Structured 3D CNT Electrode .....	31
3.1.1. Motivation .....	31
3.1.2. Characterization of 3D CNTs.....	33
3.1.3. Characterizations and Electrochemical Investigations of Pt-3D CNTs .....	38
3.1.4. Conclusion .....	48
3.1.5. Supplementary Information.....	49
3.2. Hierarchically Structured 3D CNTs/CNTs/GC Electrode .....	52

3.2.1. Motivation .....	52
3.2.2. Preparation and Characterization of Hierarchically Nanostructured Electrodes ....	54
3.2.3. Electrochemical Investigations .....	62
3.2.4. Conclusion .....	69
3.2.5. Supplementary Information.....	71
3.3. Nanostructured NCNTs/RGO/CC Composite Electrode.....	79
3.3.1. Motivation .....	79
3.3.2. Preparation and Characterization of the Nanostructured Electrodes.....	81
3.3.3. Electrochemical Investigations .....	87
3.3.4. Conclusion .....	92
3.3.5. Supplementary Information.....	94
3.4 Hierarchically Structured Electrodes for Supercapacitors.....	99
3.4.1. Motivation .....	99
3.4.2. Characterization of PANI/CNTs/CC Electrode .....	100
3.4.3. Electrochemical Investigations .....	103
3.4.4. Conclusion .....	109
3.4.5 Supplementary Information.....	110
<b>CONCLUSION AND OUTLOOK .....</b>	<b>111</b>
4.1. Conclusion.....	111
4.2. Outlook .....	113
<b>EXPERIMENTAL SECTION.....</b>	<b>115</b>
5.1. Chemicals.....	115
5.2. Preparation of Hierarchically Nanostructured Electrodes .....	117
5.2.1. General Procedure of Carbon Nanotube Growth over Fe catalyst by CVD .....	117
5.2.2. Preparation of Pt supported 3D CNT Electrodes .....	118
5.2.3. Preparation of Pt supported CNTs/CNTs/GC Electrodes.....	119
5.2.4. Preparation of Pt supported RGO/CNTs/CC Electrodes.....	121
5.2.5. Preparation of PANI/CNTs/CC Electrodes.....	123
5.3. Structural Characterization.....	124
5.3.1. Scanning- and Transmission-Electron Microscopy .....	124
5.3.2. Raman Spectroscopy .....	124



5.3.3. X-ray Diffraction.....	124
5.3.4. Inductively Coupled Plasma-Optical Emission Spectroscopy.....	125
5.3.5. Nitrogen Physisorption Measurement.....	125
5.3.6. Elemental Analysis .....	125
5.4. Electrochemical Characterization.....	126
5.4.1. Preparation of Working Electrode.....	126
5.4.2. Initial Characterization by Cyclic Voltammetry .....	127
5.4.3. Carbon Monoxide Stripping Voltammetry .....	128
5.4.4. Oxygen Reduction Reaction.....	128
5.4.5. Accelerated Stress Test .....	129
5.4.6. Methanol Oxidation Reaction.....	129
5.4.7. Measurements of Multilayered Membrane Electrode Assembly.....	129
5.4.8. Capacitance Test .....	131
5.4.9. Electrochemical Impedance Spectroscopy .....	131
<b>REFERENCES .....</b>	<b>133</b>
<b>APPENDICES .....</b>	<b>155</b>
Abbreviations .....	155
Symbols .....	157
List of Tables.....	158
List of Figures.....	159
Publications and Conference Contributions.....	165
Research Articles .....	165
Conference Contributions .....	165
Curriculum Vitae.....	167



# Abstract

---

## English Version

As efficient, clean and promising power sources polymer electrolyte membrane fuel cells (PEMFCs) and direct methanol fuel cells (DMFCs), which can be employed in transportation, stationary power generation, power for portable electronics, etc., attract considerable attention. However, the sluggish kinetics of oxygen reduction reaction at the cathode and methanol oxidation reaction at the anode of DMFCs along with the degradation of the catalysts have impeded the broad market implementation of PEMFCs and DMFCs besides high costs of Platinum (Pt), poor durability of electrolyte membrane and methanol crossover through the electrolyte membrane. To solve these issues, research has a strong focus on improving the performance of catalysts by developing novel catalysts like alloying Pt or modified preparation methods like microwaved-assisted synthesis. However, an exceptional catalyst support is of equal importance as it can provide a large deposited surface area along with a highly porous structure, good conductivity and long-term stability. Therefore, hierarchically structured catalyst supports were proposed. Carbon nanotubes (CNTs) or graphene were assembled to the hierarchical structure via bottom-up approaches. CNTs were deposited by a sequence of iron (Fe) deposition and chemical vapor deposition (CVD) on the surface of oxidized commercial CNTs (primary CNTs), glassy carbon (GC) and reduced graphene oxide (RGO) covered carbon cloth (CC), respectively, to form 3D CNTs, CNTs/CNTs/GC and CNTs/RGO/CC hierarchical electrodes. In this way, CNTs can be tailored by tuning the parameters of Fe electrodeposition and CVD. In the preparation of CNTs/CNTs/GC, consecutive CNT growths were carried out, in which primary CNTs were grown over Fe nanoparticles by CVD step followed by a second Fe deposition and CVD growth of secondary CNTs. Afterwards, Pt nanoparticles were homogeneously deposited onto 3D CNTs (without substrates) by wet impregnation and onto the CNTs/CNTs/GC and NCNTs/RGO/CC by electrochemical deposition, respectively. Each preparation step was followed by scanning electron microscopy (SEM) or transmission electron microscopy (TEM) to verify the success of the preparations. Meanwhile, the successful CNT growth was

also demonstrated by Raman spectroscopy. Additionally, before Pt deposition the hierarchically structured electrodes display increased double layer capacitances in cyclic voltammograms, compared to oxidized commercial CNTs, CNTs/GC and CNTs/CC, respectively, indicating larger available surface area for the further Pt deposition. After Pt deposition, the three types of prepared hierarchical electrodes show enhanced electrochemical surface area calculated by  $H_{ads/des}$  peak and  $CO_{ad}$  oxidation in the cyclic voltammograms. The Pt-3D CNTs electrode shows a higher specific activity for oxygen reduction reaction (ORR) and an improved long-term stability in the accelerated stress test, as well as an enhanced maximum power density in the membrane electrode assemblies (MEAs) single cell test compared to Pt-CNTs. Meanwhile, Pt-CNTs/CNTs/GC and Pt-CNTs/RGO/CC exhibit enhanced mass specific activities for methanol oxidation reaction (MOR) and improved poisoning tolerances, in comparison with Pt-CNTs/GC and Pt-CNTs/CC, respectively. In addition, polyaniline (PANI) deposited CNTs/CC was prepared for the application in supercapacitors. The PANI/CNTs/CC electrode shows high capacitances calculated by cyclic voltammetry and galvanostatic charge/discharge curves, while CNTs/CNTs/CC and CNTs/RGO/CC expose their long-term electrochemical stability.

## German Version

Als effiziente, saubere und vielversprechende Energiequellen ziehen Polymerelektrolytmembran-Brennstoffzellen (PEMFCs) und Direktmethanol-Brennstoffzellen (DMFCs), die im Transportwesen, der stationären Stromerzeugung und als Stromquelle für tragbare Elektrogeräte, etc., eingesetzt werden können große Aufmerksamkeit auf sich. Die träge Kinetik der Sauerstoffreduktionsreaktion an der Kathode und der Methanoloxidationsreaktion an der Anode von DMFCs zusammen mit der Alterung der Katalysatoren haben jedoch die breite Marktimplementierung von PEMFCs und DMFCs behindert, zusammen mit hohen Kosten für Platin (Pt) und der schlechten Haltbarkeit der Elektrolytmembran und Methanol-Crossover durch die Elektrolytmembran. Um diese Probleme zu lösen, konzentriert sich die Forschung stark auf die Verbesserung der Leistung von Katalysatoren durch die Entwicklung neuartiger Katalysatoren wie legiertes Pt oder modifizierter Herstellungsverfahren wie der Mikrowellen-unterstützten Synthese. Der Katalysatorträger ist jedoch von ebenso großer Bedeutung, da er über eine große abgeschiedene Oberfläche zusammen mit einer hochporösen Struktur, einer guten Leitfähigkeit sowie Langzeitstabilität verfügen kann. Daher wurden hierarchisch strukturierte Katalysatorträger verwendet. Kohlenstoffnanoröhren (CNTs) oder Graphen wurden durch Bottom-up-Ansätze zur hierarchischen Struktur zusammengesetzt. CNTs wurden durch eine Abfolge von Abscheidung von Eisen (Fe) und chemischer Gasphasenabscheidung (CVD) auf der Oberfläche von oxidierten kommerziellen CNTs, Glaskohlenstoff (GC) und mit reduziertem Graphenoxid (RGO) bedecktem Kohlenstoffgewebe (CC) abgeschieden, jeweils zur Bildung von dreidimensionalen CNTs (3D-CNTs), CNTs/CNTs/GC und CNTs/RGO/CC-Elektroden. Auf diese Weise können CNTs durch Einstellen der Parameter der Fe-Elektroabscheidung und der CVD-Schritte angepasst werden. Bei der Herstellung von CNTs/CNTs/GC wurde aufeinanderfolgendes CNT-Wachstum durchgeführt, bei dem primäre CNTs durch CVD über Fe-Nanopartikeln präpariert wurden, gefolgt von einer zweiten Fe-Abscheidung und CVD-Wachstum von sekundären CNTs. Anschließend wurden Pt-Nanopartikel durch Nassimprägnierung homogen auf 3D-CNTs (ohne Substrate) und durch elektrochemische Abscheidung auf CNTs/CNTs/GC und NCNTs/RGO/CC abgeschieden. Auf jeden Präparationsschritt folgte Rasterelektronenmikroskopie (SEM) oder Transmissionselektronenmikroskopie (TEM), um den Erfolg der Präparationen zu

überprüfen. Währenddessen wurde das erfolgreiche CNT-Wachstum auch durch Raman-Spektroskopie nachgewiesen. Zusätzlich zeigen die hierarchisch strukturierten Elektroden vor der Pt-Abscheidung die erhöhten Doppelschichtkapazitäten in Zyklovoltammogrammen im Vergleich zu oxidierten kommerziellen CNTs, CNTs/GC bzw. CNTs/CC, was auf eine größere verfügbare Oberfläche für die weitere Pt-Abscheidung hinweist. Die drei präparierten hierarchischen Elektroden zeigen eine erhöhte elektrochemische Oberfläche, berechnet durch  $H_{ads/des}$ -Ströme und  $CO_{ad}$ -Oxidation der zyklischen Voltammetrie. Pt-3D-CNTs bietet im Vergleich zu Pt-CNTs eine höhere spezifische Aktivität der Sauerstoffreduktionsreaktion (ORR) und eine verbesserte Langzeitstabilität im beschleunigten Stresstest sowie eine verbesserte maximale Leistungsdichte im Einzelzellentest der Membranelektrodenanordnungen (MEAs). Währenddessen zeigen Pt-CNTs/CNTs/GC und Pt-CNTs/RGO/CC verbesserte massenspezifische Aktivitäten für die Methanoxidationsreaktion (MOR) und verbesserte Vergiftungstoleranzen im Vergleich zu Pt-CNTs/GC bzw. Pt-CNTs/CC. Zusätzlich wurde die mit Polyanilin (PANI) abgeschiedene CNTs/CC für die Anwendung in Superkondensatoren hergestellt. PANI/CNTs/CC zeigt hohe Kapazitäten, die durch zyklische Voltammogrammen und galvanostatische Lade-/Entladekurven berechnet wurden, während CNTs/CNTs/CC und CNTs/RGO/CC eine ausgezeichnete elektrochemische Stabilität aufweisen.

# *Chapter 1:*

## **Motivation and Aim**

---

The World Health Organization reports that outdoor air pollution, which includes particulate matter, ozone, nitrogen dioxide and sulphur dioxide, is a major threat to global climate and health. About 4.2 million premature deaths per year are associated with ambient air pollution, mainly from lung cancer, stroke, heart disease, chronic obstructive pulmonary disease, etc., probably caused by PM 10 (particulate matter in the 2.5-10  $\mu\text{m}$  range) and PM 2.5 (particulate matter  $\geq 2.5 \mu\text{m}$  in aerodynamic diameter) in the air penetrating the thoracic region of the respiratory system [1]. PM 2.5 is a stronger risk factor than PM 10 and 25% of PM 2.5 is caused by traffic [2–4]. Furthermore, since the population worldwide has increased rapidly in the last few decades, the energy demand is continuously rising, along with emissions of innumerable greenhouse gases like  $\text{CO}_2$ ,  $\text{NO}_x$ , etc., that are primarily produced by combustion of fossil fuels (e.g., petroleum, coal, natural gas) in transportation and electricity production, leading to global warming [5–7]. Additionally, depletion of fossil fuels is an irreversible process, while the efficient nuclear power generation suffers from challenges regarding safety and the disposal of its radioactive waste. Therefore, the development and application of renewable energies is of crucial importance. At present, solar, water, wind and tidal, etc., have been used as renewable energies to varying degrees, depending on regional topographies and climate conditions, but they highly depend on weather conditions resulting in fluctuations in the availability of energy, impacting produced electrical energy and the stability of power grids [8, 9]. Meanwhile, hydrogen ( $\text{H}_2$ ) is also considered as one solution to the energy problem and greenhouse effect since  $\text{H}_2$  is a clean and sustainable energy carrier without emission of greenhouse gases. It can be an alternative to fossil fuels in many

applications [9–12]. Application of hydrogen in fuel cells, in which H<sub>2</sub> can be utilized as a fuel for electricity generation, has received considerable attention.

Fuel cells are electrochemical energy conversion devices that directly convert chemical energy into electrical energy. They are used for stationary power generation, portable power for laptops and power for transportation like automobiles, forklifts, airplanes, etc., depending on their power. The power is determined by the varying electrolytes and fuels, as well as the size of the electrodes and their efficiency. The representative models of current fuel cell vehicles (e.g., Toyota's Mirai, Honda's Clarity and Hyundai's NEXO) employ hydrogen as fuel in polymer electrolyte membrane fuel cell (PEMFCs) and possess a power range of about 113-130 KW, an average cruising range of about 500-750 km and a hydrogen refueling time of a few minutes. [13–16] These factors are competitive to vehicles using lithium battery systems. However, the large-scale commercialization of PEMFCs is hindered by the high costs and scarcity of Pt, sluggish kinetics and the corrosion of catalyst supports [17–19], along with a lack of sufficient hydrogen infrastructure [16, 20] as well as high costs and poor durability of the polymer electrolyte membrane [21, 22]. Meanwhile, the practical application of direct methanol fuel cells (DMFCs) suffers from similar issues, such as slow kinetics of methanol oxidation, catalyst poisoning and methanol crossover [23–25]. Additionally, the typical polarization curve of a fuel cell displays decreased cell voltage attributed to activation related losses, Ohmic losses and mass transport related losses [26–31] (see Figure 1.1).

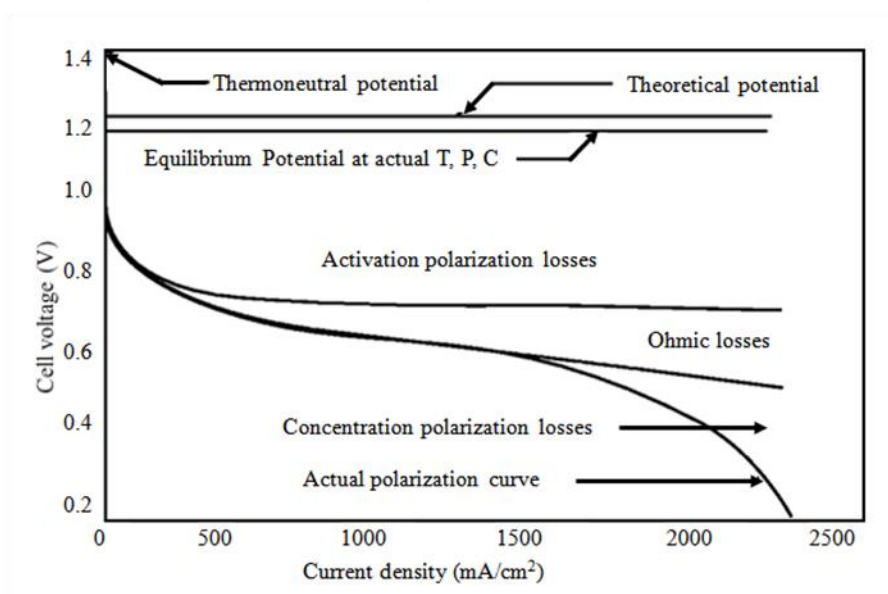


**Figure 1.1.** Typical polarization curve of a PEM fuel cell, reprinted from [30, 31] with permission.



Considering these challenges, numerous studies were focused on the development of catalysts for PEMFCs and DMFCs [32–36], for the purpose of reducing Pt contents and enhancing catalytic activity and stability. However, catalyst supports are also of crucial importance to facilitate the catalysts distribution, catalytic activity and stability. Carbon black is currently used as the commercial catalyst support, but it suffers from corrosion at high potentials, resulting in the dissolution or aggregation of Pt nanoparticles and thus the loss of electrical contact [19, 37, 38]. Meanwhile, different carbon-based catalyst supports such as carbon nanotube (CNTs), graphene and carbon-based composites were studied, where the deposited catalysts showed improved electrochemical performance and stability [17, 38–45]. Moreover, the 3-dimensional (3D) nanostructure based CNTs exhibited enhanced specific surface area and specific double layer capacitance, along with improved pore size distribution and reduced equivalent series resistance [46, 47]. To combine these advantages, CNT-based hierarchically nanostructured catalyst supports were proposed to provide large surface area, high electrical conductivity and proper pore structure, improving catalyst deposition as well as mass transport.

In this work, a toolbox strategy was developed using bottom-up approaches to prepare the hierarchical nanostructure. In the toolbox, the materials of required functionalities were assembled by a stepwise approach with respect to a given electrochemical application, in which each step was tuned. In the preparation of CNT-based hierarchically structured electrodes, the major steps were catalyst deposition and CNT growth over the deposited catalysts by chemical vapor deposition (CVD). In this way, CNTs were grown onto the commercial CNTs and the reduced graphene oxide deposited carbon cloth (RGO/CC) to form 3-dimensional (3D) CNTs and CNTs/RGO/CC, respectively, while the CNTs/CNTs/GC was synthesized by repeating the sequence of catalyst deposition and CNT growth on glassy carbon (GC). Additionally, polyaniline was further introduced into the hierarchical structure for supercapacitors. The materials produced by each step of the bottom-up synthesis were monitored employing scanning electron microscopy (SEM) or transmission electron microscopy (TEM). Raman spectroscopy, elemental analysis and X-ray diffraction were used to characterize them. Furthermore, Pt nanoparticles were deposited on the prepared hierarchically structured materials. The electrochemical available surface area was determined by  $H_{ads/des}$  and  $CO_{ad}$  oxidation in cyclic

voltammograms, respectively. Finally, their electrocatalytic performances were evaluated using oxygen reduction reaction or methanol oxidation reaction as test reactions.

## *Chapter 2:*

# **Basic Concepts**

---

### **2.1. Fuel Cells [28, 31, 48–51]**

The fuel cell principle was firstly observed in 1838 by the German-Swiss chemist Christian Friedrich Schönbein [52]. William Grove demonstrated the fuel cell in 1839 and realized a first gaseous voltaic battery in 1842 providing electrical energy produced by combining hydrogen and oxygen [53, 54]. In 1952, a 5 kW fuel cell stack was constructed by Francis Bacon. Since the early 1960s, the alkaline fuel cell was practically developed in the space missions of NASA such as Gemini and Apollo space programs, supplying electricity for guidance, communication and life support, while providing electrical needs in a shuttle orbiter. In the mid-1960s, the fuel cells produced by Union Carbide were tested as a power for vans by General Motors (GM), and Ballard developed a PEMFCs-powered submarine in 1989 and fuel cell-powered buses in 1993. In the same year, the first PEMFCs-powered passenger car was presented by Energy Partner. After that, fuel cell-powered vehicles are developed by many car manufacturers, like Honda, Toyota, Daimler Chrysler, GM, BMW, etc.

#### **2.1.1. Working Principle [28, 31, 48–51]**

A fuel cell is one of electrochemical energy conversion devices that directly converts chemical energy into electrical energy by a working principle similar to reversing water electrolysis.[48] It consists of a cathode catalyst layer, an anode catalyst layer, an electrolyte, and a gas diffusion layer on the cathode side and the anode side (see Figure 2.1).

Existing fuel cells operate in a similar manner. At the anode, the primary fuel is oxidized to protons that are transported to the cathode through the electrolyte, and then the oxygen at the cathode is reduced to water and the electrical energy is released. Alternatively, the oxygen at the cathode is reduced to hydroxide or oxide ions that are transported through the electrolyte to the anode where the primary fuel is oxidized to water, or water and carbon dioxide to produce electrical energy. The electrolyte should be electrically insulating and promote the transport of protons, hydroxide or oxide ions between the cathode and anode side.

### **2.1.2. Types of Fuel Cells and their Applications [28, 31, 48–51]**

According to the electrolyte and primary fuels employed in fuel cells, the fuel cells can be classified into proton exchange membrane fuel cells (PEMFCs), direct methanol fuel cells (DMFCs), phosphoric acid fuel cells (PAFCs), alkaline fuel cells (AFCs), molten carbonate fuel cells (MCFCs) and solid oxide fuel cells (SOFCs) as shown in Table 2.1, in which each type shows its oxidation and reduction reaction in the anode and cathode, common catalysts, electrolytes and different operating temperatures. Generally, fuel cells can be categorized by the operating temperature, namely low or high-temperature fuel cells. Additionally, DMFCs are essentially polymer membrane fuel cells using methanol instead of hydrogen as a fuel. To distinguish from PEMFCs ( $H_2/O_2$ ), they are categorized as another type of fuel cells in this work.

Because of their different operating temperatures and powers, fuel cells are used in stationary or portable applications. Compared to the first four fuel cells, the operating temperatures of SOFCs and MCFCs are very high and can produce a power of 10–100 MW to supply power and heating in industrial plants, but they are not easy to start or shut down. PAFCs have a power range of 10-250 kW, which can be used as a medium-sized power generation for hospitals and telecommunications. A power rating of 10 kW or lower is needed for small fixed power generation like residential distributed energy, in which AFCs or PEMFCs can be applied. Moreover, PEMFCs and DMFCs can be used as portable power generators in vehicles, laptops, etc., because of their high efficiency without pollution and noise as well as low temperature and vibration-free operation. Since DMFC use methanol as a liquid fuel,

their applications can be implemented with fewer constraints in terms of fuel handling, refueling and storages compared to hydrogen. [48, 31]

**Table 2.1.** Types of fuel cells, their reactions at anode and cathode, electrolyte and operating temperatures.

Types Catalyst	Anode	Electrolyte	Cathode	Operating temperature
<b>PEMFCs</b> Platinum	$\text{H}_2 \rightarrow 2 \text{H}^+ + 2 \text{e}^-$	$\xrightarrow{\text{H}^+}$ Polymer membrane	$\text{O}_2 + 4 \text{H}^+ + 4 \text{e}^-$ $\rightarrow 2 \text{H}_2\text{O}$	60~80 °C
<b>DMFCs</b> Platinum	$\text{CH}_3\text{OH} + \text{H}_2\text{O}$ $\rightarrow 6 \text{H}^+ + \text{CO}_2 + 6 \text{e}^-$	$\xrightarrow{\text{H}^+}$ Polymer membrane	$\frac{3}{2} \text{O}_2 + 6 \text{H}^+ + 6 \text{e}^-$ $\rightarrow 3 \text{H}_2\text{O}$	80~110 °C
<b>PAFCs</b> Platinum	$\text{H}_2 \rightarrow 2 \text{H}^+ + 2 \text{e}^-$	$\xrightarrow{\text{H}^+}$ $\text{H}_3\text{PO}_4$	$\text{O}_2 + 4 \text{H}^+ + 4 \text{e}^-$ $\rightarrow 2 \text{H}_2\text{O}$	~205 °C
<b>AFCs</b> Platinum	$\text{H}_2 + 2 \text{OH}^-$ $\rightarrow 2 \text{H}_2\text{O} + 2 \text{e}^-$	$\xleftarrow{\text{OH}^-}$ KOH or NaOH	$\text{O}_2 + 2 \text{H}_2\text{O} + 4 \text{e}^-$ $\rightarrow 4 \text{OH}^-$	65~220 °C
<b>MCFCs</b> Nickel	$\text{H}_2 + \text{CO}_3^{2-} \rightarrow \text{CO}_2 +$ $\text{H}_2\text{O} + 2 \text{e}^-$ $\text{CO} + \text{CO}_3^{2-}$ $\rightarrow 2 \text{CO}_2 + 2 \text{e}^-$	$\xleftarrow{\text{CO}_3^{2-}}$ Molten carbonate in $\text{LiAlO}_2$	$\text{O}_2 + \text{CO}_2 + 4 \text{e}^-$ $\rightarrow 2 \text{CO}_3^{2-}$	~650 °C
<b>SOFCs</b> Perovskites	$\text{CO} + \text{O}^{2-}$ $\rightarrow \text{CO}_2 + 2 \text{e}^-$ $\text{CH}_4 + 4 \text{O}^{2-}$ $\rightarrow 2 \text{H}_2\text{O} + \text{CO}_2$ $+ 2 \text{e}^-$	$\xleftarrow{\text{O}^{2-}}$ Ceramic	$\text{O}_2 + 4 \text{e}^- \rightarrow 2 \text{O}^{2-}$	600~1000 °C

## 2.2. Basic Concept of PEMFCs and DMFCs

### 2.2.1. Design of Cells [28, 31, 48–51]

Figure 2.1 shows a schematic representation of a unit in PEMFCs and DMFCs. A polymer electrolyte membrane (PEM), which is the center of the cell and utilized as electrolyte between two electrodes, conducts protons from anode to cathode, but  $H_2$ ,  $O_2$  or  $CH_3OH$  should not permeate through the film. Electrochemical reactions occur on the surface of the catalyst in the catalyst layer (CL) at the interface between gas diffusion layer and polymer film. Firstly, hydrogen or methanol is fed through the gas diffusion layer (GDL) to the surface of catalyst at the anode side, and liberates protons and electrons. The electrons transport through the electrically conductive electrodes and the current collectors as well as the outside circuit and arrive at the other side of the membrane, while protons transport through the membrane to the catalyst layer of the cathode side. Meanwhile, oxygen or air is fed through gas diffusion layer to the catalyst layer at the cathode side and meets the traveled proton and electrons to produce  $H_2O$ . In the process, a direct electrical current and a theoretical voltage of about 1.23 V are generated in an external circuit. In actual applications, a voltage of about 1 V is achieved. More cells can be stacked up to achieve higher output voltage with respect to the given application. [28, 31, 48–50]

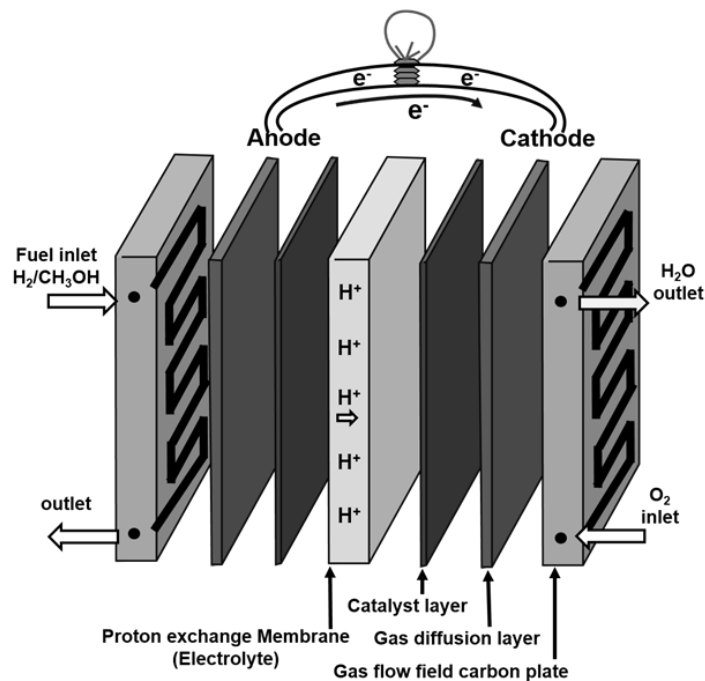


Figure 2.1. Schematic representation of PEMFCs and DMFCs.

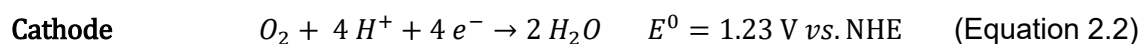
The gas diffusion layer (GDL) should provide simultaneous electricity and heat transfer, and a porous structure, through which  $H_2$ ,  $CH_3OH$  or  $O_2$  can be fed from the back of the GDL and easily diffuse to the catalyst layer, while leading the produced water and excess gas to flow away in the reverse direction without accumulation. GDL is usually prepared from carbon fiber paper or carbon cloth that is covered with hydrophobic polymer (PTFE) to facilitate water release. The catalyst layer may be assembled on the GDL or the PEM, depending on the preparation process. At the catalyst layer, platinum supported on carbon materials typically serves as a catalyst of oxygen reduction reaction and hydrogen oxidation reaction or methanol oxidation reaction, which is crucial to affect performances of PEMFCs and DMFCs, which is discussed in detail below. Moreover, the PEM is also an important factor to influence the durability and lifetime of PEMFCs, and should possess high proton conductivity, be insulating towards electrons and prevent fuel and reactive gas mixtures crossover between the two electrodes along with chemical and mechanical stability. Commonly, perfluorosulfonic acid (PFSA) is used as a PEM, in which the proton can be transported by the sulfonic acid groups. As a well-known PEM, the Nafion<sup>TM</sup> membrane manufactured by Dupont<sup>TM</sup> is made of perfluoro-2-(2-fluorosulfonylethoxy) propyl vinyl ether (PSEPVE). [31, 55] Thus, the GDL, CL and PEM between the two electrodes assemble to a multilayer film that is called membrane electrode assembly (MEA).

Additionally, the MEA is located between bipolar plates. The bipolar plates have a channel structure on their surface to feed fuel and provide structural support for a single cell along with hydrophobicity, electrical and thermal conductivity. In a multi-cell construction, the bipolar plates separate the unit cells and connect the cathode of a cell with the anode of an adjacent cell physically and electrically. Since their materials are gas-impermeable, they have channels on two sides. Through the channels hydrogen or methanol is supplied to the anode of one unit on one side, while oxygen is supplied to the cathode of another adjacent unit on the other side, and the produced water at the cathode and excess gases transport out of the cell. Graphite plates are commonly used as bipolar plates because they are chemically inert. Meanwhile, some metal plates need to be coated by a protection layer with corrosion resistance and electrical conductivity to be proper bipolar plates. [56–58]

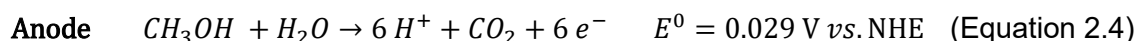
### 2.2.2. Basic Reactions of PEMFCs and DMFCs [28, 31, 48–51]

In the design of PEMFCs and DMFCs, platinum supported on carbon materials is generally used as catalyst layer at the cathode and anode, respectively, which is coated onto gas diffusion layer or the polymer film. Over Pt particles, the complete reaction at the anode is  $H_2$  oxidation or methanol oxidation owing to the fed fuels, while oxygen reduction reaction occurs at the cathode and water is produced, as given by the following equations, in which several intermediate steps or side reactions may occur, as discussed in 2.2.3 and 2.2.4.

*Complete reaction in  $H_2/O_2$  PEMFCs:*



*Complete reaction in DMFCs:*



Compared to hydrogen oxidation, the kinetics of oxygen reduction and methanol oxidation are much slower [59], which has hindered the wide commercialization of PEMFCs and DMFCs, so that the mechanism of ORR and MOR have been widely studied and discussed.

### 2.2.3. Mechanism of Oxygen Reduction Reaction [28, 48, 31, 35, 60]

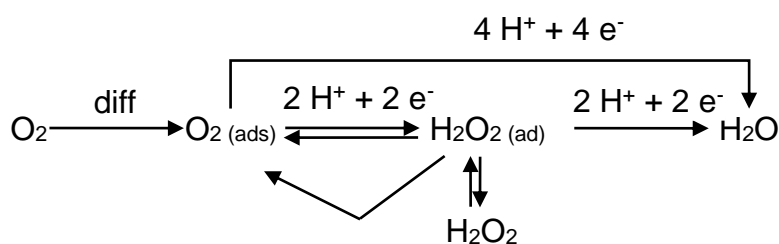


**Figure 2.2.** The mechanism of the oxygen reduction on Pt. [48, 60]



The mechanism of the oxygen reduction reaction on Pt has attracted extensive attention. Many mechanism schemes concerning the possible pathways of oxygen reduction and their different intermediates have been reported [60–64], since oxygen reduction is a multi-electron process accompanied by different reaction intermediates. The simplified mechanism displayed in Figure 2.2 was firstly suggested by Wroblowa *et al.* [60], in which oxygen is directly reduced to water by a 4-electron transfer process in a direct reduction pathway, while the indirect reduction pathway utilizes a series of 2-electron transfer processes to initially reduce oxygen to hydrogen peroxide that may be further reduced to water or be a final product.

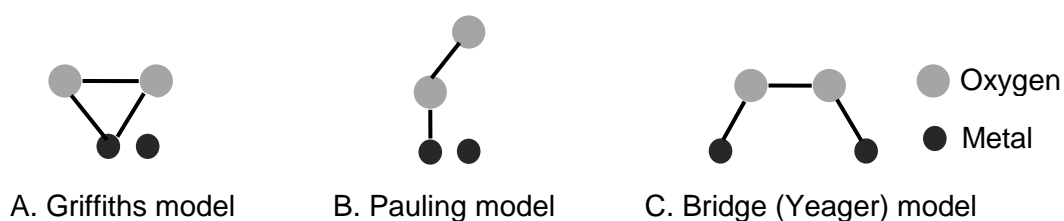


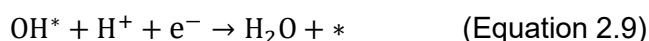
**Figure 2.3.** Possible configurations of O<sub>2</sub> on the metal surface.

Furthermore, three adsorption modes for oxygen on the metal surface, namely the Griffiths-, Pauling- and bridge mode, were proposed [62]. The modes and the interactions of the adsorbed oxygen on the metal surface can influence the oxygen reduction pathway [65]. In the Griffiths model and bridge model, the O–O bond is weakened due to the overlap between the oxygen  $\pi$ -orbitals and metal empty d-orbitals so that the O–O bond could be weakened to the further dissociation, in which the four-electron pathway is favored to occur. In the Pauling model, only one oxygen is adsorbed on the metal surface so that the O–O bond cannot be sufficiently weakened and cannot easily be dissociated, and only partial charge can be transferred, resulting in the formation of peroxides.

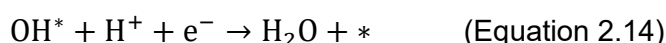
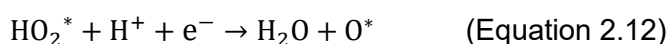
Additionally, the dissociative mechanism at low current density and the associative mechanism at high current density were proposed by Nørskov *et al.* [63], which were theoretically determined through the density functional theory (DFT) (see Equation 2.7-2.14). In the dissociative mechanism, the O–O bond is broken by oxygen adsorption and adsorbed atomic O was formed followed by subsequently combining with electrons and protons to form water, which compares to the direct oxygen reduction pathway [51]. However, the hydrogen peroxide as intermediates in indirect

oxygen reduction pathway is not shown in associative mechanism, still the O-O bond is not broken at the start so that hydrogen peroxide might be formed.

*Dissociative mechanism:*



*Associative Mechanism:*



where \* denotes a site on the Pt surface.

#### **2.2.4. Mechanism of Methanol Oxidation Reaction [28, 48, 50]**

Pt is considered as the most active monometallic catalyst for methanol oxidation [66–70]. Many studies have focused on its mechanism, in which a dual path mechanism has been suggested along with many possible intermediates and competing reaction pathways [70–78, 68]. On Pt, methanol oxidation can proceed in two parallel reaction pathways: direct reaction pathways and indirect reaction pathways, which are governed by the initial activation of C-H and O-H bond [74], respectively, as shown in Figure 2.4. In the indirect pathway  $\text{CO}_{\text{ad}}$  is formed by a series of dehydrogenation steps of methanol and subsequently oxidized to  $\text{CO}_2$ , while in the direct pathway the formation of soluble intermediates like formaldehyde and formic acid proceeds and  $\text{CO}_2$  can be formed by their subsequent oxidation.  $\text{CO}_{\text{ad}}$  was recognized as the most stable adsorbate and could poison the Pt surface at low potentials [79, 80, 72], because CO is formed on the Pt surface and occupies the sites required for the formation of hydroxyl intermediates that probably facilitate the subsequent oxidation of  $\text{CO}_{\text{ad}}$ . Additionally, it was observed that the rate of methanol dehydrogenation on Pt was dependent on potential and surface structure [75, 81, 78],

while the ratio of surface adsorbates to dissolved species was associated with electrode potential and CO adsorbed anions [82]. To solve the poisoning, novel catalysts and catalysts supports have been studied and are discussed in Chapter 2.3 and 2.4.

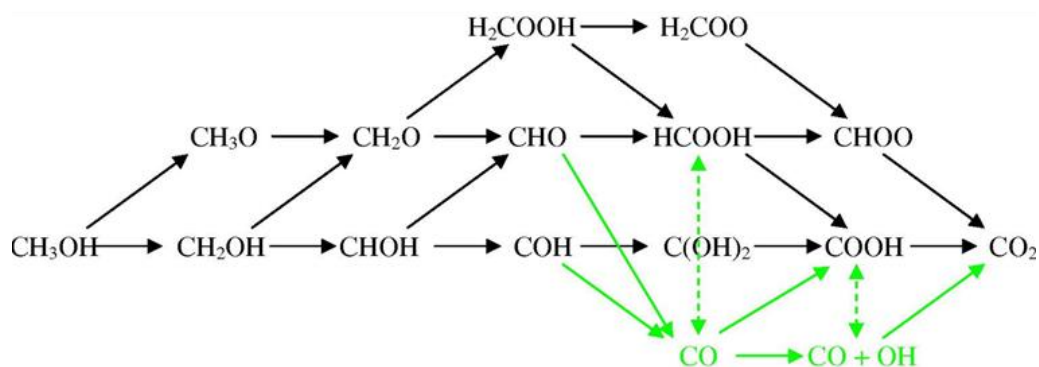


**Figure 2.4.** Schematic representation of the reaction paths and possible intermediates, green arrows indicate the indirect mechanism to CO<sub>2</sub> formation, reprinted from [70] with permission.

## 2.3. Catalysts in PEMFCs and DMFCs

### 2.3.1. Catalysts for Hydrogen Oxidation Reaction

Pt is commercially used as a catalyst in the anode and cathode of PEMFCs and DMFCs, respectively [83–86]. Compared to oxygen reduction reaction or methanol oxidation reaction, hydrogen oxidation reaction (HOR) in acid media has attracted less attention since the HOR kinetics on Pt is by a magnitude of about 5-7 faster than ORR kinetics in general conditions [87–91]. Pt-group metals (e.g., Pt, Ir, Pd, Rh, Re) were considered to have a superior activity for HOR by evaluating the kinetic parameters [51, 92, 93], while Pt displayed a much higher exchange current density for HOR in acid media, compared to Rh, Ru, Pd, Ir, etc. [94, 95] Additionally, it is reported that Pt loading was reduced to about 0.05 mg<sub>Pt</sub> cm<sup>-2</sup> in the PEMFC anode electrode and no significant cell voltage losses occurred in the fuel cell operation with pure H<sub>2</sub> [96]. Hence, Pt is appropriate for anode catalyst applications.

### 2.3.2. Catalysts for Oxygen Reduction reaction

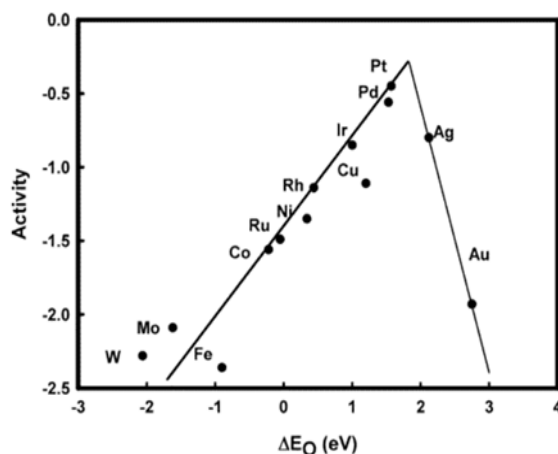


**Figure 2.5.** ORR volcano plot: ORR activity plotted as a function of oxygen binding energy, reprinted from [63] with permission.

The activities of monometallic catalysts as a function of the oxygen binding energy are displayed in Figure 2.5 [63]. Pt shows a better catalytic activity for ORR than other monometallic catalysts, which is also revealed in the trend as a function of both the O and the OH binding energy in ORR [63]. However, overpotentials were observed in studies, because there are multiple intermediates ( $\text{OOH}^*$ ,  $\text{OH}^*$ ,  $\text{O}^*$ ) in ORR that are strongly correlated and difficult to be decoupled owing to the scaling relations [63, 97–99, 88], unlike in HOR with one reaction intermediate. In addition, the theoretical thermodynamic potential of oxygen reduction is 1.23 V (see Equation 2.2). At that potential, Pt is not stable and suffers from oxidation to form PtO that has slower ORR kinetics than Pt [100].

Therefore, the research on ORR catalysts is important to promote the development of the PEMFCs and DMFCs. The controlled shape of the catalysts and alloying of Pt have been developed. The single crystalline Pt (110), (111) and (100) facets have different activities towards ORR and different electrolytes could affect the performances [101]. Thus, the ORR activities of different Pt morphologies have been reported [102–105]. For example, Pt octahedra and cubic nanocages enclosed by (111) and (100) facets showed enhanced mass activity at 0.9 V vs. RHE compared to Pt/C [102]. Supportless Pt nanotubes had increased activity and durability in ORR [103], while the specific activity of 8 nm Pt nanocubes in a (100) textured array was over twice as high as that of commercial Pt nanoparticles [104].

For Pt alloying, late transition metals like Ni and Co were used to form PtNi and PtCo for increased ORR activity, but they commonly degraded in long-term tests via dealloying [106, 17, 107]. Through further incorporation of transition metals like V, Cr, Mn, Fe, Co, Mo, W, Re on the surface of Pt alloys, the ORR activity and stability are enhanced. For example, Mo deposited octahedral Pt<sub>3</sub>Ni/C showed an 80 times increase of ORR activity and enhanced stability compared to the commercial catalyst [108]. Rare earths like Y, La and Gd were also used in Pt alloying to form Pt<sub>x</sub>Y, Pt<sub>x</sub>La and Pt<sub>x</sub>Gd and they showed an increased ORR activity, which is probably correlated to a compressive strain on platinum surface atoms [109–113]. Other than by composition, the catalytic properties are also influenced by the morphology and structure of Pt based nanocatalysts. Pt based core-shell nanoparticles (e.g., Pt/Cu, Pt/Fe, etc.) displayed significant improvements of activity and durability for ORR [114, 115], in which their structural and electronic properties can be tuned by modification of the Pt shell thickness, diameter, shape and composition of core.

Additionally, precious metal free catalysts are considered as potential alternative to costly and scarce Pt based catalysts. Carbons modified with nitrogen, boron, fluorine, phosphorus and sulfur have been used as catalysts of ORR [116–118]. The metal free nitrogen modified carbon (N-C) commonly displayed a much lower ORR activity in acidic electrolytes than Pt/C [119]. The metal-nitrogen-carbon catalysts (M-N-C) such as Fe-N-C and Co-N-C have been developed and showed increased activity of ORR compared to N-C in acidic electrolytes [119–122]. For example, PANI-Fe-C prepared by combining polyaniline (PANI) with Fe salts displayed a same current as commercial catalyst ETEK-Pt/C at a low overpotential of 60 mV in acid [123]. Furthermore, Fe-N-C synthesized with PANI and cyanamide exposed a superior ORR activity and selectivity in comparison with the precious metal free catalysts in previous reports [124]. Its current density was similar to that obtained by 0.1 mg Pt cm<sup>-2</sup> at the voltages of > 0.75 V in the kinetic region of cathode operation in H<sub>2</sub>-air PEMFC, whereas lower current densities were observed in the mass transport region, indicating a mass transport limitation. To match the performance of Pt based catalysts and replace them, the ORR activity of precious metal free catalysts should be further developed and more investigations in real applications of fuel cells should be conducted.

### 2.3.3. Catalysts for Methanol Oxidation Reaction

Pt is considered to be the most active monometallic catalyst for methanol oxidation reaction, which is demonstrated by combining the calculated adsorption free energies for various intermediates on metal surfaces with a simple electrokinetic model of MOR [70]. But its onset potential of MOR was limited by the ability of methanol and water activation as well as by poisoning by intermediates formed in the indirect pathway [73], while reducing the amount of Pt is suggested due to the scarcity and high cost of Pt. The incorporation of other metals into Pt catalysts as an effective strategy has been developed [125, 34, 126, 127].

Pt alloying with a second metal like Ru, Ni, Au, Fe, Cu, Co, Mo showed an increased electrocatalytic activity and CO poisoning tolerance towards MOR [128–131], usually explained by bifunctional mechanism and geometric and electronic effects combined [132, 133]. The bifunctional mechanism is that the incorporated metal can promote the formation of  $\text{OH}_{\text{ad}}$  species to oxidize the adsorbed intermediates on neighboring Pt sites and liberate the Pt surface for the further methanol oxidation, whereas the geometric and electronic effects originate from the lattice contraction and downshift of the d-band center of Pt on the alloy surface [128, 129, 134]. Subsequently, trimetallic Pt based alloys have been developed as efficient catalysts for MOR, such as Pt-Ni-Co, Pt-Ni-Cu, Pt-Pd-Cu, Pt-Au-Ru and so on [36, 135–138]. Meanwhile, composites of Pt and non-precious metal oxides such as  $\text{TiO}_2$ ,  $\text{CeO}_2$ ,  $\text{SnO}_2$ ,  $\text{Sn}_x\text{Ti}_{1-x}\text{O}_2$  [139–142] were also prepared and displayed the improved electrocatalytic activity, but the improvement in durability was not significant. Apart from metal oxides,  $\text{Ni}(\text{OH})_2$  was used to enhance electrocatalytic activity of Pt for MOR. Pt/ $\text{Ni}(\text{OH})_2$  supported on graphene showed exceptional activity and durability towards MOR, which was caused by the incorporation of  $\text{Ni}(\text{OH})_2$  that greatly promotes the dissociative adsorption of water molecules along with oxidizing the carbonaceous intermediates via the Langmuir–Hinshelwood pathway to reduce the Pt poisoning [143].

In addition, the activity performance could depend on the catalyst accessible surface, shape, size and structure, so that various morphologies like polyhedrons, nanodendrites, concave nanostructures, nanoframes and nanocages were studied [144–150]. For example, the trimetallic PtNiCu excavated rhombic dodecahedrons

(ERD) exhibited an enhanced electrocatalytic performance towards MOR in comparison with bimetallic PtCu ERD and PtNiCu solid rhombic dodecahedrons, because of highly excavated rhombic dodecahedral structures and abundant stepped atoms, as well as electronic and synergistic effects [144]. The MOR activity of the hexapod PtRuCu/C was higher than that of the dendrites PtRuCu/C [145].

## **2.4. Catalysts Supports for Oxygen Reduction Reaction and Methanol Oxidation Reaction**

The electrocatalytic activities were increased through the catalyst development as mentioned above, whereas optimizing the catalyst supports is of equal importance to improve the electrocatalytic performance. Catalyst supports can affect the properties of deposited catalysts like their distribution, particle size, morphology, alloying degree and stability, as well as mass transport, conductivity of catalyst layer and stability in the fuel cells [125, 151, 152, 35, 153]. Thus, the ideal catalyst support should provide a large specific surface area, optimized porosity, high electric conductivity, good chemical and mechanical stability in order to promote deposition of catalysts, resulting in the improvement of their electrocatalytic activity, corrosion resistance and long-term durability, as well as increase of mass transfer and reduction of Ohmic loss [125, 151].

Carbon black is commercially used as catalyst support at the cathode and anode due to its relative high specific surface area, stability in acidic and basic media and good electric conductivity, whereas the decreased electrocatalytic performance was exposed owing to weak interactions between carbon and catalyst particles leading to agglomeration and detachment of the catalysts during the measurement [17–19]. In particular, carbon corrosion occurs at highly positive potentials at the cathode in PEMFCs and DMFCs. The novel support materials are required to promote improvement of Pt dispersion and stability [39–42]. Highly graphitized carbon materials like CNTs, graphene and carbon nanohorns have improved corrosion resistance compared to carbon black, and have been developed as support materials in ORR [154, 38, 155–157] and MOR [158–162]. In both reactions, they displayed more efficient electrocatalytic performances, probably due to the improved

distribution and small particle size of the catalyst particles. The improved catalyst deposition was probably caused by larger surface area and higher electronic conductivity of catalyst supports. Between Pt d-orbital and  $\pi$  sites on the carbon surface there is electron delocalization, resulting in the partial formation of covalent bonding along with their strengthened interaction, which could increase Pt stability during the reactions [163, 164]. Meanwhile, ordered mesoporous carbon (OMC) was also designed as a support catalyst and it had hierarchical nanostructure with high surface area and ordered pores to facilitate Pt dispersion and mass transport of reactants and products. Pt supported on OMC showed enhanced ECSA and higher electrocatalytic activity for MOR and ORR with respect to the commercial Pt/C [165].

Furthermore, functional groups or heteroatom containing O, N, B, S and P are incorporated to modify the carbon structure to improve the binding strength between catalyst and carbon along with modifying the electronic structure of the catalyst, leading to a high dispersion with narrower size distributions of the catalyst. The catalysts showed increased catalytic activities and durability towards MOR [166, 167] and ORR [168]. Pt supported on thiolated CNTs exposed enhanced tolerance against Pt dissolution at more positive electrode potentials in ORR and less decrease of ECSA in the durability test. Their improved stability was achieved through the increased interaction of the S-Pt [169]. Additionally, nitrogen doping in ordered mesoporous carbon as support increased Pt:Ru atomic ratio at the near surface of catalyst to 70:30 compared to that before N-doping. This led to a faster oxidation of methanol, due to Pt enrichment and an increased intrinsic activity of PtRu nanoparticles [170].

To further obtain an effective electron transport pathway with increased available surface area and porosity of supports, 3-dimensional (3D) or hierarchical nanostructure supports are designed, such as CNTs-graphene hybrid, CNT-carbon black hybrids, polyaniline-reduced graphene oxide, CNTs-CNTs (3D CNTs) [171–173] [174–180]. The formed 3D CNTs had increased specific surface area, improved pore size distribution and electron transfer [46, 181, 182, 47]. Pt deposited on 3D CNTs/carbon cloth exposed a higher reduction current for ORR compared to Pt on CNTs/carbon cloth and on carbon cloth [47]. Pt, PtRu or PtRuMo supported on CNTs-RGO composites showed increased electrocatalytic performances including



MOR activity and CO tolerance owing to their hierarchical structure [183, 174, 184–186]. Furthermore, it was reported that the composites formed by directly growing CNTs onto graphene as Pt support favored an increased MOR activity of Pt with respect to the composites produced by simply mixing [186]. Meanwhile, Nitrogen doped CNTs-RGO composites were prepared and investigated, which showed a larger surface area and an enhanced pore size. The Pt supported on them showed improved MOR kinetics and long-term stability, and the mass transfer loss reduced in the cell test [173, 172].

Additionally, non-carbonaceous materials like  $\text{TiO}_2$ ,  $\text{WO}_x$ , TiC, WC have been studied as Pt supports. There is a similar interaction between Pt and supports like those described above in Chapter 2.3.3, so that the Fermi level or electronic states of Pt were changed and the electrocatalytic activity and durability of catalysts was increased [187]. For example, the surface electronic structure of Pt was modified by the lattice contraction and downshift of the d-band center of Pt after deposition on  $\text{Ti}_{0.7}\text{Mo}_{0.3}\text{O}_2$ . The catalyst showed increased ORR current densities and high stability [187], while the durability and CO tolerance for methanol oxidation increased [188, 189].

#### **2.4.1. Carbon Nanotubes and their Growth Mechanism by Thermal Chemical Vapor Deposition**

CNTs or graphene can be utilized as catalyst supports in the development of catalyst supports mentioned above. In this work, the preparation of hierarchically nanostructured Pt supports was achieved by consecutively synthesizing carbon nanotubes or reduced graphene oxide. Hence, a basic introduction to CNTs, graphene and their synthesis mechanism is given below.

Apart from CNT applications in electrochemical conversion devices like PEMFCs and DMFCs mentioned above, CNTs can be utilized in acoustic sensors, field emission devices, mechanical devices, optical devices, electrical devices, chemical storage devices and so on, due to their unique properties, large surface area, high electrical conductivity, extremely high tensile strengths, electronic structure, as well as high chemical, mechanical and electrochemical stability, etc. [190–198] CNTs can be described as a seamless hollow cylinder rolled up from a layer or multiple layers

of graphene, and can be categorized into single wall carbon nanotubes (SWCNTs) and multi-walled carbon nanotubes (MWCNTs) (see Figure 2.6a and 2.6b) [199].

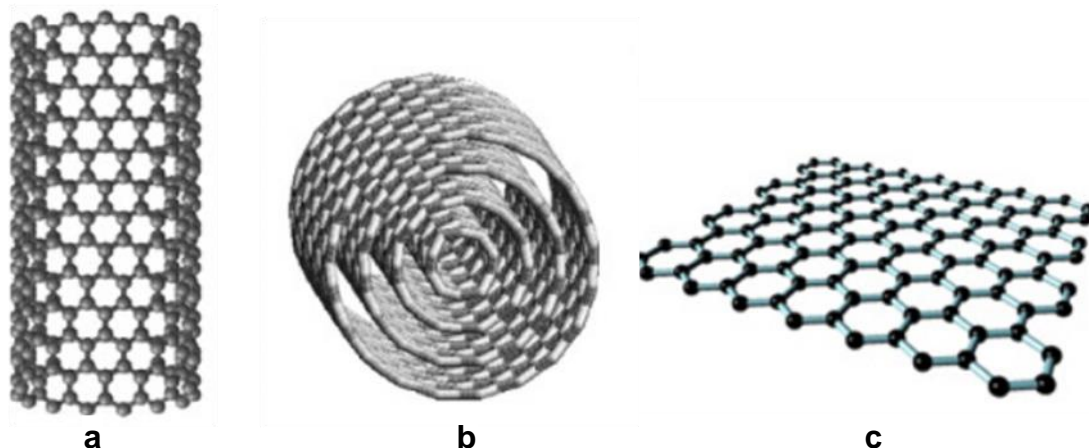


**Figure 2.6.** Schematic diagram of (a) single wall carbon nanotube, (b) multi-wall carbon nanotube, reprinted from [199] with permission; and (c) graphene, reprinted from [237] with permission.

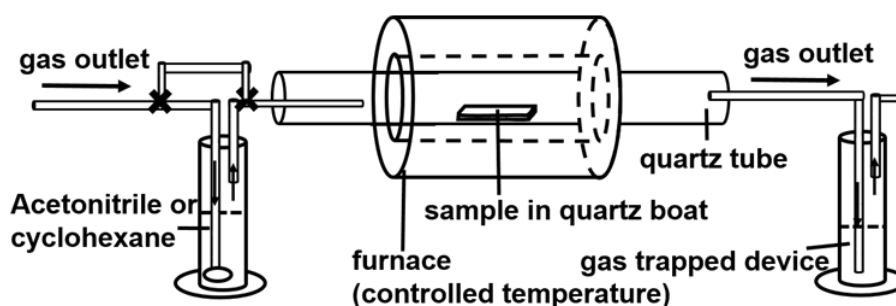


**Figure 2.7.** Schematic diagram of thermal CVD technique setup.

CNT synthesis can be achieved via chemical vapor deposition, laser ablation, flame method, hydrothermal method, arc discharge, etc. From the formation of tubular carbon filaments, threads and nanofibers over iron in 1950s–1970s to the CNT growth [200–205], the thermal chemical vapor deposition (CVD) is widely used and is considered as standard method of CNT growth due to its high CNT yield, relatively low cost, easy setup and operation as well as its scalability and high degree of control [206, 207]. In this method, thermal pyrolysis of hydrocarbon vapor or gaseous carbon-containing substance proceeds firstly followed by growing CNTs over a metal catalyst. CNT growth can be influenced not only by the size and shape of the catalysts and their interactions with other components but also by the reactor

---

geometry, carbon precursors, temperature, gas flow rate and deposition time [208–217].

Figure 2.7 displays a schematic representation of an experimental CVD set up, in which CNT growth is carried out over the metal catalyst by decomposing hydrocarbons at high temperatures of 600–1200°C. Commonly, Fe, Ni and Co serve as CNT growth catalysts, since carbon species have high solubility and diffusion rate in these metals at a high temperature as well as stronger adhesion [218, 206]. Besides Fe, Co and Ni, other metals and their compounds were also found as catalysts for CNT growth, such as transition metals like Mn, Mo, Pd, Ru, noble metals like Ag, Au, lanthanides like Gd, Eu, carbon family elements like Si, Ge, mixed compounds like TiO<sub>2</sub>/Al<sub>2</sub>O<sub>3</sub>, and binary metals like FeNi [219–228]. It was also observed that the CNT growth as well as their diameter and the number of their wall-layers like single wall CNTs (SWCNTs) and multi-walled CNTs (MWCNTs) can be affected by the size of the catalyst nanoparticles [229–231]. Sinnott *et al.* reported that the diameters of SWCNTs increased and MWCNTs were subsequently formed as well as their wall layer number and diameter were increased, while raising the size of the catalyst [229]. Additionally, temperature is an influencing factor for CNT growth. SWCNT growth was commonly achieved at higher temperatures of 900–1200 °C through decomposition of selected carbon precursors like methane and carbon monoxide, while the temperatures of 600-900 °C are more proper for MWCNT growth. [206].

Furthermore, various carbon precursors can be used, such as methane, ethanol, benzene, carbon monoxide, cyclohexane, acetonitrile, and so on. The precursor molecular structure can affect the CNT morphology [232]. Short-chain hydrocarbons like methane and ethylene are decomposed to atomic carbons or linear carbon species probably followed by forming straight CNTs, while curved CNTs are grown via cyclic hydrocarbons like benzene and cyclohexane as carbon precursors [231, 233]. When the efficient precursors for MWCNTs growth at 600–900 °C are used at a higher temperature, they are unstable and decompose to excess carbon that can hinder the MWCNT growth [206]. Thus, the adjustment of temperatures is important for different carbon precursors, since the CNT growth and their diameters can be

impacted. Additionally, CNT growth influenced by vapor pressure, gas phase diffusion, gas ratio, catalyst supports, etc. was also studied. [208–217]

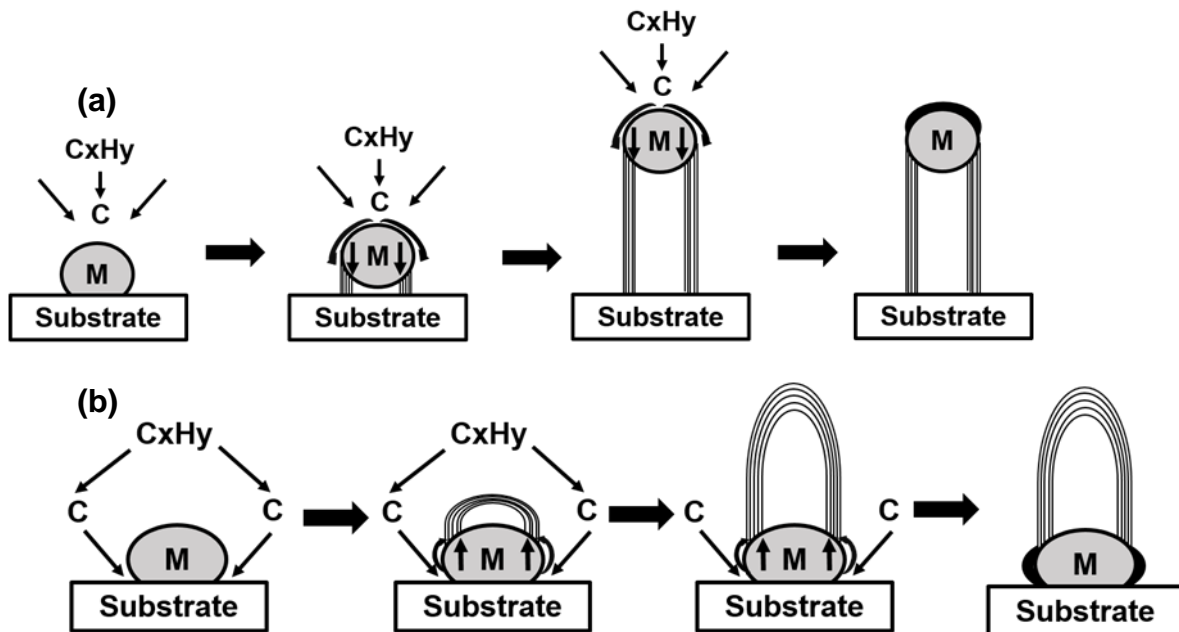
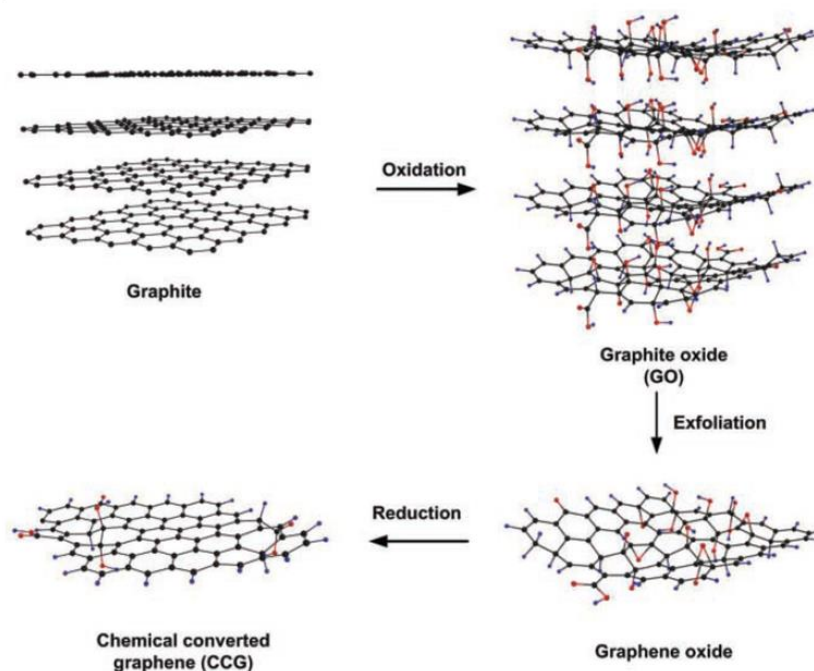


Figure 2.8. CNT growth mechanisms [206]: (a) tip-growth model and (b) base-growth model.

Moreover, various mechanisms of CNT growth were postulated. The typical models for CNT growth are the tip-growth model and the base-growth model (see Figure 2.8) [206]. Hydrocarbon vapor as carbon precursor decomposes into hydrogen and carbon species at a high temperature in the furnace. The carbon species are adsorbed on the surface of the catalyst. In the tip growth model, a weak interaction between catalyst nanoparticles and the substrate is a precondition. Carbon fragments diffuse down through catalyst nanoparticles or on the surface of the catalyst and reach the carbon solubility limit in the catalyst, and then precipitate and crystallize out across the catalyst bottom in the form of a cylindrical network. Meanwhile, the CNT precipitation pushes the catalyst nanoparticles up from the substrate. Through the subsequent fresh hydrocarbon pyrolysis and carbon diffusion, CNT growth continuously proceeds until excess carbon species cover the whole surface of catalysts and cease the catalysis. In the base growth model, the decomposition of hydrocarbon and the diffusion of carbon proceed like that in the tip growth model. But the catalyst is anchored on the substrate with a stronger interaction, so that the catalyst cannot be pushed up by CNT precipitation and CNTs

crystallize on the top of the catalyst with a hemispherical form. CNTs continue to grow by hydrocarbon deposition on the lower peripheral catalyst surface along with upward diffusion of the carbon fragments. When the surface of catalyst is fully covered with excess carbon, CNT growth is stopped [206].

#### 2.4.2. Graphene and its Synthesis Mechanism



**Figure 2.9.** Schematic representation of the preparation of reduced graphene oxide (RGO) from graphite; reprinted from [258] with permission.

As mentioned above, graphene was studied as one of the novel catalyst supports in PEMFCs and DMFCs. Graphene is a one-atom-thick sheet of carbon atoms arranged in a hexagonal lattice with  $sp^2$  hybridization (Figure 2.6c). Its surface area, electron mobility, thermal conductivity and chemical durability are high, respectively, along with a strong Young's modulus [234–237]. Hence, it can be used in field emission, sensors, electronics, energy conversion and storage [238–247]. Depending on different applications, modulating the electronic properties of graphene can be achieved by introducing heteroatoms like nitrogen or boron atoms into the graphene lattice or by adsorbing metal or organic molecules on the graphene surface [248–250].

To synthesize graphene, different effective techniques have been developed, such as mechanical exfoliation (scotch-tape method), thermal decomposition of SiC wafer

in ultrahigh vacuum [251], chemical vapor deposition growth on metal substrates like Ru, Ni, Cu, Pt [40, 252–256] and chemical exfoliation [257, 258]. Through these methods, except chemical exfoliation, defect-free or defect-less graphene can be formed and applied in electronics applications, but mass production is difficult, whereas a large area synthesis of graphene might be feasible in CVD growth [259]. Nevertheless, the typical chemical exfoliation approach developed by Hummers *et al.* [260], which involves graphite oxidation, exfoliation and reduction, has been widely used due to its relatively low cost, large-scale and reproducible manufacture [244]. As shown in Figure 2.9, graphene oxide is synthesized by the oxidation of graphite powder with strong acids and oxidants (such as  $\text{KMnO}_4$  and  $\text{NaNO}_3$  in concentrated  $\text{H}_2\text{SO}_4$ ). Then it is exfoliated in water by ultrasonication followed by purification with washing and centrifugation to remove inorganic impurities and aggregates. Since the exfoliated GO is a stable aqueous dispersion, it can be homogeneously decorated on the surface of substrates like carbon cloth. Afterwards, graphene oxide can be reduced by thermal reduction at a high temperature, photo reduction and chemical reduction using reducing agents such as sodium borohydride, hydrazine monohydrate, etc. [261, 262]. Generally, the graphene formed by GO reduction called reduced graphene oxide has structural defects and functional groups along with a couple of carbon atomic layers, which can be beneficial in electrochemical applications [247].

## *Chapter 3:*

# Results and Discussion

---

In this work, hierarchically nanostructured materials were designed as catalyst supports to improve the performances of catalysts in electrocatalytic applications (e.g., oxygen reduction reaction and methanol electro-oxidation reaction). To prepare the hierarchically structured materials, a toolbox strategy was developed via bottom-up approaches, where the materials of required functionalities can be assembled in the hierarchical structure to meet the requirements of certain applications. Each step was tuned. Given high electrical conductivity, large surface area, good chemical and mechanical stability, carbon nanotubes (CNTs) or reduced graphene oxide (RGO) were introduced in the hierarchical structure to form novel nanostructured catalyst supports for oxygen reduction reaction and methanol electro-oxidation reaction.

In the preparation of CNT-based hierarchical structures, the major steps were catalysts deposition for the CVD step and CNT growth. In Chapter 3.1 and 3.3, CNTs were directly grown on the oxidized commercial CNTs as well as reduced graphene oxide covered carbon cloth to form 3D CNTs and CNTs/RGO/CC, while the CNTs/CNTs/GC was prepared by two consecutive sequences of Fe deposition and CNT growth on glassy carbon (Chapter 3.2). Afterwards, Pt nanoparticles were deposited on the hierarchically structured materials, followed by determining their electrochemical surface area by  $H_{ads/des}$  and  $CO_{ad}$  stripping. To evaluate their suitability for electrochemical applications, Pt-3D CNTs was investigated for oxygen reduction reaction in Chapter 3.1. Considering the shapes of glassy carbon and carbon cloth, Pt-CNTs/CNTs/GC and CNTs/RGO/CC were evaluated for methanol oxidation reaction in Chapter 3.2 and 3.3, respectively. In Chapter 3.4, the CNTs/CC, CNTs/CNTs/CC and CNTs/RGO/CC electrodes were studied for electrical double

---

layer capacitor (EDLC) applications. Additionally, polyaniline was further assembled on CNTs/CC to form PANI/CNTs/CC for pseudo-EDLC supercapacitors.



### 3.1. Hierarchically Structured 3D CNT Electrode

The content of this chapter will be submitted as 'Preparation of hierarchically structured 3D CNTs as a catalyst support for a proton exchange membrane fuel cell, Pei Wang, Benedikt Peter, Titus Lendenberg, Christina Roth and Michael Bron'.

#### 3.1.1. Motivation

Proton exchange membrane fuel cells (PEMFCs) are considered one of the most attractive and promising power sources for future energy supply due to their high power density and nonpolluting nature. However, their low operation temperature (60-80 °C) requires catalysts to provide fast reaction kinetics, where platinum is the most active single metal for both the anodic oxidation of hydrogen and the cathodic reduction of oxygen [83–86]. Due to the limited resources and high cost of platinum, research is focusing on catalysts with increased activity compared to Pt or on its replacement, and different platinum alloys such as Pt/Cu, Pt/Fe, core-shell catalysts as well non-noble metal systems mainly based on Fe/N/C have been studied [107, 86, 42, 263–268]. However, from an application point of view it is equally important to provide a suitable support for the deposition of the active catalyst material. Requirements towards the catalyst support are high surface area, optimal porosity, high chemical and mechanical stability as well as high electric conductivity in addition to anchoring sites for the catalytic nanoparticles.

Currently, mainly carbon black is used as catalyst support material in PEM-FCs, but carbon black-supported Pt nanoparticles show degradation and decreased electrochemical catalytic performance with operating time at the cathode, which is often attributed carbon corrosion and agglomeration or loss of Pt nanoparticles [17–19]. Meanwhile, carbon nanotubes (CNTs) are widely investigated as support materials due to their favorable properties including large surface area, high electrical conductivity, as well as good chemical and mechanical stability. Earlier investigations demonstrated that Pt supported on CNTs shows improved stability and that the CNTs provide higher electrochemical corrosion resistance compared to commercial carbon black supports [17]. To further improve their suitability as carbon supports, nitrogen- or oxygen-doping was used to modify the surface of CNTs to introduce anchoring sites and to obtain stronger bonding between the metal and carbon, preventing

agglomeration of metal particles during electrochemical aging [39–42]. Increased surface area was reported in such cases as well [269].

Hierarchical structuring of CNTs is a feasible strategy to enhance the surface area and improve porosity of the catalyst support by preventing agglomeration. As a general approach, one-dimensional primary CNTs may serve as substrate to grow secondary CNTs on their surface to form three-dimensional CNTs (3D CNTs). For example, secondary CNTs were grown onto multi-walled CNTs by chemical vapor deposition (CVD) over Ni deposited via wet impregnation using toluene as carbon precursor. These 3D CNTs show improved specific surface area and pore size distribution as determined by N<sub>2</sub> physisorption, reduced equivalent series resistance and enhanced specific double-layer capacitance [46]. Susi *et al.* successfully prepared secondary CNTs on primary CNTs using sputter-deposited Ni catalysts in a mixture of CO or C<sub>2</sub>H<sub>2</sub>, H<sub>2</sub> and Ar, while iron particles were inactive as catalyst in the same approach [181]. Iron nanoparticles electrodeposited onto primary CNTs were also used as catalyst to grow secondary CNTs using cyclohexane and ethylene as carbon source [182, 270, 47]. Furthermore, after Pt deposition over 3D CNTs grown on carbon cloth the samples exhibited a higher oxygen reduction current compared to Pt on primary CNTs/carbon cloth and Pt on carbon cloth [47], indicating that hierarchically structured CNTs are a promising catalyst support for electrochemical applications. However, it should be mentioned that kinetic parameters were not determined in the mentioned paper due to the rough surface of carbon cloth and the distorted hydrodynamics in front of the electrodes.

In this work, we report on the electrocatalytic performance of Pt supported on 3D CNTs (i.e., secondary CNTs directly grown onto primary CNTs), where the secondary CNTs are N-doped CNTs grown by chemical vapor deposition (CVD) over wet-impregnated iron nanoparticles using acetonitrile as carbon source. The morphology of the 3D CNTs was studied using transmission electron microscopy (TEM). Afterwards, Pt deposition onto 3D CNTs was achieved by wet impregnation to obtain Pt-3D CNTs. Electrochemical activity and durability of the prepared catalysts were investigated for the electrocatalytic oxygen reduction reaction (ORR) using linear sweep voltammetry with a rotating disk electrode (RDE), oxygen aging tests and

single cell tests of multilayered MEAs. For the comparison, Pt deposited on primary CNTs was prepared and investigated in the same manner.

### 3.1.2. Characterization of 3D CNTs

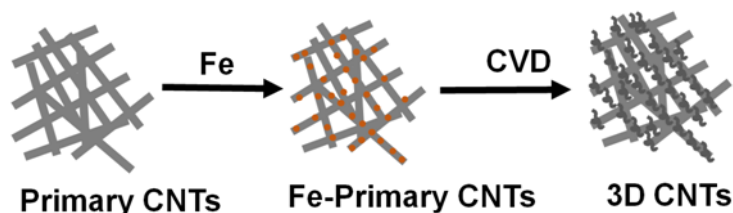


**Figure 3.1.1.** Schematic representation of the preparation of 3D CNTs network.

To form the hierarchically structured 3D CNTs, Fe nanoparticles were deposited onto primary CNTs, and then secondary CNTs were grown over the Fe particles via chemical vapor deposition (CVD) onto the primary CNTs (Figure 3.1.1). Generally, CNT growth via CVD depends on many parameters, such as temperature, pressure, carbon source, reactor geometry, and so on [206, 207, 211, 214, 209, 232, 271–274]. In preliminary studies, the optimum conditions for CNTs growth in our CVD system were evaluated using a common and well established catalyst ( $\text{Fe}/\text{SiO}_2$ ). 20% Fe were deposited onto  $\text{SiO}_2$  similar to a procedure described in [275] (see in Figure S3.1.1). After Fe deposition, CNTs were grown via CVD in  $3 \text{ L h}^{-1}/3 \text{ L h}^{-1} \text{ H}_2/\text{Ar}$  saturated with acetonitrile at room temperature for 120 min at  $750^\circ\text{C}$ ,  $850^\circ\text{C}$ ,  $950^\circ\text{C}$  and  $1050^\circ\text{C}$ , respectively. The diameter of the CNTs increases with rising temperature as shown in Figure S3.1.2. Furthermore, yields and N contents decrease with growth temperature (Table S3.1.1), as reported in literature [275]. Additionally, different gas flow rates as well as cyclohexane as carbon source were also tested, and the yields of CNTs were lower. Thus, the growth of secondary CNTs onto primary CNTs was carried out via CVD in  $3 \text{ L h}^{-1}/3 \text{ L h}^{-1} \text{ H}_2/\text{Ar}$  atmosphere saturated with acetonitrile for 120 min at  $750^\circ\text{C}$ .

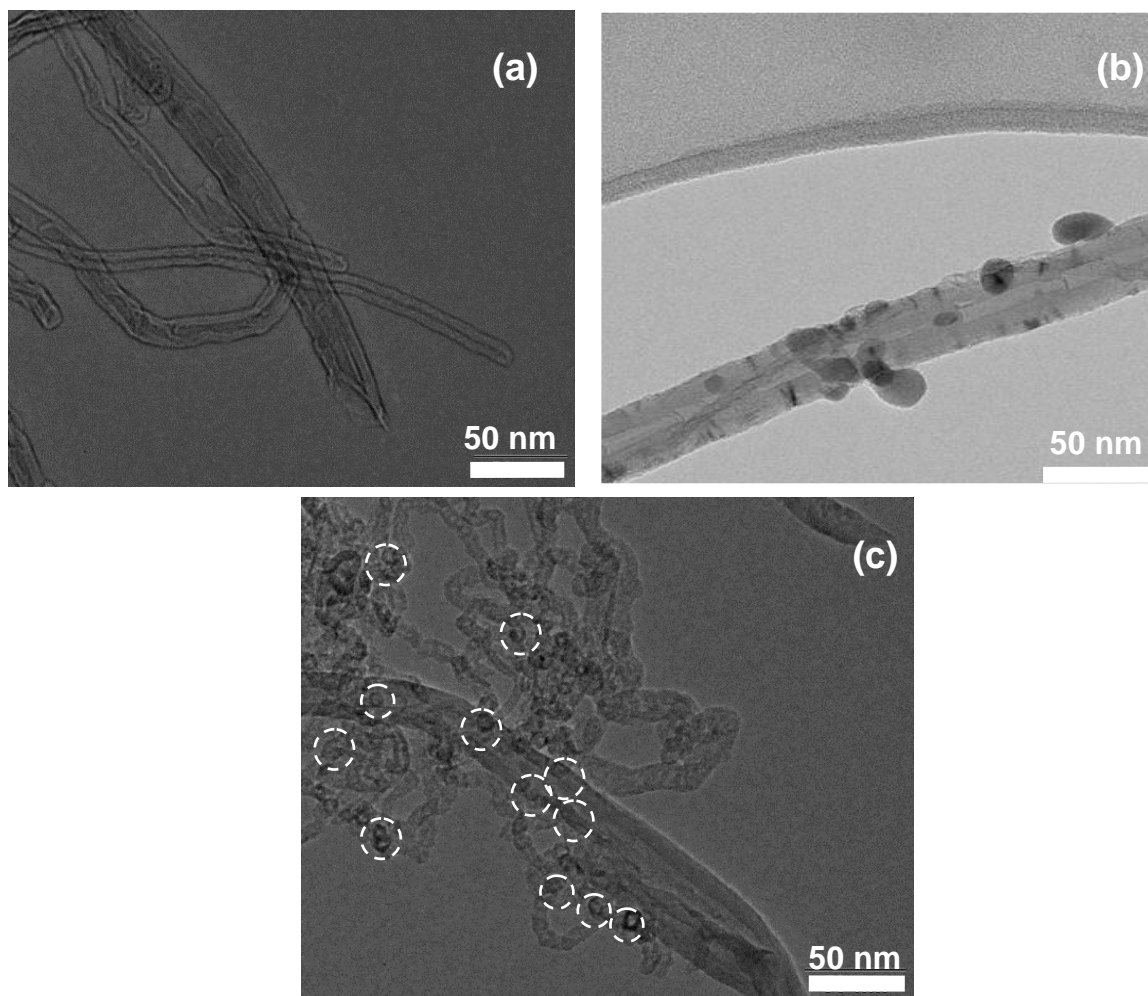


**Figure 3.1.2.** TEM images of (a) primary CNTs and (b) Fe-primed CNTs and (c) 3D-CNTs via secondary CNTs grown onto primary CNTs.

Transmission electron microscopy was employed to investigate the morphology of the samples before and after growth of secondary CNTs. Figure 3.1.2a shows TEM images of primary CNTs, while Figure 3.1.2b demonstrates the successful deposition of Fe nanoparticles onto these primary CNTs. The structures resulting after growth of the secondary CNTs (i.e., 3D CNTs) is displayed in Figure 3.1.2c. Different to the primary CNTs, the secondary CNTs exhibit a curled nanostructure, which might indicate higher defect density (however, see below) and a smaller diameter. Despite this curled structure, the tubular and hollow nature of the secondary CNTs is clearly indicated by the bright contrasts visible not only on the top also in the inner of the secondary CNT.

To further substantiate the presence of secondary CNTs, the nitrogen content of primary as well as 3D CNTs was determined by elemental analysis as shown in Table 3.1.1. After CVD, the nitrogen content increased from 0.3% to 3.8%, which together with the TEM images, reveals the formation of secondary CNTs.

**Table 3.1.1.** Elemental analysis of nitrogen and carbon content in primary CNTs and 3D CNTs.

Catalyst support	N/%	C/%
Primary CNTs	0.3%	93.6%
3D CNTs	3.8%	86.1%

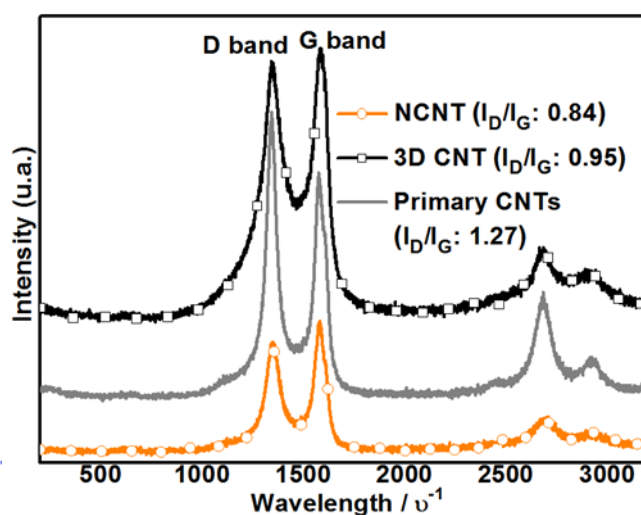


**Figure 3.1.3.** The Raman spectroscopy of primary CNTs, 3D CNTs and NCNTs exposing the different graphitization degree/defect degree of carbon system.

Raman spectra of primary and 3D CNTs are presented in Figure 3.1.3. CNT-based carbon materials usually show two characteristic bands: the D band at ca.  $1350\text{ cm}^{-1}$  and the G band at ca.  $1580\text{ cm}^{-1}$ . The D band is associated with structure defects and impurities in the CNTs, and the G band represents the highly ordered  $\text{sp}^2$ -hybridised graphitic carbon. Often, the intensity ratio of the D and G band ( $I_D/I_G$ ) is used to qualitatively estimate the carbon ordering or carbon defect degree. After growth of secondary CNTs the relative  $I_D/I_G$  intensity of the 3D CNTs is 0.95, which is lower than that of the primary CNTs ( $I_D/I_G$ : 1.27) and higher than that of CVD-grown NCNTs without substrate ( $I_D/I_G$ : 0.84, prepared in preliminary study). This seems to

be at contradiction with the observation of highly curled CNTs in the TEM images, which seem to indicate a defect-rich structure. But it is noticed that the NCNTs itself has lower defect degree than primary CNTs. Nevertheless, the strong changes in Raman spectra may be considered a further proof of the growth of additional carbon structures, i.e. CNTs.

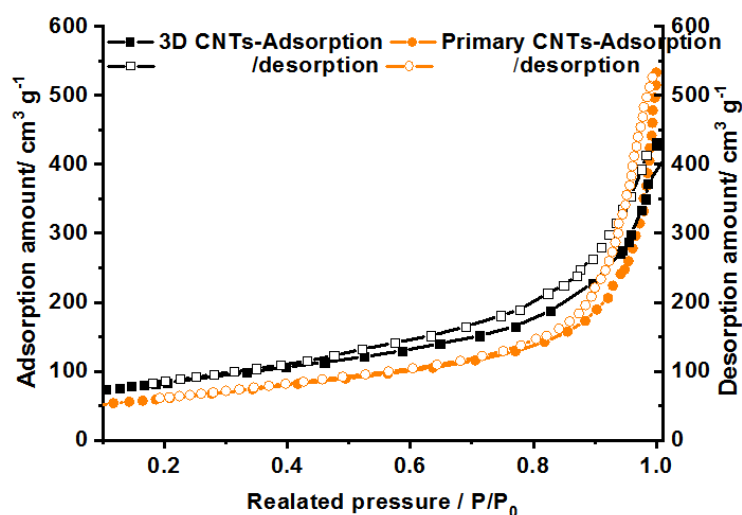


**Figure 3.1.4.** Nitrogen physisorption at 77 K for primary CNTs and 3D CNTs.

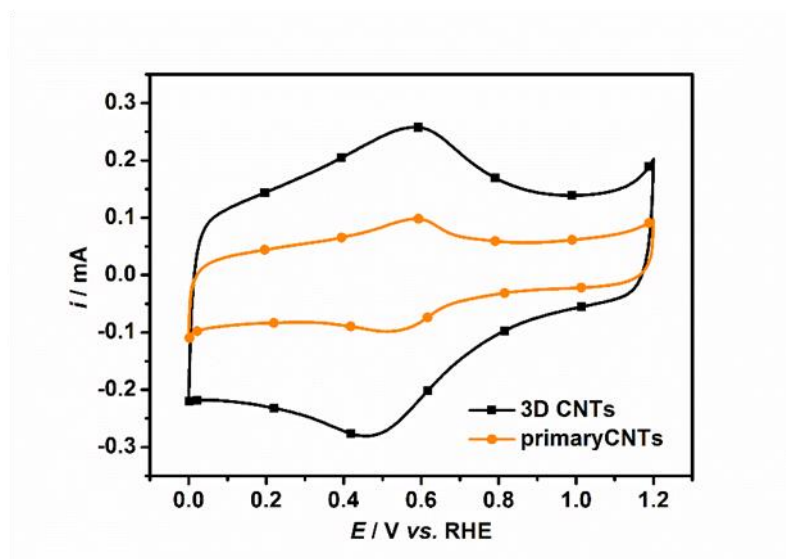


**Figure 3.1.5.** Cyclic voltammograms of primary CNTs and 3D CNTs on glassy carbon electrodes recorded at a scan rate of  $100 \text{ mV s}^{-1}$  at room temperature in  $0.5 \text{ M H}_2\text{SO}_4$  aqueous electrolyte solution purged with  $\text{N}_2$ .

Nitrogen adsorption and desorption isotherms of primary CNTs and 3D CNTs were recorded at 77 K and the results are shown in Figure 3.1.4. According to the IUPAC classification, the isotherms can be considered as type II isotherms. At low relative pressure, the nitrogen is adsorbed slowly on the CNT surface to form a monolayer, while a hysteresis loop is observed at high relative pressure in the adsorption isotherm. With respect to the primary CNTs, the amount of nitrogen adsorbed onto 3D CNTs is higher, indicating higher surface area. The 3D CNTs provide  $301 \text{ cm}^2 \text{ g}^{-1}$  BET surface area, while the primary CNTs have  $230 \text{ cm}^2 \text{ g}^{-1}$ . The increase in specific surface area is in line with the observation that the secondary CNTs are smaller in diameter compared to the primary ones (compare TEM images).

Finally, the CNT samples were characterized electrochemically by cyclic voltammetry at a scan rate of  $100 \text{ mV s}^{-1}$  in  $0.5 \text{ M H}_2\text{SO}_4$  (Figure 3.1.5). Please note that different to the studies on oxygen reduction reaction, which were, as an accepted standard in literature, carried out in perchloric acid (see below), sulfuric acid was used for electrochemical carbon materials characterization to allow comparison with other results on carbon materials in our lab. The observed currents mainly correspond with the charging and discharging of the electrical double layer of the CNTs. In comparison to primary CNTs, 3D CNTs show enhanced currents and thus larger double layer capacity, caused by the successful growth of secondary CNTs providing a higher amount of electrochemically available specific surface area. This was in accordance with the above mentioned results and evaluations. Besides the increased double layer capacity, redox peak pairs, which are typically attributed to oxygen containing functional groups (quinone/hydroquinone) [276], are observed in the potential range between  $0.5 \text{ V}$  and  $0.7 \text{ V}$  vs. RHE for both samples. These functional groups are likely introduced into the surface of the CNTs during removal of iron particles with  $\text{HNO}_3$ . It should be mentioned that the oxygen containing functional groups may be one reason for the increase in double layer capacitance [269].

In summary, results of TEM, Raman spectroscopy, BET measurements and cyclic voltammetry confirm the successful growth of secondary CNTs onto the primary CNTs to form the 3D CNTs. The secondary CNTs are smaller in diameter and curled with a higher specific surface area, however, provide a less defect-rich structure.



### 3.1.3. Characterizations and Electrochemical Investigations of Pt-3D CNTs

#### Characterizations of Pt Catalysts

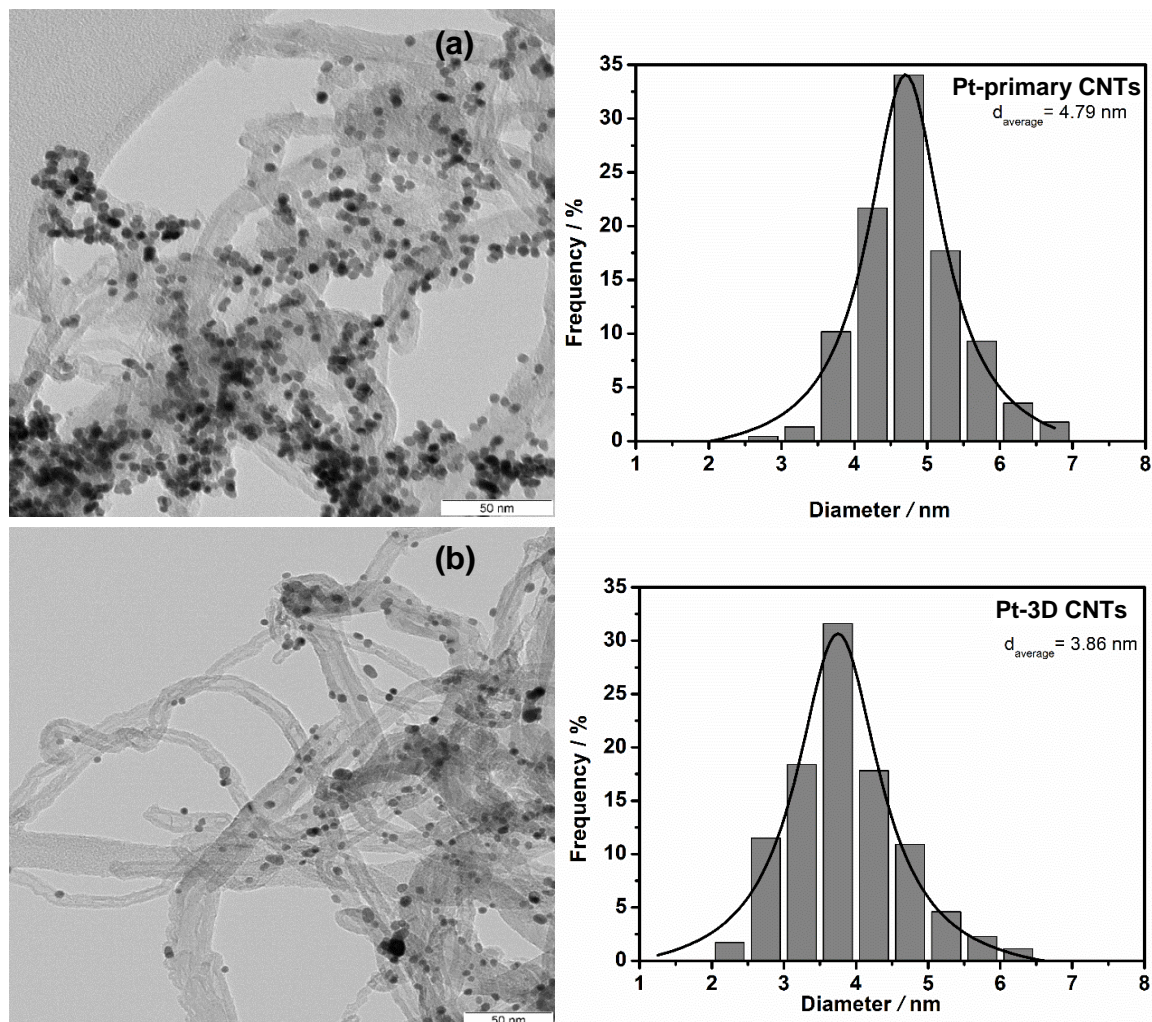


**Figure 3.1.6.** TEM images and particles size distribution of Pt nanoparticles supported on (a) primary CNTs and (b) 3D CNTs.

After growth of secondary CNTs, Pt nanoparticles were deposited by wet chemical reduction onto 3D CNTs and primary CNTs, respectively. The Pt content, morphology and particle size of the Pt nanoparticles were characterized by ICP-OES, TEM and XRD. The Pt loadings in Pt-primary CNTs and Pt-3D CNTs were 19 % and 20 % as determined by ICP-OES analysis, respectively. Figure 3.1.6a and 6b show TEM micrographs of Pt/CNTs and Pt/3D CNTs, where Pt nanoparticles were almost uniformly anchored onto both carbon supports. Some agglomerates of Pt nanoparticles are however also visible. The average sizes of Pt nanoparticles on the



primary CNTs and 3D CNTs are 4.8 nm and 3.9 nm. XRD analysis (Figure 3.1.7, determined by Dr. Benedikt Peter) reveals a Pt crystallite size for Pt-primary CNTs of 4.5 nm, whereas the size for the Pt-3D CNTs is 3.2 nm, determined by the FULLPROF software package with Rietveld refinement. The sizes of Pt crystallites determined by XRD measurement are slightly smaller than those of the nanoparticles determined by TEM, which is reasonable assuming that there might be less crystalline material at the outer parts of the nanoparticles.

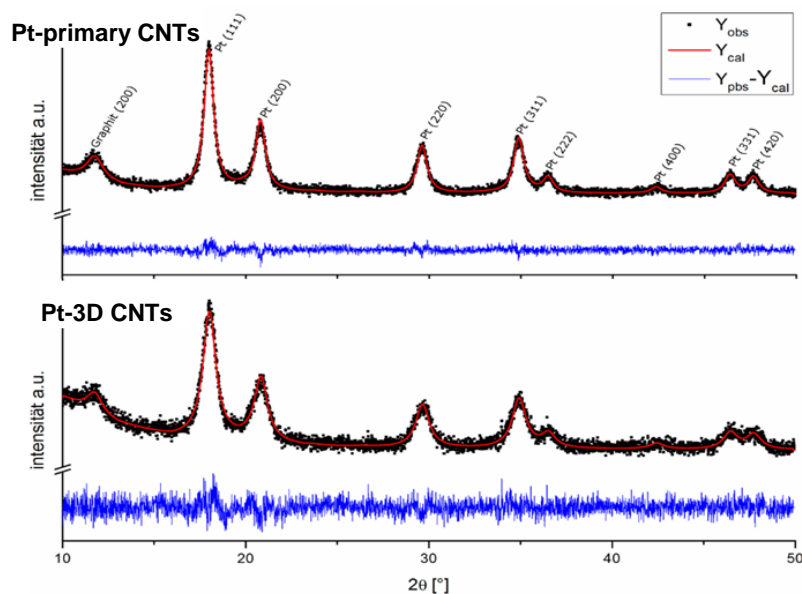


**Figure 3.1.7.** X-ray diffraction profile of the Pt-primary CNTs and Pt-3D CNTs (determined by Dr. Benedikt Peter).

### Electrochemical Investigations of the Pt-CNT Catalysts

The prepared Pt catalysts were investigated with different electrochemical techniques, e.g. cyclic voltammetry, CO stripping voltammetry, linear sweep voltammetry to determine oxygen reduction reaction as well as stress tests. The results are compared with those obtained on commercial Pt/C catalysts.

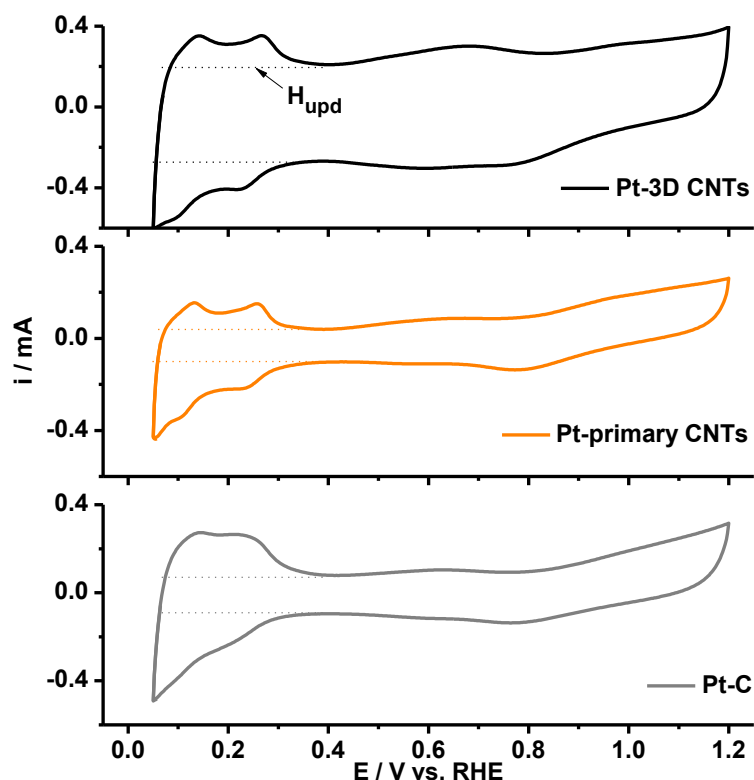


**Figure 3.1.8.** Cyclic voltammograms measured at  $100 \text{ mV s}^{-1}$  scan rate in aqueous  $0.1 \text{ M HClO}_4$  electrolyte solution for Pt-3D CNTs, Pt-primary CNTs and Pt-C. The double layer charging subtracted for ECSA determination is indicated by the dashed line.

Cyclic voltammograms recorded at a scan rate of  $100 \text{ mV s}^{-1}$  in  $\text{N}_2$  purged  $0.1 \text{ M HClO}_4$  aqueous solution are shown in Figure 3.1.8, while  $\text{CO}_{\text{ad}}$  stripping voltammograms, recorded at  $20 \text{ mV s}^{-1}$  in  $\text{N}_2$  purged  $0.1 \text{ M HClO}_4$  solution after  $\text{CO}$  adsorption on the Pt surface are shown in Figure 3.1.9. The electrochemical surface area (ECSA) was calculated from the coulombic charge of the double layer charge corrected hydrogen adsorption and desorption peaks ( $H_{\text{ads/des}}$ ) in the potential range  $0.06\text{-}0.4 \text{ V}$ . Similarly, the ECSA was determined from the charge of the corrected  $\text{CO}_{\text{ad}}$  oxidation peaks. The results of ECSA determination are summarized in Table 3.1.2. The ECSA determined from  $H_{\text{ads/des}}$  for Pt/3D CNTs is significantly higher compared to that of Pt/primary CNTs and slightly higher compared to the commercial Pt/C catalyst, and similar results were obtained for the ECSA value determined by  $\text{CO}_{\text{ad}}$  stripping. The higher ECSA of Pt/3D CNTs is in accordance with the lower Pt particle size of this catalyst. This better Pt dispersion is attributed to the higher surface area of the 3D support material compared to the primary CNTs and may also stem from nitrogen surface functional groups acting as anchoring sites for the Pt

particles. In literature, it was reported that the addition of secondary CNTs may decrease charge transfer resistance and thus improve the electron transfer [47], which may also have an influence on the observed ECSA. Note that the ECSAs of Pt/3D CNTs and Pt/C evaluated from  $\text{CO}_{\text{ad}}$  stripping are higher compared to those calculated from  $H_{\text{upd}}$ . This, however, is in accordance with reports in literature. [277]. It should further be noted that the baseline correction used for the integration of  $H_{\text{upd}}$  or  $\text{CO}_{\text{ad}}$  stripping-peak always leads to an unavoidable deviation in the calculated ECSA.

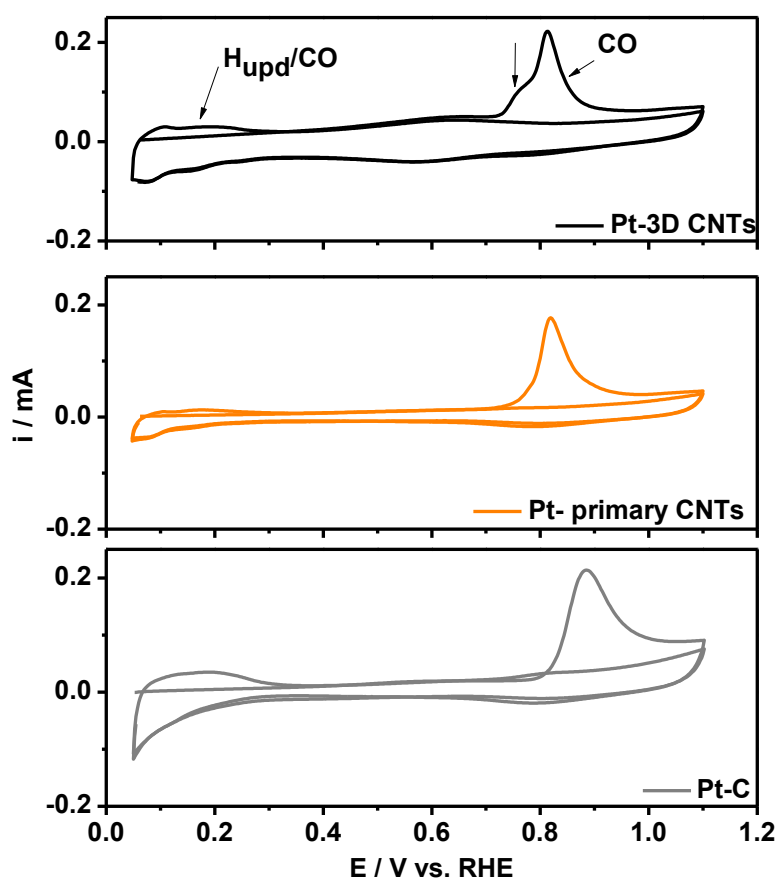


**Figure 3.1.9.**  $\text{CO}_{\text{ad}}$  stripping voltammogram recorded at  $20 \text{ mV s}^{-1}$  scan rate in aqueous  $0.1 \text{ M HClO}_4$  electrolyte solution for Pt-3D CNTs, Pt-primary CNTs and Pt-C.

In Figure 3.1.9 the CVs of CO oxidation over the different carbon-supported Pt catalysts are displayed. Pt/primary CNTs shows a single CO oxidation peak centered at  $0.82 \text{ V vs. RHE}$ , whereas the CO oxidation peak for Pt/3D CNTs is shifted to a slightly more negative potential with the appearance of a shoulder centered and is at ca.  $0.75 \text{ V vs. RHE}$ . In literature such shoulders were attributed agglomerated

catalyst particles or increased graphitization degree of carbon based catalyst supports [278–280]. Since the dispersion of Pt on 3D CNTs is improved compared to Pt on primary CNTs as described above, the appearance of the shoulder is likely not related to particle agglomeration. However, as shown in Figure 3.1.3 (Raman spectra), the secondary CNTs grown on primary ones exhibit a lower  $I_D/I_G$  ratio, indicating a higher degree of graphitization. The shoulder at the CO oxidation peak might be caused by this increased degree of graphitization in Pt/3D CNTs compared to Pt/primary CNTs and Pt/C leading to a specific interaction between Pt and the graphitized domains with probably changed electronic properties [280]. Nevertheless, it is important to note that a shift of the CO oxidation peak to less positive potentials indicates a more facile CO oxidation over the Pt/3D CNT catalyst compared to the other samples used in this study, including the commercial one.

**Table 3.1.2.** ECSA values determined by  $H_{\text{upd}}$  and  $\text{CO}_{\text{ad}}$  for Pt on 3D CNTs, primary CNTs and C

	ECSA by $H_{\text{upd}}/\text{m}^2 \text{g}_{\text{Pt}}^{-1}$	ECSA by $\text{CO}_{\text{ad}}/\text{m}^2 \text{g}_{\text{Pt}}^{-1}$
<b>Pt-3D CNTs</b>	37.1	37.5
<b>Pt-primary CNTs</b>	25.1	25.9
<b>Pt-C</b>	34.8	36.9

The electrocatalytic activity of all samples towards the oxygen reduction reaction was studied in oxygen-saturated 0.1 M  $\text{HClO}_4$  electrolyte by linear sweep voltammetry using an RDE recorded from 0.05 V to 1.1 V vs. RHE at a scan rate of 5  $\text{mV s}^{-1}$  with three different electrode rotation speeds of 400, 900 and 1600 rpm. Figure 3.1.10a shows the comparison of the curves obtained at 1600 rpm. The typical kinetically, mixed kinetically and diffusion- as well as diffusion-controlled regions are visible. Pt/3D CNTs exhibits slightly increased diffusion limited currents and a slightly more positive onset potential compared to Pt/primary CNTs with values comparable to that of the commercial Pt/C catalysts. The half-wave potentials ( $E_{1/2}$ ) of Pt/3D CNTs is slightly more positive.

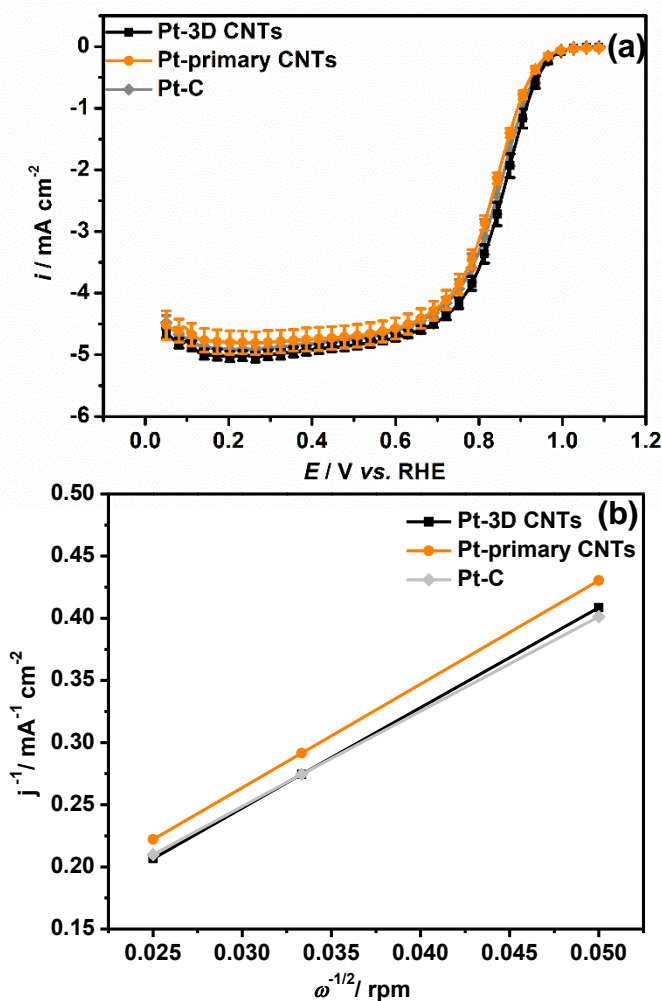


**Figure 3.1.10.** ORR polarization curves of Pt-3D CNTs, Pt-primary CNTs and Pt-C measured in oxygen saturated 0.1 M  $\text{HClO}_4$  at 1600 rpm with a scan rate of  $5 \text{ mV s}^{-1}$  in the potential range between 0.05-1.1 V vs. RHE, and (b) their Koutecky-Levich plots for ORR at 0.4 V vs. RHE, determined by Koutecky-Levich equation.

For a more quantitative analysis, the obtained RDE curves were evaluated by the Koutecky-Levich equation, and the corresponding plots for a potential of 0.4 V are displayed in Figure 3.1.10b, while those obtained at other potentials are shown in Figure S3.1.3. The slope of the Koutecky-Levich plot can be used to evaluate the average number of electrons transferred per oxygen molecule in during the oxygen reduction reaction, where the average transferred electron numbers for Pt/3D CNTs, Pt/primary CNTs and Pt/C are 3.7, 3.5 and 3.8, respectively, (Table 3.1.3). This might indicate that the transfer from the two-electron process to four-electron process is more feasible or more available active sites existed in Pt-3D CNTs to reduce intermediate hydrogen peroxide.

**Table 3.1.3.** Pt mass-specific- and surface-specific activities  $i_m$  and  $i_s$  of ORR for Pt-3D CNTs, Pt-primary CNTs and Pt-C at  $E = 0.9$  V vs. RHE.

Catalysts	n	$i_m/\text{mA mg}_{\text{Pt}}^{-1}$	$i_s/\text{mAcm}_{\text{Pt}}^{-2}$
Pt-3D CNTs	3.7	52.14	0.14
Pt-primary CNTs	3.5	26.79	0.10
Pt-C	3.8	47.44	0.13

Based on the Koutecky-Levich equation kinetic current densities were determined as a measure for the electrocatalytic activities towards oxygen reduction reaction. In Table 3.1.3 the kinetic current densities are displayed normalized to Pt mass as well as to Pt ECSA as calculated by  $\text{CO}_{\text{ad}}$ -stripping (i.e. surface specific and mass specific kinetic current densities) at a potential of 0.9 V vs. RHE. All three catalysts provide similar surface specific activities towards oxygen reduction reaction, while Pt/3D CNTs exhibits much higher mass specific activity compared to Pt/primary CNTs, which is likely related to the improved Pt dispersion/smaller sizes of Pt nanoparticles in the former sample.

To get a first impression of their long-term electrochemical stability, accelerated oxygen stress tests of the Pt catalysts were conducted using cyclic voltammetry in  $\text{O}_2$ -saturated 0.1 M  $\text{HClO}_4$  electrolyte at  $1000 \text{ mV s}^{-1}$  for 2000 cycles in the potential range from 0.05 to 1.2 V. After every 500 cycles, an ORR measurement was carried as above. Then the electrolyte was purged with  $\text{N}_2$  for 20 min and cyclic voltammograms were recorded at  $100 \text{ mV s}^{-1}$  compared to the initial curve before  $\text{O}_2$  aging stress test. This procedure was repeated 4 times. The results are shown in Figure 3.1.11 (CV) and Figure 3.1.12 (LSV of ORR).

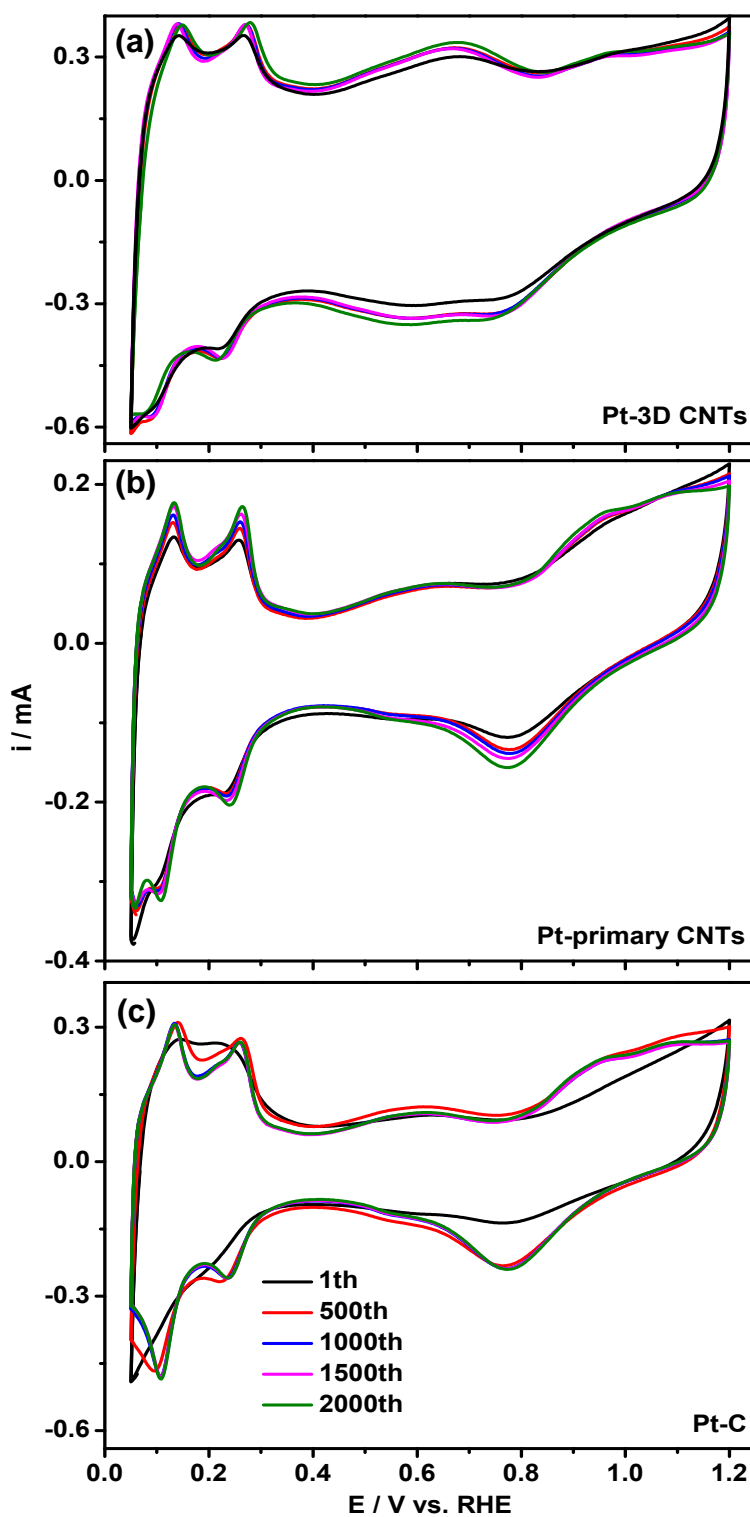


**Figure 3.1.11.** Cyclic voltammograms for (a) Pt-3D CNTs, (b) Pt-primary CNTs and (c) Pt-C recorded at a scan rate of  $100 \text{ mV s}^{-1}$  in the potential range 0.05-1.2 V vs. RHE in  $\text{N}_2$  saturated 0.1 M  $\text{HClO}_4$  before and after each oxygen stress test. Each aging stress test was performed by cyclic voltammetry for 500 cycles at a scan rate of  $1000 \text{ mV s}^{-1}$  in the potential range 0.05-1.2 V vs. RHE in  $\text{O}_2$  saturated 0.1 M  $\text{HClO}_4$  and was repeated 4 times.

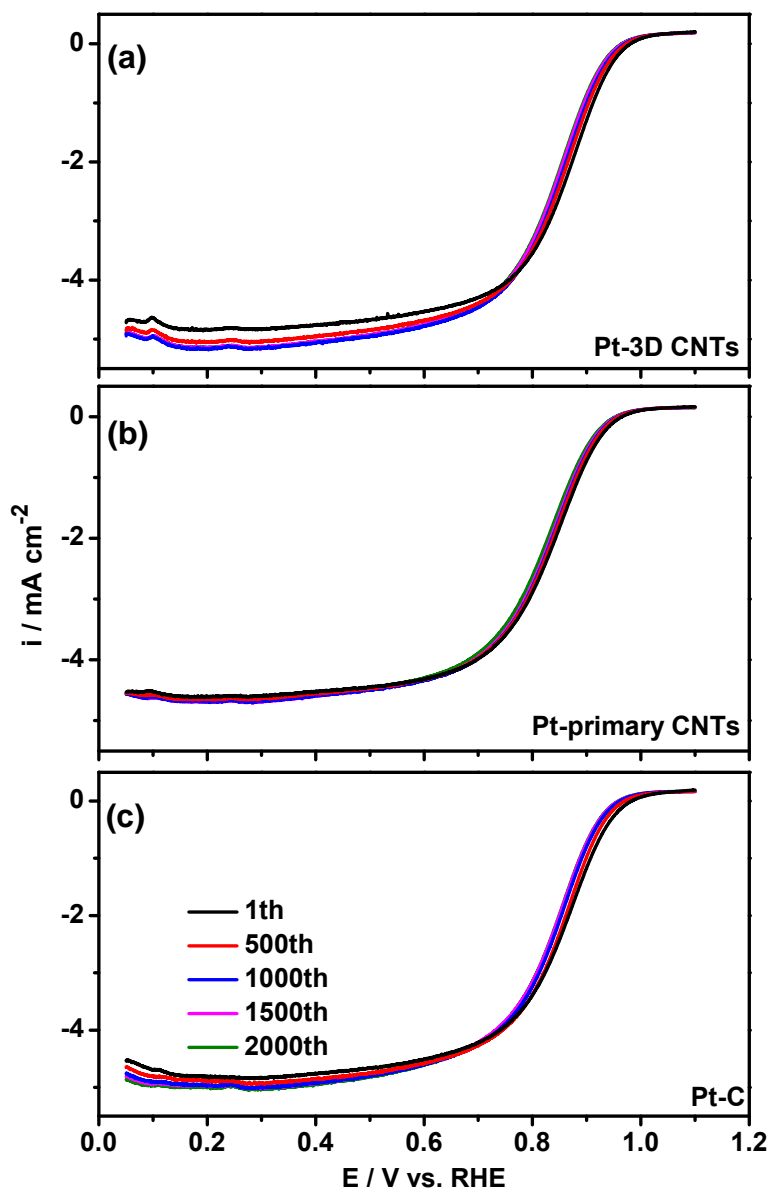


**Figure 3.1.12.** ORR polarization curves of (a) Pt-3D CNTs, (b) Pt-primary CNTs and (c) Pt-C measured in oxygen saturated 0.1 M  $\text{HClO}_4$  at 1600 rpm with a scan rate of  $5 \text{ mV s}^{-1}$  in the potential range between 0.05-1.1 V vs. RHE before and after each oxygen aging stress test. Each aging stress test was performed by cyclic voltammetry for 500 cycles at a scan rate of  $1000 \text{ mV s}^{-1}$  in the potential range 0.05-1.2 V vs. RHE in  $\text{O}_2$  saturated 0.1 M  $\text{HClO}_4$  and was repeated 4 times.

The first CVs in Figure 3.1.11 (black curves) were recorded after initial electrochemical surface cleaning (50 CV cycles). After the following fast 500 CV cycles, the  $\text{H}_{\text{upd}}$  peaks are exposed more clearly, in particular for Pt/C, which might be caused by incomplete removal of adsorbed organic species during the initial cleaning cycles. Alternatively, this observation may also be associated with the



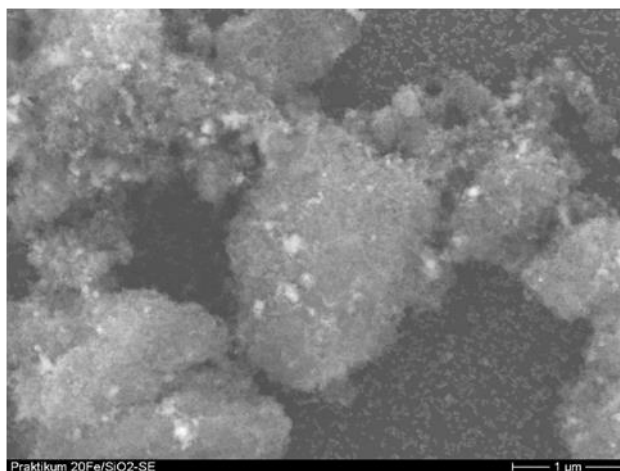
restructuring of the Pt nanoparticles during the first 500 cycles. In the following 3 repetitions of the 500 ageing CVs, the shapes of CV are scarcely changed. The  $H_{\text{upd}}$  currents show minor changes for Pt/3D CNTs and Pt/primary CNTs, while the Pt/C shows slightly reduced currents after 1000 cycles and remains stable afterwards. In Figure 3.1.12, the corresponding ORR polarization curves of Pt/3D CNTs, Pt/primary CNTs and Pt/C recorded before and after each aging test in oxygen saturated 0.1 M  $\text{HClO}_4$  at 1600 rpm with a scan rate of  $5 \text{ mV s}^{-1}$  are displayed. There is only a slight shift of the ORR onset potential of all three catalysts to more negative potentials after the first 500 ageing cycles, and very minor changes during the following aging steps. A loss of ECSA [281, 282, 39] is often attributed to an increase in Pt particle size [282] or the detachment of smaller Pt nanoparticles from the carbon support [281]. The good stability with respect to ECSA and ORR activity of the Pt /3D CNT and Pt/primary CNT samples of this study might be attributed to a higher stability of the support and thus a reduced detachment or a stabilizing effect the oxygen and nitrogen functional group on the surface of the CNTs resulting from an improved interaction between Pt particles and functional groups. It is obvious that the extend of ageing strongly depends on the testing conditions. The same Pt/C catalyst used in the present study was compared to Pt supported on CVD-grown CNTs and showed strong degradation behavior when cycled in a potential range between 0.1 V and 1.3 V vs. RHE [39], while the Pt/CNT catalysts remained stable under such conditions. However, it was not the scope of this paper to investigate the stability issue in detail.

Finally, in a preliminary application-oriented study, the catalysts of this paper were processed as the cathode of membrane electrode assemblies (MEAs) by a layer-by-layer (LBL) approach combined with Pt/polyaniline to form multilayered MEAs (see Figure S3.1.4a). Polarization and power density curves of these MEAs were recorded in a single cell test bench at  $70 \text{ }^\circ\text{C}$  under  $\text{H}_2/\text{O}_2$  atmosphere (see Figure S3.1.4b and c). Pt-3D CNTs shows increased highest output power density and decreased Ohmic loss compared to Pt-primary CNTs. In Figure S3.1.4c, 800-cycles curves were recorded for 7 days. The Pt-3D CNTs reveals a higher power density than that for Pt-primary CNTs. These results from MEAs tests were consistent with the tests mentioned above. In summary, the Pt-3D CNTs has enhanced electrochemical performances compared to the Pt-primary CNTs and can be expected to be a promising catalyst in the PEMFC.

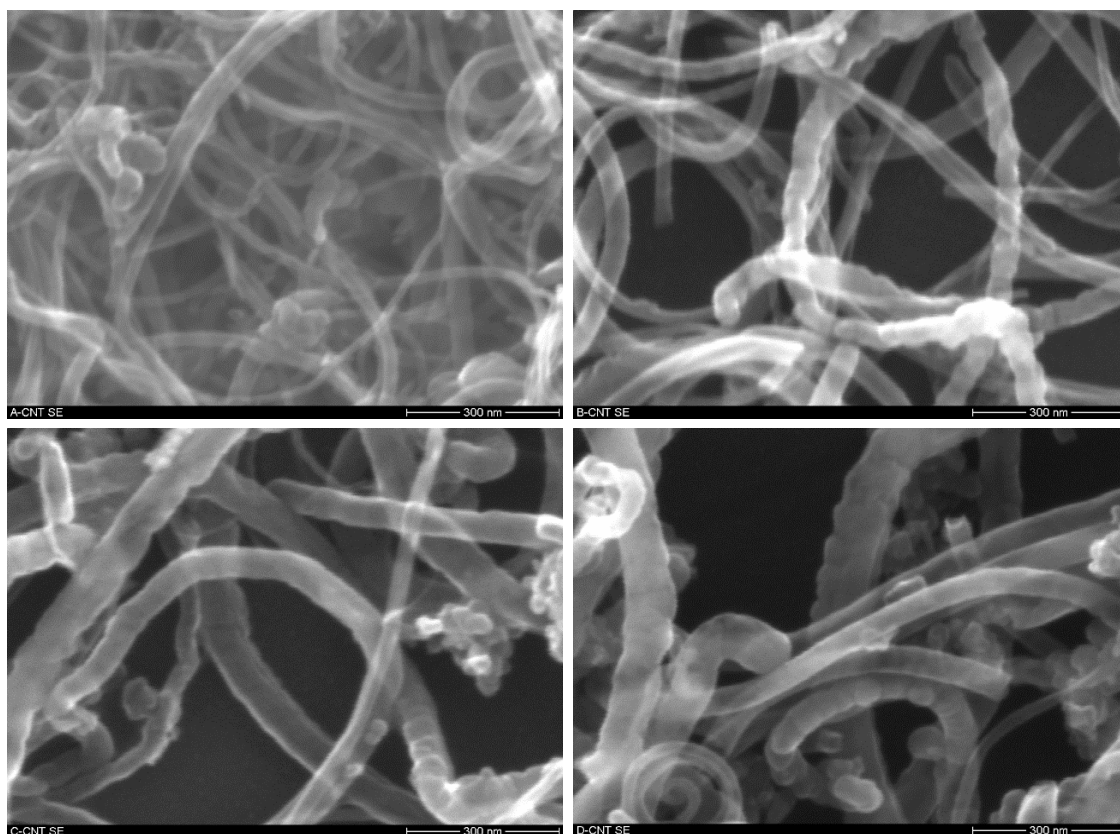
### 3.1.4. Conclusion

The preparation of hierarchically nanostructured electrodes, namely Pt/3D CNTs, for oxygen reduction reaction was achieved by growing secondary CNTs onto primary CNTs via Fe-catalyzed CVD and finally Pt deposition. Fe- and Pt-deposition were carried out using a wet-impregnation approach. TEM, elemental analysis and Raman spectra demonstrated successful growth of secondary CNTs, which led to a higher BET surface area and higher double layer capacitance compared to the primary CNTs. The Pt/3D CNT catalyst showed increased ECSA as well as a slightly more positive onset potential and higher specific activities towards oxygen reduction reaction compared to Pt/primary CNTs. This might be attributed to the improved dispersion of Pt nanoparticles and decreased in particle size, which could be caused by the larger available active surface. Moreover, Pt/3D CNTs and Pt/primary CNTs displayed improved stability properties in an accelerated stress test. Additionally, Pt/3D CNTs exposed higher maximum power density in single cell tests using LBL-prepared MEAs compared to primary CNTs. Thus Pt-3D CNTs showed improved electrochemical performances and 3D CNTs could be a superior catalyst support for the cathode in fuel cells.

### 3.1.5. Supplementary Information



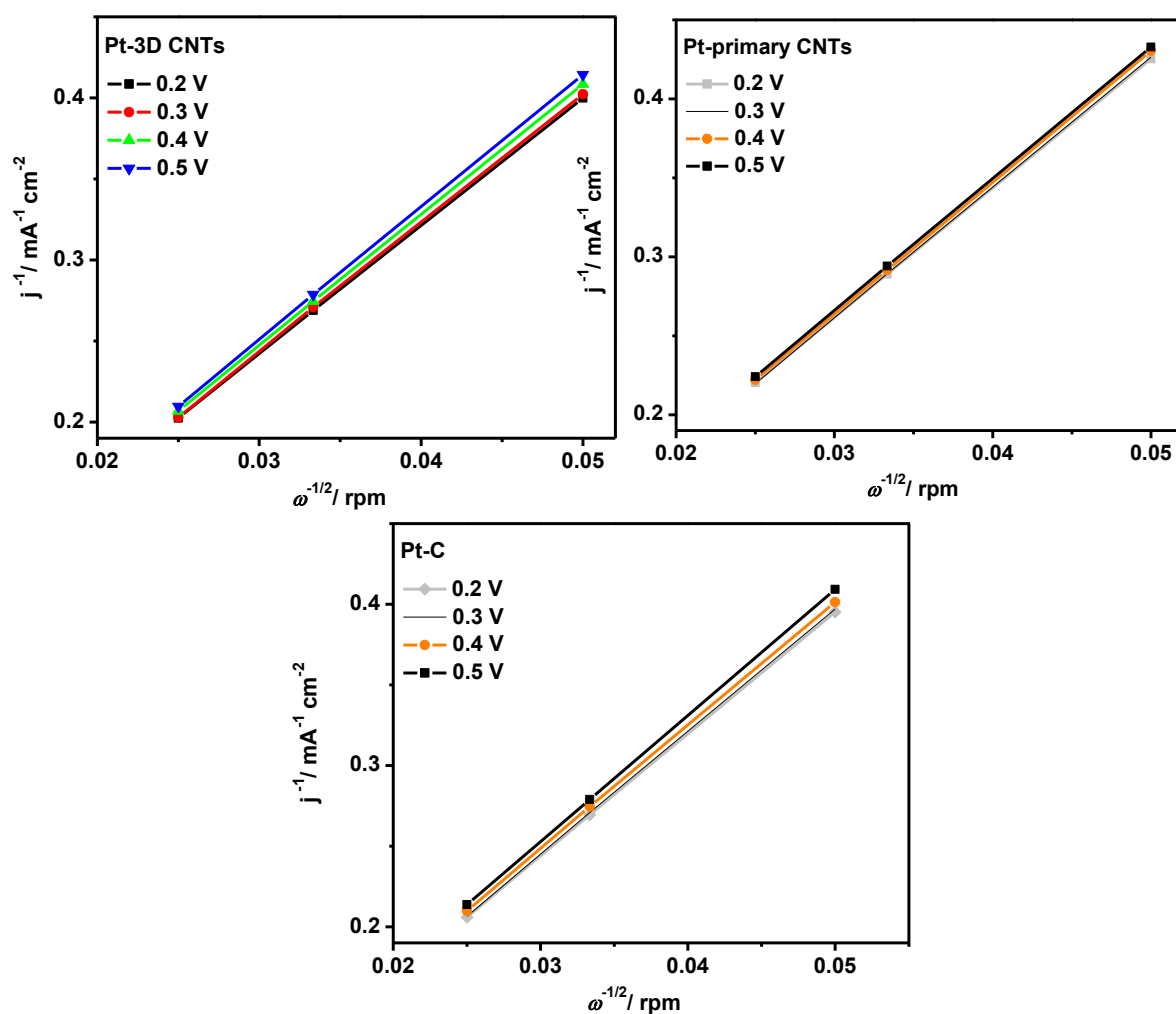
**Figure S3.1.1.** SEM images of 20% Fe as catalyst of CNT growth deposited onto SiO<sub>2</sub>.



**Figure S3.1.2.** SEM images of CNT growth onto SiO<sub>2</sub> using Fe as catalyst via CVD in 3 L h<sup>-1</sup> / 3 L h<sup>-1</sup> Ar/H<sub>2</sub> purged acetonitrile atmosphere for 120 min at (a) 750 °C, (b) 850 °C, (c) 950 °C and (d) 1050 °C, respectively.

**Table S3.1.1.** Yield ratios and N contents for CNTs grown at different temperature via CVD.

Temperature for CNT growth	Yield ratio/ $\text{mg}_{\text{CNT}} \text{mg}_{\text{Fe}}^{-1}$	N Content/ %
750 °C	12.75	3.1
850 °C	11.75	2.2
950 °C	11.16	1.3
1050 °C	9.37	0.9


**Figure S3.1.3.** Koutecky-Levich plots of Pt deposited onto 3D CNTs, primary CNTs and C at different potentials determined by Koutecky-Levich equation.

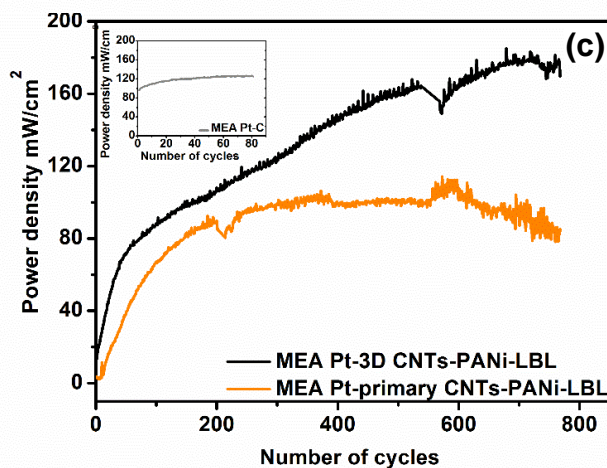
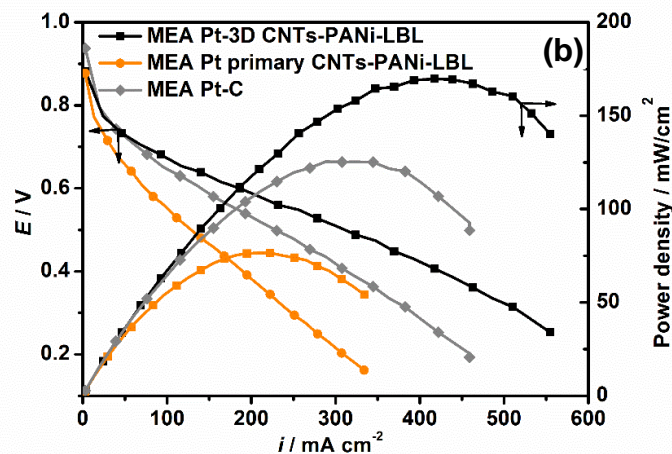
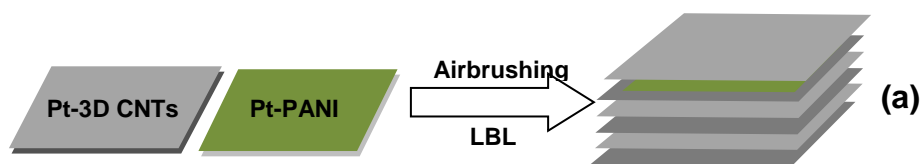


**Figure S3.1.4.** (a) Schema of multilayered MEA; (b) polarization curves of (a) multilayered MEAs assembled by Pt-3D and Pt-PANI; (b) Polarization curves of the Pt-3D CNTs-PANI-LBL, Pt-primary CNTs-PANI-LBL and Pt-C tested at 70 °C; (c) The long-term stability test of the as-prepared Pt catalysts for 7 days.

## 3.2. Hierarchically Structured 3D CNTs/CNTs/GC Electrode

The content of this chapter has been published as ‘Hierarchically structured 3D carbon nanotube electrodes for electrocatalytic applications, Pei Wang, Katarzyna Kulp and Michael Bron, *Beilstein J. Nanotechnol.* 2019, 10, 1475-1487’ [283]. In Beilstein Journal of Nanotechnology, authors retain Copyright of their article.

### 3.2.1. Motivation

Carbon nanotubes (CNTs) attracted considerable attention since their discovery in 1991 [284] due to their high electrical conductivity, large surface area, good chemical stability, high mechanical strength and high aspect ratio and are considered as promising materials for diverse applications such as field emission displays, energy storage devices, sensors, and so on [285–290, 190]. Besides the above-mentioned applications, CNTs have also been investigated as catalysts or catalyst supports for various electrocatalytic reactions [190, 198, 291, 191, 292, 293], including methanol oxidation in direct methanol fuel cells (DMFCs). DMFCs are promising power sources for future energy conversion and storage, since they, in addition to their nonpolluting nature and low operating temperature, run on an easily handled and cheap liquid fuel.

However, the slow kinetics of methanol oxidation at the anode and the methanol crossover through the electrolyte membrane from anode to cathode are still major obstacles that hinder the broad market implementation of DMFCs. The slow kinetics are mainly caused by incomplete methanol oxidation accompanied by the formation of adsorbed carbonaceous reaction intermediates, which poison the Pt surface [294–297, 125, 298]. Most strategies to solve these issues are focused on the optimization of the catalyst, such as alloying Pt with metal such as Ni, Ru and Pd [299–301, 36, 302] or using Pt-metal oxide composites such as Pt/SnO<sub>2</sub> and Pt/CeO<sub>2</sub> [302–306]. Additionally, a variety of catalyst preparation methods, e.g., colloidal synthesis [307–309], a galvanic replacement process [310–313] or microwave-assisted preparation [299, 300, 314], have been proposed to gain control over the structural features of the active nanoparticles.

However, from heterogeneous catalysis it is generally known that a suitable catalyst support is as important as the active material in order to form an optimum

catalyst. For electrocatalytic applications, the support should possess high electrical conductivity, large surface area and good chemical and mechanical stability. Furthermore, the electrode prepared with the catalyst should provide optimized pore structure and retain the high surface area of the catalyst to guarantee a high availability of active site and unhindered mass transfer for high efficiency.

Besides the classical carbon blacks, different carbon based catalyst supports (e.g., modified CNTs, functionalized reduced graphene oxide, etc.) have been recently studied to improve the reaction performance, enhance stability and thus reduce the cost [154, 38, 155–157]. It was reported that Pt supported on these optimized catalyst supports provides higher electrocatalytical activity towards methanol oxidation and increased tolerance against poisoning in comparison to those supported on carbon blacks and non-modified catalysts support. This could be due to improved Pt dispersion owing to a higher amount of functional anchoring sites of the catalyst supports and their high surface area, as well as from a good electrical contact between the conducting components [315, 162, 316, 174]. The modification of electronic and structural properties of Pt due to interaction with the support may also play a role.

To take advantage of the properties of novel carbon materials and at the same time gain control over the electrode structure, bottom-up synthesis approaches have been suggested. In these approaches, one dimensional (1D, e.g., CNTs or nano-/microfibers) or two-dimensional carbon materials (2D, e.g., graphene) are transformed into three-dimensional (3D) structures by attaching of other nanofibers or carbon materials. Examples are nanofibers distributed on polymer-based microfibers, CNTs grown on graphene, CNT-carbon black hybrids, graphene- or polymer-coated CNTs, and so on [174–180]. Another approach for hierarchical structuring is the growth of secondary CNTs on primary CNTs [47, 46, 317, 182, 181]. It was shown that such nanostructured CNT–CNT composites exhibit enhanced specific surface area as well as increased specific double-layer capacitance. Additionally, the presence of the secondary CNTs can reduce the equivalent series resistance to promote the electron transfer. CNT-CNT composites have been successfully employed as catalyst supports. Kundu *et al.* reported that Pt supported on such hierarchical structures showed enhanced surface atomic concentration indicating an

improved Pt dispersion. The oxygen reduction reaction on Pt/CNTs-CNTs yielded a much higher diffusion-limited current compared to Pt supported on other carbon based electrodes [47]. In general, CNT-based hierarchically nanostructured materials can be considered as promising support materials for electrocatalytic applications.

This work investigates the preparation of hierarchically structured CNTs on glassy carbon (GC) based on a sequential CNT growth over electrodeposited Fe nanoparticles via chemical vapor deposition (CVD) with cyclohexane as the carbon precursor. Pt electrodeposition onto these hierarchical structures leads to active electrocatalysts. The bottom-up synthesis of these nanocomposites was monitored using scanning electron microscopy (SEM) and Raman spectroscopy, and it is demonstrated that hierarchical structures can be tuned with respect to thickness, length, and density of the CNTs. The activity of the Pt-CNTs/CNTs/GC electrodes towards methanol oxidation was investigated and compared to that of Pt-CNTs/GC and high activity and exceptional poisoning stability were demonstrated.

### 3.2.2. Preparation and Characterization of Hierarchically Nanostructured Electrodes

#### Fe deposition

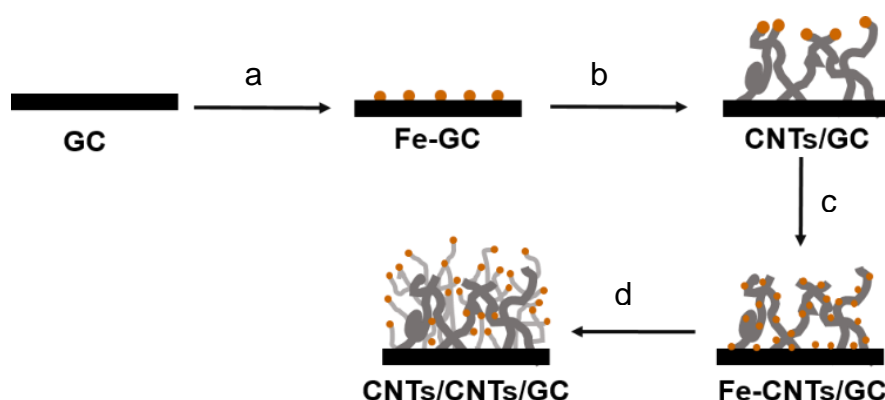


**Figure 3.2.1.** Scheme of the preparation of hierarchically nanostructured electrodes: (a) electrochemical deposition of Fe nanoparticles onto oxidized GC; (b) CNT growth onto GC through CVD; (c) Deposition of Fe nanoparticles onto CNTs and GC; and (d) growth of secondary CNTs on primary CNTs.

In Figure 3.2.1, the individual steps for the preparation of hierarchically nanostructured electrodes are displayed schematically. First, Fe nanoparticles were electrodeposited onto oxidized GC followed by CVD growth of primary CNTs to form



CNTs/GC. After a second deposition of Fe nanoparticles, another CVD step leads to the hierarchically structured electrodes (CNTs/CNTs/GC). Each step has been optimized towards structural control and high reproducibility, as detailed below. The first and critical step is the initial Fe deposition. Fe nanoparticles were electrochemically deposited onto the GC surface using double pulse deposition [318]. This method allows adjustment of nucleation and growth potential to control the distribution and size of the Fe nanoparticles. A nucleation potential of  $-1.41$  V vs. Ag|AgCl|KCl<sub>sat.</sub> and a growth potential of  $-1.27$  V vs. Ag|AgCl|KCl<sub>sat.</sub> were applied (compare also Figure S3.2.1).

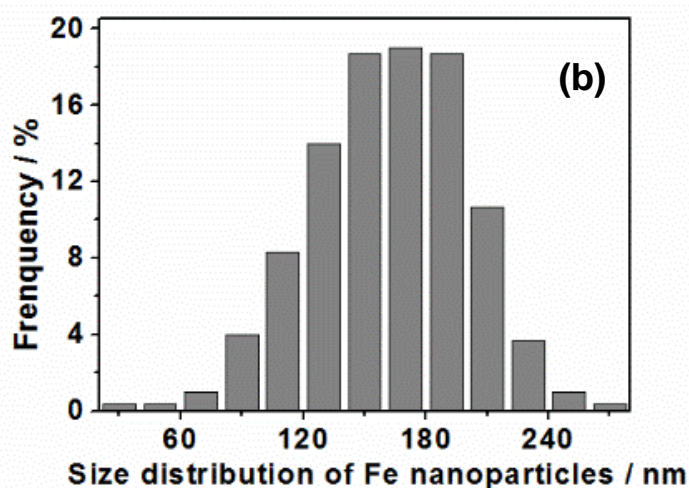
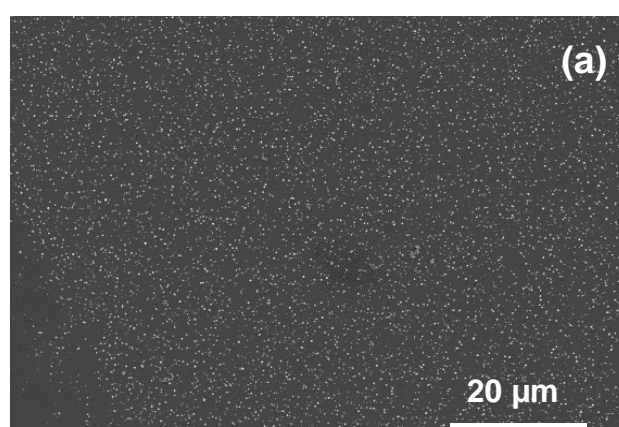


**Figure 3.2.2.** (a) SEM image and (b) particle size distribution of Fe nanoparticles electrochemically deposited onto GC.

Figure 3.2.2a shows an SEM image of Fe nanoparticles deposited onto oxidized GC. The particle diameter is in the range from 100–200 nm (Figure 3.2.2b), which is considerably large. Recent investigations in our lab, which will be published in the

near future, show that particle sizes down to 20 nm and below are possible. Fe deposition onto nonoxidized GC is possible as well but leads to poor reproducibility and inhomogeneous samples with respect to particle size and size distribution. Control over the size of the particles is necessary since it was shown that the diameter of CVD prepared CNTs can be associated with the size of the catalyst particles [206, 319].

### Growth of primary CNTs

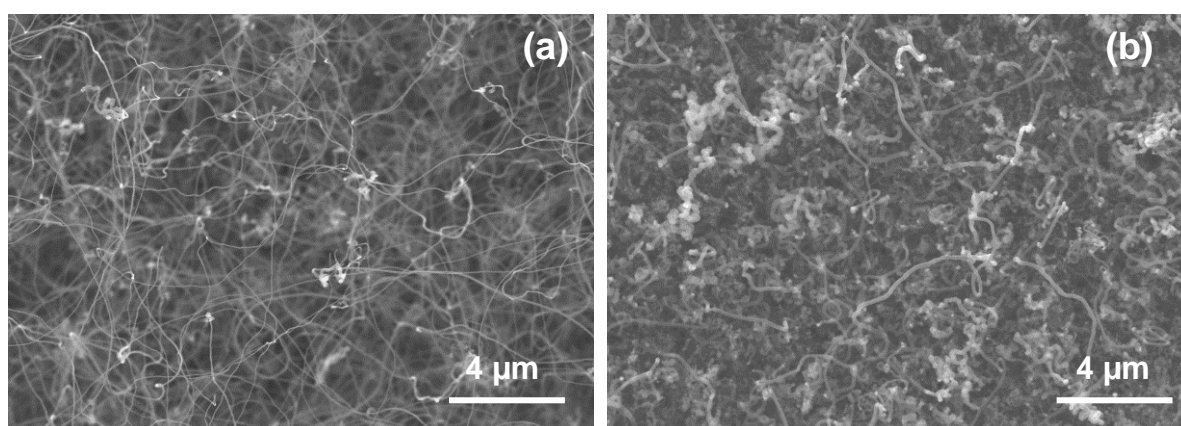


**Figure 3.2.3.** (a) SEM images of CNTs eposited onto GC by CVD at 750 °C using cyclohexane and a gas flow rate of 1.7 L h<sup>-1</sup> for 120 min with an H<sub>2</sub>/Ar ratio of 1.8 (1.1 L h<sup>-1</sup>/ 0.6 L h<sup>-1</sup>). (b) CNTs grown under the same conditions but with an increase total gas flow rate of 3.9 L h<sup>-1</sup>.

After metal catalyst deposition, CNTs were grown via CVD. During CVD growth, the CNT structure (quality) and yield of CNTs is controlled by many parameters, such as the pressure, temperature, growth time, reactor geometry, carbon precursors, gas flow rate and composition of gas mixtures, as well as the catalyst support and physical and chemical state of the catalyst [206, 272, 320, 208, 209]. It is not the aim of this paper to present a detailed study on the influence of all these parameters. However, some of them turned out to be critical for the success or failure of the preparation of hierarchically structured electrodes, as detailed in the following.

The CVD growth of primary CNTs over electrodeposited Fe nanoparticles was carried out with cyclohexane at 750 °C, a temperature that turned out to be suitable in reference experiments (not shown). Cyclohexane is brought into the CVD furnace using a H<sub>2</sub>/Ar gas mixture saturated at room temperature. To gain control over the

CVD process, the influence of growth time, gas flow rate and H<sub>2</sub>/Ar ratio were studied. In a series of experiments, using a growth time of 120 min and a gas flow rate of 1.7 L h<sup>-1</sup> the H<sub>2</sub>/Ar ratio was varied (which translates into a varied H<sub>2</sub>/cyclohexane ratio), and the results were represented in Figure 3.2.3a and Figure S3.2.2e and f. Using a H<sub>2</sub>/Ar ratio of 1.1 L h<sup>-1</sup>/ 0.6 L h<sup>-1</sup> (Figure 3.2.3a), primary CNTs were densely and nearly uniformly grown onto the surface of GC with a diameter of approximately 40 – 80 nm. Accordingly, the optical image (Figure S3.2.2g) displays a matt black thin layer at those areas of the GC chips that were covered with Fe particles. However, no CNT growth was observed with a H<sub>2</sub>/Ar ratio higher than 1.2 L h<sup>-1</sup>/ 0.5 L h<sup>-1</sup> (and thus a higher H<sub>2</sub>/cyclohexane ratio, Figure S3.2.2f), while Figure S3.2.2e shows only few CNTs and large amounts of surrounding (probably amorphous) carbon obtained with a smaller H<sub>2</sub>/Ar ratio (1.0 L h<sup>-1</sup>/ 0.7 L h<sup>-1</sup>). It was reported that the density and diameter of CNTs synthesized on carbon cloth with ethylene as the carbon precursor over a nickel catalyst at 700 °C decrease with a lower ratio of H<sub>2</sub> to N<sub>2</sub> [208], while CNTs grown on an Fe-decorated Si wafer at 825 °C using toluene increased in density and diameter with decreasing ratio of H<sub>2</sub>/Ar [209]. This demonstrates that the CNT growth strongly depends on the growth conditions. Accordingly, the above-described results reveal the sensitivity of CNT growth on the H<sub>2</sub>/cyclohexane ratio under the chosen conditions. During CVD growth, hydrogen molecules or atoms keep the metal catalyst in its active state and avoid catalyst passivation by excess carbon deposition, which would otherwise suppress CNT growth. We assumed that with the decreasing ratio of H<sub>2</sub>/cyclohexane, exactly these processes occur, resulting in suppressed CNT growth and formation of amorphous carbon. In contrast, there is no CNT growth with the increasing ratio of H<sub>2</sub>/Ar, likely because excess hydrogen hydrogenates carbon structures formed at the catalyst surface into volatile compounds, thus hindering CNT growth.

The time dependence of CNT growth was examined for growth times ranging from 30 to 120 min (Figure 3.2.3a, Figure S3.2.2a, b). After 30 min growth, no CNTs can be found, while short CNTs with a diameter of 40–80 nm are formed during 60 min of CVD growth. The diameter is similar to that of CNTs grown for 120 min (Fig. 3.2.3a). From 30 min to 120 min, the density of the CNTs is increased. Obviously, there is a considerably long conditioning period, during which the growth catalyst is likely slowly saturated with carbon until the optimum H<sub>2</sub>/cyclohexane (or carbon) ratio is reached.

Besides varying the H<sub>2</sub>/Ar ratio and the growth time, the influence of the total gas flow rate and thus the cyclohexane feed on CNT growth was studied using the optimum H<sub>2</sub>/Ar ratio (1.8) and a growth time of 120 min. Figure 3.2.3b shows CNTs grown with a total gas flow rate of 3.9 L h<sup>-1</sup>. The CNTs grow densely and homogeneously with a diameter of approximately 150 nm. This is about twice as thick as the diameter of the CNTs grown in 1.7 L h<sup>-1</sup>. Most likely, the larger amount of decomposed carbon crystallizing on the Fe nanoparticles to form a cylindrical network is the reason for this observation. Using 6.7 L h<sup>-1</sup> and 12.1 L h<sup>-1</sup> as the total gas flow rate, only few CNTs were grown (Figure S3.2.2c, d). We assume that the excess carbon surrounds the Fe nanoparticles, blocking them from further CNT growth. It might be speculated that a higher H<sub>2</sub>/cyclohexane ratio would allow CNT growth also at higher total gas flow rates, which we have not yet investigated. Regardless, the above results demonstrate that by choosing the appropriate experimental conditions, it is possible to tune the thickness and length of the primary CNTs grown on glassy carbon. Additionally, the successful CNT growth was also achieved using nickel as catalyst in the optimum condition of CNT growth (Figure S3.2.12).

### **Growth of secondary CNTs and Pt deposition**

After growth of the primary CNTs, a subsequent Fe electrodeposition and growth of secondary CNTs was carried out to form hierarchical electrodes (CNTs/CNTs/GC) as shown in the SEM images of Figure 3.2.4. These experiments were carried out with the thicker primary CNTs grown at a gas flow of 3.9 L h<sup>-1</sup>. Figure 3.2.4a shows Fe nanoparticles deposited onto the primary CNTs with quite homogeneous distribution. Double pulse deposition, as described above, was utilized but the deposition time was decreased from 12 s to 8 s, resulting in a reduced Fe particle size range from 50–90 nm. The use of thicker CNTs as the primary material and smaller Fe particles for the secondary CNTs was chosen to obtain truly hierarchical structures, facilitating the verification of the growth of secondary CNTs. The particle size can be controlled via the deposition time, as shown in Figure S3.2.3, with average particle sizes of ≈45 nm after 6 s of deposition time and ≈110 nm after 12 s of deposition. Additionally, the Fe nanoparticles seem to prefer to nucleate on cross

junction between primary CNTs, as observed from Figure S3.2.3a, which could be caused by improvement of electron transfer or preferential nucleation sites.

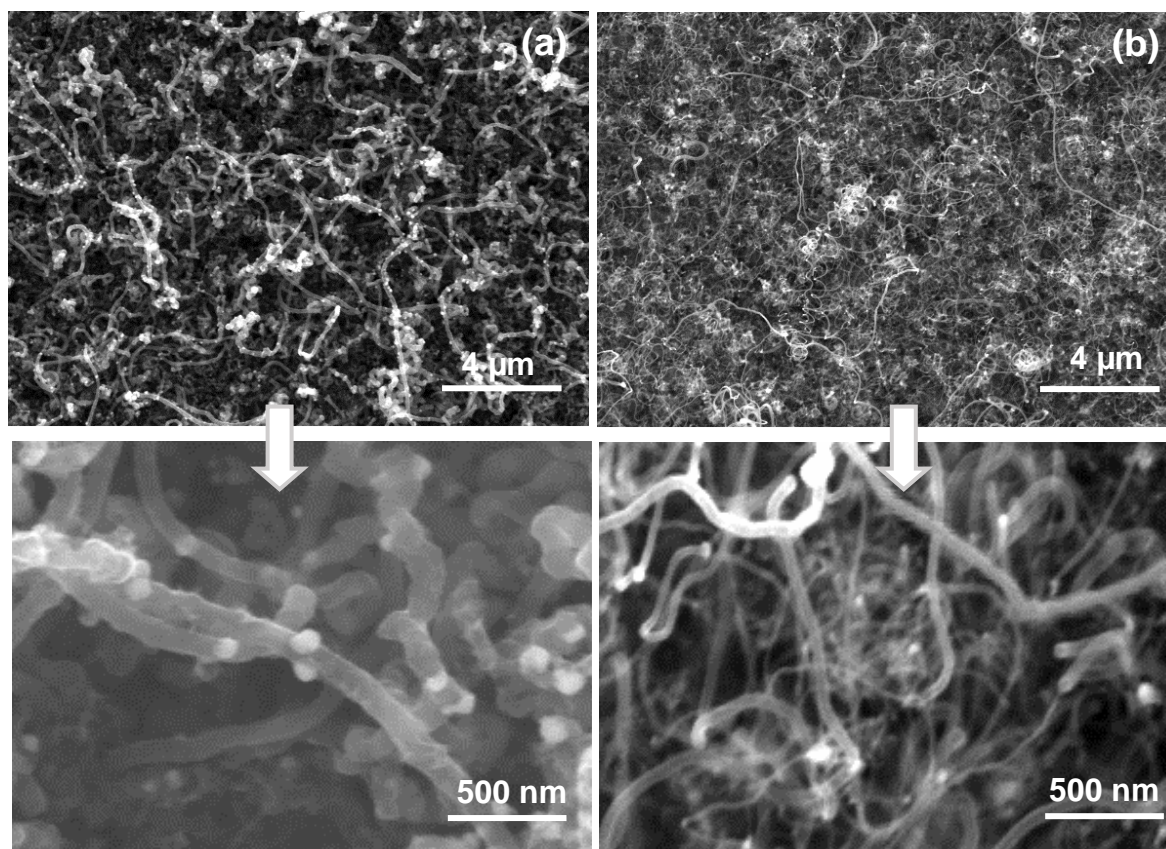


**Figure 3.2.4.** SEM images of (a) Fe nanoparticles electrodeposited onto primary CNTs and GC (8 s of deposition time) and (b) secondary CNTs grown at 750°C for 120 min with a H<sub>2</sub>/Ar ratio of 2.4 (1.2 L h<sup>-1</sup>/ 0.5 L h<sup>-1</sup>).

The growth of secondary CNTs using the same optimized gas mixture as above and a gas flow rate of 1.7 L h<sup>-1</sup> yielded unsatisfactory results. As exposed in Figure S3.2.4, larger amounts of amorphous carbon are deposited and only few CNTs are grown, indicating the dependence of CNT growth on support and structure. Learning from the results on the growth of primary CNTs, the H<sub>2</sub>/Ar ratio was adjusted to 1.2 L h<sup>-1</sup>/0.5 L h<sup>-1</sup> to avoid formation of amorphous carbon, and the growth of secondary CNTs was successfully achieved, as demonstrated in Figure 3.2.4b. The secondary CNTs were grown quite irregularly, which may be caused by the size distribution of the Fe nanoparticles but also by the fact that the gas composition within the 3-dimensional structure of the primary CNTs may change due to cyclohexane consumption by the CVD process. However, the presence of a large number of

thinner CNTs compared to the initial structures verifies the growth of secondary CNTs (compare also Figure S3.2.5). It is, however, considerably difficult to identify junctions between primary and secondary CNTs, probably due to top growth and the high density of CNTs.

Furthermore, to access the generality of our approach, the above designed procedure was successfully employed to prepare nitrogen-doped nanostructured electrodes (N-CNTs/N-CNTs/GC and N-CNTs/N-CNTs/CC) using acetonitrile ( $\text{CH}_3\text{CN}$ ) as the carbon precursors and nitrogen source instead of cyclohexane (see Figure S3.2.6 and Figure S3.2.13).

### Physicochemical characterization

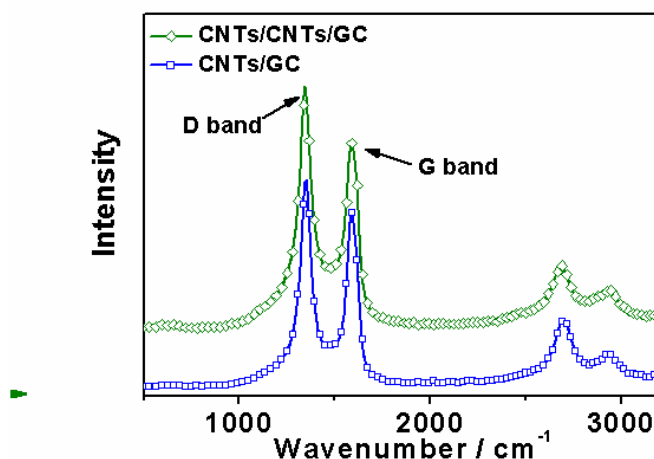


**Figure 3.2.5.** Raman spectra of CNTs/GC and CNTs/CNTs/GC electrodes. The spectra are normalized with respect to the intensity of the D-band, and horizontal lines indicate the height of the G-band.

The prepared electrodes (CNTs/GC and CNTs/CNTs/GC) were characterized by Raman spectroscopy (Figure 3.2.5) after Fe removal in concentrated  $\text{HNO}_3$  (before Pt electrodeposition). Both electrodes show the typical D-band at  $\approx 1355 \text{ cm}^{-1}$  and the G-band at  $\approx 1600 \text{ cm}^{-1}$ , which are associated with structural defects within the carbon lattice and crystalline carbon, respectively [321]. The intensity ratios of these bands ( $I_D/I_G$ ) for CNTs/GC and CNTs/CNTs/GC electrodes are 1.36 and 1.54, respectively. This indicates that the secondary CNTs are less ordered and have a higher defect density than the primary ones.



**Table 3.2.1.** Pt masse on the different supports and corresponding electrochemically active surface area (ECSA) determined by  $H_{\text{upd}}$  and  $\text{CO}_{\text{ads}}$ .

	Pt-GC	Pt-CNTs/GC	Pt-CNTs/CNTs/GC
Mass of Pt (mg) via LSV	0.147	0.101	0.065
ECSA from $H_{\text{upd}}$ ( $\text{m}^2/\text{g}$ )	1.11	6.18	12.39
ECSA from CO ( $\text{m}^2/\text{g}$ )	-	10.95	13.87
Ratio of ECSA from CO vs $H_{\text{upd}}$	-	1.61	1.12

As the last step in electrode preparation, Pt nanoparticles were electrochemically deposited onto CNTs/CNTs/GC and CNTs/GC using linear-sweep voltammetry from 0 to -0.9 V vs Ag|AgCl|KCl<sub>sat.</sub>. For comparison, Pt deposition onto oxidized GC was carried out in the same manner (compare Figure. S3.2.7 for the resulting deposition curves). The quite different double-layer capacities above -0.15 V are due to the different surface areas and was subtracted for charge integration. Based on Faraday's Law and the charge consumed during the sweep, the mass of electrodeposited Pt onto the GC, CNTs/GC and CNTs/CNTs/GC electrodes was calculated to be 0.147 mg, 0.101 mg and 0.065 mg, respectively (Table 3.2.1). It seems to be surprising that the amount of deposited Pt is highest on the sample with the lowest surface area. The reason for the decreasing Pt amount in the order GC, CNTs/GC and CNTs/CNTs/GC is not clear to us at the moment; however, this was observed in repeated experiments. Similarly it was reported by Rajesh *et al.* [185] that the amount of electrodeposited Pt on graphene/CNTs/GC was less than that on graphene/GC under the same deposition condition. As shown in the SEM/BSE images in Figure 3.2.6 and Figure S3.2.8-9, Pt nanoparticles were homogeneously and densely distributed onto the CNTs/GC and CNTs/CNTs/GC with similar particle sizes ( $\approx 7$  nm). Meanwhile, the Pt nanoparticles deposited on oxidized GC are much larger ( $\approx 50$  nm, Figure S3.2.9). Besides electrodeposition onto CNTs, it may be assumed that some Pt is directly deposited onto the GC substrate. Furthermore, it cannot be excluded that particles smaller than the mentioned 7 nm form, which are below the detection limit of our SEM.

In addition to SEM, XRD measurement was performed to analyze the Pt nanoparticles, however, no meaningful diffractograms were obtained due to the low overall Pt loading and probably due to the fact that the electrodeposited Pt

nanoparticles seem to be quite irregular and might consist of several crystallites that are too small to be detected by XRD (compare Figure S3.2.8).

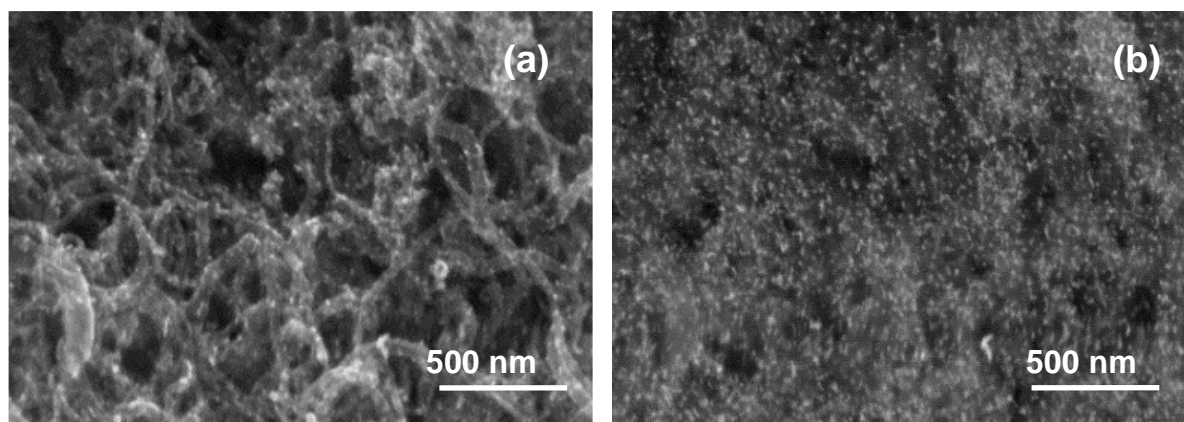


**Figure 3.2.6.** SEM und BSE images of Pt nanoparticles deposited in a aqueous 0.005 M  $\text{Pt}(\text{NO}_3)_2$  and 0.1 M  $\text{NaNO}_3$  solution via single-sweep voltammetry from 0 to -0.9 V vs.  $\text{Ag}|\text{AgCl}|\text{KCl}_{\text{sat.}}$  at a scan rate of  $5 \text{ mV s}^{-1}$  onto CNTs/CNTs/GC.

### 3.2.3. Electrochemical Investigations

#### Cyclic voltammetry

A basic electrochemical characterization of the prepared electrodes was carried out using cyclic voltammetry (CV). CVs of GC before and after oxidation in  $\text{HNO}_3$  as well as after growth of primary CNTs and additional secondary CNTs are displayed in Figure 3.2.7. The currents in the CVs are associated with the charging and discharging of the electrical double layer and denote the double-layer capacity, which can be regarded as an estimation of the surface area for the carbon-only samples. In addition to these currents, in the potential range between 0.5 V and 0.7 V vs. RHE, a redox peak pair is observed for all three samples, which is attributed to the presence of oxygen-containing groups (quinone-type) resulting from the necessary treatment with  $\text{HNO}_3$  (see experimental, preparation of GC surface or leaching of Fe particles) [276]. The double layer capacity of oxidized GC is increased compared to GC before oxidation, which may be attributed to a roughening of the surface and probably the formation of oxygen-containing groups like -OH or  $-\text{C}=\text{O}$  [276]. After the CVD growth of primary CNTs and secondary CNTs, the double layer capacity is significantly enhanced, demonstrating the successful CNT growth and the concomitant increase of electrochemically available surface area. Additionally, the functional groups of



primary and secondary CNTs, which are formed in the concentrated  $\text{HNO}_3$  during the removal of Fe nanoparticles, can also contribute to the increase in double layer capacity [269]. The same observation can be made on the above-mentioned nitrogen doped hierarchically nanostructured electrodes, where N-CNTs/N-CNTs/GC electrodes have a higher double-layer capacity (Figure S3.2.10). It should be mentioned that N-CNTs/N-CNTs/GC displays no redox peak attributed to oxygen-containing functional groups since Fe was electrochemically leached out in  $\text{H}_2\text{SO}_4$  and not chemically in concentrated  $\text{HNO}_3$  for the sake of follow-up studies not presented here. Additionally, CNTs/CNTs/GC is hydrophobic, while N-CNTs/N-CNTs/GC turned out to be hydrophilic, rendering an oxidative treatment unnecessary.

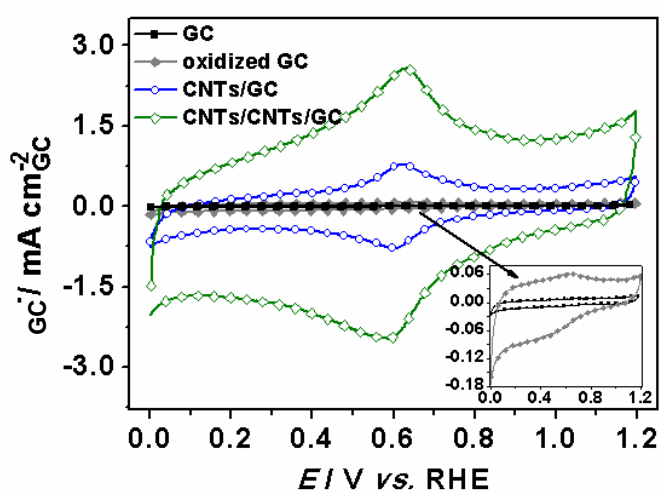


**Figure 3.2.7.** Cyclic voltammograms of GC, oxidized GC, CNTs/GC and CNTs/CNTs/GC recorded at a scan rate of  $100 \text{ mV s}^{-1}$  in  $\text{N}_2$ -saturated  $0.5 \text{ M H}_2\text{SO}_4$  aqueous electrolyte solution at room temperature.

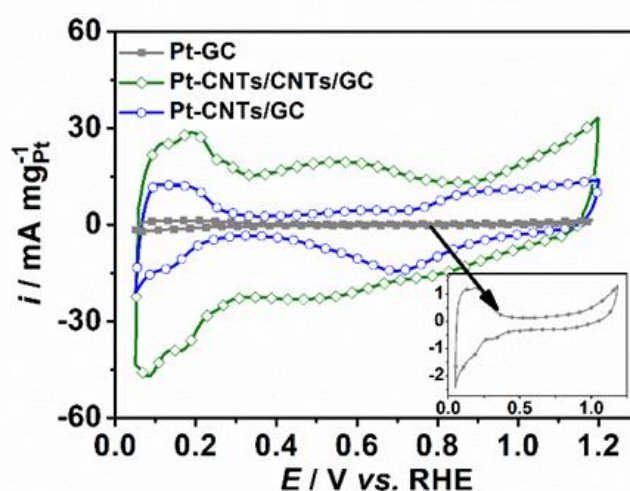


**Figure 3.2.8.** Cyclic voltammograms of Pt onto GC, CNTs/GC and CNTs/CNTs/GC electrodes recorded at a scan rate of  $100 \text{ mV s}^{-1}$  at room temperature in a  $\text{N}_2$ -purged aqueous  $0.5 \text{ M H}_2\text{SO}_4$  electrolyte solution.

As described above Pt nanoparticles were electrodeposited onto the hierarchical electrodes and, for comparison, also onto the surfaces of oxidized GC and CNTs/GC. The available catalyst surface area (electrochemical surface area (ECSA)) of Pt on GC, CNTs/GC and CNTs/CNTs/GC was determined from the  $H_{\text{upd}}$  charge and  $\text{CO}_{\text{ad}}$  stripping voltammograms. The respective cyclic voltammograms of  $H_{\text{upd}}$  were recorded in  $\text{N}_2$ -saturated aqueous 0.5 M  $\text{H}_2\text{SO}_4$  in the potential range from 0.05 to 1.2 V vs. RHE at a scan rate of  $100 \text{ mV s}^{-1}$  as displayed in Figure 3.2.8. The ECSA was calculated from the average coulombic charge obtained via integrating the area under the hydrogen adsorption/desorption peaks after subtracting the double-layer charge in the potential range between 0.05 V and 0.35 V vs. RHE [322, 277]. As shown in Figure 3.2.8, the current density (normalized to Pt mass) of Pt-CNT/CNT/GC for hydrogen adsorption/desorption increases compared to Pt-GC and Pt-CNT/GC, and the determined values are displayed in Table 3.2.1. The increase in the ECSA for Pt-CNTs/CNTs/GC may be explained by the higher CNT surface area of CNT/CNT/GC as compared to CNT/GC, as deduced from the double-layer current. The secondary CNTs provide a larger number of anchoring sites (e.g., surface functional groups or junction between primary CNTs and secondary CNTs) to form a larger numbers of Pt nuclei during electrodeposition [322]. As a consequence, the Pt particles in Pt-CNT/CNT/GC must be smaller than in Pt-CNTs/GC. This difference is scarcely observed from the SEM images (Figure 3.2.6), which may be attributed to the limited resolution of SEM and non-observable Pt nanoparticles on GC. As described in the literature [47], secondary CNTs exhibit decreased charge transfer resistance with respect to the primary CNTs as determined by electrochemical impedance spectroscopy. Thus, we speculate that the improvement in Pt dispersion is due to a better conductivity within the 3D network and a facilitated electron transfer, which may facilitate Pt nucleation at the CNT surface. As expected, Pt-GC has a much lower ECSA compared to Pt-CNTs/GC or Pt-CNTs/CNTs/GC, which is associated with the larger Pt nanoparticles (see Figure S3.2.9) resulting from the much lower surface area of GC.

### CO stripping voltammograms

In addition, CO<sub>ad</sub> stripping voltammograms were performed at a scan rate of 20 mV s<sup>-1</sup> in the potential range of 0.05–1.1 V vs. RHE after CO adsorption in N<sub>2</sub>-purged 0.1 M HClO<sub>4</sub> solution for ECSA determination as well as investigation of CO tolerance as shown in Figure 3.2.9. HClO<sub>4</sub> was used as the electrolyte for these investigations instead of H<sub>2</sub>SO<sub>4</sub> for a better comparability with literature values and to avoid disturbance of the CO<sub>ad</sub> stripping voltammograms by sulfate/bisulfate adsorption. The charge consumed during CO<sub>ad</sub> oxidation was used to calculate the ECSA, and the values are 10.95 m<sup>2</sup> g<sub>Pt</sub><sup>-1</sup> for Pt-CNTs/GC and 13.87 m<sup>2</sup> g<sub>Pt</sub><sup>-1</sup> for Pt-CNTs/CNTs/GC. The ECSAs determined from CO<sub>ad</sub> stripping are higher than those from H<sub>upd</sub> (Table 3.2.1), and the ratio of ECSA<sub>CO<sub>ad</sub></sub> to ECSA<sub>H<sub>upd</sub></sub> is 1.61 for Pt-CNTs/GC and 1.12 for Pt-CNTs/CNTs/GC. This is comparable to values reported by Mayrhofer *et al.* [277]. The calculated ECSAs of Pt-CNT/GC and Pt-CNT/CNT/GC are lower than the values of 30–80 m<sup>2</sup> g<sub>Pt</sub><sup>-1</sup> ECSA for 2–3 nm Pt nanoparticles deposited onto CNTs as reported in the literature [17, 169, 161], in accordance with the larger size of the Pt nanoparticles. The differences in the ECSA ratios between both samples originate from the much more difficult baseline determination for the H<sub>upd</sub> peaks and thus a relatively large error. In this respect, the results on the surface-specific properties (see below) are related to the ECSA determined by CO stripping, which is believed to be much more reliable due to easier baseline correction.

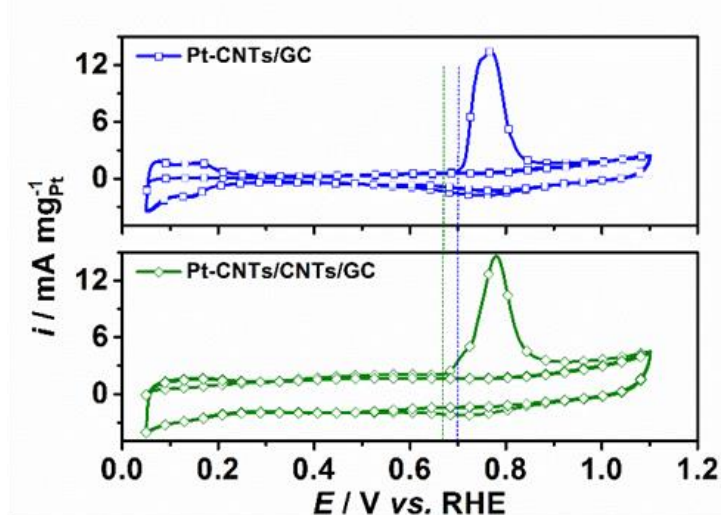


**Figure 3.2.9.** CO<sub>ad</sub> stripping voltammograms of Pt-CNTs/GC and Pt-CNTs/CNTs/GC monitored at 20 mV s<sup>-1</sup> in CO-purged and subsequently N<sub>2</sub>-purged 0.1 M HClO<sub>4</sub> solution. The vertical dashed lines are intended as a guide for the eye.

### Methanol electro-oxidation

The CVs of the methanol oxidation reaction (MOR) over the Pt-containing nanostructured electrodes were recorded in N<sub>2</sub>-purged 1 M CH<sub>3</sub>OH and 0.5 M H<sub>2</sub>SO<sub>4</sub> aqueous solution to investigate their suitability for electrocatalytic applications. Due to the large double-layer capacity of the samples, a slow scan rate of 5 mV s<sup>-1</sup> was applied. Note that the oxidation current scales with the square root of the scan rate, while the double-layer charging current linearly scales with scan rate. Thus, the slow scan rate allows for a much more reliable determination of peak potentials and currents. The fifth cycle of each measurement is represented in Figure 3.2.10. The current response for electrochemical activity towards MOR was quantified to the Pt mass and the Pt ECSA in Figure 3.2.10a and Figure 3.2.10b, respectively, where the Pt ECSA was calculated from the CO<sub>ad</sub> stripping voltammograms. Figure 3.2.10 represents the typical appearance of the CVs for methanol oxidation over Pt-based catalysts. Methanol is oxidized to CO<sub>2</sub> in the forward CV scan until Pt is oxidized, leading to a surface passivation and a sudden decrease in the oxidation current. During the backward CV scan, MeOH oxidation starts as soon as the electrode is liberated from oxides. In the literature, it is often observed that the current during the backward scan is higher and/or extends to less positive potentials than during the forward scan, since in the forward scan the electrode is blocked by intermediate carbonaceous species (e.g., CO) formed at lower potentials. Thus, the peak current ratio between the forward and backward scan ( $i_f/i_b$ ) is typically used as a qualitative measure of the poisoning tolerance of a catalyst towards carbonaceous poisoning species formed during incomplete methanol oxidation at lower potentials [323–326]. In this regard, the comparably high ( $i_f/i_b$ ) ratio (see below) indicates very good poisoning tolerance of our nanostructured samples. However, Hofstead-Duffy *et al.* [327] claimed that the forward and backward scan of methanol oxidation has the same chemical origin and the  $i_f/i_b$  ratio is inadequate to be used as a measure for CO tolerance, which is further demonstrated and complemented in [328, 329]. Thus, we attempted to obtain additional information on CO tolerance from the CO stripping voltammograms. As shown in Figure 3.2.9, the hydrogen adsorption/desorption is suppressed in the potential range from 0.05 to 0.3 V vs. RHE, indicating complete coverage of Pt with CO<sub>ad</sub>. Pt-CNTs/CNTs/GC provides a more negative onset potential for CO oxidation at around 0.66 V vs. RHE compared to Pt-CNT/GC ( $\approx 0.7$

V). The negative shift of the onset potential indicates that Pt-CNT/CNT/GC is superior for the electro-oxidation of  $\text{CO}_{\text{ad}}$  compared to Pt-CNT/GC. The reason for this improved poisoning tolerance is not known to us at the moment. However, it is known from literature that methanol as well as CO oxidation are very sensitive to Pt surface structure. It might be that a defect-rich structure of our Pt nanoparticles formed by electrodeposition is highly active for CO and MeOH oxidation and less prone to poisoning.

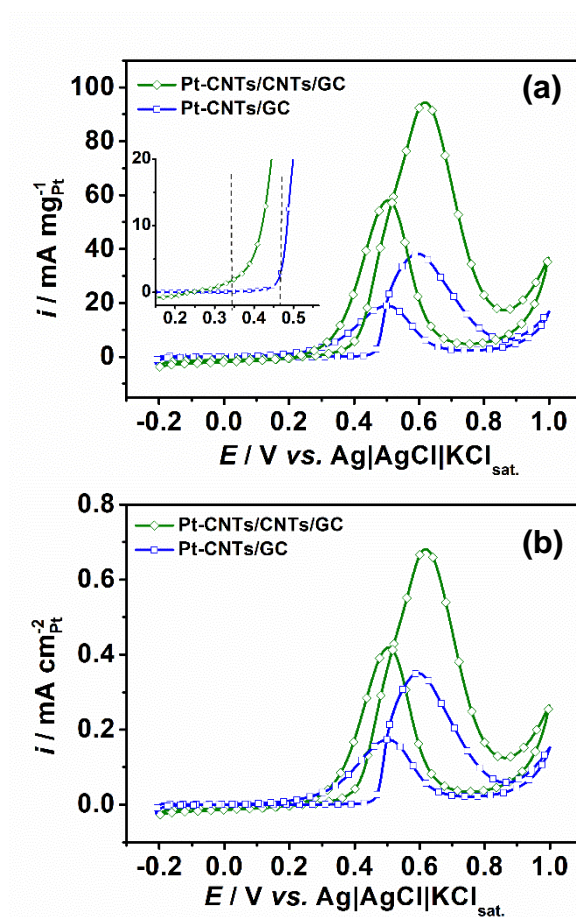


**Figure 3.2.10.** Cyclic voltammograms of Pt-CNTs/GC and Pt-CNTs/CNTs/GC in  $\text{N}_2$  saturated 1 M  $\text{CH}_3\text{OH}$  and 0.5 M  $\text{H}_2\text{SO}_4$  electrolyte solution recorded at a scan rate of  $5 \text{ mV s}^{-1}$  normalized to (a) Pt masse and (b) Pt-ECSA evaluated by  $\text{CO}_{\text{ads}}$  stripping. The vertical dashed lines are intended as a guide for the eye.

The cyclic voltammograms in Figure 3.2.10 show differences in terms of the electrocatalytic activity. In the forward scan, Pt-CNTs/CNTs/GC provides Pt mass specific and Pt surface specific peak currents of  $94.46 \text{ mA mg}_{\text{Pt}}^{-1}$  and  $0.68 \text{ mA cm}_{\text{Pt}}^{-2}$  at the peak potential of 0.83 V vs. RHE, respectively, which is much higher than those of Pt-CNTs/GC, which are  $38.54 \text{ mA mg}_{\text{Pt}}^{-1}$  and  $0.35 \text{ mA cm}_{\text{Pt}}^{-2}$  at 0.81 V vs. RHE; respectively. Pt-GC provides much lower specific peak currents of  $1.88 \text{ mA mg}_{\text{Pt}}^{-1}$  and

0.17 mA cm<sub>Pt</sub><sup>-2</sup> as expected. The inset in Figure 3.2.10a indicates the superior onset potential of Pt-CNTs/CNTs/GC ( $\approx 0.55$  V vs. RHE) compared to that of Pt-CNTs/GC ( $\approx 0.68$  V vs. RHE). Pt mass specific and Pt surface specific peak current ratios of Pt-CNTs/CNTs/GC related to Pt-CNTs/GC are 2.5 and 1.9, respectively. For the backward scans, the values for Pt-CNTs/CNTs/GC were 58.14 mA mg<sub>Pt</sub><sup>-1</sup> and 0.41 mA cm<sub>Pt</sub><sup>-2</sup> which are again, significantly higher than those of Pt-CNTs/GC (19.74 mA mg<sub>Pt</sub><sup>-1</sup> and 0.17 mA cm<sub>Pt</sub><sup>-2</sup>). These values indicate that Pt-CNTs/CNTs/GC provides higher catalytic activity for the methanol oxidation. Similarly, Pt-CNTs/CNTs/GC exhibits a 1.3 times higher surface specific current density than Pt-CNTs/GC for methanol oxidation in alkaline medium as shown in Figure S3.2.11.

Such enhancement in specific activity could be attributed to a better distribution of Pt on the high-surface-area secondary nanotubes, while on the primary CNTs, the Pt particles may be more densely packed. Furthermore, the secondary CNTs may increase the contact between GC and primary CNTs and within the CNT network, improving electron transfer pathways. Additionally, differences in particle shape or the presence of small particles invisible to SEM may contribute, however we can only speculate on this.

In the literature, graphene/CNT hybrids were demonstrated to be superior Pt catalyst supports towards MOR with respect to graphene, CNTs or commercial carbons [174, 185, 330, 184, 186, 331]. In [185] electrodeposited Pt nanoparticles were used in a similar fashion as in our paper. Using a Pt-graphene/CNTs hybrid on GC, a mass specific current of 62.02 mA mg<sub>Pt</sub><sup>-1</sup> was found in 1 M methanol solution at a scan rate of 50 mV s<sup>-1</sup>. It should be pointed that MOR measurement in literature are usually performed at scan rates of 50 or 100 mV s<sup>-1</sup>, while in our study we employ 5 mV s<sup>-1</sup> for reasons explained above, and increased mass-specific peak currents at higher scan rates are expected according to the Randles-Sevcik equation.

Furthermore, the Pt-mass specific peak current for Pt-CNTs/CNTs/GC is similar to that of the Pt-graphene/CNTs hybrid on carbon cloth (101.52 mA mg<sub>Pt</sub><sup>-1</sup>), and the Pt-surface specific peak current was two times higher than that of Pt-graphene/CNTs on carbon cloth (0.34 mA cm<sub>Pt</sub><sup>-2</sup>) reported previously [330], indicating that the introduction of secondary CNTs may provide a similar or superior beneficial effect as graphene on

the electrocatalytic activity toward MOR. In general, it can be concluded that Pt-CNT/CNT/GC, as prepared in this paper, performs similar or better compared to literature studies using similar systems.

In [47], similar nanostructures were prepared that showed high activity in the oxygen reduction reaction. The prepared materials in this work also show the similar result (Figure S3.2.14). Although there are differences in electrode preparation (in the present case, Pt is electrodeposited onto the carbon-based electrodes, probably leading to defect-rich particles (see also below), while in [47], Pt deposition has been deposited by CVD), we think that generally the high surface area and good accessibility of the active sites is a prerequisite for the enhanced electrocatalytic performance of such structures in various electrocatalytic reactions.

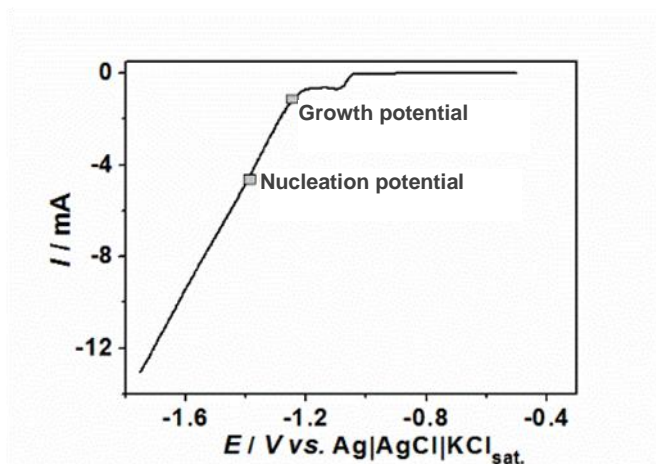
### **3.2.4. Conclusion**

The preparation of hierarchically nanostructured electrodes for electrocatalytic applications was achieved via sequential growth of primary CNTs and secondary CNTs by CVD and finally Pt electrodeposition. CNT growth was carried out over electrodeposited iron nanoparticles. By varying the growth time, gas flow rate and ratio of H<sub>2</sub>/Ar, it was shown that the structural properties of the primary and secondary CNTs could be tuned to a certain extent. The secondary CNTs were adjusted to be smaller than the primary ones to obtain truly hierarchical structures. Enhanced double-layer capacitance as well changes in the Raman spectra with respect to the primary CNTs indicate the successful growth of secondary CNTs. Pt nanoparticles were homogeneously distributed onto both primary and secondary CNTs by electrodeposition. The Pt-CNTs/CNTs/GC electrode exhibited increased ECSA and electrochemical activity as well as more negative onset potential for MOR compared with Pt-CNTs/GC. Additionally, CO<sub>ad</sub> stripping indicated improved tolerance towards CO-like carbonaceous species poisoning. The improvement of electrochemical performance is attributed to the homogenous dispersion of Pt nanoparticles on the highly cross-linked 3D network. The prepared carbon electrode was shown to be a competitive catalyst support for methanol oxidation. In general, the applied sequences of electrodeposition and CVD steps may be considered as part of a toolbox enabling the preparation of hierarchically structured electrodes by

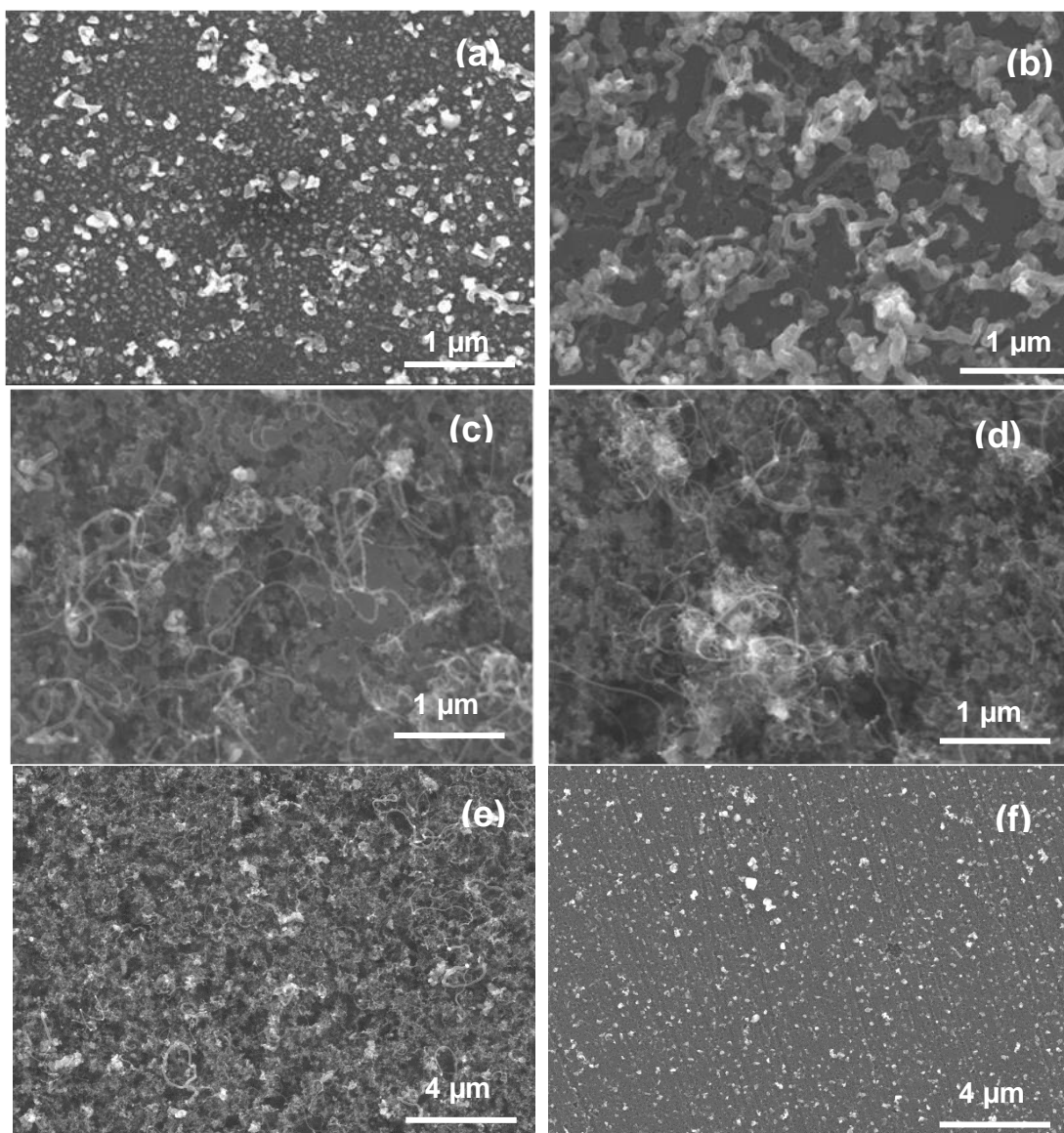
tuning every step with respect to the requirements of a given electrochemical application.



## 3.2.5. Supplementary Information



**Figure S3.2.1.** Single sweep voltammogram of iron deposition on oxidized GC recorded in the potential range between -0.5 V and -1.75 V vs. Ag|AgCl|KCl<sub>sat.</sub> with a scan rate 5 mV s<sup>-1</sup> in N<sub>2</sub> purged 0.005 M FeSO<sub>4</sub> · 7H<sub>2</sub>O and 0.5 M MgSO<sub>4</sub> · 7H<sub>2</sub>O aqueous solution. The respective potentials for double-pulse deposition are indicated.



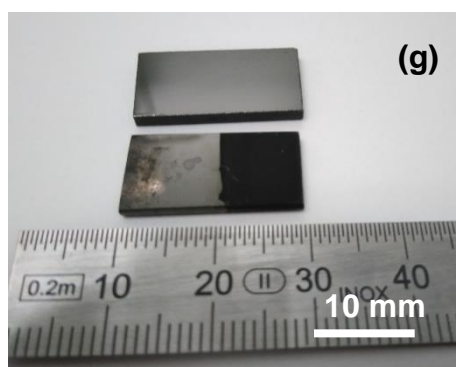


**Figure S3.2.2.** SEM images of CNTs grown at 750°C using cyclohexane as carbon source through CVD with an H<sub>2</sub>/Ar ratio of 1.8: (a) for 30 min and (b) for 60 min using 1.7 L h<sup>-1</sup> as total gas flow rate; (c) with 6.7 L h<sup>-1</sup> as total gas flow rate and (d) 12.1 L h<sup>-1</sup> as flow rate for 120 min; as well as with a gas flow rate of 1.7 L h<sup>-1</sup> for 120min with different H<sub>2</sub>/Ar ratios: (e) 1.4 (1.0 L h<sup>-1</sup>/0.7 L h<sup>-1</sup>), (f) 2.4 (1.2 L h<sup>-1</sup>/0.5 L h<sup>-1</sup>), (g) optical images of GC before and after CNT growth for 120 min.

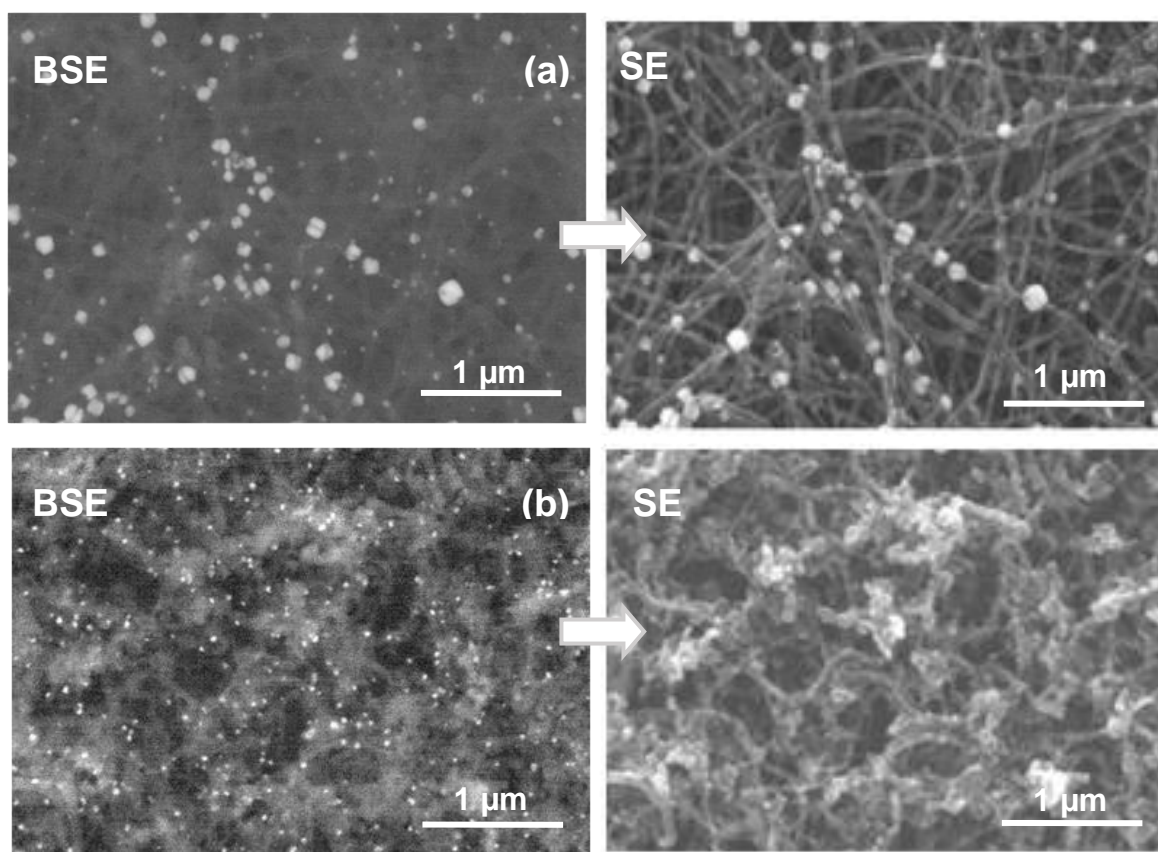


**Figure S3.2.3.** SEM and BSE images of Fe nanoparticles deposited onto primary CNTs on GC via the above mentioned electrochemical deposition with different deposition times: (a) 12 s and (b) 6 s.

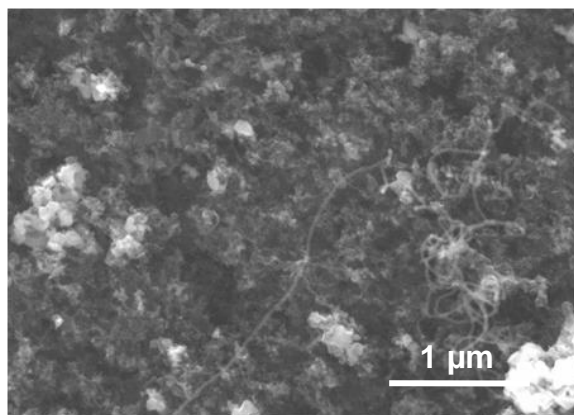


**Figure S3.2.4.** SEM image of secondary CNT growth at 750°C for 120 min with optimized  $H_2/Ar$  ratio: 1.8 ( $1.1 L h^{-1}/ 0.6 L h^{-1}$ ).

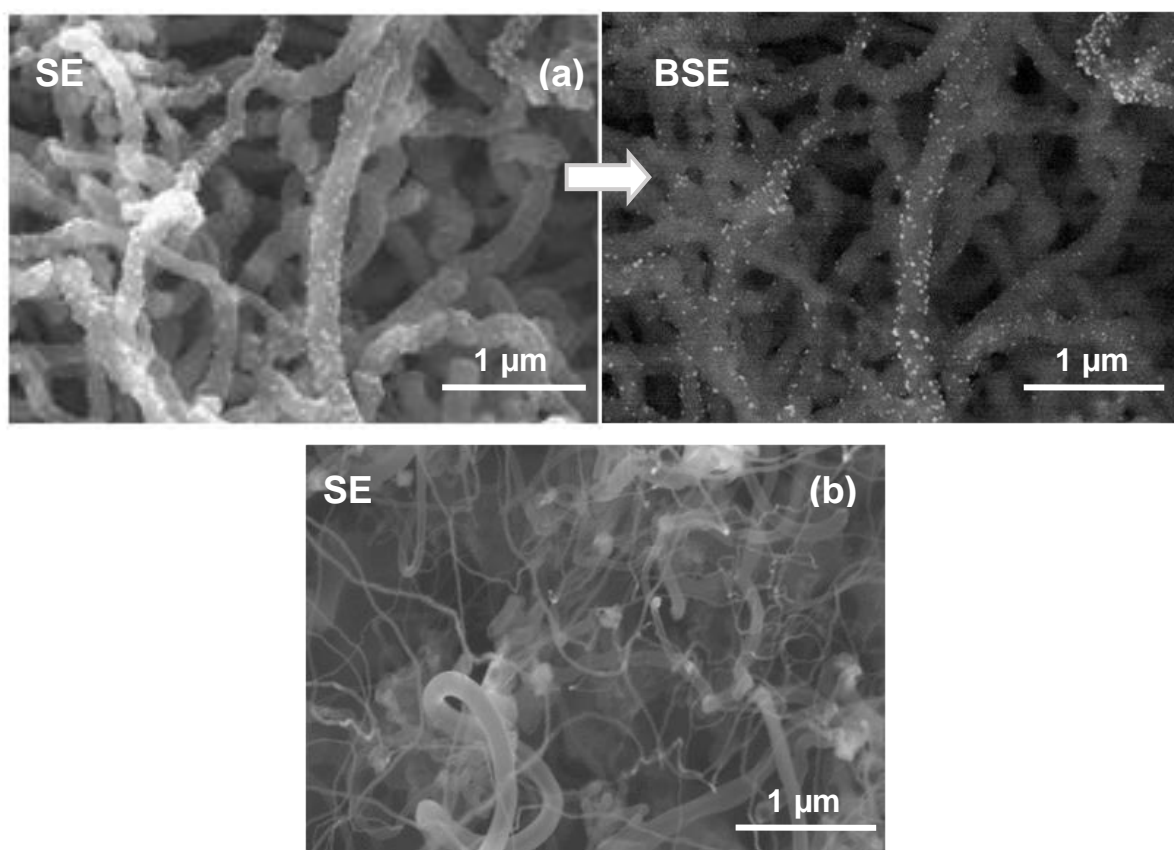


**Figure S3.2.5.** SEM and BSE images of (a) electrodeposited secondary Fe nanoparticles onto thicker CNTs and GC with 6 s deposition time as well as (b) secondary CNTs grown via optimized growth condition. (The CNTs with increased diameter were grown at bigger primary Fe nanoparticles created by longer deposition time.)



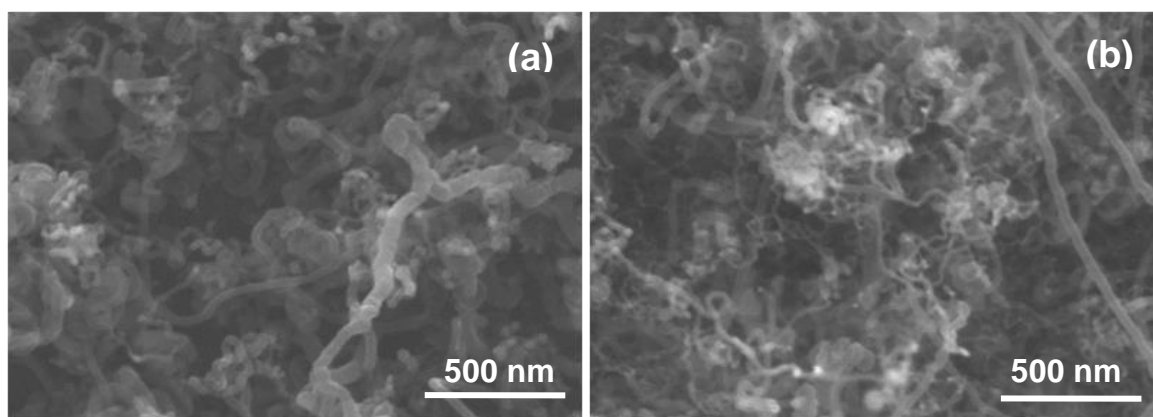


**Figure S3.2.6.** SEM images of CNTs (a) before and (b) after secondary CNT growth under acetonitrile as carbon source at 750 °C for 120 min.

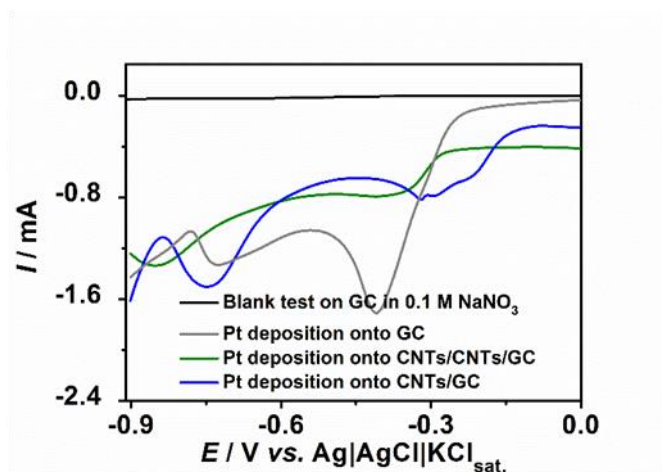


**Figure S3.2.7.** Linear sweep voltammogram for Pt deposition recorded at a scan rate of 5 mV s<sup>-1</sup> from 0 to -0.9 V vs. Ag|AgCl|KCl<sub>sat.</sub> in a 0.005 M Pt(NO<sub>3</sub>)<sub>2</sub> and 0.1 M NaNO<sub>3</sub> solution.

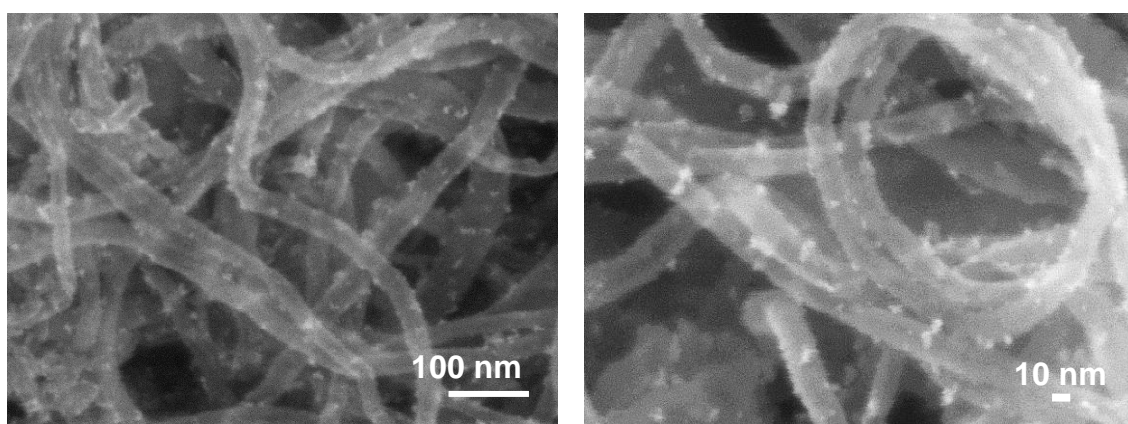


**Figure S3.2.8.** SEM images of Pt nanoparticles deposited onto CNTs/CNTs/Pt in a 0.005 M Pt(NO<sub>3</sub>)<sub>2</sub> and 0.1 M NaNO<sub>3</sub> aqueous solution via linear-sweep voltammetry from 0 to -0.9 V vs. Ag|AgCl|KCl<sub>sat.</sub> at 5 mV s<sup>-1</sup> scan rate.

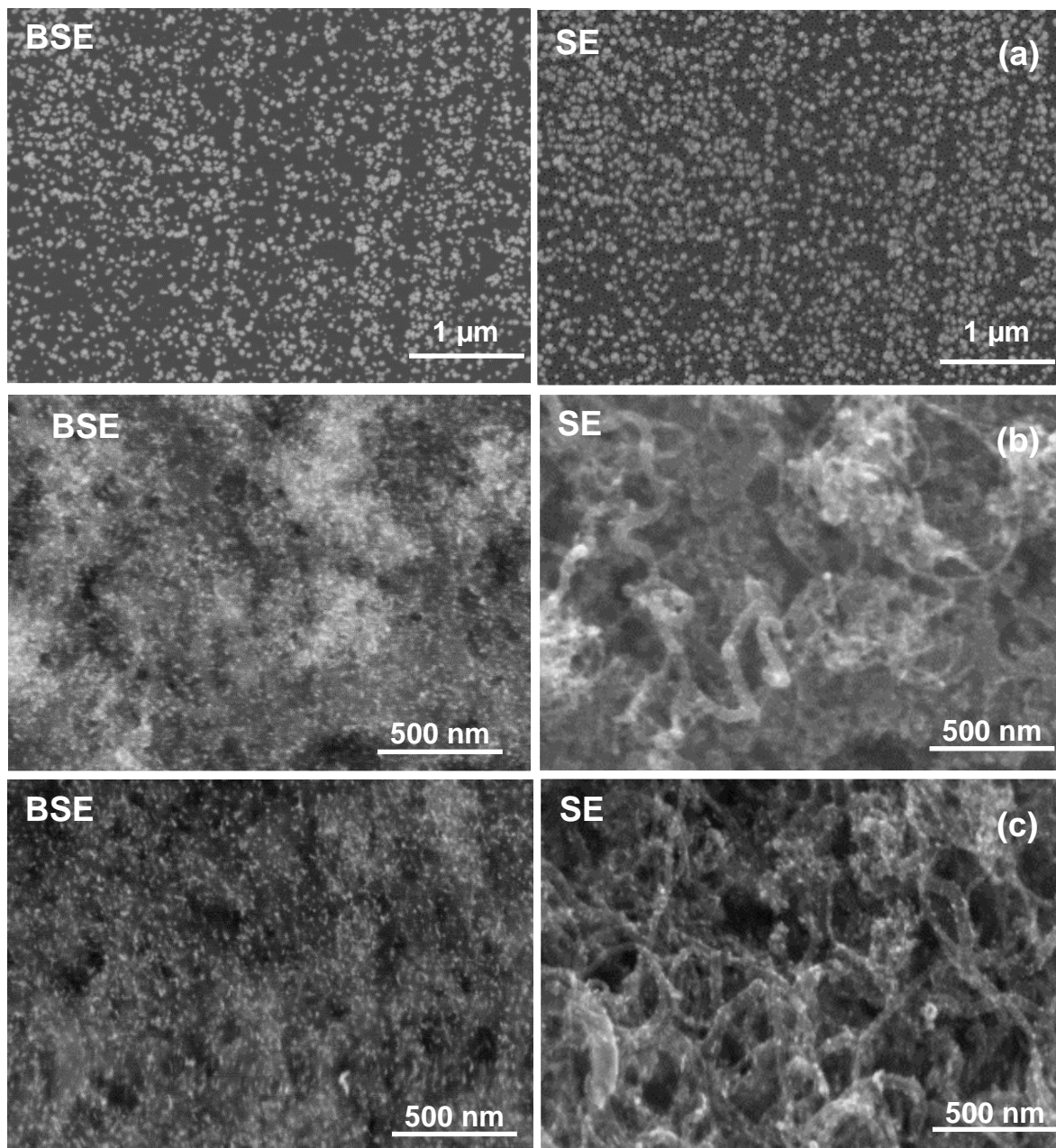


**Figure S3.2.9.** SEM und BSE images of Pt nanoparticles deposited in a aqueous 0.005 M  $\text{Pt}(\text{NO}_3)_2$  and 0.1 M  $\text{NaNO}_3$  solution via single-sweep voltammetry from 0 to -0.9 V vs.  $\text{Ag}|\text{AgCl}|\text{KCl}_{\text{sat}}$ . at  $5 \text{ mV s}^{-1}$  scan rate onto: (a) oxidized GC, (b) CNTs/GC and (c) CNTs/CNTs/GC.

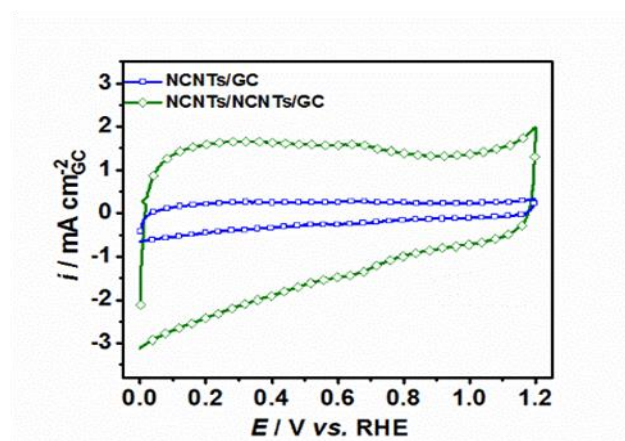


**Figure S3.2.10.** Cyclic voltammograms of N-CNTs/GC and N-CNTs/N-CNTs/GC electrodes measured at a  $100 \text{ mV s}^{-1}$  scan rate in  $0.5 \text{ M H}_2\text{SO}_4$  aqueous solution purged with  $\text{N}_2$  at room temperature.

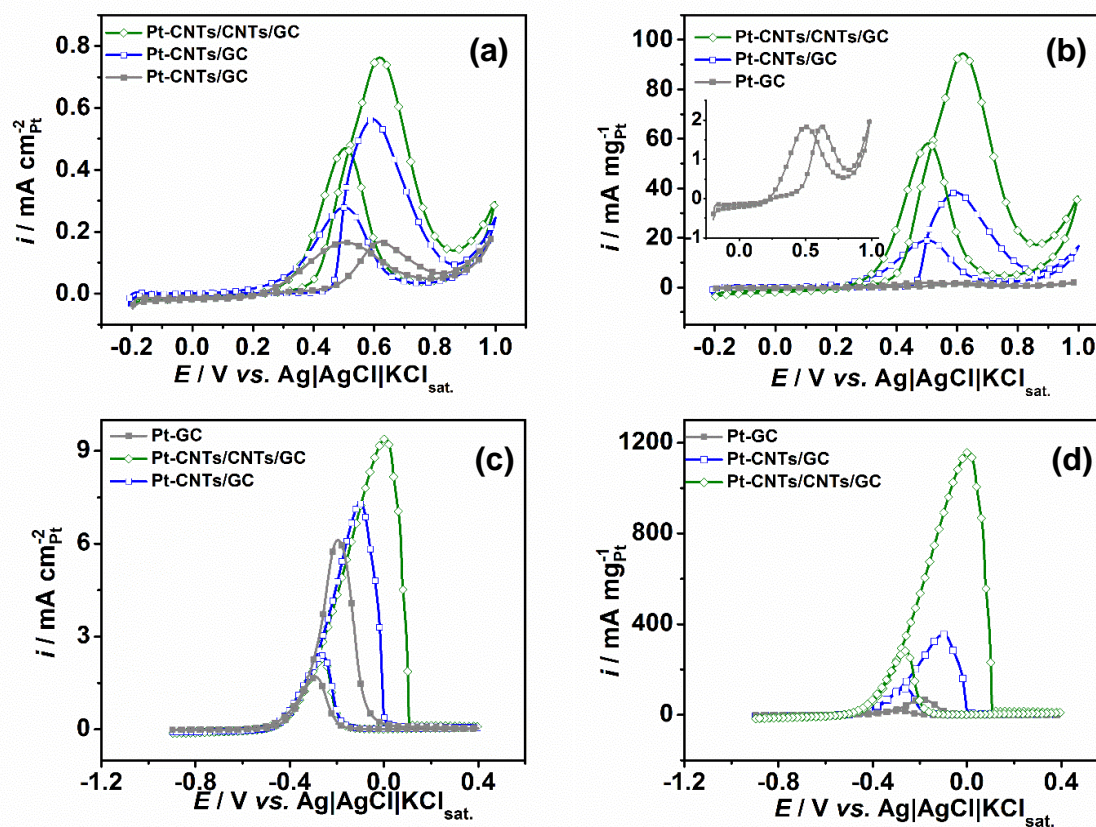


**Figure S3.2.11.** Cyclic voltammograms of Pt-GC, Pt-CNTs/GC and Pt-CNTs/CNTs/GC recorded at a scan rate of  $5 \text{ mV s}^{-1}$  respectively normalized to Pt-ECSA evaluated by  $H_{\text{ads/des}}$  and Pt mass in the potential range from  $-0.2 \text{ V}$ – $1.0 \text{ V}$  vs.  $\text{Ag}|\text{AgCl}|\text{KCl}_{\text{sat}}$  in  $\text{N}_2$  purged  $1 \text{ M CH}_3\text{OH}$  and  $0.5 \text{ M H}_2\text{SO}_4$  solution (a, b) as shown in potential range of  $-0.9 \text{ V}$ – $0.4 \text{ V}$  in  $1 \text{ M CH}_3\text{OH}$  and  $0.5 \text{ M KOH}$  solution (c, d).



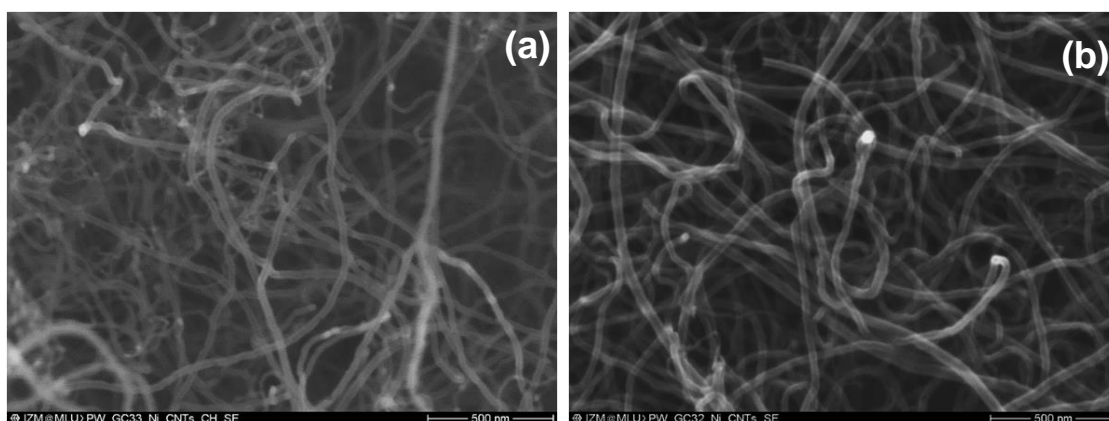


**Figure S3.2.12.** SEM images of CNT growth over Ni particles onto GC via CVD using (a) cyclohexane and (b) acetonitrile as carbon sources at 750°.

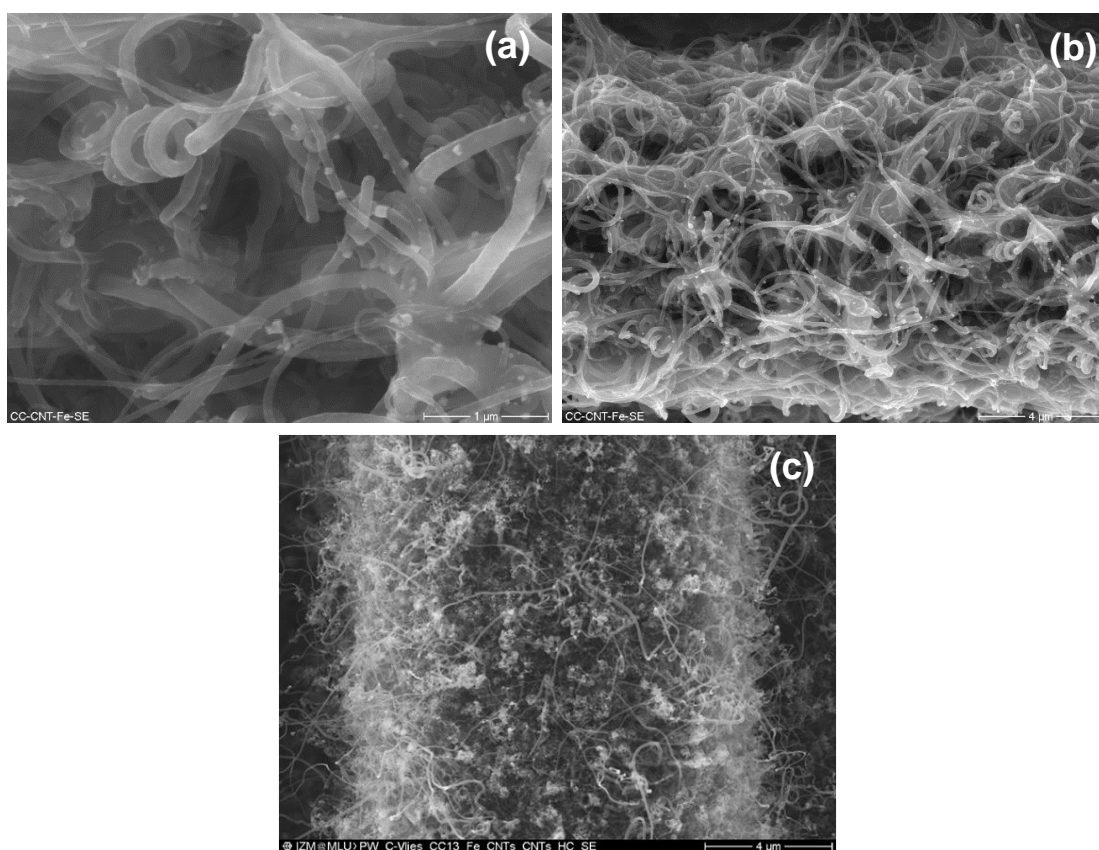


**Figure S3.2.13.** SEM images of (a) and (b) Fe deposited on primary CNTs on CC in different scales, (c) secondary CNT growth over Fe particles via CVD in 3 L h<sup>-1</sup>/3 L h<sup>-1</sup> Ar/H<sub>2</sub> purged acetonitrile atmosphere for 120 min at 750°.

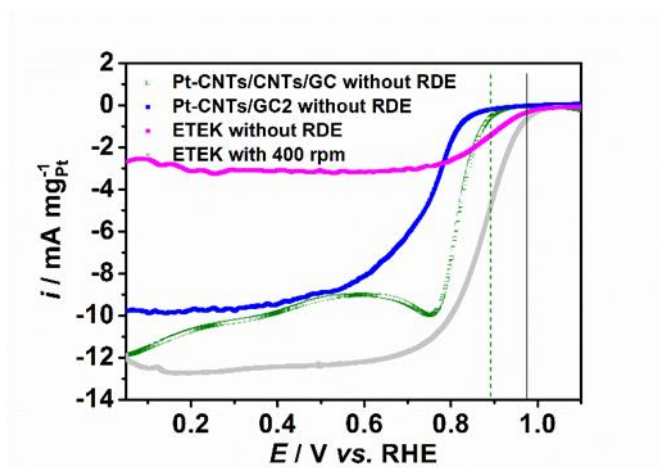


**Figure S3.2.14.** Linear-sweep voltammograms of the prepared electrodes (with Pt) recorded in  $O_2$  saturated  $0.5\text{ M H}_2\text{SO}_4$  at a scan rate of  $5\text{ mV s}^{-1}$  for ORR measurements.



### 3.3. Nanostructured NCNTs/RGO/CC Composite Electrode

The content of this chapter has been published as 'Pt supported on nanostructured NCNTs/RGO composite electrodes for methanol oxidation, Pei Wang, Dr. Tintula Kottakkat, Prof. Dr. Michael Bron, *ChemElectroChem* 2015, 2, 1396-1402' [330]. *Reproduced with permission by John Wiley and Sons and Copyright Clearance Center*

#### 3.3.1. Motivation

Direct methanol fuel cells (DMFCs) are promising power sources for portable applications due to their low temperature of operation and the fact that they run on an easily handled liquid fuel. The high energy density and low cost of methanol are further advantages. However, the methanol crossover through the electrolyte membrane from the anode to the cathode and the slow kinetics of the methanol oxidation reaction (MOR) at the anode restrain the development towards practical DMFC applications. The slow MOR kinetics arises from the various carbonaceous intermediates formed during the incomplete MOR and consequently from the surface poisoning of Pt-based catalysts [125, 332–336].

To overcome the incomplete MOR and poisoning by adsorbed intermediates, alloying of Pt with a second metal or addition of an oxophilic component have frequently been studied, such as Pt–Ru, Pt–Ni, Pt–CeO<sub>2</sub>, Pt–WO<sub>3</sub>, etc. [166, 337–340]. Moreover, new catalyst supports with large surface area, high electrical conductivity and good chemical and mechanical stability were also employed to improve the dispersion and the electrocatalytic activity towards MOR, such as carbon nanotubes (CNTs) [166, 341–344], blends of Vulcan XC-72 carbon with CNTs [345] and reduced graphene oxide (RGO) [158–162].

Earlier investigations demonstrated that Pt-based catalysts supported on nitrogen-doped carbon nanotubes (NCNTs) show increased activity towards MOR and higher power density in DMFC tests than carbon- and CNT-supported catalysts under similar conditions [166, 167]. Furthermore, Pt-based catalysts supported on RGO show enhanced catalytic activity for MOR and better tolerance against carbon monoxide poisoning in comparison to those on Vulcan and CNTs [158–162].

In recent years, graphene- and CNT-based hybrid materials or composites have been widely investigated for supercapacitor applications due to their multifunctional properties, large surface area, favorable mechanical properties, high electrical conductivity and stability in the electrolyte [346–348]. A few studies also report on CNTs/RGO composites investigated as catalyst support for Pt, PtRu or PtRuMo towards MOR activity and CO tolerance [183, 174, 184–186], where the catalysts supported on CNTs/RGO showed improved catalytic performances. CNTs/RGO composites are often prepared by two different approaches. The most common approach is to simply mix GO and CNTs followed by ultrasonic treatment and reduction to form CNTs/RGO hybrids through  $\pi$ - $\pi$  interactions between CNTs and RGO. A more sophisticated approach is to grow CNTs directly onto the surface of graphene through chemical vapor deposition (CVD), where strong interactions exist and reduced restacking of graphene leads to high stability [347, 346]. Jhan *et al.* [186] reported that Pt deposited on composites with CNTs directly grown onto graphene showed distinct enhancement in electrochemical activity with respect to Pt deposited on simply mixed graphene and CNTs.

The electrical conductivity pathway from the electrode/electrolyte interface to the gas diffusion layer (GDL) is an important aspect in membrane–electrode assemblies (MEAs). Usually, carbon paper and carbon cloth (CC) serve as the GDL in MEAs. Tsai *et al.* [349] reported on Pt/Ru nanoparticles electrodeposited on CNTs that were directly grown on carbon cloth. The electrical contact between the support and the diffusion layer was improved and the decrease in active surface area occurring during the conventional ink pasting process was avoided. Wang *et al.* [350] showed that Pt/Ru-CNTs/CC exposed higher performance compared to Pt/Ru-C/CC in MEA polarization curves.

In this work, we prepared uniformly nanostructured NCNTs/RGO hybrids directly onto carbon cloth (CC) as substrate by thermal reduction of graphene oxide (GO) followed by chemical vapor deposition (CVD) of NCNTs. This approach was chosen to directly anchor the NCNTs to the substrate. Furthermore, Pt was uniformly electrodeposited to form Pt-NCNTs/RGO/CC. The MOR surface/mass specific activities and tolerance towards adsorbed carbonaceous intermediate-poisoning of the Pt-NCNTs/RGO/CC electrode were studied and compared with Pt-NCNTs/CC.

### 3.3.2. Preparation and Characterization of the Nanostructured Electrodes

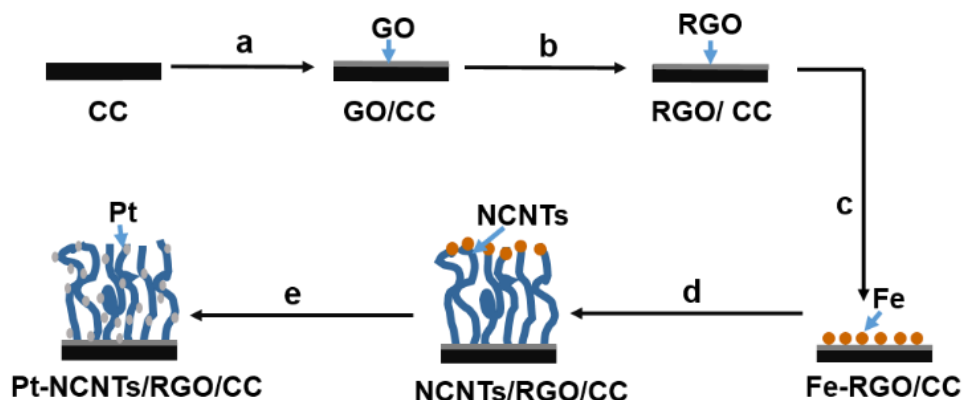


**Figure 3.3.1.** Schematic representation of the preparation of nanostructured electrodes: (a) homogeneous deposition of graphene oxide onto carbon cloth (CC) by dip-coating, (b) reduction of GO through heat-treatment at 380 °C in Ar/H<sub>2</sub> atmosphere, (c) electrodeposition of Fe nanoparticles onto RGO/CC, (d) growth of NCNTs on RGO/CC via CVD, (e) electrochemical leaching of Fe particles followed by electrodeposition of Pt nanoparticles to form Pt-NCNTs/RGO/CC.

Figure 3.3.1 displays the procedure for the preparation of Pt-NCNTs/RGO/CC nanostructured electrodes. Each preparation step has been optimized towards optimum reproducibility, density and homogeneity of the nanostructured electrodes. SEM and optical images of the CC as well as the GO- and RGO-decorated CC are shown in Figure 3.3.2. Comparison with the SEM image of bare CC (Figure 3.3.2a) indicates that the fibers of CC are homogeneously covered by thin films of GO and RGO (Figures 3.3.2c and e, additional figures with different scale bars are found in the Supporting Information, Figure S3.3.1). It is difficult to differentiate between GO and RGO from the SEM image. However, through the optical images, GO before and after reduction is easily distinguished, as shown in Figures 3.3.2d and f. RGO sheets on carbon cloth show a gray metallic gloss compared to GO sheets possibly owing to the improved electrical conductivity after reduction of GO, in a way that charge carrier concentration and mobility were enhanced and the reflection of visible light was improved. A similar observation was reported for RGO decorated onto indium tin oxide (ITO) films by Pei *et al.* [351, 352].

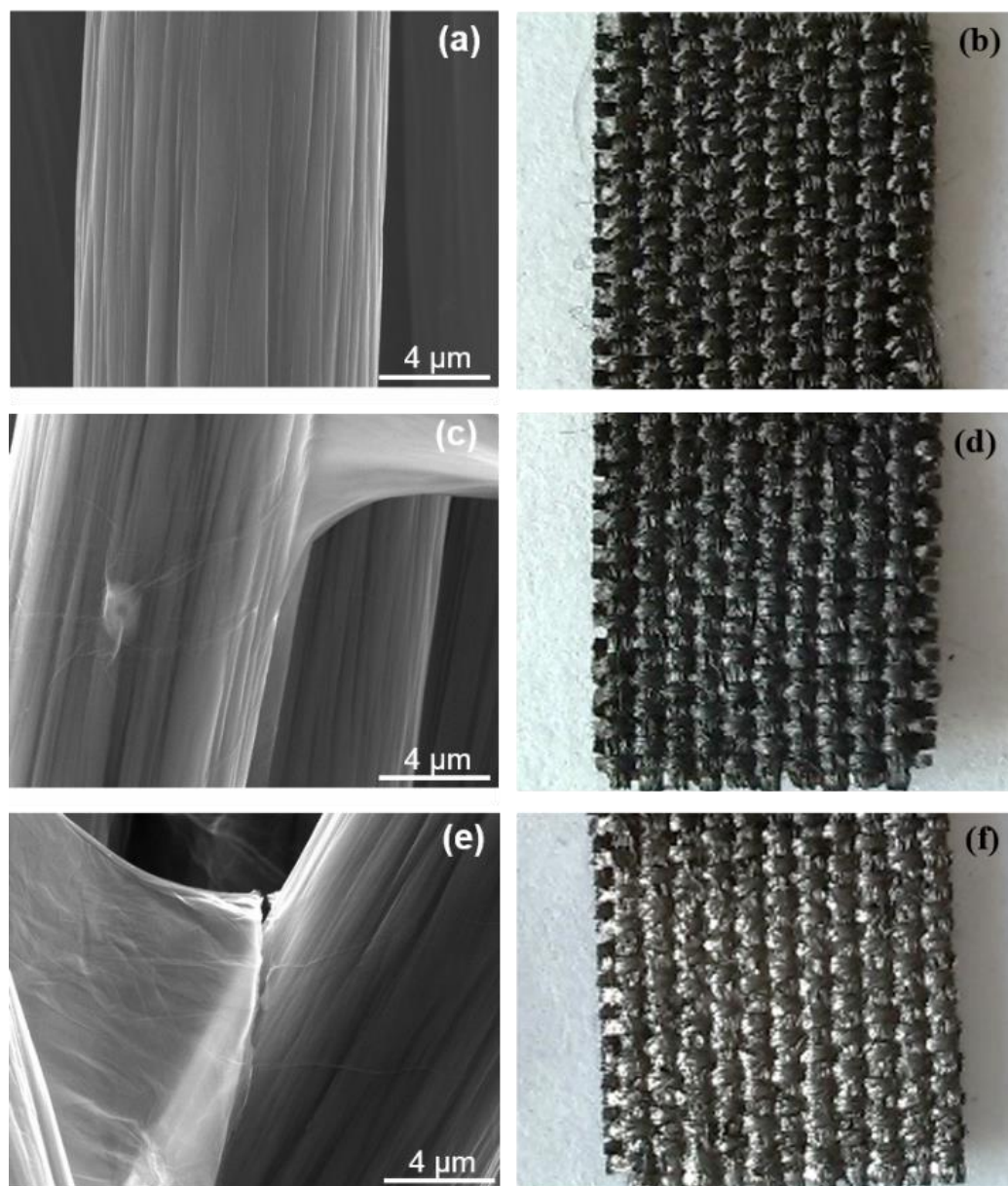


**Figure 3.3.2.** SEM images of (a) CC, (c) GO decorated on CC, (e) reduced GO/CC; optical images of (b) CC, (d) GO/CC and (f) RGO/CC.

The development of the XRD profiles with each preparation step is displayed in Figure 3.3.3b and compared to the diffractograms of graphite, GO and RGO (Figure 3.3.3a). Graphite exposes a diffraction peak at a  $2\theta$  value of  $26.4^\circ$  corresponding to the hexagonal crystalline graphite, whereas in GO the  $26.4^\circ$  peak disappears and a new diffraction peak is observed at  $10.2^\circ$ , as caused by the oxidation of graphite. Meanwhile, the bare CC also shows a shifted and broad graphite diffraction peak at  $25.1^\circ$  (Figure 3.3.3b). After GO decoration on CC, the GO/CC displays a diffraction peak at  $10.2^\circ$  owing to GO, apart from the characteristic peak of CC. On heat

treatment of GO/CC at 380 °C, the intensity of the peak at 25.1° increases and the peak at 10.4° nearly disappears, attributed to the removal of the oxygen functional groups and the formation of RGO/CC. The reduction of GO to RGO under the conditions chosen in this work is further confirmed from the XRD pattern of the heat-treated GO in the absence of CC (Figure 3.3.3a). Here the peak corresponding to GO completely vanishes after reduction. Finally, NCNTs/RGO/CC has similar diffraction patterns as those of RGO/CC.

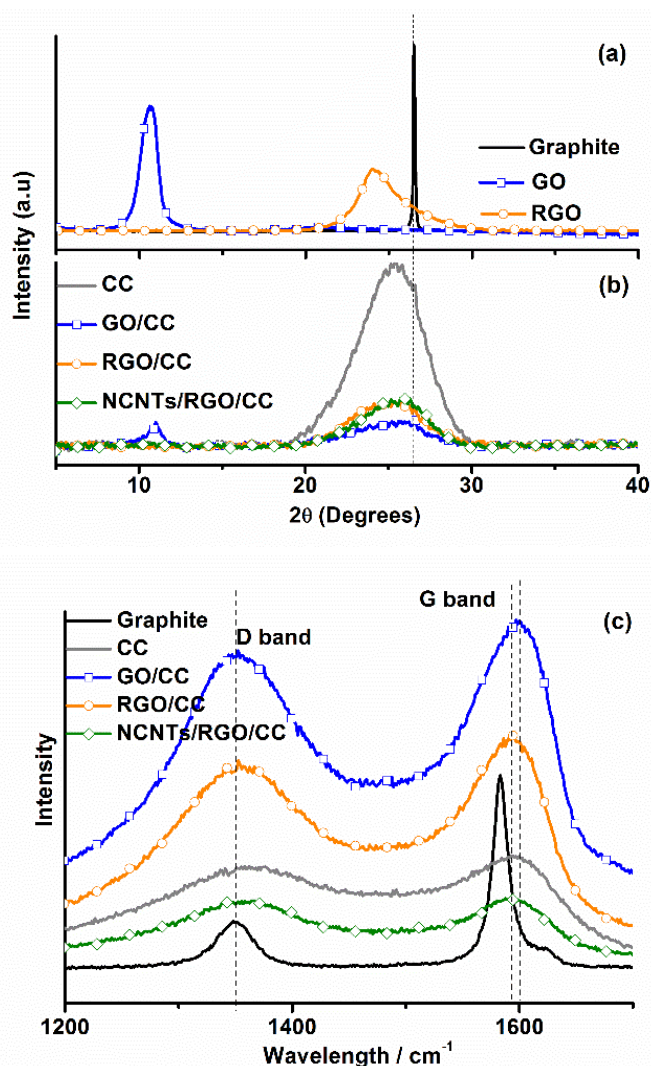


**Figure 3.3.3.** X-ray diffraction profiles of (a) graphite, GO, RGO; (b) CC, GO/CC, RGO/CC and NCNTs/RGO/CC; (c) Raman spectra of commercial graphite, CC, GO/CC and RGO/CC showing the shift in the G band. 532 nm laser as excitation. Dashed lines are intended as a help for the eye.

Furthermore, the materials were studied by Raman spectroscopy as shown in Figure 3.3.3c. Carbon materials are characterized by the typical D band at ca. 1350  $\text{cm}^{-1}$  and the G band at ca. 1600  $\text{cm}^{-1}$ . The D band corresponds to imperfections or structural defects in the carbon lattice and the G band represents the in-plane stretching vibrations of  $\text{sp}^2$  domains of crystalline carbon [347, 346, 353–355]. Due to the irregularities and impurities in commercial graphite, a small D band is visible in the corresponding Raman spectrum. GO/CC and RGO/CC display Raman spectra rather similar to that of CC, with a broad D band. However GO/CC has an increased relative intensity ( $I_D/I_G$ : 0.914) compared to graphite ( $I_D/I_G$ : 0.265) and CC ( $I_D/I_G$ : 0.908), which is associated with defects created by the formation of hydroxyl and epoxide groups in the graphitic structure during preparation. In addition, GO and RGO on CC displayed a broadened G band, which is attributed to the increased disorder in relation to graphite. The G band of GO/CC is located at 1600  $\text{cm}^{-1}$  and shifted with respect to the band of CC at 1590  $\text{cm}^{-1}$ , while graphite has a G band at the 1582  $\text{cm}^{-1}$ . Upon heat treatment of GO/CC, the G band is shifted to 1592  $\text{cm}^{-1}$  for RGO, which lies between the value of graphite and GO. Furthermore, the  $I_D/I_G$  of RGO/CC (0.895) is also lower than before reduction due to the removal of the oxygen-containing functional groups. This indicates that GO is reduced to RGO at low temperature in the presence of hydrogen, which is in good agreement with the XRD measurements.

In addition, the presence of NCNTs in NCNTs/RGO/CC does not cause any noticeable shift in G band with respect to RGO/CC. However, an increased  $I_D/I_G$  ratio ( $I_D/I_G$ : 0.961) in comparison to RGO/CC and GO/CC reveals their formation. Moreover, NCNTs/RGO/CC exhibits a slightly smaller  $I_D/I_G$  ratio of 0.942 (Figure S3.3.2), probably indicating slight differences in the CNT growth over CNT and RGO. However, these differences are minor and should not be overemphasized. In summary, XRD and Raman measurements confirm the stepwise assembly as well as the success of the reduction procedure during preparation of the nanostructured electrodes.



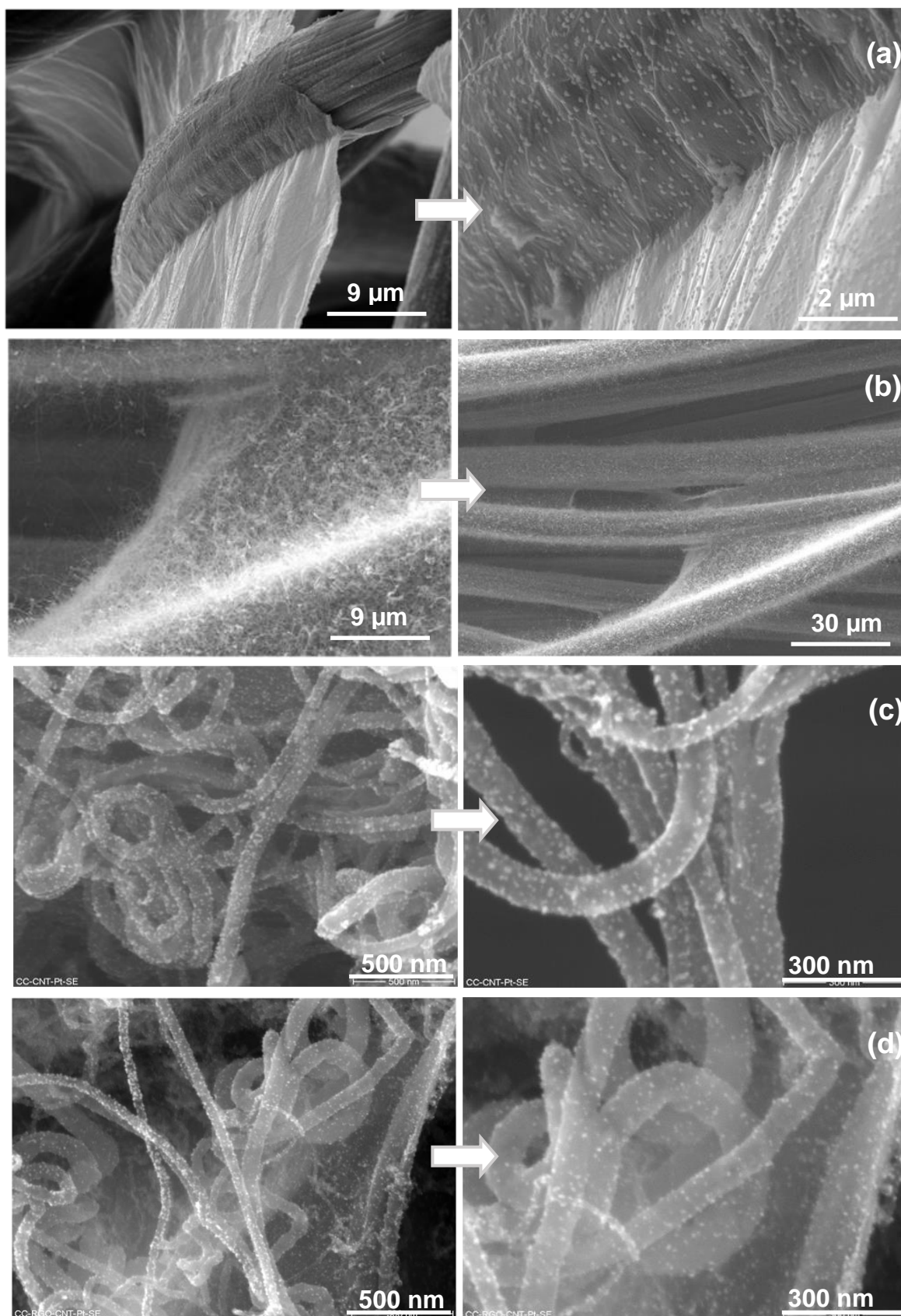


**Figure 3.3.4.** SEM images of (a) Fe nanoparticles on RGO/CC obtained by electrodeposition; (b) NCNTs grown on the RGO/CC from acetonitrile catalyzed by Fe nanoparticles at 750 °C via CVD; Pt nanoparticles electrodeposited on (c) NCNTs/CC and (d) NCNTs/RGO/CC.

For the preparation of NCNTs by chemical vapor deposition (CVD), transition metals such as Fe, Co and Ni are employed as catalysts to decompose the carbon precursors. The dissolved carbon in the metal crystallized in the form of a cylindrical network [206]. It is known that the size of catalyst particles can influence the diameter of the formed NCNTs [319, 206] (as exhibited in Figure S3.3.7b and Figure S3.3.8b). In the present work Fe nanoparticles are employed as catalyst for the NCNT growth on the surface of RGO/CC. Fe deposition on the surface of the catalyst support can easily be carried out by electrochemical deposition as demonstrated by Li *et al.* [317]. Here double-pulse electrodeposition [318] was used to deposit Fe nanoparticles on RGO/CC and, as reference, on CC, and thereby control the distribution and size of Fe nanoparticles. Fe nanoparticles were deposited with a narrow size distribution in the range from 80 nm to 100 nm as shown in Figure 3.3.4a. Obviously, this electrodeposition method worked and the homogeneously distributed Fe nanoparticles provided further evidence for the good electrical conductivity between RGO and CC throughout the electrode. Figure 3.3.4b represents the NCNTs/RGO/CC electrode, where NCNTs were densely grown on the surface of RGO decorated CC with acetonitrile as carbon precursor at 750 °C. The density of the NCNTs obtained over electrochemically deposited Fe particles is higher than that obtained by other means, for example, NCNTs grown over 1 nm thick iron particles on RGO deposited on copper foil by e-beam evaporation [185]. For further comparison, NCNTs/CC was prepared via CVD after Fe deposition on CC. (see Figure S3.3.6, 7 and 8).

An SEM image of electrochemically deposited Pt nanoparticles on NCNTs/RGO/CC is shown in Figure 3.3.4d. Pt nanoparticles were also electrodeposited onto the surface of CVD prepared NCNTs on bare CC (Figure 3.3.4c) for comparison. Densely populated Pt nanoparticles were uniformly distributed on both NCNTs/CC and NCNTs/RGO/CC with similar distribution. Furthermore, in Pt-NCNTs/RGO/CC, Pt nanoparticles were not only deposited on NCNTs but also on RGO. The absence of Pt peaks in the XRD patterns (not shown) impedes Pt crystallite size determination from the peak width. The very low Pt loading with respect to the nanostructured electrodes (NCNTs/RGO/CC and NCNTs/CC) as observed from ICP-OES analysis, ca. 0.6 wt.%, might be one reason for this. Pt nanoparticle average sizes were ca. 5.0 nm for Pt-NCNTs/RGO/CC and 5.5 nm for



Pt-NCNTs/CC as determined by TEM and shown in Figure S3.3.3. Since the TEM specimens were prepared after 2 h of ultrasonic treatment of the nanostructured electrodes to separate the CNTs, we would like to take the TEM results with caution due to the risk of CNTs structure damage and particle detachment. The absence of Pt peaks in XRD, which is surprising given a particle size of 5 nm, is attributed to the difficulties in measuring the samples (non-flat surface) and/or might indicate a polycrystalline nature of the electrodeposited particles.

### 3.3.3. Electrochemical Investigations

The electrocatalytic activities of the nanostructured electrodes towards MOR were evaluated by cyclic voltammetry and quantified with respect to the available catalyst surface area (ECSA, electrochemical surface area). The ECSAs of Pt-NCNTs/RGO/CC and Pt-NCNTs/CC were determined from both the  $H_{\text{ads/des}}$  voltammograms and  $\text{CO}_{\text{ad}}$  stripping voltammograms. The cyclic voltammograms of  $H_{\text{ads/des}}$  were recorded between -0.2 and 1.0 V vs. Ag|AgCl|KCl<sub>sat.</sub> with a scan rate of 100 mV s<sup>-1</sup> in N<sub>2</sub> saturated 0.1 M HClO<sub>4</sub> aqueous solution as represented in Figure 3.3.5, while the  $\text{CO}_{\text{ad}}$  stripping voltammograms were measured for Pt-NCNTs/RGO/CC and Pt-NCNTs/CC after CO adsorption from CO saturated 0.1 M HClO<sub>4</sub> aqueous solution at a scan rate of 20 mV s<sup>-1</sup>, as shown in Figure 3.3.6. The ECSA from  $H_{\text{ads/des}}$  voltammogram was calculated from the coulombic charge obtained by integrating the area under the hydrogen adsorption/desorption peaks observed in the potential range from -0.19 V to 0.20 V vs. Ag|AgCl|KCl<sub>sat.</sub> for platinum after subtracting the double layer charge [356]. Similarly the ECSA was calculated from the CO oxidation peak in the CO ad stripping voltammogram in the potential range between 0.44 V and 0.78 V vs. Ag|AgCl|KCl<sub>sat.</sub> [277].

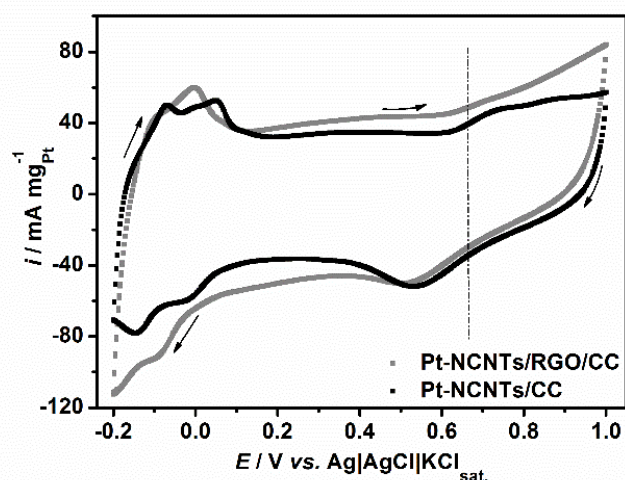


**Figure 3.3.5.** Cyclic voltammograms of Pt-NCNTs/CC and Pt-NCNTs/RGO/CC electrodes recorded at a scan rate of  $100 \text{ mV s}^{-1}$  at room temperature in  $0.1 \text{ M HClO}_4$  aqueous electrolyte solution purged with  $\text{N}_2$  after MOR measurements. Dashed lines are intended as a help for the eye.

As shown in Figure 3.3.5, Pt-NCNTs/RGO/CC shows higher current density for hydrogen adsorption/desorption compared to Pt-NCNTs/CC. The ECSA calculated for the Pt-NCNTs/RGO/CC electrode is  $27.14 \text{ m}^2 \text{ g}_{\text{Pt}}^{-1}$ , which is slightly higher than that of Pt-NCNTs/CC electrode (ECSA:  $25.86 \text{ m}^2 \text{ g}_{\text{Pt}}^{-1}$ ). Meanwhile, the values of ECSA determined from  $\text{CO}_{\text{ad}}$  stripping are  $30.13 \text{ m}^2 \text{ g}_{\text{Pt}}^{-1}$  for Pt-NCNTs/RGO/CC and  $28.63 \text{ m}^2 \text{ g}_{\text{Pt}}^{-1}$  for Pt-NCNTs/CC, which are higher than the respective values calculated from hydrogen adsorption/desorption. The differences in the ECSA measured by  $\text{CO}_{\text{ad}}$  stripping and hydrogen adsorption/desorption have been discussed in the literature [277]. However, both evaluation methods show a higher ECSA for Pt-NCNTs/RGO/CC and thus a higher surface area available for electrochemical reactions. The increase in ECSA in the presence of RGO might be attributed to the improved Pt dispersion resulting from adequate anchoring sites on the surface of RGO for nucleation during Pt deposition [357, 358].

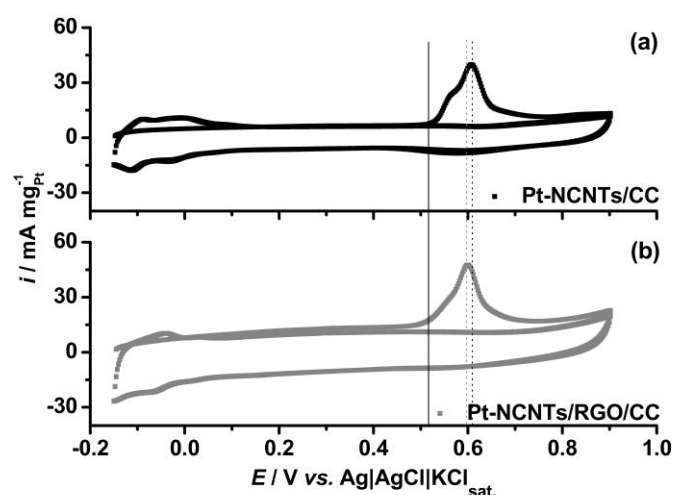


**Figure 3.3.6.** CO<sub>ad</sub> stripping voltammograms for Pt on (a) NCNTs/CC and (b) NCNTs/RGO/CC recorded at 20 mV s<sup>-1</sup> in aqueous 0.1 M HClO<sub>4</sub> electrolyte solution after MOR measurement. Dashed lines are intended as a help for the eye.

The activities of the electrodes towards methanol oxidation were investigated by CV measurements. For both types of electrodes CVs were recorded in nitrogen purged 1 M CH<sub>3</sub>OH/ 0.5 M H<sub>2</sub>SO<sub>4</sub> aqueous solution at potentials ranging from -0.21 to 1.0 V vs Ag|AgCl|KCl<sub>sat.</sub>. The tenth cycle of each measurement is represented in Figure 3.3.7. Due to the observed large double-layer capacity a scan rate of 5 mV s<sup>-1</sup> was chosen to determine the MOR activity of the prepared electrodes. The current responses in the CVs were normalized respectively to the ECSA of Pt calculated from CO<sub>ad</sub> stripping and the Pt mass loading evaluated from ICP-OES.

During the forward CV scan, methanol is oxidized to CO<sub>2</sub> and partially to intermediate carbonaceous species such as CO which will adsorb on the Pt surface, leading to poisoning. The reverse scan is associated with the removal of residual carbonaceous species formed during the forward scan and to methanol oxidation on the Pt surface liberated from poisonous species and oxides. Therefore, the ratio of forward peak current ( $i_f$ ) to the backward peak current ( $i_b$ ), namely  $i_f/i_b$  is used to describe the tolerance of the catalyst towards *poisoning* by intermediately formed carbonaceous species in numerous literatures. However, the ratio is inadequate to assess the CO tolerance, which was reported by Hofstead-Duffy *et al.* [327] (described above in chapter 3.2.3). Thus, the CO tolerance was evaluated by CO<sub>ad</sub> stripping measurements.

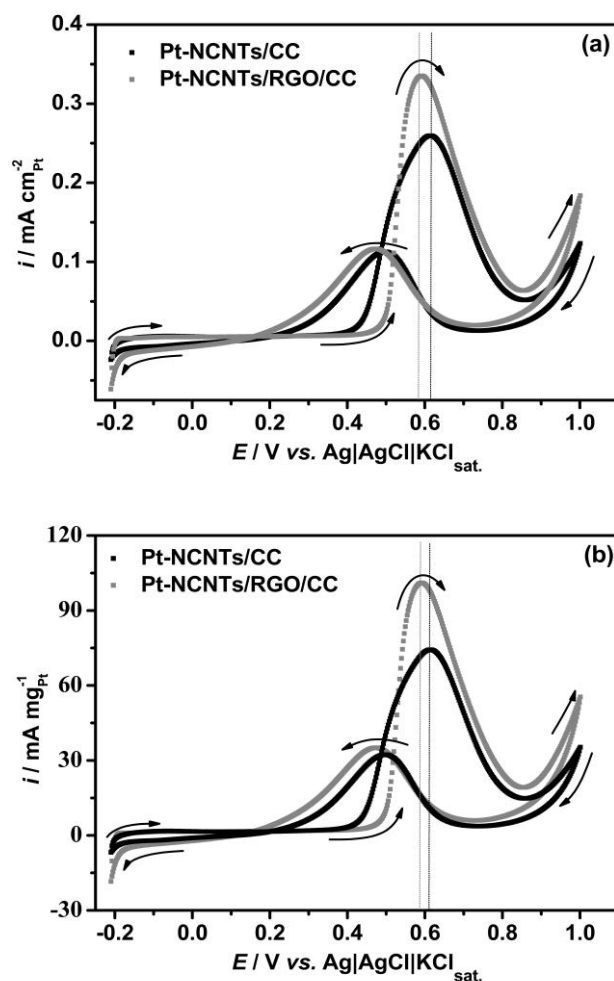


**Figure 3.3.7.** Cyclic voltammograms of Pt-NCNTs/CC and Pt-NCNTs/RGO/CC in  $N_2$  purged 1 M  $CH_3OH$  in 0.5 M  $H_2SO_4$  electrolyte solution recorded at a scan rate of  $5 \text{ mV s}^{-1}$  normalized to (a) Pt-ECSA evaluated by  $CO_{ad}$  stripping and (b) Pt mass loading. Dashed lines are intended as a help for the eye.

The voltammograms of Pt-NCNTs/RGO/CC and Pt-NCNTs/CC in Figure 3.3.7 exhibit distinct features in terms of the specific activity and the ratio of peak current densities ( $i_f/i_b$ ). In the forward scan, Pt-NCNTs/RGO/CC exhibits a higher Pt surface- and mass-specific peak current of  $0.34 \text{ mA cm}_{Pt}^{-2}$  and  $101.52 \text{ mA mg}_{Pt}^{-1}$ , respectively, with a current peak at  $0.589 \text{ V}$  compared to Pt-NCNTs/CC, which shows values of  $0.26 \text{ mA cm}_{Pt}^{-2}$  and  $74.27 \text{ mA mg}_{Pt}^{-1}$ , respectively, with a current peak at  $0.614 \text{ V}$ . The surface-specific peak current of Pt-NCNTs/RGO/CC is 1.31 times higher than that for Pt-NCNTs/CC, while the mass-specific peak current ratio of Pt-NCNTs/RGO/CC to Pt-NCNTs/CC is 1.37. Both values indicated that Pt deposited on NCNTs/RGO/CC provides higher methanol oxidation activity than Pt on NCNTs/CC.

Furthermore, the mass-specific peak current of Pt-NCNTs/RGO/CC is much higher than the  $62 \text{ mA mg}_{\text{Pt}}^{-1}$  for Pt-graphene/CNTs hybrid reported by Rajesh *et al.* at a scan rate of  $50 \text{ mV s}^{-1}$  for a 1 M methanol solution [185]. While the mass-specific peak currents of Pt/CNTs/carbon paper and commercial Pt/C electrodes were reported to be  $146.4 \text{ mA mg}_{\text{Pt}}^{-1}$  and  $62 \text{ mA mg}_{\text{Pt}}^{-1}$  at a scan rate of  $50 \text{ mV s}^{-1}$ , respectively [344], our Pt-NCNTs/RGO/CC demonstrate a  $101.52 \text{ mA mg}_{\text{Pt}}^{-1}$  mass activity at a scan rate of  $5 \text{ mV s}^{-1}$ . According to the Randles–Sevcik equation, it can be expected that increased mass-specific peak currents would be obtained at higher scan rates, indicating that the activity of our electrodes was similar or superior to activities reported in the literature. To further promote the electrochemical activities for Pt-NCNTs/RGO/CC towards MOR, the Pt nanoparticles size and distribution should be improved towards commercial Pt/C (1.5–4 nm) in further studies.

An exceptionally favorable  $i_f/i_b$  ratio of 2.86 is obtained for Pt-NCNTs/RGO/CC, which is significantly higher than the values reported for Pt on graphene–CNT composites by Rajesh *et al.* and Jhan *et al.* [185]. Additionally, the  $i_f/i_b$  ratio for Pt-NCNTs/RGO/CC is also higher than that of Pt-NCNTs/CC (2.27), commonly demonstrating the enhanced tolerance towards poisoning by intermediately formed carbonaceous species ( $\text{CO}_{\text{ad}}$  and CO-like species). However, it was reported by Hofstead-Duffy *et al.* that the  $i_f/i_b$  ratio is inadequate to measure CO tolerance. Thus,  $\text{CO}_{\text{ad}}$  stripping as shown as in Figure 3.3.6, was used to evaluate the CO tolerance. The onset potential of CO oxidation on Pt-NCNTs/RGO/CC (0.44 V) is less positive than that of Pt-NCNTs/CC (0.52 V). Similarly, the  $\text{CO}_{\text{ad}}$  stripping peak on Pt-NCNTs/RGO/CC shifts to less positive values compared to Pt-NCNTs/CC. This suggests that the electrocatalytic activity of Pt-NCNTs/RGO/CC composites for CO oxidation is superior to that of Pt-NCNTs/CC. However, the onset potential for methanol oxidation on Pt-NCNTs/CC is slightly more negative than for Pt-NCNTs/RGO/CC (Figure 3.3.7). Both oxidation reactions require different prerequisites to occur. CO oxidation requires the activation of OH species on the Pt surface, while methanol oxidation starts with the dehydrogenation of methanol on Pt. Thus, the different behavior of the onset potential for CO and MeOH oxidation is not a contradiction. It should be mentioned at this instance that, although the observed differences in peak potentials are small, they are reproducible and we thus think that

it is justified to deduce slightly different electrochemical properties. In addition, Pt-CNTs/RGO/GC shows higher oxidation current and good electrocatalytic stability in chronoamperometric measurements (Figure S3.3.4). In Figure S3.3.5 Pt-CNTs/RGO/GC displays a more positive onset potential, indicating its improved electrochemical activity for oxygen reduction reaction. Due to the shape and the rough surface of carbon cloth, the RDE measurement could not be used. In the measurement hydrodynamics on CC surface would be distorted, so that the analysis of kinetic parameters might strongly deviate and not be accurate.

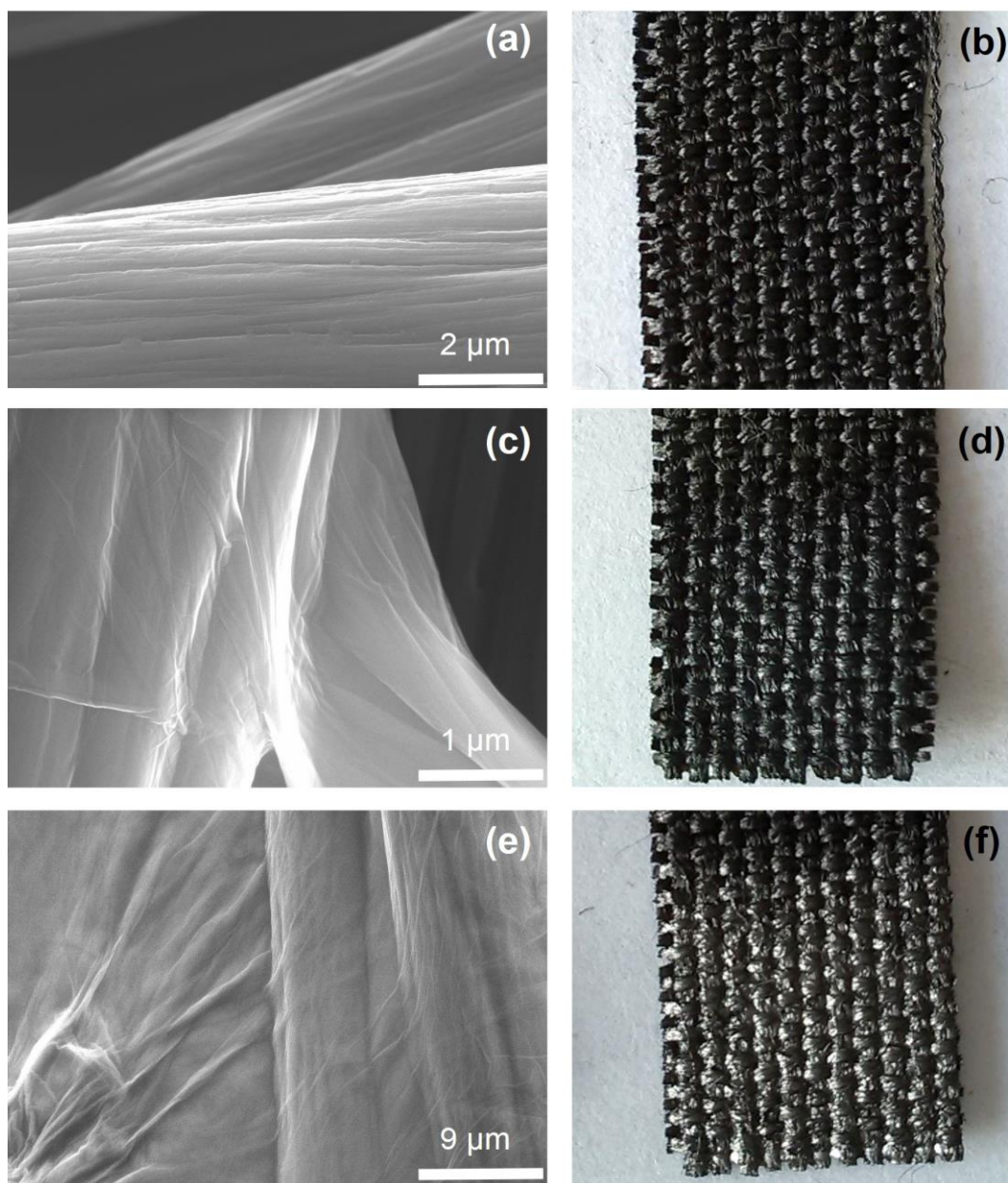
The above mentioned improved electrochemical activity of Pt-NCNTs/RGO/CC could be associated with the presence of RGO, which could be explained by the following considerations: 1) in the NCNTs/RGO hybrids, RGO could be considered as a (conductive) bridge not only between the CNTs and CC, but also between different CC fibers and between CNTs to form a conductive network, so that efficient electron transfer pathways can be provided. In the literature, 3D-nanostructured CNTs/RGO hybrids exposed smaller charge transfer resistance and contact resistance measured by electrochemical impedance spectroscopy and two-probe resistivity measurement compared to CNTs or RGO alone. This meant improvement of charge transfer between the interface of NCNTs, RGO, Pt and electrolyte, which could result in an enhanced electrochemical performance [174, 183–186, 359]. We speculate that similar mechanisms are at work in our composite materials, too; 2) CNTs are anchored stably to different sites on the surface of RGO. CNTs may serve as steric hindrances to reduce restacking of RGO in the employed aqueous electrolytes [360, 361, 183, 174, 184]. 3) Pt deposited on NCNTs/RGO/ CC provides larger ECSA and thus more active sites, resulting in better activity towards methanol oxidation; 4) few available oxygen-containing species still exist in RGO after heat treatment, which possibly promote the oxidative removal of  $\text{CO}_{\text{ad}}$  and CO-like species on Pt to reduce the adsorbed carbonaceous intermediate-poisoning.

### 3.3.4. Conclusion

We have developed a strategy to prepare highly active nanostructured electrodes for methanol oxidation by implementing RGO into a NCNTs/CC composite before NCNT growth and Pt electrodeposition. A layered structure of RGO/CC was achieved by  $\text{H}_2$ -assisted thermal reduction of GO deposited onto the surface of CC and NCNTs

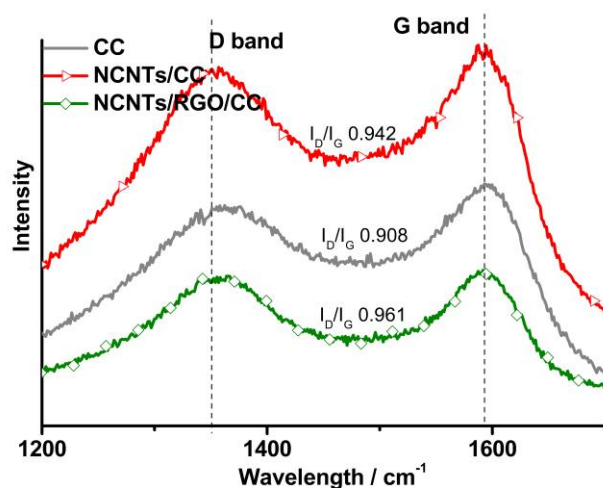
were grown by chemical vapor deposition over electrodeposited iron particles. NCNTs with high density were obtained, and a homogeneous and dense distribution of Pt nanoparticles was achieved. The Pt-NCNTs/RGO/CC electrode provided higher ECSA and MOR activity in comparison to Pt-NCNTs/CC. The  $\text{CO}_{\text{ad}}$  stripping voltammetry revealed high tolerance of Pt-NCNTs/RGO/CC towards poisoning, leading to efficient methanol oxidation. This brings us to the conclusion that RGO played a vital role in improving the overall activity of the nanostructured electrode. This work is part of a project aimed at the full bottom-up synthesis of gas-diffusion electrodes. While the feasibility of this approach and the fundamental benefits were clearly demonstrated in this paper, follow-up research is necessary. Next steps will include an improvement of the Pt dispersion as well as a scale-up of the synthesis, which are the requirements to conduct fuel cell tests as a definite proof of the advantages of our structures.

### 3.3.5. Supplementary Information

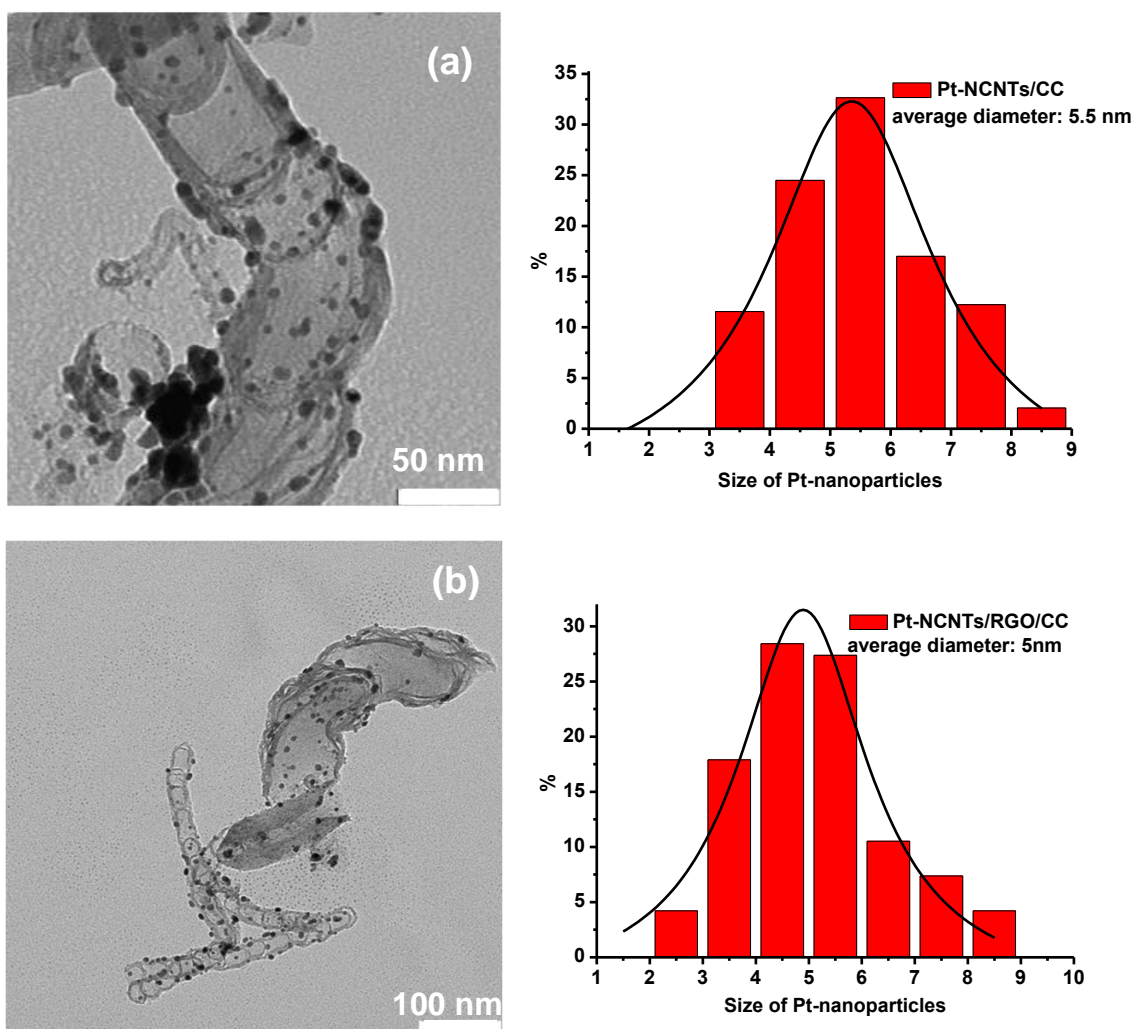


**Figure S3.3.1.** SEM images of (a) CC, (c) GO decorated on CC, (e) reduced GO/CC; optical images of (b) CC, (d) GO/CC and (f) RGO/CC.

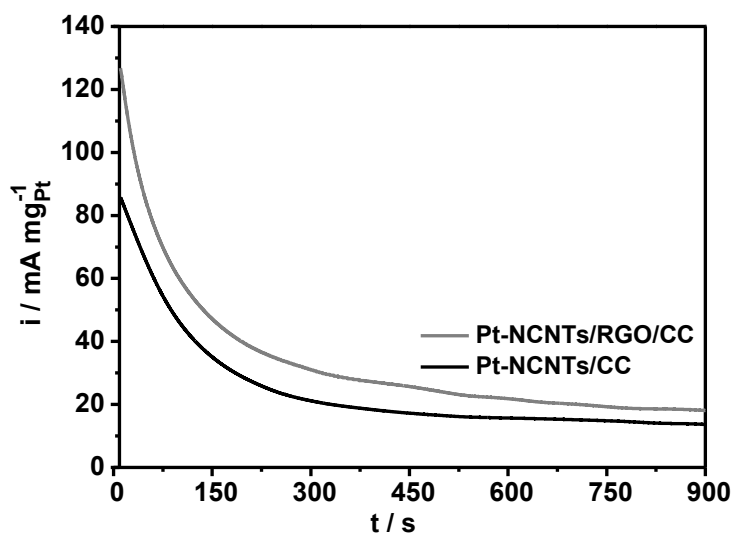




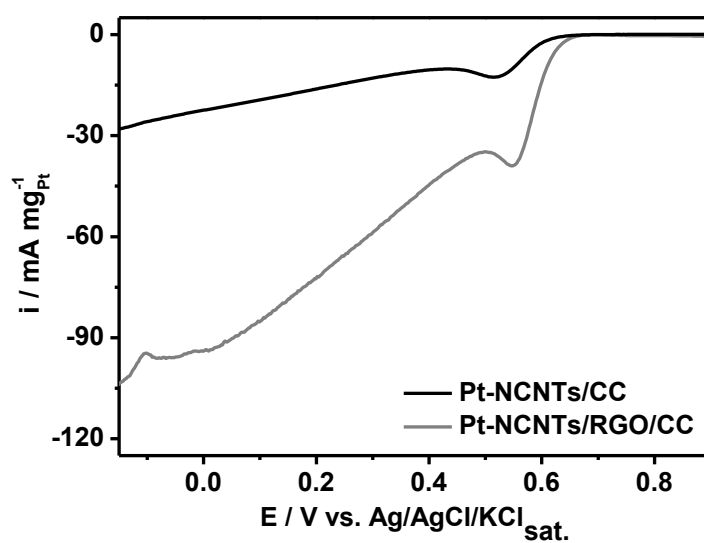
**Figure S3.3.2:** Raman spectra of commercial CC, NCNTs/CC and NCNTs/RGO/CC measured by 532 nm laser as excitation. Dashed lines are intended as a help for the eye.



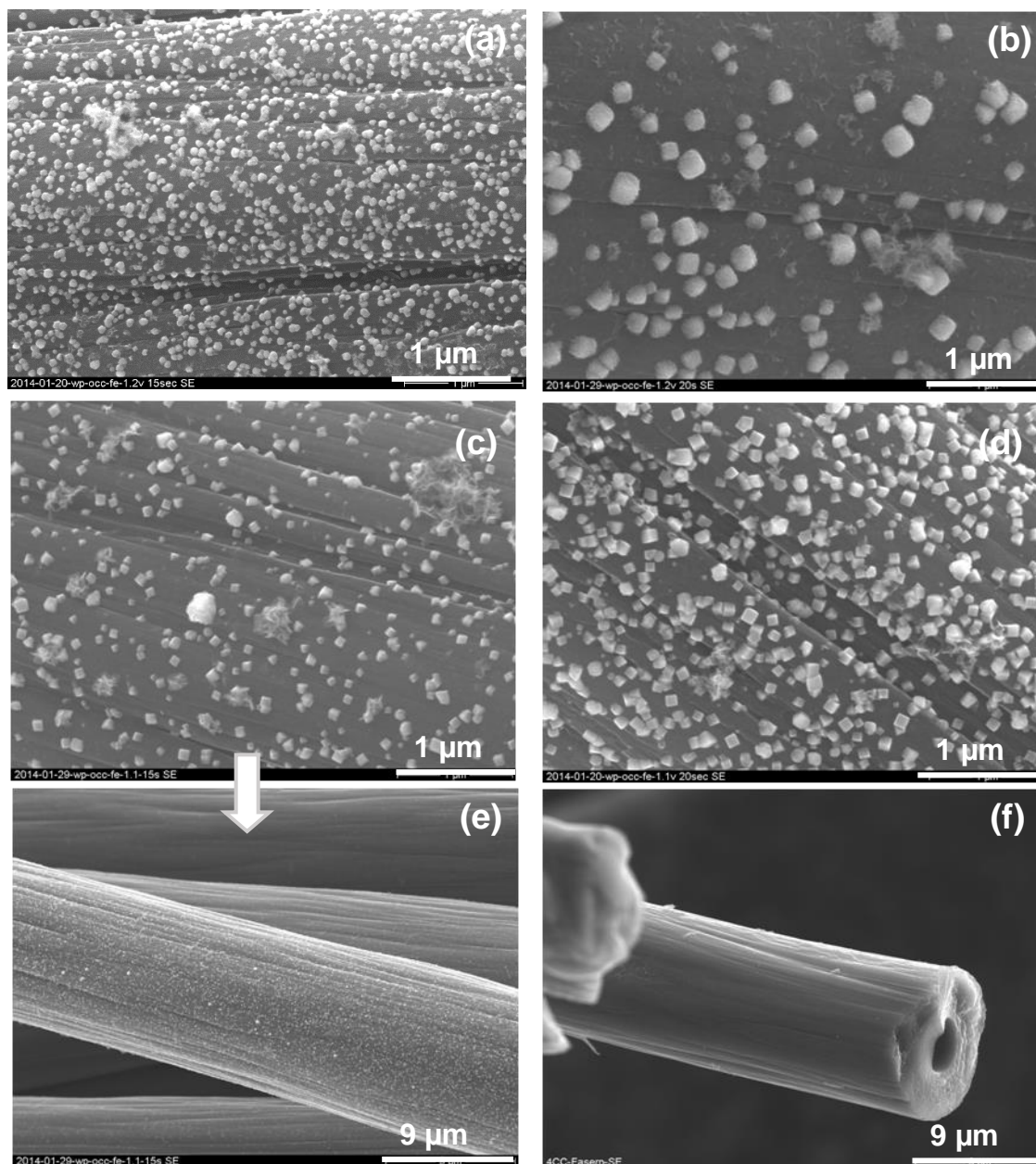
**Figure S3.3.3.** TEM images and particles size distributions for (a) Pt-NCNTs/CC and (b) Pt-NCNTs/RGO/CC



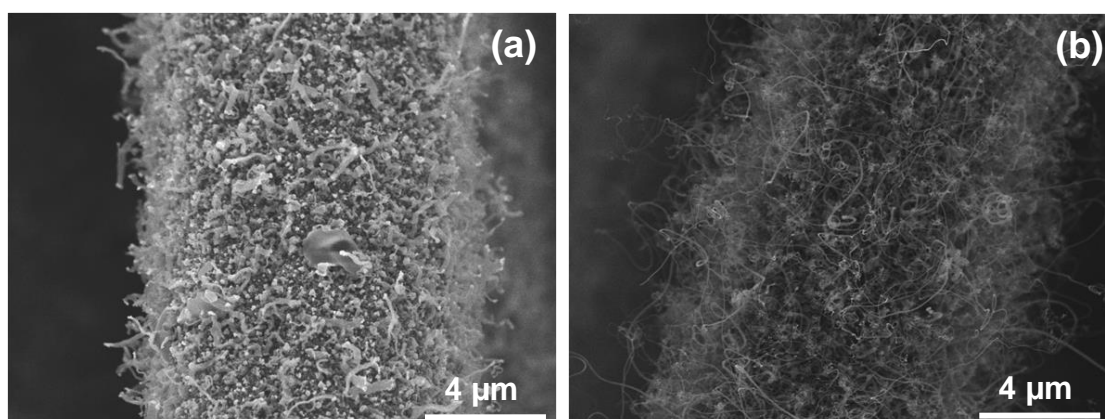
**Figure S3.3.4.** Chronoamperometric curves of methanol oxidation for Pt-NCNTs/RGO/CC and Pt-NCNTs/CC in  $\text{N}_2$  purged 1 M  $\text{CH}_3\text{OH}$  and 0.5 M  $\text{H}_2\text{SO}_4$  at a fixed potential of 0.6 V vs.  $\text{Ag}|\text{AgCl}|\text{KCl}_{\text{sat.}}$ . The currents were normalized by the mass of Pt.



**Figure S3.3.5.** ORR polarization curves of Pt-NCNTs/RGO/CC and Pt-NCNTs/CC in  $\text{O}_2$  purged 0.1 M  $\text{HClO}_4$  with a scan rate of  $5 \text{ mV s}^{-1}$  in the potential range between -0.15-0.9 V vs.  $\text{Ag}|\text{AgCl}|\text{KCl}_{\text{sat.}}$ .



**Figure S3.3.6.** SEM images of Fe nanoparticles on CC obtained via double pulse electrodeposition with nucleation potential  $-1.75$  V and growth pulse potential vs.  $\text{Ag}|\text{AgCl}|\text{KCl}_{\text{sat}}$ . (a)  $-1.2$  V,  $15$  s ( $\approx 82$  nm diameter); (b)  $-1.2$  V,  $20$  s; (c) and (e)  $-1.1$  V,  $15$  s in different scale; (d)  $-1.1$  V,  $20$  s; (f) CC without Fe deposition as reference electrode.



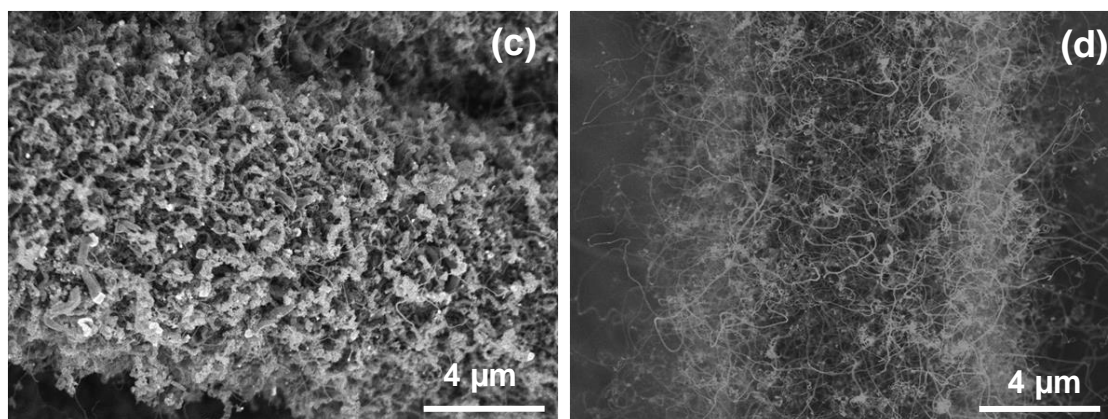


**Figure S3.3.7.** SEM images of NCNT growth over Fe particles onto CC via CVD in  $3 \text{ L h}^{-1}/3 \text{ L h}^{-1} \text{ H}_2/ \text{ Ar}$  purged acetonitrile atmosphere for 120 min at (a)  $650^\circ$  and (b)  $750^\circ$ . (c) and (d) NCNT growth were repeated in the same conditions at  $650^\circ$  and  $750^\circ$ , respectively.

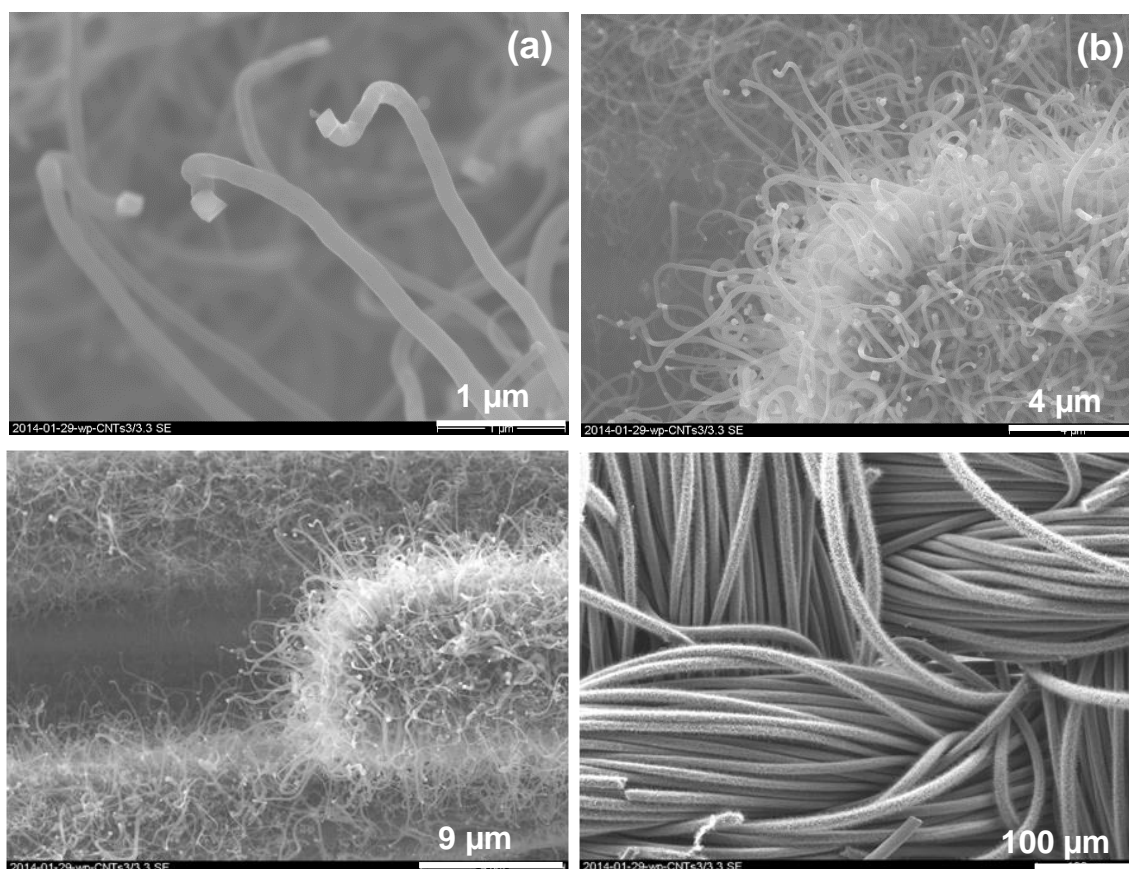


**Figure S3.3.8.** SEM images of NCNT growth over the electrodeposited bigger Fe particles onto CC via CVD in  $3 \text{ L h}^{-1}/3 \text{ L h}^{-1} \text{ H}_2/ \text{ Ar}$  purged acetonitrile atmosphere for 120 min at  $750^\circ$ .

## 3.4 Hierarchically Structured Electrodes for Supercapacitors

### 3.4.1. Motivation

In the chapters above, the hierarchically structured electrodes have increased electrochemical activities, probably due to their enhanced available electrochemical surface area and improved electron transfer. Before Pt deposition, prepared hierarchically structured electrodes show enhanced CV currents, indicating higher double layer capacitances. The CC-based electrodes have much higher double layer capacitances than the electrodes based on GC. This performance might be adequate for supercapacitors.

Supercapacitors are promising energy storage devices due to their high power density, high reliability, long lifetime and fast charging and discharging in seconds [362, 363]. To obtain the high capacitive performance and good rate capability for electrical double layer capacitors (EDLC), the mesoporous structure of carbonaceous materials and 3D hierarchically structured electrodes were studied by many researchers [364–371]. In the previous reports carbon fabric or carbon paper was used as current collectors, and CNTs grown on carbon fabric or carbon paper showed improved specific capacitance, rate capability and cycling stability. The structures led to the improved electron transport and penetration of electrolyte [372–377]. Meanwhile, transition metal oxides (such as  $\text{MnO}_2$ ,  $\text{Ni}(\text{OH})_2$ ) [378–380] and conductive polymers (such as polypyrrole, polyaniline) [381–383] were used for pseudocapacitors, which had higher capacitance but reduced cycling stability compared to EDLC. Additionally, a combination of EDLC and pseudocapacitors was studied, resulting in improved properties for supercapacitors [384–387].

The hierarchical materials based on CC (namely CNTs/CC, CNTs/CNTs/CC and RGO/CC) prepared above were characterized for supercapacitors. Moreover, polyaniline was further deposited on CNTs/CC due to its high conductivity and easy synthesis, leading to a combination of EDLC and pseudocapacitors. The electrochemical properties of the electrodes based on CC were determined using cyclic voltammetry, galvanostatic charge/discharge and electrochemical impedance spectroscopy. Additionally, the electrochemical stability was measured through consecutive charge/discharge cycles.



## 3.4.2. Characterization of PANI/CNTs/CC Electrode

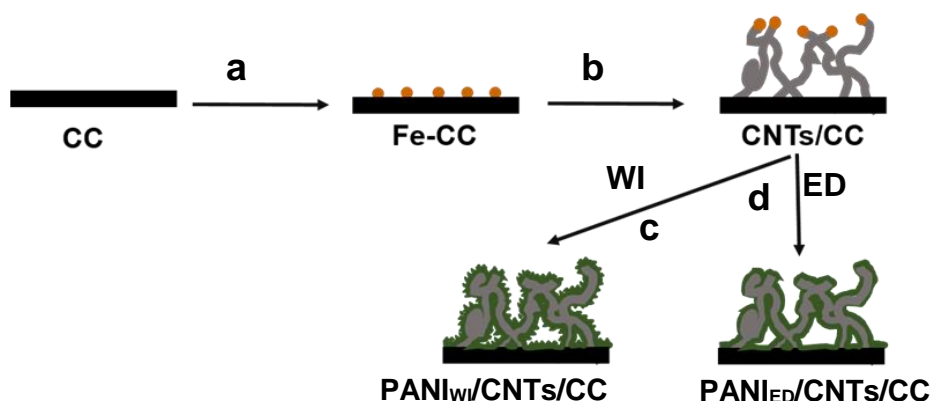


**Figure 3.4.1.** Scheme of the preparation of hierarchical PANI/CNTs/CC electrodes: (a) electrochemical deposition of Fe nanoparticles onto CC, (b) CNT growth onto CC over Fe particles via CVD, (c) deposition of PANI film onto CNTs/CC by wet impregnation, (d) Electrochemical deposition of PANI film onto CNTs/CC.

Figure 3.4.1 represents the procedure of the preparation of PANI/CNTs/CC. CNTs/CC was grown by CVD under acetonitrile/Ar/H<sub>2</sub> atmosphere at 750 °C for 120 min in the same conditions mentioned above. Afterwards, the PANI was deposited onto the surface of the CNTs/CC via wet impregnation (WI, chemical oxidation polymerization) and electrochemical deposition (ED) to form PANI<sub>w</sub>/CNTs/CC and PANI<sub>ED</sub>/CNTs/CC, respectively. In wet impregnation polyaniline was synthesized in different acids (see Figure S3.4.1). Figure 3.4.2 shows SEM images of CNTs/CC before and after PANI deposition in low and high resolution, in which PANI was prepared in 0.1 M aniline + 1 M H<sub>2</sub>SO<sub>4</sub> solution. The CNTs were densely grown onto CC. Their average diameter was evaluated by statistical analysis of 50-100 CNTs with the Lince software (TU Darmstadt, Germany) [388]. In Figure 3.4.2a CNTs grow homogeneously on CC with the average diameter of  $35 \pm 7$  nm. After polyaniline deposition by wet impregnation, PANI is homogeneously covered on the surface of CNTs with small needle-like shapes. The average diameter of PANI decorated CNTs is increased to  $162 \pm 22$  nm (Figure 3.4.2b). In addition, a few long PANI nanofibers are left on the surface after washing with de-ionized water.

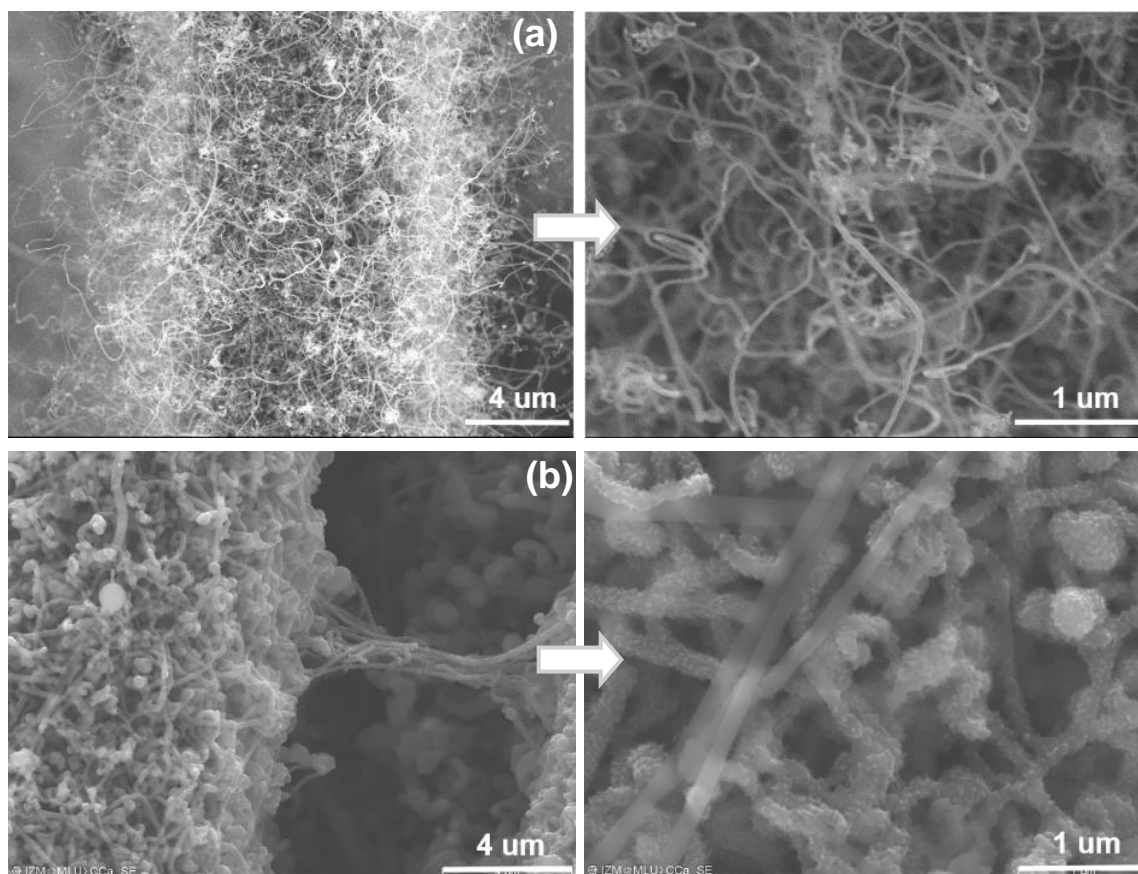


**Figure 3.4.2.** SEM images of (a) CNTs/CC and (b) PANI<sub>W</sub>/CNTs/CC prepared by wet impregnation in low and high resolution.

PANI electrodeposition was carried out via cyclic voltammetry in the potential range from -0.4 V to 1.0 V vs. Ag|AgCl|KCl<sub>sat.</sub> at a scan rate of 100 mV s<sup>-1</sup> in a 0.25 M aniline and 0.5 M H<sub>2</sub>SO<sub>4</sub> solution saturated with N<sub>2</sub> at room temperature. In Figure 3.4.3a and b, PANI was electrochemically deposited onto CC and CNTs/CC by cyclic voltammogram for 20 cycles, respectively, while PANI was decorated on CNTs/CC by CV for 10 cycles (Figure 3.4.3c). With absence of CNTs, short and granular PANI is agglomerated on the surface of CC and is not uniformly coated, whereas the PANI is deposited homogeneously onto the surface of CNTs/CC in a form of film. In Figure 3.4.3c, the PANI film coated on CC is not obviously recognized, but the average diameter of PANI coated CNTs is 70 ± 19 nm. This is wider than that before PANI decoration. It is observed that the PANI film prepared by CV for 20 cycles is covered not only onto surface of CNTs but also between CNTs. The average diameter of PANI covered CNTs is 89 ± 20 nm. Comparing the two deposition methods, the

prepared PANI shows two different shapes: needle-like by wet impregnation and a film form by electrodeposition.

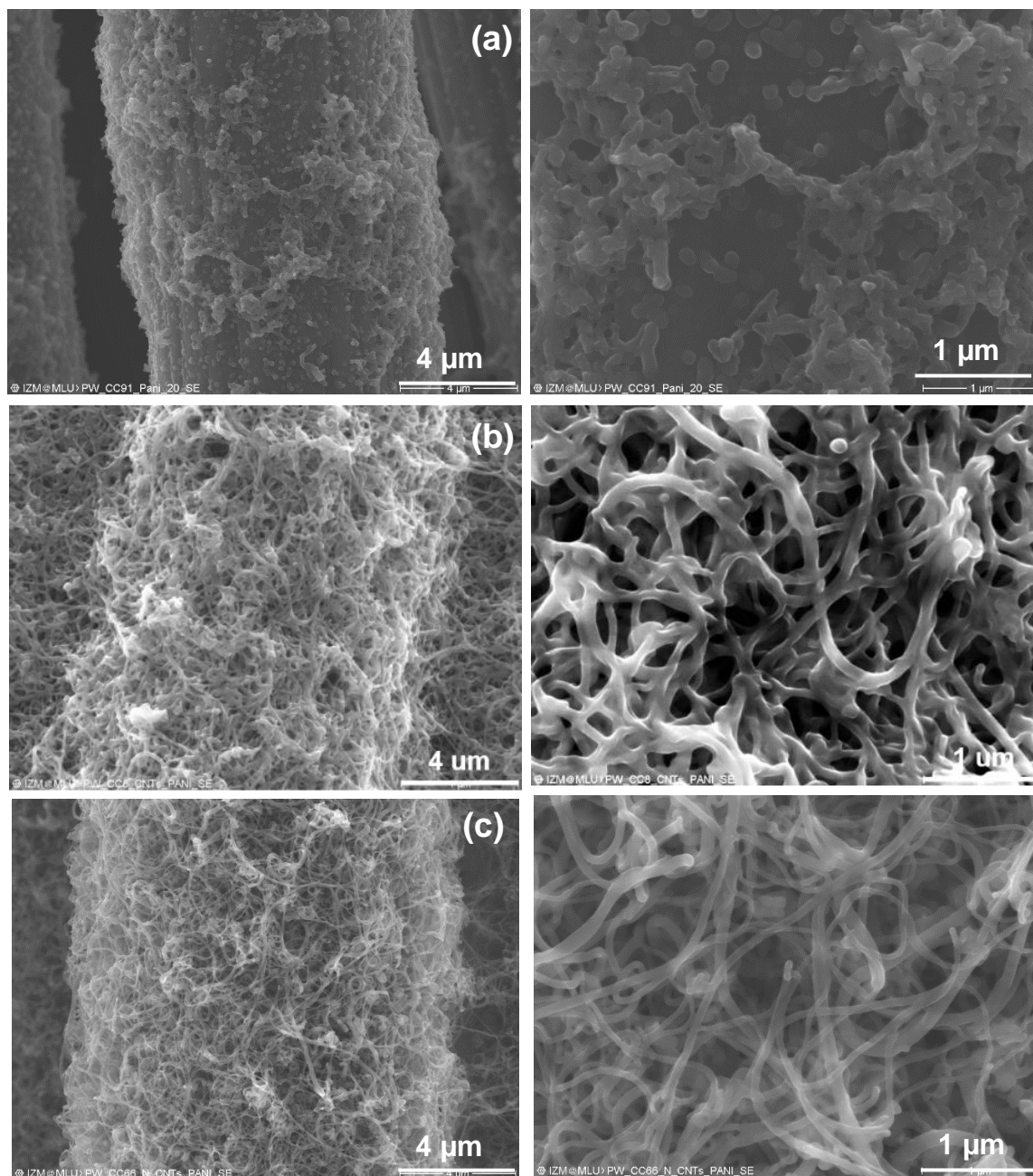


**Figure 3.4.3.** SEM images of PANI electrodeposited on (a) CC and (b) CNTs/CC surface via cyclic voltammetry at a scan rate of  $100 \text{ mV s}^{-1}$  in a potential range of  $-0.4\text{--}1.0 \text{ V}$  vs.  $\text{Ag}|\text{AgCl}|\text{KCl}_{\text{sat}}$  in a  $\text{N}_2$  purged  $0.25 \text{ M}$  aniline and  $0.5 \text{ M}$   $\text{H}_2\text{SO}_4$  solution for 20 cycles; (c) PANI coated CNTs/CC by CV for 10 cycles in low and high resolution.



## 3.4.3. Electrochemical Investigations

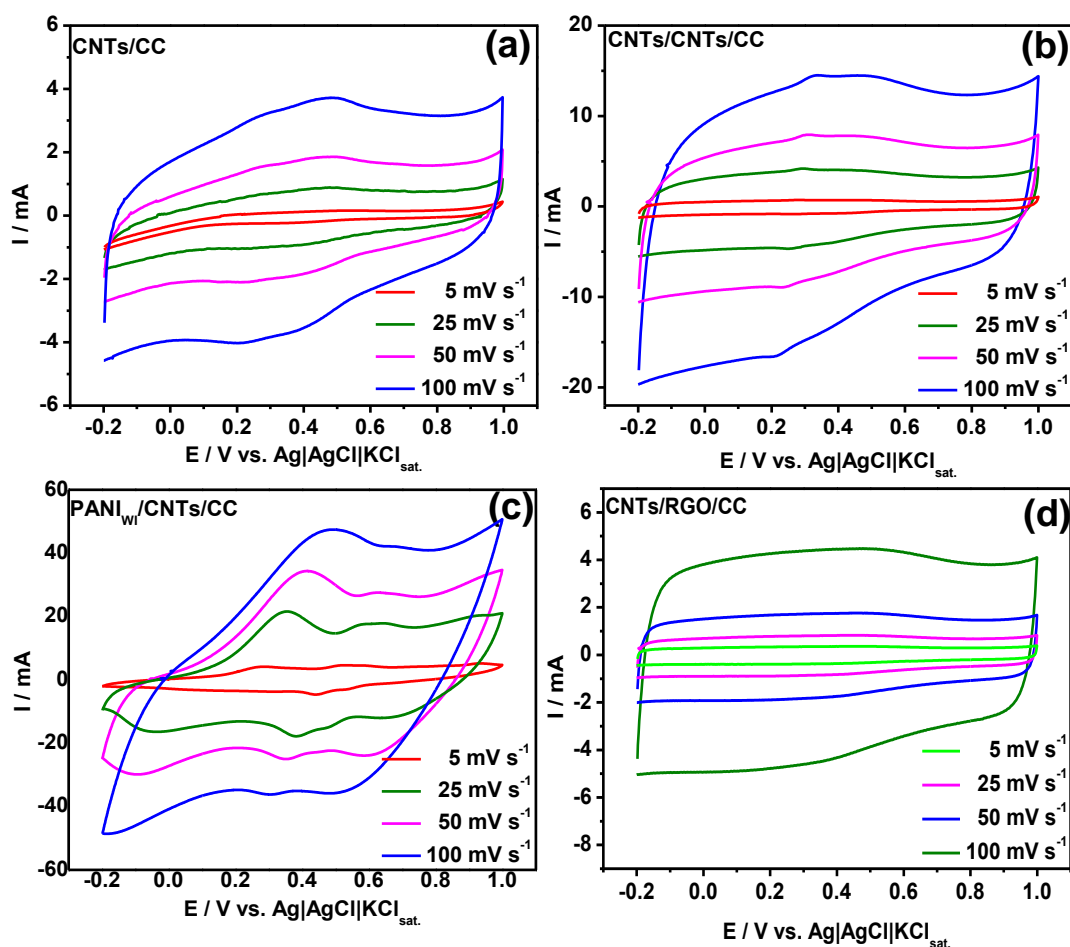


**Figure 3.4.4.** Cyclic voltammograms of (a) CNTs/CC, (b) CNTs/CNTs/CC, (c) PANI<sub>W</sub>/CNTs/CC, (d) CNTs/RGO/CC electrodes recorded at different scan rates of 5, 25, 50, 100 mV s<sup>-1</sup> in N<sub>2</sub> purged 0.5 M H<sub>2</sub>SO<sub>4</sub> at room temperature.

To evaluate the capacitance performances, the prepared materials were investigated by cyclic voltammetry, galvanostatic charge/discharge and electrochemical impedance spectra. In Figure 3.4.4, PANI<sub>W</sub>/CNTs/CC and the CNTs/CC, CNTs/CNTs/CC, and CNTs/RGO/CC mentioned above were monitored by CV tests at different scan rates of 5, 25, 50, 100 mV s<sup>-1</sup> in a potential range of -0.2–1.0 V vs. Ag|AgCl|KCl<sub>sat.</sub> in N<sub>2</sub>-saturated 0.5 M H<sub>2</sub>SO<sub>4</sub> electrolyte. The four materials show nearly unchanged shape and mirror images of CV curves at each scan rate, which demonstrates a good reversibility. CNTs/RGO/CC shows the nearly rectangular shape of CV curves in Figure 3.4.4d, while the CNTs/CC and CNTs/CNTs/CC show redox peaks in CV curves, due to the oxidation in the process of Fe removal in HNO<sub>3</sub>. In Figure 3.4.4c, two pairs of redox peaks are shown in the CV curves of

PANI<sub>wf</sub>/CNTs/CC. The redox peaks are attributed to the oxidation and reduction between leucoemeraldine, emeraldine and pernigraniline bases, which are three oxidation states forms of polyaniline (PANI): fully reduced, half oxidized and fully oxidized forms [389, 390]. This is pseudocapacitance behavior that follows the faradaic process. However, the oxidation peaks shift to more positive potentials and the reduction peaks shift to more negative potentials at the higher scan rates, probably due to the increased resistance. Meanwhile, the increased double layer currents are observed with increasing scan rates in all CV curves, which is consistent with the Randles-Sevcik equation.

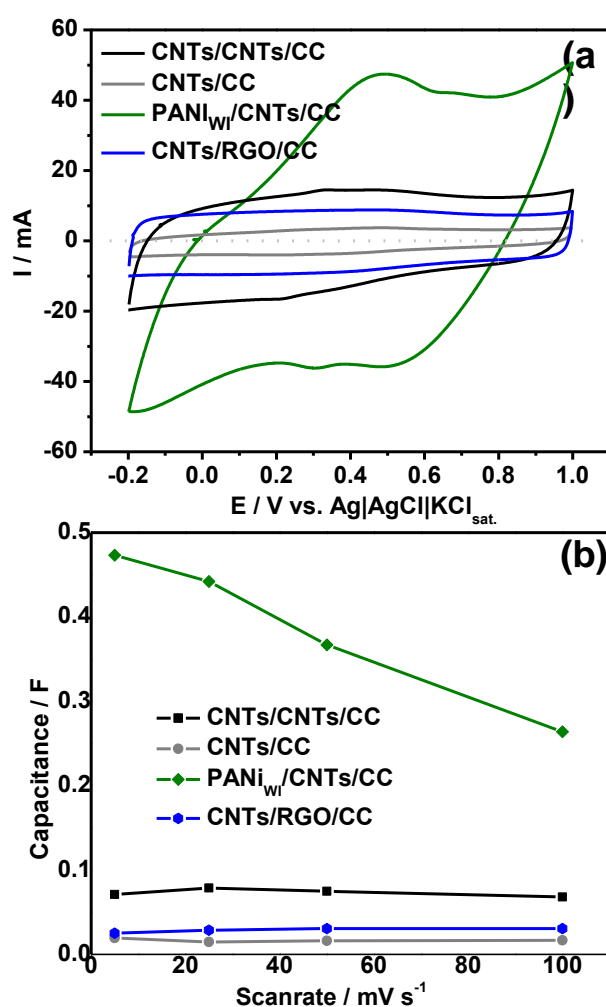


**Figure 3.4.5.** (a) Cyclic voltammograms of CNTs/CC, CNTs/CNTs/CC, PANI<sub>wf</sub>/CNTs/CC and CNTs/RGO/CC electrodes recorded at a scan rate of 100 mV s<sup>-1</sup> in 0.5 M H<sub>2</sub>SO<sub>4</sub> aqueous electrolyte solution purged with N<sub>2</sub> at room temperature and (b) their capacitances calculated through CV at different scan rates.

Figure 3.4.5 displays the CV curves of the different CC based electrodes recorded at a scan rate of 100 mV s<sup>-1</sup> and their capacitances calculated by CV curves (see

Chapter 5.3.8) at different scan rates of 5-100  $\text{mV s}^{-1}$ . After the introduction of secondary CNTs, RGO and PANI<sub>WI</sub> on CC, the double layer currents and capacitances increased to varying degrees compared to CNTs/CC, depending on their tunable amount and their own properties. Due to a thin RGO layer covered on CC, the capacitance of CNTs/RGO/CC does not strongly increase like CNTs/CNTs/CC and PANI<sub>WI</sub>/CNTs/CC. PANI<sub>WI</sub>/CNTs/CC exposes much higher capacitance than the other electrodes. With an increase in the scan rates, the capacitances of PANI<sub>WI</sub>/CNTs/CC calculated at a scan rate of 100  $\text{mV s}^{-1}$  decreases to 56% of the value calculated at 10  $\text{mV s}^{-1}$  as shown in Figure 3.4.5b, probably since the resistance of electrolyte ions transport increases at higher scan rates and the electrolyte ions could not react completely with interior matrix like that at lower scan rates [391]. However, CNTs/CC and CNTs/CNTs/CC display slightly decreased capacitances and the capacitance of CNTs/RGO/CC scarcely changes, which demonstrates that the process on these electrodes is stable and repeatable [392–394].

Afterwards, the galvanostatic charge-discharge test was carried out via chronopotentiometry measurements with different current densities of 5, 10, 20, 30  $\text{mA cm}^{-2}$  in a potential range of -0.2–1.0 V vs. Ag|AgCl|KCl<sub>sat.</sub> in  $\text{N}_2$  purged 0.5 M  $\text{H}_2\text{SO}_4$ . In Figure 3.4.6, galvanostatic charge-discharge curves of the prepared electrode without PANI display a nearly triangular shape with nearly symmetric and linear shape, which is the typical characteristic shape of electrical double layer capacitance and demonstrates a good capacitive performance and electrochemical reversibility [362]. Meanwhile, the PANI<sub>WI</sub>/CNTs/CC electrode shows almost symmetric charge/discharge curves in Figure 3.4.6c, whereas there is a deviation to the linearity owing to the pseudocapacitive behavior in the Faradaic process. Furthermore, while the current density increases, the charge-discharge time decreases and the charge-discharge curves of all CC based electrodes maintain similar shapes, demonstrating a good electrochemical stability towards a wide range of current densities.

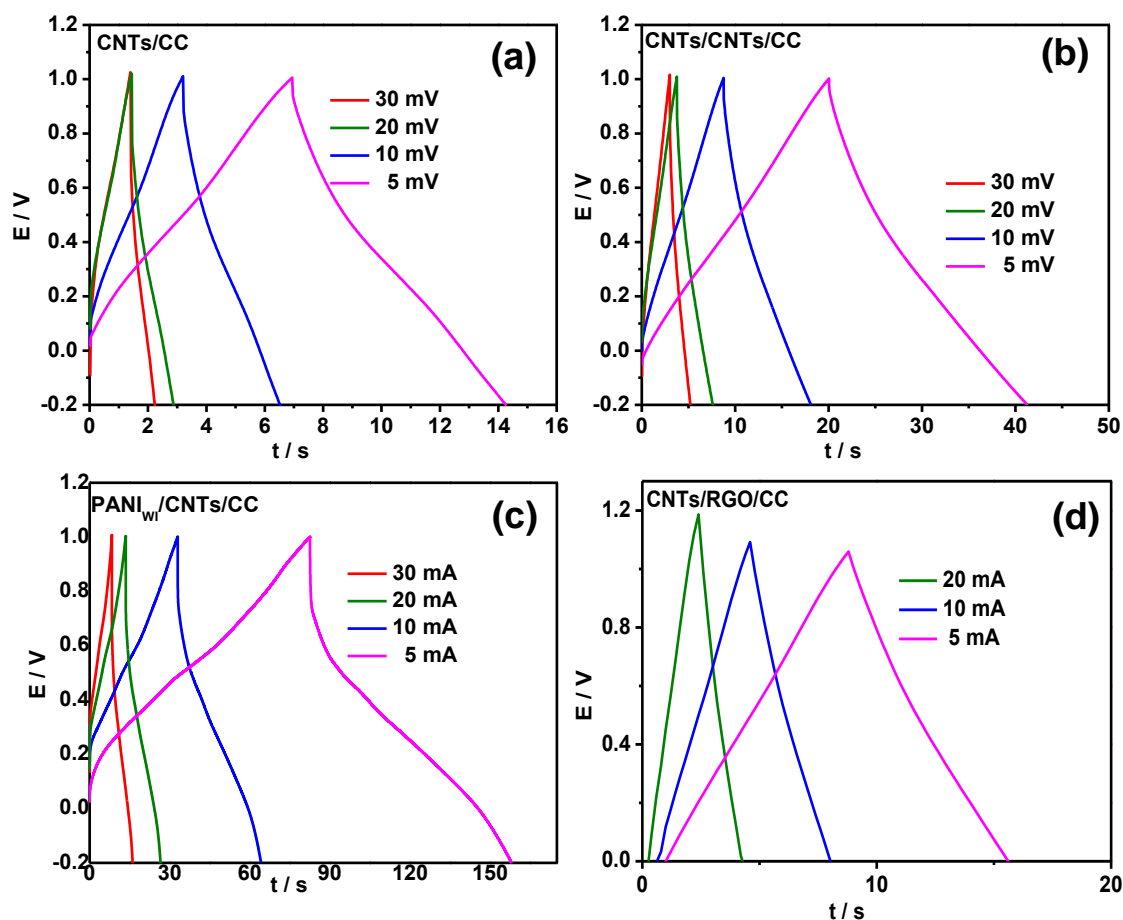


**Figure 3.4.6.** Galvanostatic charge-discharge curves of (a) CNTs/CC, (b) CNTs/CNTs/CC, (c) PANI<sub>WI</sub>/CNTs/CC, (d) CNTs/RGO/CC electrodes measured at different current densities of 5, 10, 20, 30 mA cm<sup>-2</sup> in N<sub>2</sub>-purged 0.5 M H<sub>2</sub>SO<sub>4</sub>.

Figure 3.4.7 shows the comparison of galvanostatic charge-discharge behaviors of the prepared electrodes at a current density of 10 mA cm<sup>-2</sup>, and the capacitances determined by the charge-discharge curves at different current densities. The capacitance of PANI<sub>WI</sub>/CNTs/CC is much higher than that of the other CC based electrodes, which is consistent with the CV measurements. This is probably because PANI of nanoneedle arrays can provide high electrochemical active surface in electrode/electrolyte interface areas and short diffusion paths for ion, leading to electrochemical accessibility [395, 396]. The capacitances of the CC based electrodes without PANI slightly decrease with an increase in current densities, whereas the capacitance of PANI<sub>WI</sub>/CNTs/CC calculated at 30 mA cm<sup>-2</sup> of current density shows a significant decrease by 39%, in comparison with the capacitance calculated at 5 mA cm<sup>-2</sup> of current density, probably caused by decreased dopants into/out the PANI in a higher current density [397].

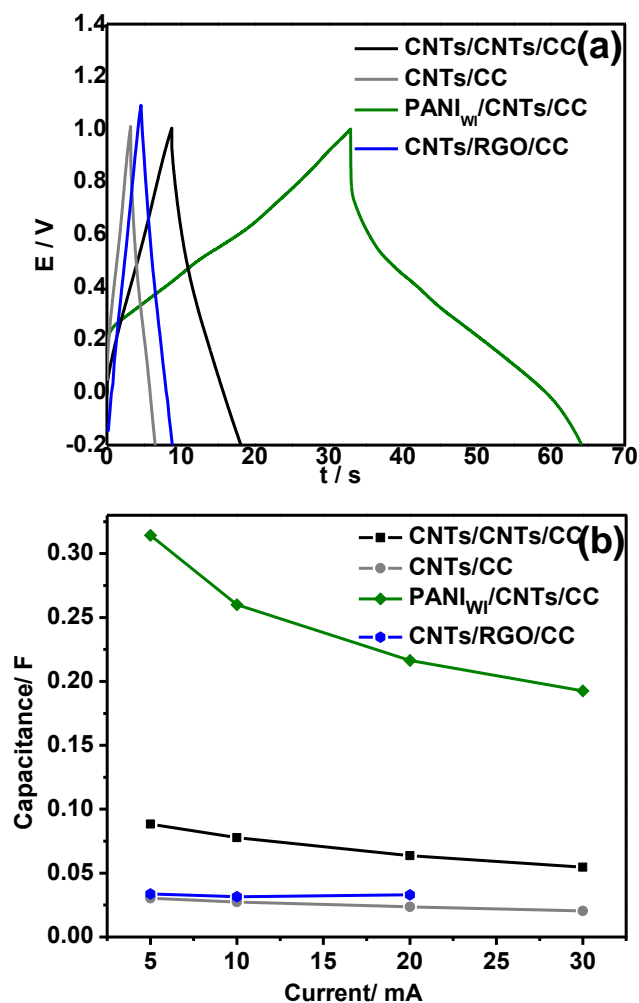


**Figure 3.4.7.** (a) Galvanostatic charge-discharge curves of CNTs/CC, CNTs/CNTs/CC, PANI<sub>WI</sub>/CNTs/CC and CNTs/RGO/CC electrodes recorded at a current density of 10 mA cm<sup>-2</sup> in N<sub>2</sub> purged 0.5 M H<sub>2</sub>SO<sub>4</sub> aqueous electrolyte solution and (b) plot of their capacitances calculated via galvanostatic charge-discharge curves at different current densities.

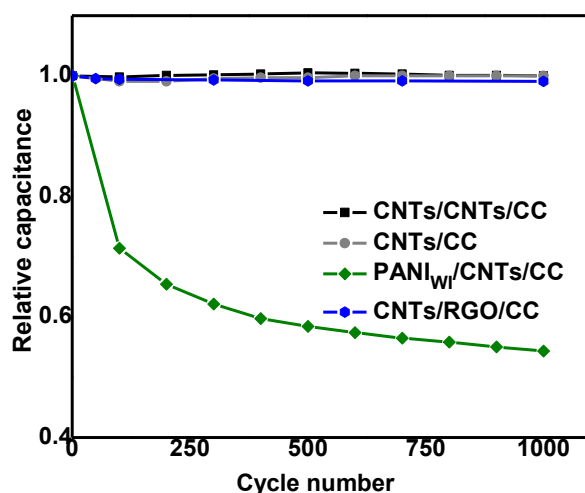


**Figure 3.4.8.** Relative capacitance of CNTs/CC, CNTs/CNTs/CC, CNTs/RGO/CC, PANI<sub>WI</sub>/CNTs/CC after each 100 cycles of charge-discharge curves at a current density of 10 mA cm<sup>-2</sup>.

To further study the electrochemical stability of the prepared electrodes, a long-term test was carried out via 1000 consecutive galvanostatic charge-discharge cycles at a current density of  $10 \text{ mA cm}^{-2}$ . The capacitance retention was calculated after each 100 cycles as shown in Figure 3.4.8. After 1000 cycles, the capacitance of the CC based electrodes without PANI scarcely changes, which indicates their high long-term cycle stability and reversibility. However, the PANI<sub>wf</sub>/CNTs/CC reveals a poor cyclic stability due to the cyclic mechanical stress of conducting polymers, in which a significant decay is displayed in the first 300 cycles and then a slight decrease occurs. After 1000 cycles, 55% of the initial capacitance is left, which is higher than that of the other electrodes (see Table S3.4.1). This decrease is probably caused by swelling and shrinking of PANI during the doping and dedoping process [398]. Here, it is mentioned that the exact mass of CNTs could not be determined, since the etching and loss of carbon cloth occur to varying degrees in the CVD procedure of CNT growth. Instead of the mass specific capacitances, the surface specific capacitances were calculated. After 1000 cycles, the surface specific capacitances of CNTs/CNTs/CC and PANI<sub>wf</sub>/CNTs/CC are  $79 \text{ mF cm}^{-2}$  and  $120 \text{ mF cm}^{-2}$ , respectively, which are much higher than those of the reported vertically aligned carbon nanotubes grown on carbon fabric ( $32.7 \text{ mF cm}^{-2}$ ) [373].

Additionally, the Nyquist plots of CNTs/CC, CNTs/CNTs/CC and PANI<sub>wf</sub>/CNTs/CC are shown in Figure S3.4.2. The semicircle is not shown at high frequency, which corresponds to the charge transfer resistance at the interface between electrode and electrolyte. The equivalent series resistances (ESR) of the prepared electrodes are low, which is attributed to a good contact resistance, charge transfer resistance and electrolyte resistance. In the region of low frequency, a nearly vertical line is displayed, indicating a low diffusion resistance. The Nyquist plots of CNT/CNTs/CC scarcely changes after a long-term test, indicating a high electrochemical stability, while the ESR of PANI<sub>wf</sub>/CNTs/CC has slightly increased. In addition, PANI<sub>wf</sub>/CNTs/CC shows a deviation of the initial slope after 1000 cycling, revealing the increased ionic resistance [399]. This might be caused by the fouling of the diffusion pathway or the swelling and shrinkage of PANI during the doping and dedoping process.

#### **3.4.4. Conclusion**

In this work, hierarchically structured electrodes were studied for EDLCs and pseudocapacitance by directly assembling secondary CNTs, RGO and PANI onto CNTs/CC. PANI was homogenously covered on the CNTs/CC surface to form the PANI/CNTs/CC by wet impregnation (chemical oxidation polymerization) and electrochemical deposition. The CVs of CNTs/CNTs/CC, CNTs/RGO/CC and PANI/CNTs/CC display increased capacitances to varying degrees compared to CNTs/CC, due to their tunable amount and their unique hierarchical structure. PANI<sub>wi</sub>/CNTs/CC shows much enhanced capacitances, while CNTs/CNTs/CC and CNTs/RGO/CC expose an excellent electrochemical stability. Thus, the hierarchical structure could be a promising approach for supercapacitor applications.

## 3.4.5 Supplementary Information

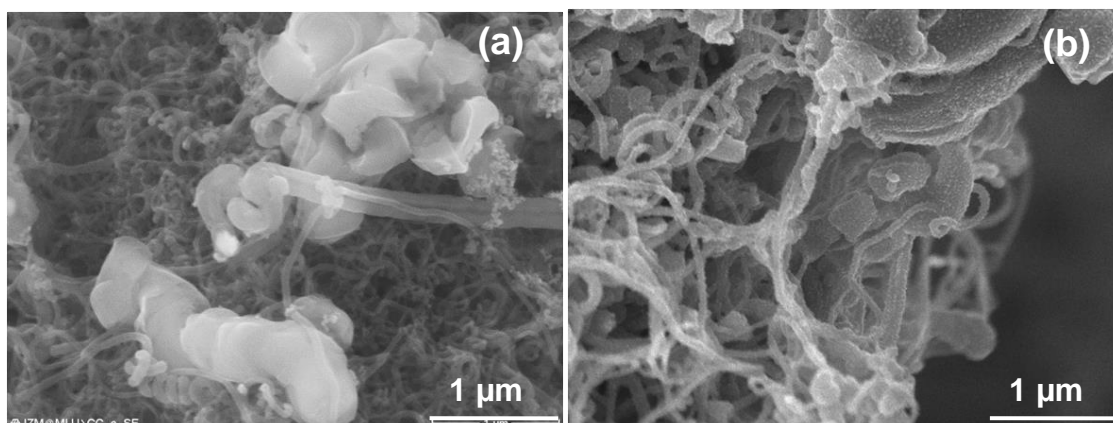


**Figure S3.4.1.** SEM images of PANI decorated onto CNTs/CC via wet impregnation (chemical oxidative polymerization) in (a) 0.1 M aniline + 1 M HClO<sub>4</sub> solution and (b) 0.1 M aniline + 0.1 M HClO<sub>4</sub> solution for 24 h, respectively.

**Table S3.4.1.** Capacitance values determined before and after 1000 cycles long-term test for CNTs/CC, CNTs/CNTs/CC, CNTs/RGO/CC, PANI<sub>wf</sub>/CNTs/CC.

	$C_{\text{start}}/F$	$C_{\text{after 1000 cycles}}/F$
<b>CNTs/CC</b>	0.027	0.027
<b>CNTs/CNTs/CC</b>	0.078	0.079
<b>PANI<sub>wf</sub>/CNTs/CC</b>	0.251	0.120
<b>CNTs/RGO/CC</b>	0,032	0,032

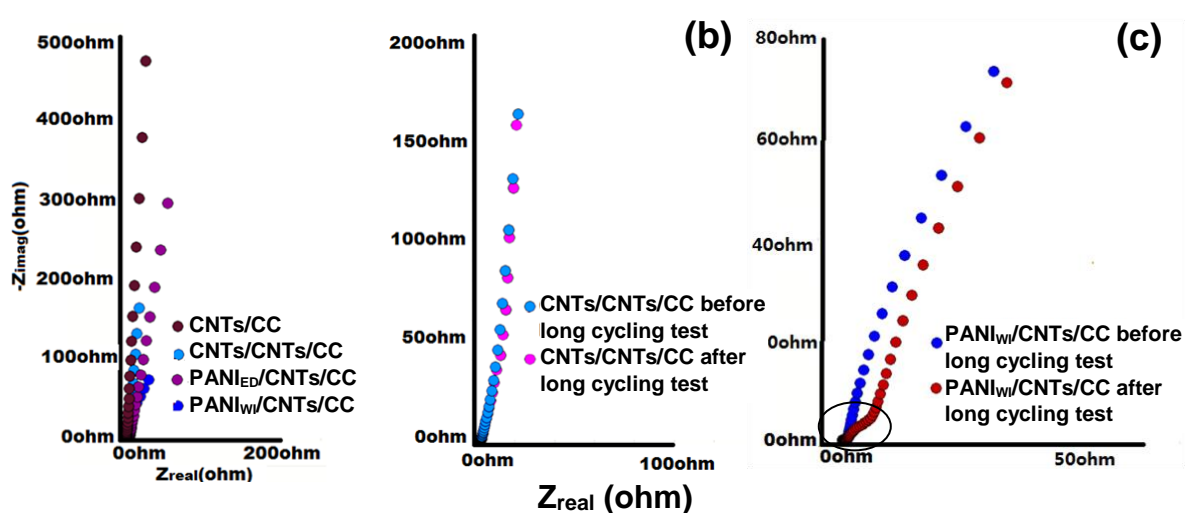


**Figure S3.4.2.** Nyquist plots measured in the frequency range of 10<sup>5</sup>-0.01 Hz with 5 mV amplitude of (a) CNTs/CC, CNTs/CNTs/CC and PANI<sub>wf</sub>/CNTs/CC; (b) CNTs/CNTs/CC and (c) PANI<sub>wf</sub>/CNTs/CC before and after long-term test.



## *Chapter 4:*

# Conclusion and Outlook

---

### 4.1. Conclusion

In this work, the hierarchically nanostructured catalyst support is designed to improve the Pt deposition and its electrochemical performance for the PEMFCs and DMFCs. To prepare the nanostructured materials, a toolbox strategy is developed via bottom-up approaches, in which the materials of required functionalities can be assembled by a stepwise build-up in accordance with a certain application. CNTs and RGO were chosen to synthesize the hierarchical structures.

In the bottom-up approaches, CNTs were successfully grown onto oxidized commercial CNTs, GC and RGO covered CC, respectively, via a sequence of Fe deposition and CVD step to form 3D CNTs (CNTs/CNTs), CNTs/CNTs/GC, CNTs/RGO/CC (Chapter 3.1-3.3). In Chapter 3.2, the CNTs/CNTs/GC was prepared via primary CNTs growth and secondary CNTs growth. After primary CNTs growth over electrodeposited Fe by CVD, secondary CNT growth was carried out via a secondary Fe electrodeposition and CVD step. In Chapter 3.3, RGO/CC was prepared by H<sub>2</sub>-assisted thermal reduction of GO covered on CC before CNT growth, and then NCNT growth on RGO/CC was carried out via CVD with acetonitrile as carbon precursor. Each preparation step was monitored by SEM or TEM. CNTs with high density are observed in 3D CNTs (CNTs/CNTs), CNTs/CNTs/GC, CNTs/RGO/CC, respectively. Furthermore, tuning structural properties of CNTs is achieved by varying Fe electrodeposition time and potential as well as by varying the growth time, gas flow rate and ratio of H<sub>2</sub>/Ar in CVD step. In Chapter 3.1 the secondary CNTs were tailored with smaller diameter than primary ones to verify the successful preparation of the hierarchical structure, while the diameters of primary

CNTs and secondary CNTs were adjusted by tuning the size of Fe nanoparticles in Chapter 3.2. Additionally, the successful synthesis of hierarchical materials is also demonstrated by Raman spectra. The prepared hierarchically structured electrodes show much higher double layer capacitances in cyclic voltammograms, compared to the primary CNTs, CNTs/GC and CNTs/CC, respectively, demonstrating larger available surface area for the further Pt deposition.

Afterwards, Pt deposition was achieved onto the prepared hierarchically structured materials. In Chapter 3.1 Pt nanoparticles were homogeneously deposited onto 3D CNTs by a wet-impregnation approach, while Pt deposition onto CNTs/CNTs/GC, CNTs/RGO/CC with a homogeneous distribution was achieved by electrodeposition (Chapter 3.2, 3.3), observed in TEM and SEM. The three types of prepared hierarchical electrodes show enhanced ECSA calculated by  $H_{ads/des}$  and  $CO_{ad}$  oxidation of the cyclic voltammograms, respectively. To demonstrate the suitability of the hierarchical electrodes for electrocatalytic applications, Pt-3D CNTs electrode (without substrate) was evaluated for ORR (Chapter 3.1), while Pt-CNTs/CNTs/GC and Pt-CNTs/RGO/CC electrodes were characterized for MOR (Chapter 3.2, 3.3).

In Chapter 3.1, Pt-3D CNTs electrode has higher specific activities towards ORR and improved long-term stability in the accelerated stress test compared with Pt-primary CNTs. In the MEAs single cell test, enhanced maximum power density of Pt-3D CNTs maximum is shown. In Chapter 3.2, Pt-CNTs/CNTs/GC exhibits an approximately 2.5 times higher Pt mass specific activity for methanol oxidation with respect to Pt-CNTs/GC, while the Pt mass specific activity of Pt-NCNTs/RGO/CC for MOR is about 1.37 times higher than that of Pt-NCNTs/CC in Chapter 3.3. Meanwhile, improved tolerances towards CO poisoning are displayed. These improvements of electrochemical performance are probably attributable to the improved dispersion of Pt nanoparticles, which can arise from the larger available active surface, increased conductivity and efficient transport pathway caused by the hierarchical structures. Additionally, polyaniline was deposited on the surface of CNTs/CC by wet impregnation and electrodeposition to form hierarchical PANI/CNTs/CC electrodes for supercapacitors (Chapter 3.4). The PANI/CNTs/CC shows high capacitances, which were calculated by cyclic voltammetry and galvanostatical charge/discharge curves, respectively, compared to CNTs/CC, CNTs/CNTs/CC and CNTs/RGO/CC. In

summary, the CNT-based hierarchically structured electrodes show improved performances in electrochemical applications and the hierarchical structure strategy is suitable to develop a competitive catalyst support for PEMFCs and DMFCs.

## 4.2. Outlook

In this research, we focused on the preparation of the catalyst supports, namely the formation of CNT-based hierarchical structure. Since the dispersion and sizes of Pt-nanoparticles can affect the electrochemical activities for oxygen reduction and methanol oxidation, the optimization of Pt deposition on hierarchical materials should be studied in follow-up research. Furthermore, a scale-up synthesis of Pt-CNTs/CNTs/CC and Pt-CNTs/RGO/CC can be attempted in the same manner to realize fuel cell tests. In this way, the advantages of hierarchically structured materials could be further evaluated in practical applications. Additionally, the hierarchically structured materials based CNTs and CC (CNTs/CNTs/CC and CNTs/RGO/CC) have enhanced double layer capacitances and stability, and are appropriate electrode materials for EDLC. Apart from polyaniline, a new component like metal oxides can be introduced to the hierarchical electrodes for further research of pseudo-EDLC supercapacitors.



## Chapter 5:

# Experimental Section

---

In this experimental section, the preparation of Pt supported CNTs/CNTs/GC electrode, preparation of Pt supported RGO/CNTs/GC electrode and their structural and electrochemical characterizations have been published in ‘Hierarchically structured 3D carbon nanotube electrodes for electrocatalytic applications, Pei Wang, Katarzyna Kulp and Michael Bron, *Beilstein J. Nanotechnol.* 2019, 10, 1475-1487’ [283] and ‘Pt supported on nanostructured NCNTs/RGO composite electrodes for methanol oxidation, Pei Wang, Dr. Tintula Kottakkat, Prof. Dr. Michael Bron, *ChemElectroChem* 2015, 2, 1396-1402’ [330]. (Reproduced with permission)

### 5.1. Chemicals

Name	Specification	Supplier
Iron(III) nitrate $\text{Fe}(\text{NO}_3)_3 \cdot 9\text{H}_2\text{O}$	99.999 %	Carl Roth, Germany
Iron(II) sulfate	$\geq 99.5$ %	Carl Roth, Germany
Magnesium sulfate	$\geq 99$ %, p.a.	Carl Roth, Germany
Silica	aerosil® 200, $\text{SiO}_2$ -aerosil 38	Evonik
Primary CNTs (Multi walled carbon nanotubes)	Baytubes® C 150P	Bayer Material Science AG
Glassy carbon	Sigradur® G	HTW, Germany
Carbon cloth	CC-G-8N without PTFE	Quintech, Germany
Alummina Suspension	1 $\mu\text{m}$ and 0.3 $\mu\text{m}$	LECO Corporation, Germany
Nitric Acid, $\text{HNO}_3$	$\geq 65$ %, p.a.	Carl Roth, Germany
Sulfuric acid, $\text{H}_2\text{SO}_4$	98 %	Carl Roth, Germany

## Experimental Section

Acetonitrile, CH <sub>3</sub> CN	≥ 99.5 %	Carl Roth, Germany
Cyclohexane, C <sub>6</sub> H <sub>6</sub> OH	≥ 99 %, p.a.	Carl Roth, Germany
Ethylene Glycol, C <sub>2</sub> H <sub>6</sub> O <sub>2</sub>	≥ 99 %	Carl Roth, Germany
Sodium nitrate, NaNO <sub>3</sub>	≥ 99.0 %	Sigma-Aldrich, USA
Potassium permanganat, KMnO <sub>4</sub>	≥ 99 %, p.a.	Carl Roth, Germany
Hydrochloric acid, HCl	37 %	Carl Roth, Germany
Argon, Ar	99.999 %	Air Liquid, Germany
Hydrogen, H <sub>2</sub>	99.999 %	Air Liquid, Germany
Sodium hydroxide, NaOH	≥ 99 % p.a. ISO, Pellets	Carl Roth, Germany
Potassium hydroxide, KOH	≥ 85 %, p.a.	Carl Roth, Germany
Sodium Borohydride, NaBH <sub>4</sub>	99 %	Acros organics, USA
Nafion® 117 solution	5% in mixture of lower aliphatic alcohol and water	Sigma-Aldrich, USA
Hexachloroplatinic acid, H <sub>2</sub> PtCl <sub>6</sub> · 6 H <sub>2</sub> O	99.9 %	Acros organics, USA
Platinum (II) nitrate, Pt(NO <sub>3</sub> ) <sub>2</sub>	99.99 %	-
Pt/C	20 wt. % Pt on carbon Vulcan XC-72	E-TEK, USA
Glassy carbon rod	Sigradur® G	HTW, Germany
Perchloric acid, HClO <sub>4</sub>	70 %	Carl Roth, Germany
Nitrogen, N <sub>2</sub>	99.999 %	Air Liquid, Germany
Carbon oxide, CO	10 % CO 1.8 in He 5.0	Air Liquid, Germany
Oxygen, O <sub>2</sub>	99.995 %	Air Liquid, Germany
2-Propanol, C <sub>3</sub> H <sub>8</sub> O	≥ 99.98 %	Carl Roth, Germany
Ethanol, C <sub>2</sub> H <sub>5</sub> OH	≥ 99 % HPLC gradient grade	Carl Roth, Germany

## 5.2. Preparation of Hierarchically Nanostructured Electrodes

### 5.2.1. General Procedure of Carbon Nanotube Growth over Fe catalyst by CVD

Growth of carbon nanotubes (CNTs) was carried out by thermal chemical vapor deposition (CVD). In this work the transition metal Fe was employed as a catalyst for CNT growth and CNTs were grown on different substrates, such as glassy carbon (GC), carbon cloth (CC), reduced graphene oxide (RGO) deposited on carbon cloth, etc. The parameters for Fe deposition and the conditions of the CVD process were studied on different substrates shown in the chapters above, respectively. To efficient CNT growth on different substrates, CNT growth over Fe deposited silica by CVD was carried out in preliminary study.

#### Fe Deposition via Impregnation

For CNT growth, the silica (SiO<sub>2</sub>-aerosil 380, Evonik) served as Fe support. According to the method of Van Dommele *et al.* [275], 3.62 g Fe(NO<sub>3</sub>)<sub>3</sub>·9H<sub>2</sub>O (20% Fe) were mixed with 1.61 g Urea and 2.02 g SiO<sub>2</sub> in 200 ml H<sub>2</sub>O at 90 °C under stirring for 16 h. Then the mixture was filtered and washed with deionized water, and was dried at 100 °C for 24 h. Afterwards, the Fe/SiO<sub>2</sub> was calcinated at 500 °C for 3 h.

#### Electrochemical Fe Deposition

The Fe deposition onto substrates such as glassy carbon or carbon cloth was achieved using double pulse deposition [318] in a 0.005 M FeSO<sub>4</sub>·7H<sub>2</sub>O (≥ 99.5%, Roth, Germany) and 0.5 M MgSO<sub>4</sub>·7H<sub>2</sub>O (pure, Roth, Germany) solution, where no-effect potential, nucleation potential and growth potential were applied. The three potentials were identified by linear sweep voltammetry at a scan rate of 5 mV s<sup>-1</sup> in the potential range of -0.5- -1.75 V vs. Ag|AgCl|KCl<sub>sat.</sub> in the Fe containing solution, and is shown in Figure S3.2.1.

#### CVD Process

After Fe deposition, chemical vapor deposition was used to grow CNTs. The different substrates with Fe nanoparticles were put in a quartz boat inside a quartz tube in horizontal furnace (see Figure 2.7). First, the quartz tube was flushed with Ar

(6 L h<sup>-1</sup>) for 50 min to remove the air, and then was heated to 750°C with a heating rate of 10 K min<sup>-1</sup> with 3 L h<sup>-1</sup> H<sub>2</sub> /3 L h<sup>-1</sup> Ar. During the process, the Fe nanoparticles were annealed and reduced. Afterwards, the gas was saturated with carbon precursors (acetonitrile or cyclohexane) and flowed into the quartz tube for 120 min to provide the carbon for decomposition for CNT growth, followed by cooling down the furnace to room temperature with Ar. In growth of CNTs different temperatures of 750°C, 850°C, 950°C and 1050°C were studied. Afterwards, CNTs were separately grown onto primary CNTs, GC, CNTs/GC, CC, RGO/CC via CVD at 750 °C. The ratio of gas flow was slightly adjusted due to different carbon precursors and substrates as shown in the Chapters 5.2.2, 5.2.3 and 5.2.4.

### **5.2.2. Preparation of Pt supported 3D CNT Electrodes**

Pt supported on 3D CNTs was prepared as illustrated in Figure 3.1.1. The 3D CNTs were formed by growing secondary CNTs onto the primary CNTs (commercial CNTs). Afterwards, Pt nanoparticles were deposited on the 3D CNTs.

### **Oxidation of Commercial MWCNTs**

Commercial multi-walled CNTs (MWCNTs, Baytubes® C 150 P; Bayer Materials Science) were initially treated at 800°C under Ar atmosphere for 2 h to remove impurities as well as decompose oxygen functional groups on the CNT surface and to provide a homogeneous starting material. To activate the surface of CNTs and introduce surface functional groups, oxidation of CNTs to form OCNTs was carried out by refluxing in 5 M HNO<sub>3</sub> (prepared by diluting ≥ 65% HNO<sub>3</sub>, p.a, Roth, Germany) at 100 °C for 6 hours, which led to the formation of the functional groups such as carboxyl, carbonyl or hydroxyl [269]. After oxidation, the OCNTs were separated by centrifuge and washed with MilliQ water until the pH was neutral. Then the OCNTs were dried at 100°C in an oven for 24 hours. The OCNTs were utilized as primary CNTs and are labelled as such in the following.

### **Fe Deposition onto primary CNTs by Impregnation**

After oxidation of commercial MWCNTs Fe nanoparticles were deposition onto the primary CNTs as reported in [400]. 220 mg primary CNTs were dispersed in 40 ml of 0.05 M FeSO<sub>4</sub>\*7 H<sub>2</sub>O (≥ 99.5%, Roth, Germany) aqueous solution stabilized with 0.5



M ascorbic acid. Then the dispersion was stirred under Ar atmosphere for 2 h to allow  $\text{Fe}^{2+}$  to deposit onto the primary CNTs. After 2 h 0.1 M 150 ml  $\text{NaBH}_4$  solution was slowly added at  $0.1 \text{ mL s}^{-1}$  using a peristaltic pump. This process reduces  $\text{Fe}^{2+}$ . The primary CNTs with deposited Fe particles were then separated by filtration, washed with MilliQ water and dried at  $100 \text{ }^\circ\text{C}$  overnight, followed calcination in air at  $350 \text{ }^\circ\text{C}$  for 120 min after applying a  $3 \text{ K min}^{-1}$  heating ramp.

### **Growth of Secondary CNTs onto primary CNTs via CVD**

Secondary CNTs growth onto primary CNTs was carried out through CVD at  $750 \text{ }^\circ\text{C}$  for 2 hours in a mixture atmosphere of  $\text{H}_2$  ( $3 \text{ L h}^{-1}$ ) and Ar ( $3 \text{ L h}^{-1}$ ) saturated with acetonitrile ( $\text{CH}_3\text{CN}$ , Roth) to create the 3D CNT network. Acetonitrile was used as carbon precursor. Before purging the gas saturated with acetonitrile (namely before the secondary CNT growth), the Fe nanoparticles were reduced under  $\text{H}_2$  and Ar in the heating process. To remove the Fe nanoparticles in the 3D CNTs after CVD, the samples were treated in the mixture of concentrated  $\text{HNO}_3$  and  $\text{H}_2\text{SO}_4$  at a ratio of 1:1 for 2 hours by ultrasonication. For a valid comparison, the primary CNTs without secondary ones were also treated in concentrated  $\text{HNO}_3$  and  $\text{H}_2\text{SO}_4$ .

### **Deposition of Pt Nanoparticles onto Primary and 3D CNTs**

Pt nanoparticles onto primary CNTs as well as 3D CNTs were produced according to [401]. First, 90 mg of primary CNTs or 3D CNTs were dispersed in 30 mL ethylene glycol (EG) using an ultrasonication finger to obtain a homogenous suspension. Then chloroplatinic acid ( $\text{H}_2\text{PtCl}_6 \cdot 6 \text{ H}_2\text{O}$ , Acros Organics) and 30 mL ethylene glycol were added to this solution. The amount of Pt in the catalyst was adjusted to 20 wt.% Pt. The solution was stirred for 1 hour at room temperature. Afterwards, the mixture was heated to  $150 \text{ }^\circ\text{C}$  for 3 hours followed by stirring at room temperature for 24 hours. The prepared samples were filtered and washed with MiliQ water and dried at  $100 \text{ }^\circ\text{C}$  overnight.

#### **5.2.3. Preparation of Pt supported CNTs/CNTs/GC Electrodes**

The procedure for the preparation of hierarchically nanostructured electrodes is illustrated in Figure 3.2.1. Firstly, the iron nanoparticles were electrodeposited onto oxidized glassy carbon followed by CNT growth via chemical vapor deposition.

Secondary Fe deposition and CNT growth were subsequently carried out to form a hierarchically structured electrode, onto which Pt was finally deposited by electrochemical method. This electrode preparation has been published in [283].

### **Modification of Glassy Carbon**

Glassy carbon chips (GC, 2 x 1 cm<sup>2</sup>) were oxidized by refluxing in 5 M HNO<sub>3</sub> (prepared by diluting ≥ 65% HNO<sub>3</sub>, p.a, Roth, Germany) at 100 °C for 2 hours to activate their surface and form oxygen functional groups as anchor sites.

### **Fe Deposition onto GC using Electrochemical Method**

Fe nanoparticles were formed by double pulse deposition [318] in 0.005 M FeSO<sub>4</sub>·7H<sub>2</sub>O (≥ 99.5%, Roth, Germany) and 0.5 M MgSO<sub>4</sub>·7H<sub>2</sub>O (pure, Roth, Germany) aqueous solution. A potential sequence consisting of a no-effect potential (E= -0.75V vs. Ag|AgCl|KCl<sub>sat.</sub>; t= 5 s), a nucleation potential (E= -1.41 V vs. Ag|AgCl|KCl<sub>sat.</sub>; t= 0.2 s) and a growth potential (E= -1.27 V vs. Ag|AgCl|KCl<sub>sat.</sub>; t= 12 s) was applied. The potentials were determined from linear sweep voltammograms recorded in the potential range from -0.5 V and -1.75 V vs. Ag|AgCl|KCl<sub>sat.</sub> with a scan rate of 5 mV s<sup>-1</sup> as shown in Figure S3.2.1. The deposited Fe nanoparticles served as catalyst of CNT growth.

### **Growth of Primary and Secondary CNT Growth onto GC**

Growth of primary CNTs onto GC was carried out through chemical vapor deposition (CVD) at 750 °C in H<sub>2</sub>/Ar mixtures saturated with cyclohexane (Roth) at room temperature. The influence of growth time (30 min, 60 min and 120 min), gas flow rate and Ar/H<sub>2</sub> ratio on the CNT growth was investigated, where gas flow rates were adjusted by mass flow controllers (Bronkhorst High-Tech, Germany). Prior to the CVD process, the Fe catalysts were conditioned at 750°C for 30 min in a H<sub>2</sub>/Ar gas mixture. After the CNT growth, the surface of CNTs/GC is highly hydrophobic. To remove the Fe nanoparticles, the CNTs/GC were immersed in concentrated HNO<sub>3</sub> at room temperature for 12 h, where the CNTs were also oxidized to form anchor spots for a second Fe deposition, which was carried out in the same way as above but with 8 s of growth time. Secondary CNTs were grown on the Fe-CNTs/GC under appropriate growth condition as discussed in Chapter 3.2.2 above, in which a gas

mixture of H<sub>2</sub> (1.2 L h<sup>-1</sup>) and Ar (0.5 L h<sup>-1</sup>) at 750 °C for 120 min was chosen. Afterwards, the Fe nanoparticles were leached out in concentrated HNO<sub>3</sub>. Furthermore, the same procedure was performed using acetonitrile as carbon source to yield NCNTs/NCNTs/GC.

### Pt Electrodeposition onto CNTs/CNTs/GC

Pt nanoparticles were electrochemically deposited onto CNTs/CNTs/GC in an aqueous 0.005 M Pt(NO<sub>3</sub>)<sub>2</sub> and 0.1 M NaNO<sub>3</sub> solution via linear-sweep voltammetry from 0 to -0.9 V vs. Ag|AgCl|KCl<sub>sat.</sub> at a scan rate of 5 mV s<sup>-1</sup> to form Pt-CNTs/CNTs/GC. For comparison, Pt deposition onto GC and CNTs/GC was performed in the same manner.

The amount of deposited Pt was calculated from the charge consumed during the linear sweep voltammetry according to the following faradic reaction (Equation 5.1) and Faraday's law (Equation 5.2):



$$Q_{Pt} = n \times \frac{m_{Pt}}{M_{Pt}} \times F \quad (\text{Equation 5.2})$$

With  $Q_{Pt}$  is the charge consumed to reduce Pt ions to Pt;

$n$  is the number of transfer electrons;

$m_{Pt}$  is the amount of Pt;

$M_{Pt}$  is the atomic weight of Pt (195.09 g mol<sup>-1</sup>);

$F$  is Faraday's constant (96485.31 C mol<sup>-1</sup>).

#### 5.2.4. Preparation of Pt supported RGO/CNTs/CC Electrodes

RGO, NCNTs and Pt were assembled on the CC in a bottom-up approach as represented in Figure 3.3.1. Initially, the surface of carbon cloth was uniformly decorated by thin RGO film followed by electrodeposition of iron nanoparticles onto RGO. Then CNTs were grown over the iron nanoparticles via chemical vapor deposition. Afterwards, Pt electrodeposition was carried out on CNT decorated RGO/CC to form Pt-CNT/RGO/CC. This experimental part has been published in [330].

### **Modification of Carbon Cloth**

CC pieces (CC-G-8N without PTFE, Quintech, Germany) with dimensions in the range of 2.5 x 0.7 cm<sup>2</sup> were refluxed in 5 M HNO<sub>3</sub> (prepared by diluting ≥ 65% HNO<sub>3</sub>, p.a, Roth, Germany) at 100 °C for 2 h.

### **Preparation of Graphene Oxide and their Deposition onto CC**

The graphene oxide (GO) was prepared by Hummer's method [260]. 250 mg NaNO<sub>3</sub> were mixed in a 250 mg graphite and 25 ml concentrated H<sub>2</sub>SO<sub>4</sub> solution under stirring for 1 h, and then 1.50 g KMnO<sub>4</sub> were added very slowly in the solution in an ice bath. The temperature was kept below 20 °C. Afterwards, 11.50 ml 70 °C deionized water was added into the above solution followed by addition of ca. 5 ml 30% H<sub>2</sub>O<sub>2</sub> until color of the solution is changed from dark brown to bright yellow. In the end, the solution was washed with 5% HCl and deionized water until it was neutral.

The graphene oxide was dip-coated onto the surface of the CC (ca. 0.7 x 0.7 cm<sup>2</sup>) from a prepared 0.5 wt.% graphene oxide (GO) suspension and the resulting GO/CC was dried in an oven at 40°C for 24 h. The GO in GO/CC was reduced by heat-treatment at 380 °C in a 2:1 mixture of H<sub>2</sub> and Ar to form reduced graphene oxide decorated carbon cloth (RGO/CC).

### **Electrochemical Deposition of Fe onto RGO/CC**

Fe nanoparticles were electrodeposited onto RGO/CC via the above mentioned double-pulse deposition from 0.005 M FeSO<sub>4</sub>·7H<sub>2</sub>O and 0.5 M MgSO<sub>4</sub>·7H<sub>2</sub>O aqueous solution. A no-effect potential (E= -0.3 V vs. Ag|AgCl|KCl<sub>sat.</sub>; t=10 s), nucleation potential (E= -1.75 V vs. Ag|AgCl|KCl<sub>sat.</sub>; t=0.2 s) and growth potential (E= -1.2 V vs. Ag|AgCl|KCl<sub>sat.</sub>; t=15 s) were applied. The deposited Fe nanoparticles act as catalyst for NCNT growth.

### **CNT Growth onto RGO/CC and CC**

NCNTs were grown through CVD at 750 °C for 2 h in an atmosphere of H<sub>2</sub> (3 L h<sup>-1</sup>) and Ar (3 L h<sup>-1</sup>) saturated with acetonitrile (CH<sub>3</sub>CN, Roth). After cooling down, the Fe nanoparticles were leached out using cyclic voltammetry in the range of -0.2–1.0 V vs. Ag|AgCl|KCl<sub>sat.</sub> in 0.5 M H<sub>2</sub> SO<sub>4</sub>.

## Pt Deposition onto CNTs/RGO/CC and CC

Pt nanoparticles were electrodeposited onto the surface of NCNTs/RGO/CC by performing single-sweep voltammetry from 0 to -0.5 V at a scan rate of 5 mV s<sup>-1</sup> in 0.005 M Pt(NO<sub>3</sub>)<sub>2</sub> and 0.1 M NaNO<sub>3</sub> solution to form Pt-NCNTs/RGO/CC. Pt-NCNTs/CC was prepared in exactly the same manner but without RGO. The Pt loadings of the NCNTs/CC and NCNTs/RGO/CC were 0.097 mg cm<sub>CC</sub><sup>-2</sup> (0.63 wt.%) and 0.080 mg cm<sub>CC</sub><sup>-2</sup> (0.52 wt.%) respectively, calculated based on ICP-OES results (see below).

### 5.2.5. Preparation of PANI/CNTs/CC Electrodes

First, CNTs/CC was prepared by the method mentioned above (see Chapter 5.2.4) followed by PANI deposition onto surface of CNTs/CC (Figure 3.4.1). The PANI coating was performed using chemical oxidation polymerization (PD) and electrochemical polymerization (ED).

#### Chemical Oxidation Polymerization for PANI Coating

PANI was synthesized onto the CNTs/CC by chemical oxidation polymerization of aniline. 142.5 mg ammonium persulfate (APS) and 45 μL aniline monomer were dissolved in 5 ml 1 M H<sub>2</sub>SO<sub>4</sub> solution and stirred for 1 h in an ice bath, respectively. The molar ratio of aniline and APS was 1. The suspensions of the APS and aniline were mixed, and then the CNTs/CC was dipped in the mixed solution for 24 h. Afterwards, the PANI/CNTs/CC was formed and was washed with de-ionized water, and then was dried at 30 °C for 48 h.

#### Electrochemical Polymerization for PANI Coating

The prepared CNTs/CC as working electrode was dipped in a 0.25 M aniline and 0.5 M H<sub>2</sub>SO<sub>4</sub> solution, where the electrochemical polymerization of PANI was carried out by CV at 100 mV s<sup>-1</sup> in a potential range between -0.21–0.9 V vs. Ag|AgCl|KCl<sub>sat.</sub> for 20 cycles to form the PANI film coated onto the surface of CNTs/CC.

## 5.3. Structural Characterization

### 5.3.1. Scanning- and Transmission-Electron Microscopy

The morphology and structural properties of the nanostructured electrodes were estimated via scanning electron microscopy (SEM) employing an ESEM XI 30 FEG (PHILIPS, Germany) or transmission electron microscopy (TEM) with a LEO912 OMEGA (Japan) microscope operating at 120 kV acceleration voltage. For TEM measurement the samples were dispersed via ultrasonication in ethanol and were dropped on a holey carbon filmed copper grid (300 mesh). The average particle size and size distribution of Fe and Pt nanoparticles were determined by statistical analysis of 200–300 particles with the Lince software (TU Darmstadt, Germany) [388] and the diameters of CNTs were be evaluated.

### 5.3.2. Raman Spectroscopy

Raman spectroscopy is employed to provide information on chemical structures and physical forms by detecting vibrations in molecules based on the processes of infrared absorption and Raman scattering [402, 403]. Raman spectra was measured with a Renishaw InVia spectrometer employing 532 nm excitation wavelength from a Cobolt CW DPSS laser to evaluate the prepared carbon materials by displayed D and G band, which are associated with structural defects within the carbon lattice and crystalline carbon, respectively.

### 5.3.3. X-ray Diffraction

X-ray diffraction (XRD) was carried out on a D8 advanced X-ray diffractometer from Bruker AXS using  $\text{CuK}\alpha$  radiation ( $\lambda=1.5406 \text{ \AA}$ ) and a step size of  $0.0138 (2^\circ \text{ min}^{-1})$  in the  $2\theta$  range of  $5\text{--}80^\circ$  to evaluate the crystalline nature. For GC and CC samples, XRD did not yield useful results regarding Pt structure and particle size due to the amorphous carbon and roughness of the GC and CC surface and the considerably thin film of Pt-CNTs. Additionally, XRD for Pt-CNTs and Pt-3D CNT powders was carried out with a STOE STADI-P diffractometer using germanium monochromized  $\text{MoK}\alpha$  radiation ( $\lambda = 0.71069 \text{ \AA}$ ) in the cooperation group (Prof. Dr. Christina Roth Workgroup). Here, the interplanar distance and crystallite size of catalysts could be determined by Equation 5.3 and Equation 5.4 [404, 405].

$$L = \frac{0.9\lambda}{B_{2\theta} \cos \theta_{\max}} \quad (\text{Equation 5.3})$$

$$d = \frac{\lambda}{2 \sin \theta_{\max}} \quad (\text{Equation 5.4})$$

With  $\lambda$  is the wavelength;  
 $\theta_{\max}$  is the  $2\theta$  angle at the peak maximum;  
 $B_{2\theta}$  is the full width at half maximum (FWHM) in radians;  
 $L$  is the average crystallite size in nm;  
 $d$  is the interplanar distance in nm;  
 $0.9$  is a shape factor.

#### 5.3.4. Inductively Coupled Plasma-Optical Emission Spectroscopy

The Pt loadings in the nanostructured electrodes were determined by inductively coupled plasma-optical emission spectroscopy (ICP-OES; Ultima 2, Horiba scientific). The Pt-loaded electrodes were digested in aqua regia under microwave radiation followed by dilution with de-ionized water.

#### 5.3.5. Nitrogen Physisorption Measurement

The nitrogen physisorption measurements were carried out at 77K, where specific surface area, average pore size as well as pore size distribution of the CNTs based carbon materials were determined using the Brunauer-Emmett-Teller (BET) and Barret-Joyner-Halenda (BJH) (for mesopores) approaches.

#### 5.3.6. Elemental Analysis

Elemental analysis was achieved using a Vario EL (CHNS) analyzer to obtain the nitrogen contents after nitrogen doped CNT growth.

## 5.4. Electrochemical Characterization

All electrochemical syntheses and measurements were carried out in a conventional one-compartment three-electrode electrochemical cell employing a computer-controlled Autolab potentiostat/galvanostat PGstat 302 (Eco Chemie, Netherlands) or a Gamry potentiostat PGI 4 (Gamry Framework 2.67 software) at room temperature. The three-electrode electrochemical cell consisted of a working electrode, a reference electrode and a counter electrode. The prepared nanostructured materials served as working electrode, while Pt mesh (GoodFellow, Germany) was employed as counter electrode and Ag|AgCl|KCl<sub>sat.</sub> electrode (SE20, Sensortechnik Meinsberg, Germany) or a reversible hydrogen electrode (RHE, built in-house) was used as reference electrode. An RHE was used as reference electrode for characterization in acid, while Ag|AgCl|KCl<sub>sat.</sub> was used as reference electrode for iron deposition, methanol oxidation, etc. For the electrochemical measurements, cyclic voltammetry (CV) and linear sweep voltammetry (LSV) were used to investigate the electrochemical properties of the catalyst materials towards methanol oxidation reaction or oxidation reduction reaction.

### 5.4.1. Preparation of Working Electrode

In this work, supported (namely glassy carbon or carbon cloth) or unsupported catalyst materials were studied. The catalyst materials based on glassy carbon or carbon cloth (size of 1 x 2 cm<sup>2</sup>) were directly measured as working electrode. But for the unsupported catalyst materials an ink was prepared. 4 mg catalyst material were suspended by ultrasonication in 800  $\mu$ L of a mixture of isopropanol (780  $\mu$ L) and Nafion® 117 solution (Aldrich) (20  $\mu$ L) for 30–60 min followed by stirring overnight to obtain a homogeneous catalyst suspension. The mass ratio between the Nafion® and catalyst was 0.2. Then 5  $\mu$ L catalyst suspension was dropped onto a glassy carbon rod inserted in Teflon cylinder with 4 mm diameter (0.125 cm<sup>2</sup> area) and dried in isopropanol saturated atmosphere at room temperature. The catalyst loading was kept at 200  $\mu$ g cm<sup>-2</sup>. The covered with catalyst film glassy carbon was employed as working electrode. Since the glassy carbon can be reused, it was important to clean the surface of glassy carbon before coating the catalyst materials, which can affect electrochemical properties. Therefore, the surface of glassy carbon was polished with



1 and 0.3  $\mu\text{m}$  alumina slurry on a polishing cloth, respectively. Afterwards, it was separately washed with ethanol/water mixture and water in ultrasonic bath for 30 min.

#### 5.4.2. Initial Characterization by Cyclic Voltammetry

Before Pt deposition, the carbon-based materials prepared above were electrochemically cleaned to remove the adsorbed impurities on the electrode surface using cyclic voltammetry (CV) in the potential range of 0 – 1.2 V vs. RHE. at a scan rate of 200  $\text{mV s}^{-1}$  for 50 – 100 cycles in  $\text{N}_2$  saturated 0.5 M  $\text{H}_2\text{SO}_4$  (prepared by dilution from 98%  $\text{H}_2\text{SO}_4$ , Roth, Germany) or 0.1 M  $\text{HClO}_4$  aqueous solution ( $\text{HClO}_4$ , Roth, Germany) until the CVs did not change anymore, while Pt containing working electrodes were cleaned and activated in the potential range of 0.05-1.2 V vs. RHE.  $\text{Ag}|\text{AgCl}|\text{KCl}_{\text{sat}}$  electrode can be also employed as reference electrode, where the potential ranges of -0.2-1.0 V and -0.15-1.0 V vs.  $\text{Ag}|\text{AgCl}|\text{KCl}_{\text{sat}}$  were used for the prepared materials before and after Pt deposition, respectively.

After the above treatment, the double layer currents of electrodes without Pt and the hydrogen adsorption/desorption ( $H_{\text{ads/des}}$ ) of the electrodes containing Pt were monitored by CV at 100  $\text{mV s}^{-1}$  in a fresh  $\text{N}_2$ -saturated aqueous 0.5 M  $\text{H}_2\text{SO}_4$  or 0.1 M  $\text{HClO}_4$  solution. The hydrogen adsorption/desorption feature of Pt was used to calculate Pt-electrochemical surface area (ECSA). In the determination the average coulombic charge obtained by integrating the area under the  $H_{\text{ads/des}}$  peaks after subtracting the double layer charge [406, 356, 322] was used as shown in the following equations:

$$\text{ECSA} = \frac{A_{H(\text{des})}[\mu\text{A V}] + A_{H(\text{ads})}[\mu\text{A V}]}{2 \times 210 [\mu\text{C cm}^{-2}] \times L_{\text{Pt}} [\mu\text{g}] \times v [\mu\text{V s}^{-1}]} \quad (\text{Equation 5.5})$$

With  $A_{H(\text{ads/des})}$ : average integrated area under the  $H_{\text{ads}}$  and  $H_{\text{des}}$  peaks after subtracting the double layer charge;

210  $\mu\text{C cm}^{-2}$ : the required charge density to  $H_{\text{ads}}$  and  $H_{\text{des}}$  on surface of Pt;

$v$ : scan rate in the CV measurements;

$L_{\text{Pt}}$ : Pt loading on the electrode.

Additionally, ECSA can also be evaluated by  $\text{CO}_{\text{ad}}$  stripping voltammetry as shown in below paragraphs.

### 5.4.3. Carbon Monoxide Stripping Voltammetry

Carbon monoxide ( $\text{CO}_{\text{ad}}$ ) stripping voltammetry, namely oxidation of an adsorbed monolayer of CO on the surface of Pt was used to calculate the electrochemically active surface area and to evaluate the activation of OH species on the Pt surface. The 0.1 M  $\text{HClO}_4$  or 0.5 M  $\text{H}_2\text{SO}_4$  solution was purged with CO for 20 min to allow for CO adsorption on the Pt catalyst, subsequently followed by purging  $\text{N}_2$  for 20 minutes so that the dissolved CO was removed in the solution and only adsorbed CO on the Pt surface remained. The working electrode was held at 0.05 V during this procedure until the stripping voltammogram was recorded.  $\text{CO}_{\text{ad}}$  stripping voltammetry was recorded at a scan rate of  $20 \text{ mV s}^{-1}$  in the potential range from 0.05 to 1.1 V vs. RHE or from -0.15 to 0.9 V vs.  $\text{Ag|AgCl|KCl}_{\text{sat.}}$ .

The ECSA from  $\text{CO}_{\text{ad}}$  oxidation reaction was estimated from the coulombic charge obtained by integrating the area under the  $\text{CO}_{\text{ad}}$  oxidation peak after subtracting the double layer charge [277] using the following equation:

$$\text{ECSA} = \frac{A_{\text{CO}} [\mu\text{A V}]}{420 [\mu\text{C cm}^{-2}] \times L_{\text{Pt}} [\mu\text{g}] \times \nu [\mu\text{V s}^{-1}]} \quad (\text{Equation 5.6})$$

With  $A_{\text{CO}}$ : integrated area under the  $\text{CO}_{\text{ad}}$  oxidation peaks after subtracting the double layer charge;

$420 \mu\text{C cm}^{-2}$ : the required charge density to oxidize a monolayer of CO on surface of Pt;

$\nu$ : scan rate in the CV measurements;

$L_{\text{Pt}}$ : Pt loading on the electrode.

### 5.4.4. Oxygen Reduction Reaction

For the activity towards oxygen reduction reaction (ORR), linear sweep voltammetry (LSV) was performed in the 0.05 – 1.1 V vs. RHE or -0.15–0.9 V vs.  $\text{Ag|AgCl|KCl}_{\text{sat.}}$  potential range at a scan rate of  $5 \text{ mV s}^{-1}$  in  $\text{O}_2$  saturated  $\text{H}_2\text{SO}_4$  or  $\text{HClO}_4$  solution. Due to the double layer capacitance of the electrode surface, the results were normalized by the data carried out in  $\text{N}_2$  purged solution as reference measurements (baseline) in the same manner.

As described above, GC rods as well as integrated GC and CC served as working electrodes, respectively. GC rod can be used as a rotating disc electrode (RDE),

which was measured with three rotation speeds of 400, 900 and 1600 rpm, while integrated GC and CC could not serve as RDE and their ORR activities were measured without rotation speeds.

#### 5.4.5. Accelerated Stress Test

The catalysts durability towards an accelerated stress test was monitored by CV in O<sub>2</sub> saturated 0.5 M H<sub>2</sub>SO<sub>4</sub> or 0.1 M HClO<sub>4</sub> in the potential range of 0.05 – 1.2 V vs. RHE at 1000 mV s<sup>-1</sup> for 500 cycles followed by ORR activity measurement via the method mentioned above. Then N<sub>2</sub> was purged in the acid electrolyte for 30 min and the CVs were recorded again at 100 mV s<sup>-1</sup> for 3 cycles in comparison with the initial one. The measurement was repeated four times.

#### 5.4.6. Methanol Oxidation Reaction

The activity of the Pt containing electrodes for methanol oxidation reaction (MOR) was investigated by cyclic voltammetry at a low scan rate of 5 mV s<sup>-1</sup> in a N<sub>2</sub> purged 1 M CH<sub>3</sub>OH and 0.5 M H<sub>2</sub>SO<sub>4</sub> aqueous solution in the potential range of -0.2–1.0 V vs. Ag|AgCl|KCl<sub>sat.</sub>. A low scan rate was chosen due to the large double-layer capacity of the hierarchical composite electrode based on CNTs deposited GC and CC.

#### 5.4.7. Measurements of Multilayered Membrane Electrode Assembly

To monitor polarization behaviors and power densities the multilayered membrane electrode assemblies (MEAs) were prepared by the LBL method employing separate Pt-3D CNTs, Pt-primary CNTs and Pt-C with Pt deposited Polyaniline (Pt-PANI, prepared by workgroup of Prof. Dr. Christina Roth) as cathode.

#### Preparation of PANI Nanofibers and Pt-PANI

PANI nanofibers were prepared by oxidative polymerization [407]. 0.45 mL Aniline and 1.428 g ammonium peroxodisulfate (APS) were dissolved in 50 ml 0.4 M H<sub>2</sub>SO<sub>4</sub>, respectively. APS solution was added into the aniline solution under stirring at room temperature overnight. The prepared PANI was washed by filtration and MilliQ water until the pH value was neutral. The precipitate was green and was dried in vacuum at 80 °C.

The deposition of Pt nanoparticles onto the PANI was carried out by the method proposed by Guo *et al.* [408]. 290 mg PANI nanofibers were ultrasonicated in 25 mL MilliQ water followed by adding 165 mg  $\text{H}_2\text{PtCl}_6 \cdot 6 \text{H}_2\text{O}$ . The solution was stirred for 1 hour. Then 3 mL of formic acid were injected into the suspension, which was stirred at room temperature for 24 h. After filtration and washing, the Pt-PANI was dried under vacuum at 80 °C.

### **Preparation of Multilayer Membrane Electrode Assembly**

The preparation of the multilayer membrane electrode assembly (MEA) was carried out using the airbrushing method spraying catalyst ink onto the polymer exchange membranes (Nafion® 117) that were fixed at 100 °C in an upright spraying mask for an electrode area of 5 x 5 cm<sup>2</sup> to form a uniform catalyst film. For the multilayer (Figure S3.1.4a), Pt-PANI and Pt-3D CNTs inks were separately prepared. 100 mg Pt-PANI were homogenously ultrasonicated in 50 ml mixture aqueous solution of ethanol and water (1:1). The pH value of the suspension was adjusted to 2.6 by the addition of  $\text{H}_2\text{SO}_4$ . Meanwhile, the prepared 100 mg Pt-3D CNTs were suspended in the 50 ml ethanol/water solution and the pH value was adjusted to 12 by the addition of NaOH. Afterwards, 1 ml Pt-PANI ink was first sprayed onto the Nafion® membrane according to the method described above with zig-zagging spraying mode and was dried for 2–3 s. Then 1 ml Pt-3D CNTs ink was sprayed. This alternate coating manner was repeated until the inks ran out. For the opposite electrode, commercial 20% Pt/C (Alfa Aesar, platinum nominally 20 % on carbon black) was used. The 200 mg Pt/C was dispersed in 9 ml MilliQ water, 1 ml Nafion and 20 ml isopropanol by Ultra-Turrax (IKA 25 digital) to form the homogenous ink. The Pt/C ink was sprayed on the other side of Nafion® membrane using the same method. For a comparison, Pt-primary CNTs with Pt-PANI were assembled in the multilayered MEAs in the same manner.

### **Single Cell Testing**

The polarization curves of the MEAs were tested in a homemade single cell test bench via a Quickconnect® fixture (5 bar contact pressure) in  $\text{H}_2/\text{O}_2$  operation (FU Berlin, Germany). The MEAs were assembled between two gas diffusion layers (Freudenberg I3, Weinheim) and two graphitic gas flow plates. The Pt/C side as

anode and the LBL prepared side as cathode were prepared for MEAs. The cell temperature and the humidifier temperature were set to 70 °C and 80 °C, respectively. Meanwhile, 150 ml/min of hydrogen mixed with water was fed into anode and 80 ml/min of oxygen were injected into the cathode. As a reference, the MEA was tested using Pt/C as anode and cathode in the same measurement conditions.

#### 5.4.8. Capacitance Test

Capacitance test was carried out by CV and galvanostatic charge/discharge in 0.5 M H<sub>2</sub>SO<sub>4</sub> aqueous solution at room temperature. The CV curves were monitored at different scan rates of 5–100 mV s<sup>-1</sup>. Galvanostatic charge/discharge was measured via chronopotentiometry in a voltage range of -0.2–1.0 V vs. Ag|AgCl|KCl<sub>sat.</sub> at 5 mA cm<sup>-2</sup>, 10 mA cm<sup>-2</sup>, 20 mA cm<sup>-2</sup> and 30 mA cm<sup>-2</sup> of current density, respectively. Capacitance was estimated by CV and charge/discharge curves according to the following equations, respectively:

$$C = \frac{1}{2 \times v \times \Delta V} \int I_{(V)} dV \quad (\text{Equation 5.7})$$

$$C = \frac{i}{2dV/dt} \quad (\text{Equation 5.8})$$

Here, C is capacitance (F), v is scan rate in the CV measurements (mV s<sup>-1</sup>), ΔV is the potential window (1.2 V), ∫I<sub>(V)</sub>dV is integrated area of CV curve, i is the discharge current (A) and dV/dt is the slope of the discharge curve.

#### 5.4.9. Electrochemical Impedance Spectroscopy

Electrochemical impedance spectroscopy (EIS) was performed with the above mentioned Gamry potentiostat PGI 4, which was recorded at open circuit potential with 5 mV AC voltage amplitude in the frequency range from 10<sup>5</sup> to 0.01 Hz in 0.5 M H<sub>2</sub>SO<sub>4</sub> aqueous solution.



# Chapter 6:

## References

---

1. <https://www.who.int/airpollution/en/>.
2. Karagulian, F.; Belis, C. A.; Dora, C. F. C.; Prüss-Ustün, A. M.; Bonjour, S.; Adair-Rohani, H.; Amann, M. *Atmos. Environ.* **2015**, *120*, 475–483. doi:10.1016/j.atmosenv.2015.08.087
3. Samoli, E.; Peng, R.; Ramsay, T.; Pipikou, M.; Touloumi, G.; Dominici, F.; Burnett, R.; Cohen, A.; Krewski, D.; Samet, J. *Environ. Health Perspect.* **2008**, *116* (11), 1480–1486.
4. Anderson, J. O.; Thundiyil, J. G.; Stolbach, A. *J. Med. Toxicol.* **2012**, *8* (2), 166–175. doi:10.1007/s13181-011-0203-1
5. Meinshausen, M.; Meinshausen, N.; Hare, W.; Raper, S. C. B.; Frieler, K.; Knutti, R.; Frame, D. J.; Allen, M. R. *Nature* **2009**, *458* (7242), 1158–1162. doi:10.1038/nature08017
6. Malik, A.; Lan, J.; Lenzen, M. *Environ. Sci. Technol.* **2016**, *50* (9), 4722–4730. doi:10.1021/acs.est.5b06162
7. Liu, D.; Guo, X.; Xiao, B. *Sci. Total Environ.* **2019**, *661*, 750–766. doi:10.1016/j.scitotenv.2019.01.197
8. Ritchie, H.; Roser, M. Renewable energy; *Our World in Data* **2017**.
9. Quaschnig, V. *Understanding renewable energy systems*; Routledge, **2016**.
10. Hosseini, S. E.; Wahid, M. A. *Renew. Sustain. Energy Rev.* **2016**, *57*, 850–866. doi:10.1016/j.rser.2015.12.112
11. Singh, S.; Jain, S.; PS, V.; Tiwari, A. K.; Nouni, M. R.; Pandey, J. K.; Goel, S. *Renew. Sustain. Energy Rev.* **2015**, *51*, 623–633. doi:10.1016/j.rser.2015.06.040
12. Lubitz, W.; Tumas, W. *Chem. Rev.* **2007**, *107* (10), 3900–3903. doi:10.1021/cr050200z
13. Toyota DE, <https://www.toyota.de/automobile/mirai/>, Toyota Mirai, **2020**.
14. Hyundai DE, <https://www.hyundai.de/modelle/nexo/>, Hyundai NEXO, **2020**.
15. Honda DE, <https://www.honda.de/cars/world-of-honda/news-events/2019-08-08-honda-uebergibt-brennstoffzellenfahrzeug.html>, **2020**.
16. Staffell, I.; Scamman, D.; Velazquez Abad, A.; Balcombe, P.; Dodds, P. E.; Ekins, P.; Shah, N.; Ward, K. R. *Energy Environ. Sci.* **2019**, *12* (2), 463–491. doi:10.1039/C8EE01157E

17. Hasche, F.; Oezaslan, M.; Strasser, P. *Phys. Chem. Chem. Phys.* **2010**, *12* (46), 15251–15258. doi:10.1039/c0cp00609b
18. Zhao, Z.; Castanheira, L.; Dubau, L.; Berthomé, G.; Crisci, A.; Maillard, F. *J. Power Sources* **2013**, *230*, 236–243. doi:10.1016/j.jpowsour.2012.12.053
19. Yu, X.; Ye, S. *J. Power Sources* **2007**, *172* (1), 145–154. doi:10.1016/j.jpowsour.2007.07.048
20. Greene, D. L.; Ogden, J. M.; Lin, Z. *eTransportation* **2020**, *6*, 100086. doi:10.1016/j.etrans.2020.100086
21. Peighambardoust, S. J.; Rowshanzamir, S.; Amjadi, M. *Int. J. Hydrogen Energy* **2010**, *35* (17), 9349–9384. doi:10.1016/j.ijhydene.2010.05.017
22. Bakangura, E.; Wu, L.; Ge, L.; Yang, Z.; Xu, T. *Prog. Polym. Sci.* **2016**, *57*, 103–152. doi:10.1016/j.progpolymsci.2015.11.004
23. Munjewar, S. S.; Thombre, S. B.; Mallick, R. K. *Ionics* **2017**, *23* (1), 1–18. doi:10.1007/s11581-016-1864-1
24. Munjewar, S. S.; Thombre, S. B.; Mallick, R. K. *Renew. Sustain. Energy Rev.* **2017**, *67*, 1087–1104. doi:10.1016/j.rser.2016.09.002
25. Mehmood, A.; Scibioh, M.A.; Prabhuram, J.; An, M.-G.; Ha, H. Y. *J. Power Sources* **2015**, *297*, 224–241. doi:10.1016/j.jpowsour.2015.07.094
26. Weber, A. Z.; Borup, R. L.; Darling, R. M.; Das, P. K.; Dursch, T. J.; Gu, W.; Harvey, D.; Kusoglu, A.; Litster, S.; Mench, M. M. *J. Electrochem. Soc.* **2014**, *161* (12), F1254.
27. Ramani, V.; Kunz, H. R.; Fenton, J. M. *Interface* **2004**, *13* (3), 17–19.
28. EG&G Technical Services, Inc. *Fuel Cell Handbook (Seventh Edition)*, **2004**.
29. Bednarek, T.; Tsotridis, G. *J. Power Sources* **2017**, *343*, 550–563. doi:10.1016/j.jpowsour.2017.01.059
30. Wu, J.; Yuan, X. Z.; Wang, H.; Blanco, M.; Martin, J. J.; Zhang, J. *Int. J. Hydrogen Energy* **2008**, *33* (6), 1735–1746. doi:10.1016/j.ijhydene.2008.01.013
31. Barbir, F. *PEM fuel cells: Theory and Practice 2nd ed.*, 2nd ed.; Elsevier: USA, **2012**.
32. Stacy, J.; Regmi, Y. N.; Leonard, B.; Fan, M. *Renew. Sustain. Energy Rev.* **2017**, *69*, 401–414. doi:10.1016/j.rser.2016.09.135
33. Moura, A.; Fajín, J.; Mandado, M.; Cordeiro, M. *Catalysts* **2017**, *7* (12), 47. doi:10.3390/catal7020047
34. Ramli, Z. A. C.; Kamarudin, S. K. *Nanoscale research letters* **2018**, *13* (1), 410. doi:10.1186/s11671-018-2799-4
35. Sui, S.; Wang, X.; Zhou, X.; Su, Y.; Riffat, S.; Liu, C.-j. *J. Mater. Chem. A* **2017**, *5* (5), 1808–1825. doi:10.1039/C6TA08580F
36. Antolini, E. *Energies* **2017**, *10* (1), 42. doi:10.3390/en10010042
37. Sharma, R.; Andersen, S. M. *Appl. Catal. B: Environ.* **2018**, *239*, 636–643. doi:10.1016/j.apcatb.2018.08.045



- 
38. Liu, J.; Liu, C.-T.; Zhao, L.; Zhang, J.-J.; Zhang, L.-M.; Wang, Z.-B. *Int. J. Hydrogen Energy* **2016**, *41* (3), 1859–1870. doi:10.1016/j.ijhydene.2015.11.103
39. Mezalira, D. Z.; Bron, M. *J. Power Sources* **2013**, *231*, 113–121. doi:10.1016/j.jpowsour.2012.12.025
40. Chen, Z.; Higgins, D.; Tao, H.; Hsu, R. S.; Chen, Z. *J. Phys. Chem. C* **2009**, *113* (49), 21008–21013. doi:10.1021/jp908067v
41. Higgins, D. C.; Meza, D.; Chen, Z. *J. Phys. Chem. C* **2010**, *114* (50), 21982–21988. doi:10.1021/jp106814j
42. Neyerlin, K. C.; Srivastava, R.; Yu, C.; Strasser, P. *J. Power Sources* **2009**, *186* (2), 261–267. doi:10.1016/j.jpowsour.2008.10.062
43. Shahgaldi, S.; Hamelin, J. *Carbon* **2015**, *94*, 705–728. doi:10.1016/j.carbon.2015.07.055
44. Daş, E.; Yurtcan, A. B. *Int. J. Hydrogen Energy* **2016**, *41* (30), 13171–13179. doi:10.1016/j.ijhydene.2016.05.167
45. Wang, H.; Kakade, B. A.; Tamaki, T.; Yamaguchi, T. *J. Power Sources* **2014**, *260*, 338–348. doi:10.1016/j.jpowsour.2014.03.014
46. Hsieh, C.-T.; Lin, J.-Y.; Chou, Y.-W. *Chem. Phys. Lett.* **2007**, *444* (1-3), 149–154. doi:10.1016/j.cplett.2007.07.001
47. Kundu, S.; Nagaiah, T. C.; Chen, X.; Xia, W.; Bron, M.; Schuhmann, W.; Muhler, M. *Carbon* **2012**, *50* (12), 4534–4542. doi:10.1016/j.carbon.2012.05.037
48. Hoogers, G., Ed. *Fuel cell technology handbook*, 2nd ed.; CRC: Boca Raton, Fla., **2013**.
49. O'Hayre, R.; Cha, S.-W.; Colella, W.; Prinz, F. B. *Fuel cell fundamentals*; John Wiley & Sons, **2016**.
50. Liu, H.; Zhang, J. *Electrocatalysis of direct methanol fuel cells: from fundamentals to applications*; Wiley-VCH, **2009**.
51. Zhang, J. *PEM Fuel Cell Electrocatalysts and Catalyst Layer*; Springer: London, **2008**.
52. Bossel, U. *The birth of the fuel cell*, **1835-1845**.
53. Grove, W. R. *Philos. Mag. J. Sci.* **1842**, *21* (140), 417–420.
54. Grove, W. R. *Philos. Mag. J. Sci.* **1839**, *14* (86-87), 127–130.
55. Mehta, V.; Cooper, J. S. *J. Power Sources* **2003**, *114* (1), 32–53. doi:10.1016/S0378-7753(02)00542-6
56. Song, Y.; Zhang, C.; Ling, C.-Y.; Han, M.; Yong, R.-Y.; Sun, D.; Chen, J. *Int. J. Hydrogen Energy* **2020**, *45* (54), 29832–29847. doi:10.1016/j.ijhydene.2019.07.231
57. Husby, H.; Kongstein, O. E.; Oedegaard, A.; Seland, F. *Int. J. Hydrogen Energy* **2014**, *39* (2), 951–957. doi:10.1016/j.ijhydene.2013.10.115
58. Hu, Q.; Zhang, D.; Fu, H.; Huang, K. *Int. J. Hydrogen Energy* **2014**, *39* (25), 13770–13776. doi:10.1016/j.ijhydene.2014.01.201

## References

---

59. Markovic, N. *Surface Sci. Rep.* **2002**, *45* (4-6), 117–229. doi:10.1016/S0167-5729(01)00022-X
60. Wroblowa, H. S.; Yen-Chi-Pan; Razumney, G. *J. Electroanal. Chem. Interfacial Electrochem.* **1976**, *69* (2), 195–201. doi:10.1016/S0022-0728(76)80250-1
61. Sha, Y.; Yu, T. H.; Merinov, B. V.; Shirvanian, P.; Goddard, W. A. *J. Phys. Chem. Lett.* **2011**, *2* (6), 572–576. doi:10.1021/jz101753e
62. Yeager, E. *J. Mol. Catal.* **1986**, *38* (1-2), 5–25. doi:10.1016/0304-5102(86)87045-6
63. Nørskov, J. K.; Rossmeisl, J.; Logadottir, A.; Lindqvist, L.; Kitchin, J. R.; Bligaard, T.; Jónsson, H. *J. Phys. Chem. B* **2004**, *108* (46), 17886–17892. doi:10.1021/jp047349j
64. Lim, D.-H.; Wilcox, J. *J. Phys. Chem. C* **2012**, *116* (5), 3653–3660. doi:10.1021/jp210796e
65. Feliu, J. M.; Fernandez-Vega, A.; Aldaz, A.; Clavilier, J. *J. Electroanal. Chem. Interfacial Electrochem.* **1988**, *256* (1), 149–163. doi:10.1016/0022-0728(88)85014-9
66. Greeley, J.; Mavrikakis, M. *J. Am. Chem. Soc.* **2002**, *124* (24), 7193–7201. doi:10.1021/ja017818k
67. Greeley, J.; Mavrikakis, M. *J. Am. Chem. Soc.* **2004**, *126* (12), 3910–3919. doi:10.1021/ja037700z
68. Cao, D.; Lu, G.-Q.; Wieckowski, A.; Wasileski, S. A.; Neurock, M. *J. Phys. Chem. B* **2005**, *109* (23), 11622–11633. doi:10.1021/jp0501188
69. Breiter, M. W. *Electrochim. Acta* **1963**, *8* (12), 973–983. doi:10.1016/0013-4686(62)87051-0
70. Ferrin, P.; Nilekar, A. U.; Greeley, J.; Mavrikakis, M.; Rossmeisl, J. *Surf. Sci.* **2008**, *602* (21), 3424–3431. doi:10.1016/j.susc.2008.08.011
71. Liu, S. X.; Liao, L. W.; Tao, Q.; Chen, Y. X.; Ye, S. *Phys. Chem. Chem. Phys.* **2011**, *13* (20), 9725–9735. doi:10.1039/c0cp01728k
72. Lu, G.-Q.; Chrzanowski, W.; Wieckowski, A. *J. Phys. Chem. B* **2000**, *104* (23), 5566–5572. doi:10.1021/jp000193c
73. Tritsarlis, G. A.; Rossmeisl, J. *J. Phys. Chem. C* **2012**, *116* (22), 11980–11986. doi:10.1021/jp209506d
74. Neurock, M.; Janik, M.; Wieckowski, A. *Faraday Discuss.* **2009**, *140* (18), 363–378. doi:10.1039/B804591G
75. Housmans, T. H. M.; Koper, M. T. M. *J. Phys. Chem. B.* **2003**, *107* (33), 8557–8567. doi:10.1021/jp034291k
76. Lai, S. C. S.; Lebedeva, N. P.; Housmans, T. H. M.; Koper, M. T. M. *Top. Catal.* **2007**, *46* (3), 320–333. doi:10.1007/s11244-007-9010-y
77. Hamnett, A. *Catalysis Today* **1997**, *38* (4), 445–457. doi:10.1016/S0920-5861(97)00054-0
78. Iwasita, T. *Electrochim. Acta* **2002**, *47* (22-23), 3663–3674. doi:10.1016/S0013-4686(02)00336-5

- 
79. Herrero, E.; Chrzanowski, W.; Wieckowski, A. *J. Phys. Chem.* **1995**, *99* (25), 10423–10424. doi:10.1021/j100025a054
80. Jusys, Z.; Kaiser, J.; Behm, R. J. *Langmuir* **2003**, *19* (17), 6759–6769. doi:10.1021/la020932b
81. Housmans, T. H. M.; Wonders, A. H.; Koper, M. T. M. *J. Phys. Chem. B* **2006**, *110* (20), 10021–10031. doi:10.1021/jp055949s
82. Cohen, J. L.; Volpe, D. J.; Abruña, H. D. *Phys. Chem. Chem. Phys.* **2007**, *9* (1), 49–77. doi:10.1039/b612040g
83. Lin, Y.; Cui, X.; Yen, C.; Wai, C. M. *J. Phys. Chem. B* **2005**, *109* (30), 14410–14415. doi:10.1021/jp0514675
84. Guo, S.; Zhang, S.; Sun, S. *Angew. Chem. Int. Ed.* **2013**, *52* (33), 8526–8544. doi:10.1002/anie.201207186
85. Nie, Y.; Li, L.; Wei, Z. *Chem. Soc. Rev.* **2015**, *44* (8), 2168–2201. doi:10.1039/C4CS00484A
86. Gasteiger, H. A.; Kocha, S. S.; Sompalli, B.; Wagner, F. T. *Appl. Catal. B* **2005**, *56* (1–2), 9–35. doi:10.1016/j.apcatb.2004.06.021
87. Nørskov, J. K.; Bligaard, T.; Logadottir, A.; Kitchin, J. R.; Chen, J. G.; Pandelov, S.; Stimming, U. *J. Electrochem. Soc.* **2005**, *152* (3), J23. doi:10.1149/1.1856988
88. Seh, Z. W.; Kibsgaard, J.; Dickens, C. F.; Chorkendorff, I.; Nørskov, J. K.; Jaramillo, T. F. *Science (New York)* **2017**, *355* (6321). doi:10.1126/science.aad4998
89. Skúlason, E.; Tripkovic, V.; Björketun, M. E.; Gudmundsdóttir, S.; Karlberg, G.; Rossmeisl, J.; Bligaard, T.; Jónsson, H.; Nørskov, J. K. *J. Phys. Chem. C* **2010**, *114* (42), 18182–18197. doi:10.1021/jp1048887
90. Gasteiger, H. A.; Gu, W.; Makharia, R.; Mathias, M. F.; Sompalli, B. *Beginning-of-life MEA performance — efficiency loss contributions*, **2010**.
91. Sheng, W.; Gasteiger, H. A.; Shao-Horn, Y. *J. Electrochem. Soc.* **2010**, *157* (11), B1529. doi:10.1149/1.3483106
92. Neyerlin, K. C.; Gu, W.; Jorne, J.; Gasteiger, H. A. *J. Electrochem. Soc.* **2007**, *154* (7), B631. doi:10.1149/1.2733987
93. Chen, S.; Kucernak, A. *J. Phys. Chem. B* **2004**, *108* (37), 13984–13994. doi:10.1021/jp048641u
94. Appleby, A. J.; Chemla, M.; Kita, H.; Bronoel, G. *Encyclopedia of Electrochemistry of the Elements; Bard, A. J. Eds, Marcel Dekker, New York* **1982**, *9* (Part A), 383.
95. Durst, J.; Simon, C.; Hasché, F.; Gasteiger, H. A. *J. Electrochem. Soc.* **2014**, *162* (1), F190.
96. Gasteiger, H. A.; Panels, J. E.; Yan, S. G. *J. Power Sources* **2004**, *127* (1), 162–171. doi:10.1016/j.jpowsour.2003.09.013
97. Vojvodic, A.; Nørskov, J. K. *Nat. Sci. Rev.* **2015**, *2* (2), 140–149. doi:10.1093/nsr/nwv023

98. Pedersen, C. M.; Escudero-Escribano, M.; Velázquez-Palenzuela, A.; Christensen, L. H.; Chorkendorff, I.; Stephens, I. E. L. *Electrochim. Acta* **2015**, *179*, 647–657. doi:10.1016/j.electacta.2015.03.176
99. Viswanathan, V.; Hansen, H. A.; Rossmeisl, J.; Nørskov, J. K. *ACS Catal.* **2012**, *2* (8), 1654–1660. doi:10.1021/cs300227s
100. Wang, J. X.; Markovic, N. M.; Adzic, R. R. *J. Phys. Chem. B* **2004**, *108* (13), 4127–4133. doi:10.1021/jp037593v
101. Marković, N. M.; Adžić, R. R.; Cahan, B. D.; Yeager, E. B. *J. Electroanal. Chem.* **1994**, *377* (1-2), 249–259. doi:10.1016/0022-0728(94)03467-2
102. Zhang, L.; Roling, L. T.; Wang, X.; Vara, M.; Chi, M.; Liu, J.; Choi, S.-I.; Park, J.; Herron, J. A.; Xie, Z.; Mavrikakis, M.; Xia, Y. *Science (New York)* **2015**, *349* (6246), 412–416. doi:10.1126/science.aab0801
103. Chen, Z.; Waje, M.; Li, W.; Yan, Y. *Angew. Chem. (Int. Ed. Engl.)* **2007**, *46* (22), 4060–4063. doi:10.1002/anie.200700894
104. Wang, C.; Daimon, H.; Lee, Y.; Kim, J.; Sun, S. *J. Am. Chem. Soc.* **2007**, *129* (22), 6974–6975. doi:10.1021/ja070440r
105. Lim, B.; Jiang, M.; Camargo, P. H. C.; Cho, E. C.; Tao, J.; Lu, X.; Zhu, Y.; Xia, Y. *Science (New York)* **2009**, *324* (5932), 1302–1305. doi:10.1126/science.1170377
106. Cui, C.; Gan, L.; Heggen, M.; Rudi, S.; Strasser, P. *Nat. Mater.* **2013**, *12* (8), 765–771. doi:10.1038/nmat3668
107. Bing, Y.; Liu, H.; Zhang, L.; Ghosh, D.; Zhang, J. *Chem. Soc. Rev.* **2010**, *39* (6), 2184–2202. doi:10.1039/b912552c
108. Huang, X.; Zhao, Z.; Cao, L.; Chen, Y.; Zhu, E.; Lin, Z.; Li, M.; Yan, A.; Zettl, A.; Wang, Y. M.; Duan, X.; Mueller, T.; Huang, Y. *Science (New York)* **2015**, *348* (6240), 1230–1234. doi:10.1126/science.aaa8765
109. Escudero-Escribano, M.; Verdaguer-Casadevall, A.; Malacrida, P.; Grønbjerg, U.; Knudsen, B. P.; Jepsen, A. K.; Rossmeisl, J.; Stephens, I. E. L.; Chorkendorff, I. *J. Am. Chem. Soc.* **2012**, *134* (40), 16476–16479. doi:10.1021/ja306348d
110. Greeley, J.; Stephens, I. E. L.; Bondarenko, A. S.; Johansson, T. P.; Hansen, H. A.; Jaramillo, T. F.; Rossmeisl, J.; Chorkendorff, I.; Nørskov, J. K. *Nature Chemistry* **2009**, *1*, 552 EP -. doi:10.1038/nchem.367
111. Hernandez-Fernandez, P.; Masini, F.; McCarthy, D. N.; Strebel, C. E.; Friebel, D.; Deiana, D.; Malacrida, P.; Nierhoff, A.; Bodin, A.; Wise, A. M.; Nielsen, J. H.; Hansen, T. W.; Nilsson, A.; Stephens, I. E. L.; Chorkendorff, I. *Nature Chemistry* **2014**, *6*, 732 EP -. doi:10.1038/nchem.2001
112. Velázquez-Palenzuela, A.; Masini, F.; Pedersen, A. F.; Escudero-Escribano, M.; Deiana, D.; Malacrida, P.; Hansen, T. W.; Friebel, D.; Nilsson, A.; Stephens, I. E. L.; Chorkendorff, I. *J. Catal.* **2015**, *328*, 297–307. doi:10.1016/j.jcat.2014.12.012
113. Escudero-Escribano, M.; Malacrida, P.; Hansen, M. H.; Vej-Hansen, U. G.; Velázquez-Palenzuela, A.; Tripkovic, V.; Schiøtz, J.; Rossmeisl, J.; Stephens, I. E. L.;

- Chorkendorff, I. *Science (New York)* **2016**, *352* (6281), 73–76. doi:10.1126/science.aad8892
114. Kulp, C.; Gillmeister, K.; Widdra, W.; Bron, M. *ChemPhyChem* **2013**, *14* (6), 1205–1210. doi:10.1002/cphc.201200891
115. Oezaslan, M.; Hasché, F.; Strasser, P. *J. Phys. Chem. Lett.* **2013**, *4* (19), 3273–3291. doi:10.1021/jz4014135
116. Mamtani, K.; Ozkan, U. S. *Catal. Lett.* **2015**, *145* (1), 436–450. doi:10.1007/s10562-014-1434-y
117. Zhou, X.; Qiao, J.; Yang, L.; Zhang, J. *Adv. Energy Mater.* **2014**, *4* (8), 1301523. doi:10.1002/aenm.201301523
118. Hu, C.; Dai, L. *Angew. Chem. Int. Ed.* **2016**, *55* (39), 11736–11758. doi:10.1002/anie.201509982
119. Masa, J.; Xia, W.; Muhler, M.; Schuhmann, W. *Angewandte Chemie (International ed. in English)* **2015**, *54* (35), 10102–10120. doi:10.1002/anie.201500569
120. Tian, J.; Morozan, A.; Sougrati, M. T.; Lefèvre, M.; Chenitz, R.; Dodelet, J.-P.; Jones, D.; Jaouen, F. *Angew. Chemie (International ed. in English)* **2013**, *52* (27), 6867–6870. doi:10.1002/anie.201303025
121. Li, J.; Ghoshal, S.; Liang, W.; Sougrati, M.-T.; Jaouen, F.; Halevi, B.; McKinney, S.; McCool, G.; Ma, C.; Yuan, X.; Ma, Z.-F.; Mukerjee, S.; Jia, Q. *Energy Environ. Sci.* **2016**, *9* (7), 2418–2432. doi:10.1039/C6EE01160H
122. Serov, A.; Workman, M. J.; Artyushkova, K.; Atanassov, P.; McCool, G.; McKinney, S.; Romero, H.; Halevi, B.; Stephenson, T. *J. Power Sources* **2016**, *327*, 557–564. doi:10.1016/j.jpowsour.2016.07.087
123. Wu, G.; Zelenay, P. *Acc. Chem. Res.* **2013**, *46* (8), 1878–1889. doi:10.1021/ar400011z
124. Chung, H. T.; Cullen, D. A.; Higgins, D.; Sneed, B. T.; Holby, E. F.; More, K. L.; Zelenay, P. *Science (New York)* **2017**, *357* (6350), 479–484. doi:10.1126/science.aan2255
125. Liu, H.; Song, C.; Zhang, L.; Zhang, J.; Wang, H.; Wilkinson, D. P. *J. Power Sources* **2006**, *155* (2), 95–110. doi:10.1016/j.jpowsour.2006.01.030
126. Yang, L.; Ge, J.; Liu, C.; Wang, G.; Xing, W. *Curr. Opin. Electrochem.* **2017**, *4* (1), 83–88. doi:10.1016/j.coelec.2017.10.018
127. Gurau, B.; Viswanathan, R.; Liu, R.; Lafrenz, T. J.; Ley, K. L.; Smotkin, E. S.; Reddington, E.; Sapienza, A.; Chan, B. C.; Mallouk, T. E.; Sarangapani, S. *J. Phys. Chem. B* **1998**, *102* (49), 9997–10003. doi:10.1021/jp982887f
128. Zhao, X.; Yin, M.; Ma, L.; Liang, L.; Liu, C.; Liao, J.; Lu, T.; Xing, W. *Energy Environ. Sci.* **2011**, *4* (8), 2736. doi:10.1039/c1ee01307f
129. Koper, M. T. M.; Shubina, T. E.; van Santen, R. A. *J. Phys. Chem. B* **2002**, *106* (3), 686–692. doi:10.1021/jp0134188

## References

---

130. Lu, S.; Li, H.; Sun, J.; Zhuang, Z. *Nano Res.* **2018**, *11* (4), 2058–2068. doi:10.1007/s12274-017-1822-x
131. Xia, B. Y.; Wu, H. B.; Li, N.; Yan, Y.; Lou, X. W.; Wang, X. *Angew. Chem. Int. Ed.* **2015**, *54* (12), 3797–3801. doi:10.1002/anie.201411544
132. Davies, J. C.; Hayden, B. E.; Pegg, D. J. *Surf. Sci.* **2000**, *467* (1), 118–130. doi:10.1016/S0039-6028(00)00743-3
133. Roth, C.; Benker, N.; Buhrmester, T.; Mazurek, M.; Loster, M.; Fuess, H.; Koningsberger, D. C.; Ramaker, D. E. *J. Am. Chem. Soc.* **2005**, *127* (42), 14607–14615. doi:10.1021/ja050139f
134. Watanabe, M.; Motoo, S. *J. Electroanal. Chem.* **1975**, *60* (3), 267–273. doi:10.1016/S0022-0728(75)80261-0
135. Sriphathoorat, R.; Wang, K.; Luo, S.; Tang, M.; Du, H.; Du, X.; Shen, P. K. *J. Mater. Chem. A* **2016**, *4* (46), 18015–18021. doi:10.1039/C6TA07370K
136. Sun, J.; Ma, H.; Jiang, H.; Dang, L.; Lu, Q.; Gao, F. *J. Mater. Chem. A* **2015**, *3* (31), 15882–15888. doi:10.1039/C5TA01613D
137. Zhao, X.; Zhang, J.; Wang, L.; Li, H. X.; Liu, Z.; Chen, W. *ACS Appl. Mater. Interfaces* **2015**, *7* (47), 26333–26339. doi:10.1021/acsami.5b09357
138. He, Q.; Shyam, B.; Nishijima, M.; Yang, X.; Koel, B.; Ernst, F.; Ramaker, D.; Mukerjee, S. *J. Phys. Chem. C* **2013**, *117* (3), 1457–1467. doi:10.1021/jp308133q
139. Li, Y.; Liu, C.; Liu, Y.; Feng, B.; Li, L.; Pan, H.; Kellogg, W.; Higgins, D.; Wu, G. *J. Power Sources* **2015**, *286*, 354–361. doi:10.1016/j.jpowsour.2015.03.155
140. Du, W.; Yang, G.; Wong, E.; Deskins, N. A.; Frenkel, A. I.; Su, D.; Teng, X. *J. Am. Chem. Soc.* **2014**, *136* (31), 10862–10865. doi:10.1021/ja505456w
141. Guo, D.-J.; Jing, Z.-H. *J. Power Sources* **2010**, *195* (12), 3802–3805. doi:10.1016/j.jpowsour.2009.12.115
142. Anitha, V. C.; Zazpe, R.; Krbal, M.; Yoo, J.; Sopha, H.; Prikryl, J.; Cha, G.; Slang, S.; Schmuki, P.; Macak, J. M. *J. Catal.* **2018**, *365*, 86–93. doi:10.1016/j.jcat.2018.06.017
143. Huang, W.; Wang, H.; Zhou, J.; Wang, J.; Duchesne, P. N.; Muir, D.; Zhang, P.; Han, N.; Zhao, F.; Zeng, M.; Zhong, J.; Jin, C.; Li, Y.; Lee, S.-T.; Dai, H. *Nat. commun.* **2015**, *6*, 10035 EP -. doi:10.1038/ncomms10035
144. Tang, M.; Luo, S.; Wang, K.; Du, H.; Sriphathoorat, R.; Shen, P. *Nano Res.* **2018**, *11* (9), 4786–4795. doi:10.1007/s12274-018-2063-3
145. Xue, S.; Deng, W.; Yang, F.; Yang, J.; Amiin, I. S.; He, D.; Tang, H.; Mu, S. *ACS Catal.* **2018**, *8* (8), 7578–7584. doi:10.1021/acscatal.8b00366
146. Fu, G.; Liu, H.; You, N.; Wu, J.; Sun, D.; Xu, L.; Tang, Y.; Chen, Y. *Nano Res.* **2016**, *9* (3), 755–765. doi:10.1007/s12274-015-0954-0
147. Dhavale, V. M.; Kurungot, S. *ACS Catal.* **2015**, *5* (3), 1445–1452. doi:10.1021/cs501571e

- 
148. Wang, Y.; Chen, Y.; Nan, C.; Li, L.; Wang, D.; Peng, Q.; Li, Y. *Nano Res.* **2015**, *8* (1), 140–155. doi:10.1007/s12274-014-0603-z
149. Liu, X.; Wang, W.; Li, H.; Li, L.; Zhou, G.; Yu, R.; Wang, D.; Li, Y. *Sci. Rep.* **2013**, *3*, 1404. doi:10.1038/srep01404
150. Wang, K.; Sriphathoorat, R.; Luo, S.; Tang, M.; Du, H.; Shen, P. K. *J. Mater. Chem. A* **2016**, *4* (35), 13425–13430. doi:10.1039/C6TA05230D
151. Antolini, E. *Appl. Catal. B: Environ.* **2009**, *88* (1), 1–24. doi:10.1016/j.apcatb.2008.09.030
152. Uchida, M.; Aoyama, Y.; Tanabe, M.; Yanagihara, N.; Eda, N.; Ohta, A. *J. Electrochem. Soc.* **1995**, *142* (8), 2572–2576. doi:10.1149/1.2050055
153. Sharma, S.; Pollet, B. G. *J. Power Sources* **2012**, *208*, 96–119. doi:10.1016/j.jpowsour.2012.02.011
154. Huang, H.; Wang, X. *J. Mater. Chem. A* **2014**, *2* (18), 6266. doi:10.1039/c3ta14754a
155. Zhang, J.; Yi, X.-b.; Liu, S.; Fan, H.-L.; Ju, W.; Wang, Q.-C.; Ma, J. *J. Phys. Chem. Solids* **2017**, *102*, 99–104. doi:10.1016/j.jpcs.2016.11.006
156. Zhang, J.-J.; Wang, Z.-B.; Li, C.; Zhao, L.; Liu, J.; Zhang, L.-M.; Gu, D.-M. *J. Power Sources* **2015**, *289*, 63–70. doi:10.1016/j.jpowsour.2015.04.150
157. Yola, M. L.; Eren, T.; Atar, N.; Saral, H.; Ermiş, İ. *Electroanalysis* **2016**, *28* (3), 570–579. doi:10.1002/elan.201500381
158. Bong, S.; Kim, Y.-R.; Kim, I.; Woo, S.; Uhm, S.; Lee, J.; Kim, H. *Electrochem. Commun.* **2010**, *12* (1), 129–131. doi:10.1016/j.elecom.2009.11.005
159. Li, Y.; Tang, L.; Li, J. *Electrochem. Commun.* **2009**, *11* (4), 846–849. doi:10.1016/j.elecom.2009.02.009
160. Jehng, J.-M.; Liu, W.-J.; Pan, T.-C.; Dai, Y.-M. *Appl. Surf. Sci.* **2013**, *268*, 425–431. doi:10.1016/j.apsusc.2012.12.115
161. Li, Y.; Gao, W.; Ci, L.; Wang, C.; Ajayan, P. M. *Carbon* **2010**, *48* (4), 1124–1130. doi:10.1016/j.carbon.2009.11.034
162. Qian, W.; Hao, R.; Zhou, J.; Eastman, M.; Manhat, B. A.; Sun, Q.; Goforth, A. M.; Jiao, J. *Carbon* **2013**, *52*, 595–604. doi:10.1016/j.carbon.2012.10.031
163. Dong, L.; Gari, R. R. S.; Li, Z.; Craig, M. M.; Hou, S. *Carbon* **2010**, *48* (3), 781–787. doi:10.1016/j.carbon.2009.10.027
164. Zhu, C.; Liu, D.; Chen, Z.; Li, L.; You, T. *J. Colloid Interface Sci.* **2018**, *511*, 77–83. doi:10.1016/j.jcis.2017.09.109
165. Zhang, C.; Xu, L.; Shan, N.; Sun, T.; Chen, J.; Yan, Y. *ACS Catal.* **2014**, *4* (6), 1926–1930. doi:10.1021/cs500107t
166. Chetty, R.; Kundu, S.; Xia, W.; Bron, M.; Schuhmann, W.; Chirila, V.; Brandl, W.; Reinecke, T.; Muhler, M. *Electrochim. Acta* **2009**, *54* (17), 4208–4215. doi:10.1016/j.electacta.2009.02.073

## References

---

167. Yue, B.; Ma, Y.; Tao, H.; Yu, L.; Jian, G.; Wang, X.; Wang, X.; Lu, Y.; Hu, Z. *J. Mater. Chem.* **2008**, *18* (15), 1747. doi:10.1039/b718283j
168. Higgins, D.; Zamani, P.; Yu, A.; Chen, Z. *Energy Environ. Sci.* **2016**, *9* (2), 357–390. doi:10.1039/C5EE02474A
169. Chen, S.; Wei, Z.; Guo, L.; Ding, W.; Dong, L.; Shen, P.; Qi, X.; Li, L. *Chem. Commun. (Cambridge, England)* **2011**, *47* (39), 10984–10986. doi:10.1039/c1cc14261e
170. Sebastián, D.; Nieto-Monge, M. J.; Pérez-Rodríguez, S.; Pastor, E.; Lázaro, M. J. *Energies* **2018**, *11* (4). doi:10.3390/en11040831
171. Eris, S.; Daşdelen, Z.; Yıldız, Y.; Sen, F. *Int. J. Hydrog. Energy* **2018**, *43* (3), 1337–1343. doi:10.1016/j.ijhydene.2017.11.051
172. Lv, R.; Cui, T.; Jun, M.-S.; Zhang, Q.; Cao, A.; Su, D. S.; Zhang, Z.; Yoon, S.-H.; Miyawaki, J.; Mochida, I.; Kang, F. *Adv. Funct. Mater.* **2011**, *21* (5), 999–1006. doi:10.1002/adfm.201001602
173. Ghosh, A.; Ramaprabhu, S. *Catal. Sci. Technol.* **2017**, *7* (21), 5079–5091. doi:10.1039/C7CY01522D
174. Wang, Y.-S.; Yang, S.-Y.; Li, S.-M.; Tien, H.-W.; Hsiao, S.-T.; Liao, W.-H.; Liu, C.-H.; Chang, K.-H.; Ma, C.-C. M.; Hu, C.-C. *Electrochim. Acta* **2013**, *87*, 261–269. doi:10.1016/j.electacta.2012.09.013
175. Su, Z.; Li, C.; Cheng, Y.; Gui, Q.; Xiong, Y.; Tan, Y.; Jiang, H.; Liu, X. *RSC Adv* **2018**, *8* (59), 33742–33747. doi:10.1039/C8RA06246C
176. Ma, Y.; Wang, Q.; Miao, Y.; Lin, Y.; Li, R. *Appl. Surf. Sci.* **2018**, *450*, 413–421. doi:10.1016/j.apsusc.2018.04.094
177. Zhang, Z.; Jing, H.-K.; Liu, S.; Li, G.-R.; Gao, X.-P. *J. Mater. Chem. A* **2015**, *3* (13), 6827–6834. doi:10.1039/C4TA07183B
178. Liu, J.; Zeng, B.; Wang, X.; Wang, W.; Shi, H. *Appl. Phys. Lett.* **2013**, *103* (5), 53105. doi:10.1063/1.4816751
179. Li, Y.; Huang, Y.; Zhang, Z.; Duan, D.; Hao, X.; Liu, S. *Chem. Eng. J.* **2016**, *283*, 911–921. doi:10.1016/j.cej.2015.08.063
180. Guo, L.; Jiang, W.-J.; Zhang, Y.; Hu, J.-S.; Wei, Z.-D.; Wan, L.-J. *ACS Catal.* **2015**, *5* (5), 2903–2909. doi:10.1021/acscatal.5b00117
181. Susi, T.; Nasibulin, A. G.; Jiang, H.; Kauppinen, E. I. *J. Nanomater.* **2008**, *2008* (9), 1–7. doi:10.1155/2008/425195
182. Xia, W.; Chen, X.; Kundu, S.; Wang, X.; Grundmeier, G.; Wang, Y.; Bron, M.; Schuhmann, W.; Muhler, M. *Surf. Coat. Tech.* **2007**, *201* (22-23), 9232–9237. doi:10.1016/j.surfcoat.2007.05.031
183. Jha, N.; Jafri, R. I.; Rajalakshmi, N.; Ramaprabhu, S. *Int. J. Hydrog. Energy* **2011**, *36* (12), 7284–7290. doi:10.1016/j.ijhydene.2011.03.008
184. Ye, F.; Cao, X.; Yu, L.; Chen, S.; Lin, W. *Int. J. Electrochem. Sci.* **2012**, *7* (2), 1251–1265.



- 
185. Rajesh; Paul, R. K.; Mulchandani, A. *J. Power Sources* **2013**, *223*, 23–29. doi:10.1016/j.jpowsour.2012.08.088
186. Jhan, J.-Y.; Huang, Y.-W.; Hsu, C.-H.; Teng, H.; Kuo, D.; Kuo, P.-L. *Energy* **2013**, *53*, 282–287. doi:10.1016/j.energy.2013.03.002
187. van Ho, T. T.; Pan, C.-J.; Rick, J.; Su, W.-N.; Hwang, B.-J. *J. Am. Chem. Soc.* **2011**, *133* (30), 11716–11724. doi:10.1021/ja2039562
188. Huynh, T. T.; Pham, H. Q.; van Nguyen, A.; Ngoc Mai, A. T.; Nguyen, S. T.; Bach, L. G.; Vo, D.-V. N.; van Thanh Ho, T. *Int. J. Hydrog. Energy* **2018**. doi:10.1016/j.ijhydene.2018.10.029
189. Wang, D.; Subban, C. V.; Wang, H.; Rus, E.; DiSalvo, F. J.; Abruña, H. D. *J. Am. Chem. Soc.* **2010**, *132* (30), 10218–10220. doi:10.1021/ja102931d
190. De Volder, Michael F L; Tawfick, S. H.; Baughman, R. H.; Hart, A. J. *Science (New York)* **2013**, *339* (6119), 535–539. doi:10.1126/science.1222453
191. Liu, J.; Lai, L.; Sahoo, N. G.; Zhou, W.; Shen, Z.; Chan, S. H. *Aust. J. Chem.* **2012**, *65* (9), 1213. doi:10.1071/CH12128
192. GONG, K.; YAN, Y.; ZHANG, M.; SU, L.; XIONG, S.; MAO, L. *Anal. Sci.* **2005**, *21* (12), 1383–1393. doi:10.2116/analsci.21.1383
193. Le Cai; Song, L.; Luan, P.; Zhang, Q.; Zhang, N.; Gao, Q.; Zhao, D.; Zhang, X.; Tu, M.; Yang, F.; Zhou, W.; Fan, Q.; Luo, J.; Zhou, W.; Ajayan, P. M.; Xie, S. *Sci. Rep.* **2013**, *3*, 3048. doi:10.1038/srep03048
194. Chung, H. T.; Won, J. H.; Zelenay, P. *Nat. commun.* **2013**, *4*, 1922. doi:10.1038/ncomms2944
195. Dumitrescu, I.; Unwin, P. R.; Macpherson, J. V. *Chem. Commun. (Cambridge, England)* **2009** (45), 6886–6901. doi:10.1039/b909734a
196. Firme, C. P.; Bandaru, P. R. *Nanomed. Nanotechnol. Biol. Med.* **2010**, *6* (2), 245–256. doi:10.1016/j.nano.2009.07.003
197. Gao, C.; Guo, Z.; Liu, J.-H.; Huang, X.-J. *Nanoscale* **2012**, *4* (6), 1948–1963. doi:10.1039/c2nr11757f
198. Luo, C.; Xie, H.; Wang, Q.; Luo, G.; Liu, C. *J. Nanomateri.* **2015**, *2015* (7), 1–10. doi:10.1155/2015/560392
199. Dresselhaus, M. S.; Lin, Y. M.; Rabin, O.; Jorio, A.; Souza Filho, A. G.; Pimenta, M. A.; Saito, R.; Samsonidze, G.; Dresselhaus, G. *Mater. Sci. Eng. C* **2003**, *23* (1-2), 129–140. doi:10.1016/S0928-4931(02)00240-0
200. Tesner, P. A.; Echeistova, A. I. *Dokl. Akad. Nauk SSSR* **1952**, *87*, 1029–1031.
201. DAVIS, W. R.; SLAWSON, R. J.; RIGBY, G. R. *Nature* **1953**, *171* (4356), 756. doi:10.1038/171756a0
202. Hofer, L. J. E.; Sterling, E.; McCartney, J. T. *J. Phys. Chem.* **1955**, *59* (11), 1153–1155. doi:10.1021/j150533a010
-

## References

---

203. Walker, P. L.; Rakszawski, J. F.; Imperial, G. R. *J. Phys. Chem.* **1959**, *63* (2), 133–140. doi:10.1021/j150572a002
204. Baird, T.; Fryer, J. R.; Grant, B. *Nature* **1971**, *233* (5318), 329–330. doi:10.1038/233329b0
205. Radushkevich, L. V.; Luk'yanovich, V. M. *Zh. Fiz. Khim.* **1952**, *26*, 88–95.
206. Kumar, M.; Ando, Y. *J. Nanosci. Nanotech.* **2010**, *10* (6), 3739–3758. doi:10.1166/jnn.2010.2939
207. Jourdain, V.; Bichara, C. *Carbon* **2013**, *58*, 2–39. doi:10.1016/j.carbon.2013.02.046
208. Cheng, T.-C. *Mater. Chem. Phys.* **2012**, *136* (1), 140–145. doi:10.1016/j.matchemphys.2012.06.043
209. Raney, J. R.; Misra, A.; Daraio, C. *Carbon* **2011**, *49* (11), 3631–3638. doi:10.1016/j.carbon.2011.04.066
210. P. Vinten, P. Marshall, T. Quance, J. Lefebure, P. Finnie. *Carbon* **2013**, *2013* (61), 22–32.
211. Guellati, O.; Janowska, I.; Bégin, D.; Guerioune, M.; Mekhalif, Z.; Delhalle, J.; Moldovan, S.; Ersen, O.; Pham-Huu, C. *Appl. Catal. A* **2012**, *423–424*, 7–14. doi:10.1016/j.apcata.2012.02.036
212. Du, F.; Qu, L.; Xia, Z.; Feng, L.; Dai, L. *Langmuir* **2011**, *27* (13), 8437–8443. doi:10.1021/la200995r
213. Lee, S. S.; Zhang, C.; Lewicka, Z. A.; Cho, M.; Mayo, J. T.; Yu, W. W.; Hauge, R. H.; Colvin, V. L. *J. Phys. Chem. C* **2012**, *116* (18), 10287–10295. doi:10.1021/jp212404j
214. Nessim, G. D.; Acquaviva, D.; Seita, M.; O'Brien, K. P.; Thompson, C. V. *Adv. Funct. Mater.* **2010**, *20* (8), 1306–1312. doi:10.1002/adfm.200902265
215. Nessim, G. D.; Al-Obeidi, A.; Grisar, H.; Polsen, E. S.; Ryan Oliver, C.; Zimrin, T.; John Hart, A.; Aurbach, D.; Thompson, C. V. *Carbon* **2012**, *50* (11), 4002–4009. doi:10.1016/j.carbon.2012.04.043
216. Pattinson, S. W.; Diaz, R. E.; Stelmashenko, N. A.; Windle, A. H.; Ducati, C.; Stach, E. A.; Koziol, K. K. *Chem. Mater.* **2013**, *25* (15), 2921–2923. doi:10.1021/cm401216q
217. Schlüter, O.F.-K.; Wehner, B. I.; Hu, D.; Xia, W.; Quandt, T.; Marginean, G.; Brandl, W.; Muhler, M. *Appl. Catal. A* **2004**, *274* (1–2), 71–77. doi:10.1016/j.apcata.2004.05.023
218. Ding, F.; Larsson, P.; Larsson, J. A.; Ahuja, R.; Duan, H.; Rosén, A.; Bolton, K. *Nano Lett.* **2008**, *8* (2), 463–468. doi:10.1021/nl072431m
219. Chiang, W.-H.; Mohan Sankaran, R. *Nat. Mater.* **2009**, *8*, 882 EP -. doi:10.1038/nmat2531
220. Huang, S.; Cai, Q.; Chen, J.; Qian, Y.; Zhang, L. *J. Am. Chem. Soc.* **2009**, *131* (6), 2094–2095. doi:10.1021/ja809635s
221. Yuan, D.; Ding, L.; Chu, H.; Feng, Y.; McNicholas, T. P.; Liu, J. *Nano Lett.* **2008**, *8* (8), 2576–2579. doi:10.1021/nl801007r

222. Liu, B.; Ren, W.; Gao, L.; Li, S.; Liu, Q.; Jiang, C.; Cheng, H.-M. *J. Phys. Chem. C* **2008**, *112* (49), 19231–19235. doi:10.1021/jp8060587
223. Takagi, D.; Hibino, H.; Suzuki, S.; Kobayashi, Y.; Homma, Y. *Nano Lett.* **2007**, *7* (8), 2272–2275. doi:10.1021/nl0708011
224. Swierczewska, M.; Rusakova, I.; Sitharaman, B. *Carbon* **2009**, *47* (13), 3139–3142. doi:10.1016/j.carbon.2009.07.021
225. Bhaviripudi, S.; Mile, E.; Steiner, S. A.; Zare, A. T.; Dresselhaus, M. S.; Belcher, A. M.; Kong, J. *J. Am. Chem. Soc.* **2007**, *129* (6), 1516–1517. doi:10.1021/ja0673332
226. Qian, Y.; Wang, C.; Ren, G.; Huang, B. *Appl. Surf. Sci.* **2010**, *256* (12), 4038–4041. doi:10.1016/j.apsusc.2010.01.074
227. Esconjauregui, S.; Whelan, C. M.; Maex, K. *Carbon* **2009**, *47* (3), 659–669. doi:10.1016/j.carbon.2008.10.047
228. Takagi, D.; Homma, Y.; Hibino, H.; Suzuki, S.; Kobayashi, Y. *Nano Lett.* **2006**, *6* (12), 2642–2645. doi:10.1021/nl061797g
229. Sinnott, S. B.; Andrews, R.; Qian, D.; Rao, A. M.; Mao, Z.; Dickey, E. C.; Derbyshire, F. *Chem. Phys. Lett.* **1999**, *315* (1-2), 25–30. doi:10.1016/S0009-2614(99)01216-6
230. Moisala, A.; Nasibulin, A. G.; Kauppinen, E. I. *J. Phys.: Condens. Matter.* **2003**, *15* (42), S3011-S3035. doi:10.1088/0953-8984/15/42/003
231. Nerushev, O. A.; Dittmar, S.; Morjan, R.-E.; Rohmund, F.; Campbell, E. E. B. *J. Appl. Phys.* **2003**, *93* (7), 4185–4190. doi:10.1063/1.1559433
232. Shaikjee, A.; Coville, N. J. *Carbon* **2012**, *50* (10), 3376–3398. doi:10.1016/j.carbon.2012.03.024
233. Morjan, R. E.; Nerushev, O. A.; Sveningsson, M.; Rohmund, F.; Falk, L.K.L.; Campbell, E. E. B. *Appl. Phys. A* **2004**, *78* (3), 253–261. doi:10.1007/s00339-003-2297-z
234. Balandin, A. A.; Ghosh, S.; Bao, W.; Calizo, I.; Teweldebrhan, D.; Miao, F.; Lau, C. N. *Nano Lett.* **2008**, *8* (3), 902–907. doi:10.1021/nl0731872
235. Stoller, M. D.; Park, S.; Zhu, Y.; An, J.; Ruoff, R. S. *Nano Lett.* **2008**, *8* (10), 3498–3502. doi:10.1021/nl802558y
236. Lee, C.; Wei, X.; Kysar, J. W.; Hone, J. *Science (New York)* **2008**, *321* (5887), 385–388. doi:10.1126/science.1157996
237. Kiew, S. F.; Kiew, L. V.; Lee, H. B.; Imae, T.; Chung, L. Y. *J. Controlled Release* **2016**, *226*, 217–228. doi:10.1016/j.jconrel.2016.02.015
238. Shao, Y.; Wang, J.; Wu, H.; Liu, J.; Aksay, I. A.; Lin, Y. *Electroanalysis* **2010**, *22* (10), 1027–1036. doi:10.1002/elan.200900571
239. Nag, A.; Mitra, A.; Mukhopadhyay, S. C. *Sens. Actuators A Phys.* **2018**, *270*, 177–194. doi:10.1016/j.sna.2017.12.028
240. Kim, H.-i.; Moon, G.-h.; Monllor-Satoca, D.; Park, Y.; Choi, W. *J. Phys. Chem. C* **2011**, *116* (1), 1535–1543. doi:10.1021/jp209035e

## References

---

241. Jang, H.; Park, Y. J.; Chen, X.; Das, T.; Kim, M.-S.; Ahn, J.-H. *Adv. Mater. Weinheim* **2016**, *28* (22), 4184–4202. doi:10.1002/adma.201504245
242. Kim, H.; Ahn, J.-H. *Carbon* **2017**, *120*, 244–257. doi:10.1016/j.carbon.2017.05.041
243. Ji, L.; Meduri, P.; Agubra, V.; Xiao, X.; Alcoutlabi, M. *Adv. Energy Mater.* **2016**, *6* (16), 1502159. doi:10.1002/aenm.201502159
244. Chen, D.; Feng, H.; Li, J. *Chem. Rev.* **2012**, *112* (11), 6027–6053. doi:10.1021/cr300115g
245. Singh, E.; Meyyappan, M.; Nalwa, H. S. *ACS Appl. Mater. Interfaces* **2017**, *9* (40), 34544–34586. doi:10.1021/acsami.7b07063
246. Varghese, S. S.; Lonkar, S.; Singh, K. K.; Swaminathan, S.; Abdala, A. *Sens. Actuators B Chem.* **2015**, *218*, 160–183. doi:10.1016/j.snb.2015.04.062
247. Zhu, Y.; Murali, S.; Cai, W.; Li, X.; Suk, J. W.; Potts, J. R.; Ruoff, R. S. *Adv. Mater. Weinheim* **2010**, *22* (35), 3906–3924. doi:10.1002/adma.201001068
248. Wang, H.; Maiyalagan, T.; Wang, X. *ACS Catal.* **2012**, *2* (5), 781–794. doi:10.1021/cs200652y
249. Chen, W.; Chen, S.; Qi, D. C.; Gao, X. Y.; Wee, A. T. S. *J. Am. Chem. Soc.* **2007**, *129* (34), 10418–10422. doi:10.1021/ja071658g
250. Giovannetti, G.; Khomyakov, P. A.; Brocks, G.; Karpan, V. M.; van den Brink, J.; Kelly, P. J. *Phys. Rev. Lett.* **2008**, *101* (2), 26803. doi:10.1103/PhysRevLett.101.026803
251. Emtsev, K. V.; Bostwick, A.; Horn, K.; Jobst, J.; Kellogg, G. L.; Ley, L.; McChesney, J. L.; Ohta, T.; Reshanov, S. A.; Röhrli, J.; Rotenberg, E.; Schmid, A. K.; Waldmann, D.; Weber, H. B.; Seyller, T. *Nat. Mater.* **2009**, *8* (3), 203–207. doi:10.1038/nmat2382
252. Reina, A.; Jia, X.; Ho, J.; Nezich, D.; Son, H.; Bulovic, V.; Dresselhaus, M. S.; Kong, J. *Nano Lett.* **2009**, *9* (1), 30–35. doi:10.1021/nl801827v
253. Kim, K. S.; Zhao, Y.; Jang, H.; Lee, S. Y.; Kim, J. M.; Kim, K. S.; Ahn, J.-H.; Kim, P.; Choi, J.-Y.; Hong, B. H. *Nature* **2009**, *457* (7230), 706–710. doi:10.1038/nature07719
254. Li, X.; Cai, W.; An, J.; Kim, S.; Nah, J.; Yang, D.; Piner, R.; Velamakanni, A.; Jung, I.; Tutuc, E.; Banerjee, S. K.; Colombo, L.; Ruoff, R. S. *Science (New York)* **2009**, *324* (5932), 1312–1314. doi:10.1126/science.1171245
255. Kim, K.-S.; Lee, H.-J.; Lee, C.; Lee, S.-K.; Jang, H.; Ahn, J.-H.; Kim, J.-H.; Lee, H.-J. *ACS Nano* **2011**, *5* (6), 5107–5114. doi:10.1021/nn2011865
256. Zhang, Y.; Zhang, L.; Zhou, C. *Acc. Chem. Res.* **2013**, *46* (10), 2329–2339. doi:10.1021/ar300203n
257. Novoselov, K. S.; Geim, A. K.; Morozov, S. V.; Jiang, D.; Zhang, Y.; Dubonos, S. V.; Grigorieva, I. V.; Firsov, A. A. *Science (New York)* **2004**, *306* (5696), 666–669. doi:10.1126/science.1102896
258. Bai, H.; Li, C.; Shi, G. *Adv. Mater. Weinheim* **2011**, *23* (9), 1089–1115. doi:10.1002/adma.201003753
259. Obratzsov, A. N. *Nat. Nanotechnol.* **2009**, *4*, 212 EP -. doi:10.1038/nnano.2009.67

- 
260. Hummers, W. S.; Offeman, R. E. *J. Am. Chem. Soc.* **1958**, *80* (6), 1339. doi:10.1021/ja01539a017
261. Fan, X.; Peng, W.; Li, Y.; Li, X.; Wang, S.; Zhang, G.; Zhang, F. *Adv. Mater.* **2008**, *20* (23), 4490–4493. doi:10.1002/adma.200801306
262. Schniepp, H. C.; Li, J.-L.; McAllister, M. J.; Sai, H.; Herrera-Alonso, M.; Adamson, D. H.; Prud'homme, R. K.; Car, R.; Saville, D. A.; Aksay, I. A. *J. Phys. Chem. B* **2006**, *110* (17), 8535–8539. doi:10.1021/jp060936f
263. Toda, T. *J. Electrochem. Soc.* **1999**, *146* (10), 3750. doi:10.1149/1.1392544
264. Lin, L.; Zhu, Q.; Xu, A.-W. *J. Am. Chem. Soc.* **2014**, *136* (31), 11027–11033. doi:10.1021/ja504696r
265. Kulp, C.; Gillmeister, K.; Widdra, W.; Bron, M. *ChemPhysChem* **2013**, *14* (6), 1205–1210. doi:10.1002/cphc.201200891
266. El-Deeb, H.; Bron, M. *J. Power Sources* **2015**, *275*, 893–900. doi:10.1016/j.jpowsour.2014.11.060
267. Xiong, Y.; Xiao, L.; Yang, Y.; DiSalvo, F. J.; Abruña, H. D. *Chem. Mater.* **2018**, *30* (5), 1532–1539. doi:10.1021/acs.chemmater.7b04201
268. Strasser, P.; Kühl, S. *Nano Energy* **2016**, *29*, 166–177. doi:10.1016/j.nanoen.2016.04.047
269. Steimecke, M.; Rümmler, S.; Bron, M. *Electrochim. Acta* **2015**, *163*, 1–8. doi:10.1016/j.electacta.2015.02.142
270. Li, N.; Chen, X.; Stoica, L.; Xia, W.; Qian, J.; Aßmann, J.; Schuhmann, W.; Muhler, M. *Adv. Mater.* **2007**, *19* (19), 2957–2960. doi:10.1002/adma.200602625
271. Li, W. Z.; Wen, J. G.; Ren, Z. F. *Appl. Phys. A* **2002**, *74* (3), 397–402. doi:10.1007/s003390201284
272. Li, W. Z.; Wen, J. G.; Tu, Y.; Ren, Z. F. *Appl Phys A* **2001**, *73* (2), 259–264. doi:10.1007/s003390100916
273. P. Vinten, P. Marshall, T. Quance, J. Lefebvre, P. Finnie. *Carbon* **2013**, *2013* (61), 22–32.
274. Vinten, P.; Marshall, P.; Quance, T.; Lefebvre, J.; Finnie, P. *Carbon* **2013**, *61*, 22–32. doi:10.1016/j.carbon.2013.04.007
275. van Dommele, S.; De Jong, K. P.; Romero-Izquierdo, A.; Bitter, J. H.; Gaigneaux, E. M.; Deviller, M.; De Vos, D. E.; Hermans, S.; Jacobs, P. A.; Martens, J. A.; Ruiz, P. (Eds.) *Studies in Surface Science and Catalysis*; vol.162; Elsevier: Amsterdam, Boston, **2006**; pp 29–36.
276. Alexeyeva, N.; Tammeveski, K. *Electrochem. Solid-State Lett.* **2007**, *10* (5), F18. doi:10.1149/1.2713657
277. Mayrhofer, K.J.J.; Strmcnik, D.; Blizanac, B. B.; Stamenkovic, V.; Arenz, M.; Markovic, N. M. *Electrochim. Acta* **2008**, *53* (7), 3181–3188. doi:10.1016/j.electacta.2007.11.057
-

## References

---

278. Ma, J.; Habrioux, A.; Pisarek, M.; Lewera, A.; Alonso-Vante, N. *Electrochem. Commun.* **2013**, *29*, 12–16. doi:10.1016/j.elecom.2012.12.028
279. Ma, J.; Habrioux, A.; Morais, C.; Lewera, A.; Vogel, W.; Verde-Gómez, Y.; Ramos-Sanchez, G.; Balbuena, P. B.; Alonso-Vante, N. *ACS Catal.* **2013**, *3* (9), 1940–1950. doi:10.1021/cs4003222
280. Ma, J.; Habrioux, A.; Guignard, N.; Alonso-Vante, N. *J. Phys. Chem. C* **2012**, *116* (41), 21788–21794. doi:10.1021/jp304947y
281. Hartl, K.; Hanzlik, M.; Arenz, M. *Energy Environ. Sci.* **2011**, *4* (1), 234–238. doi:10.1039/C0EE00248H
282. Ball, S. C.; Hudson, S. L.; Leung, J. H.; Russell, A. E.; Thompsett, D.; Theobald, B. R. *ECS Trans.* **2007**, *11*, 1247–1257.
283. Wang, P.; Kulp, K.; Bron, M. *Beilstein J. Nanotechnol.* **2019**, *10* (1), 1475–1487. doi:10.3762/bjnano.10.146
284. Iijima, S. *Nature* **1991**, *354* (6348), 56–58. doi:10.1038/354056a0
285. Lin, Z.; Zeng, Z.; Gui, X.; Tang, Z.; Zou, M.; Cao, A. *Adv. Energy Mater.* **2016**, *6* (17), 1600554. doi:10.1002/aenm.201600554
286. Gogotsi, Y. *Nanomaterials Handbook*; CRC Press: Taylor & Francis Group, Boca Raton, FL 33487-2742, **2017**.
287. Chouhan, V.; Noguchi, T.; Kato, S. *J. Appl. Phys.* **2016**, *119* (13), 134303. doi:10.1063/1.4945581
288. Sun, L.; Wang, X.; Wang, Y.; Zhang, Q. *Carbon* **2017**, *122*, 462–474. doi:10.1016/j.carbon.2017.07.006
289. Gupta, S.; Murthy, C. N.; Prabha, C. R. *Int. J. Biol. Macromol.* **2018**, *108*, 687–703. doi:10.1016/j.ijbiomac.2017.12.038
290. Rana, M.M.; Ibrahim, D. S.; Mohd Asyraf, M. R.; Jarin, S.; Tomal, A. *Sens. Rev.* **2017**, *37* (2), 127–136. doi:10.1108/SR-10-2016-0230
291. Yuan, W.; Lu, S.; Xiang, Y.; Jiang, S. P. *RSC Adv* **2014**, *4* (86), 46265–46284. doi:10.1039/C4RA05120C
292. Nakashima, N., Ed. *Nanocarbons for Energy Conversion. Supramolecular Approaches*; Springer International Publishing: Cham, **2019**.
293. You, P. Y.; Kamarudin, S. K. *Chem. Eng. J.* **2017**, *309*, 489–502. doi:10.1016/j.cej.2016.10.051
294. Gao, W.; Zhao, M.; Jiang, Q. *ChemPhysChem* **2008**, *9* (14), 2092–2098. doi:10.1002/cphc.200800150
295. Zhang, L. Y.; Zhang, W.; Zhao, Z.; Liu, Z.; Zhou, Z.; Li, C. M. *RSC Adv* **2016**, *6* (56), 50726–50731. doi:10.1039/C6RA06517A
296. DeLuca, N. W.; Elabd, Y. A. *J. Polym. Sci. B Polym. Phys.* **2006**, *44* (16), 2201–2225. doi:10.1002/polb.20861
297. Larminie, J.; Dicks, A. *Fuel Cell Systems Explained*, 2nd ed.; Wiley: New York, **2003**.

298. Cheng, X.; Shi, Z.; Glass, N.; Zhang, L.; Zhang, J.; Song, D.; Liu, Z.-S.; Wang, H.; Shen, J. *J. Power Sources* **2007**, *165* (2), 739–756. doi:10.1016/j.jpowsour.2006.12.012
299. Nassr, Abu Bakr Ahmed Amine; Bron, M. *ChemCatChem* **2013**, *5* (6), 1472–1480. doi:10.1002/cctc.201200742
300. Nassr, Abu Bakr Ahmed Amine; Sinev, I.; Pohl, M.-M.; Grünert, W.; Bron, M. *ACS Catal.* **2014**, *4* (8), 2449–2462. doi:10.1021/cs401140g
301. Zhang, G.; Huang, C.; Qin, R.; Shao, Z.; An, D.; Zhang, W.; Wang, Y. *J. Mater. Chem. A* **2015**, *3* (9), 5204–5211. doi:10.1039/C4TA06076H
302. Kakati, N.; Maiti, J.; Lee, S. H.; Jee, S. H.; Viswanathan, B.; Yoon, Y. S. *Chem. Rev.* **2014**, *114* (24), 12397–12429. doi:10.1021/cr400389f
303. Huang, M.; Zhang, J.; Wu, C.; Guan, L. *ACS Appl. Mater. Interfaces* **2017**, *9* (32), 26921–26927. doi:10.1021/acsami.7b07866
304. Xu, H.; Wang, A.-L.; Tong, Y.-X.; Li, G.-R. *ACS Catal.* **2016**, *6* (8), 5198–5206. doi:10.1021/acscatal.6b01010
305. Hameed, R. A.; Amin, R. S.; El-Khatib, K. M.; Fetohi, A. E. *Appl. Surf. Sci.* **2016**, *367*, 382–390. doi:10.1016/j.apsusc.2016.01.087
306. Elezovic, N. R.; Radmilovic, V. R.; Krstajic, N. V. *RSC Adv* **2016**, *6* (8), 6788–6801. doi:10.1039/C5RA22403A
307. Oliveira Neto, A.; Franco, E. G.; Aricó, E.; Linardi, M.; Gonzalez, E. R. *J. Eur. Ceram. Soc.* **2003**, *23* (15), 2987–2992. doi:10.1016/S0955-2219(03)00310-8
308. Xu, Y.; Chen, L.; Wang, X.; Yao, W.; Zhang, Q. *Nanoscale* **2015**, *7* (24), 10559–10583. doi:10.1039/c5nr02216a
309. Bönemann, H.; Brijoux, W.; Brinkmann, R.; Joußen, T.; Korall, B.; Dinjus, E. *Angew. Chem. Int. Ed. Engl.* **1991**, *30* (10), 1312–1314. doi:10.1002/anie.199113121
310. Zhao, Z.-G.; Yao, Z.-J.; Zhang, J.; Zhu, R.; Jin, Y.; Li, Q.-W. *J. Mater. Chem.* **2012**, *22* (32), 16514. doi:10.1039/c2jm32769d
311. van Pham, V.; Ta, V.-T.; Sunglae, C. *Int. J. Hydrog. Energy* **2017**, *42* (18), 13192–13197. doi:10.1016/j.ijhydene.2017.01.236
312. Xu, L.; Luo, Z.; Fan, Z.; Yu, S.; Chen, J.; Liao, Y.; Xue, C. *Chem. Eur. J.* **2015**, *21* (24), 8691–8695. doi:10.1002/chem.201406677
313. Georgieva, J.; Valova, E.; Mintsouli, I.; Sotiropoulos, S.; Tatchev, D.; Arnyanov, S.; Hubin, A.; Dille, J.; Hoell, A.; Raghuwanshi, V.; Karanasios, N.; Malet, L. *J. Electroanal. Chem.* **2015**, *754*, 65–74. doi:10.1016/j.jelechem.2015.07.001
314. Sahin, N. E.; Napporn, T. W.; Dubau, L.; Kadirgan, F.; Léger, J.-M.; Kokoh, K. B. *Appl. Catal. B: Environ.* **2017**, *203*, 72–84. doi:10.1016/j.apcatb.2016.09.026
315. Jiang, H.; Zhao, T.; Li, C.; Ma, J. *Chem. Commun. (Cambridge, England)* **2011**, *47* (30), 8590–8592. doi:10.1039/c1cc12942b
316. Huang, H.; Wang, X. *J. Mater. Chem.* **2012**, *22* (42), 22533. doi:10.1039/c2jm33727d

## References

---

317. Li, N.; Chen, X.; Stoica, L.; Xia, W.; Qian, J.; Aßmann, J.; Schuhmann, W.; Muhler, M. *Adv. Mater.* **2007**, *19* (19), 2957–2960. doi:10.1002/adma.200602625
318. Ueda, M.; Dietz, H.; Anders, A.; Kneppe, H.; Meixner, A.; Plieth, W. *Electrochim. Acta* **2002**, *48* (4), 377–386. doi:10.1016/S0013-4686(02)00683-7
319. Sato, S.; Kawabata, A.; Nihei, M.; Awano, Y. *Chem. Phys. Lett.* **2003**, *382* (3-4), 361–366. doi:10.1016/j.cplett.2003.10.076
320. Li, W. Z.; Wen, J. G.; Ren, Z. F. *Appl. Phys. A* **2002**, *74* (3), 397–402. doi:10.1007/s003390201284
321. Heise, H. M.; Kuckuk, R.; Ojha, A. K.; Srivastava, A.; Srivastava, V.; Asthana, B. P. *J. Raman Spectrosc.* **2009**, *40* (3), 344–353. doi:10.1002/jrs.2120
322. Ralph, T. R., Hards, G. A., Keating, J. E., Campbell, S. A., Wilkinson, D. P., Davis, M., St-Pierre, M., Johnson, M. C. *J. Electrochem. Soc.* **1997**, *144* (11), 3845. doi:10.1149/1.1838101
323. Bedolla-Valdez, Z. I.; Verde-Gómez, Y.; Valenzuela-Muñiz, A. M.; Gochi-Ponce, Y.; Oropeza-Guzmán, M. T.; Berhault, G.; Alonso-Núñez, G. *Electrochim. Acta* **2015**, *186*, 76–84. doi:10.1016/j.electacta.2015.10.084
324. Mancharan, R.; Goodenough, J. B. *J. Mater. Chem.* **1992**, *2* (8), 875. doi:10.1039/jm9920200875
325. Lu, S.; Eid, K.; Ge, D.; Guo, J.; Wang, L.; Wang, H.; Gu, H. *Nanoscale* **2017**, *9* (3), 1033–1039. doi:10.1039/c6nr08895c
326. Huang, L.; Zhang, X.; Wang, Q.; Han, Y.; Fang, Y.; Dong, S. *J. Am. Chem. Soc.* **2018**, *140* (3), 1142–1147. doi:10.1021/jacs.7b12353
327. Hofstead-Duffy, A. M.; Chen, D.-J.; Sun, S.-G.; Tong, Y. J. *J. Mater. Chem.* **2012**, *22* (11), 5205. doi:10.1039/c2jm15426a
328. Zhao, Y.; Li, X.; Schechter, J. M.; Yang, Y. *RSC Adv* **2016**, *6* (7), 5384–5390. doi:10.1039/C5RA24249E
329. Chung, D. Y.; Lee, K.-J.; Sung, Y.-E. *J. Phys. Chem. C* **2016**, *120* (17), 9028–9035. doi:10.1021/acs.jpcc.5b12303
330. Wang, P.; Kottakkat, T.; Bron, M. *ChemElectroChem* **2015**, *2* (9), 1396–1402. doi:10.1002/celec.201500044
331. Zhang, X.; Zhang, J.; Huang, H.; Jiang, Q.; Wu, Y. *Electrochim. Acta* **2017**, *258*, 919–926. doi:10.1016/j.electacta.2017.11.142
332. Arico, A. S.; Srinivasan, S.; Antonucci, V. *Fuel Cells* **2001**, *1* (2), 133–161.
333. Caillard, A.; Coutanceau, C.; Brault, P.; Mathias, J.; Léger, J.-M. *J. Power Sources* **2006**, *162* (1), 66–73. doi:10.1016/j.jpowsour.2006.07.009
334. Iwasita, T.; Hoster, H.; John-Anacker, A.; Lin, W. F.; Vielstich, W. *Langmuir* **2000**, *16* (2), 522–529. doi:10.1021/la990594n
335. Krausa, M.; Vielstich, W. *J. Electroanal. Chem.* **1994**, *379* (1-2), 307–314. doi:10.1016/0022-0728(94)87152-3



336. Sugimoto, W.; Aoyama, K.; Kawaguchi, T.; Murakami, Y.; Takasu, Y. *J. Electroanal. Chem.* **2005**, *576* (2), 215–221. doi:10.1016/j.jelechem.2004.10.018
337. Yuan, H.; Guo, D.; Qiu, X.; Zhu, W.; Chen, L. *J. Power Sources* **2009**, *188* (1), 8–13. doi:10.1016/j.jpowsour.2008.11.095
338. Radmilovic, V. *J. Catal.* **1995**, *154* (1), 98–106. doi:10.1006/jcat.1995.1151
339. Nassr, Abu Bakr Ahmed Amine; Sinev, I.; Grünert, W.; Bron, M. *Appl. Catal. B: Environ.* **2013**, *142-143*, 849–860. doi:10.1016/j.apcatb.2013.06.013
340. Rajesh, B.; Karthik, V.; Karthikeyan, S.; Ravindranathan Thampi, K.; Bonard, J.-M.; Viswanathan, B. *Fuel* **2002**, *81* (17), 2177–2190. doi:10.1016/S0016-2361(02)00162-X
341. Gan, L.; Lv, R.; Du, H.; Li, B.; Kang, F. *Carbon* **2009**, *47* (7), 1833–1840. doi:10.1016/j.carbon.2009.03.025
342. Prabhuram, J.; Zhao, T. S.; Tang, Z. K.; Chen, R.; Liang, Z. X. *J. Phys. Chem. B* **2006**, *110* (11), 5245–5252. doi:10.1021/jp0567063
343. Chen, Y.; Zhang, G.; Ma, J.; Zhou, Y.; Tang, Y.; Lu, T. *Int. J. Hydrog. Energy* **2010**, *35* (19), 10109–10117. doi:10.1016/j.ijhydene.2010.07.170
344. Saha, M. S.; Li, R.; Sun, X. *J. Power Sources* **2008**, *177* (2), 314–322. doi:10.1016/j.jpowsour.2007.11.036
345. Liang, Y.; Li, J.; Xu, Q.-C.; Hu, R.-Z.; Lin, J.-D.; Liao, D.-W. *J. Alloys Compd.* **2008**, *465* (1-2), 296–304. doi:10.1016/j.jallcom.2007.10.075
346. Mani, V.; Chen, S.-M.; Lou, B.-S. *Int. J. Electrochem. Sci.* **2013**, *8* (10), 11641–11660.
347. Li, J.-J.; Ma, Y.-W.; Jiang, X.; Feng, X.-M.; Fan, Q.-L.; Huang, W. *IEEE Trans. Nanotechnol.* **2012**, *11* (1), 3–7. doi:10.1109/TNANO.2011.2158236
348. Ren, W.; Cheng, H.-M. *Nature* **2013**, *497* (7450), 448–449. doi:10.1038/497448a
349. Tsai, M.-C.; Yeh, T.-K.; Tsai, C.-H. *Electrochem. Commun.* **2006**, *8* (9), 1445–1452. doi:10.1016/j.elecom.2006.07.003
350. Wang, C.-H.; Du, H.-Y.; Tsai, Y.-T.; Chen, C.-P.; Huang, C.-J.; Chen, L. C.; Chen, K. H.; Shih, H.-C. *J. Power Sources* **2007**, *171* (1), 55–62. doi:10.1016/j.jpowsour.2006.12.028
351. Pei, S.; Cheng, H.-M. *Carbon* **2012**, *50* (9), 3210–3228. doi:10.1016/j.carbon.2011.11.010
352. Pei, S.; Zhao, J.; Du, J.; Ren, W.; Cheng, H.-M. *Carbon* **2010**, *48* (15), 4466–4474. doi:10.1016/j.carbon.2010.08.006
353. Kaniyoor, A.; Baby, T. T.; Ramaprabhu, S. *J. Mater. Chem.* **2010**, *20* (39), 8467. doi:10.1039/c0jm01876g
354. Chen, W.; Yan, L. *Nanoscale* **2010**, *2* (4), 559–563. doi:10.1039/b9nr00191c
355. Moon, I. K.; Lee, J.; Ruoff, R. S.; Lee, H. *Nat. commun.* **2010**, *1*, 73. doi:10.1038/ncomms1067
356. Søggaard, M.; Odgaard, M.; Skou, E. M. *Solid State Ionics* **2001**, *145* (1-4), 31–35. doi:10.1016/S0167-2738(01)00908-0

## References

---

357. Kakaei, K.; Zhiani, M. *J. Power Sources* **2013**, *225*, 356–363. doi:10.1016/j.jpowsour.2012.10.003
358. Lu, Y.; Jiang, Y.; Wu, H.; Chen, W. *J. Phys. Chem. C* **2013**, *117* (6), 2926–2938. doi:10.1021/jp3116726
359. Rao, R.; Chen, G.; Arava, Leela Mohana Reddy; Kalaga, K.; Ishigami, M.; Heinz, T. F.; Ajayan, P. M.; Harutyunyan, A. R. *Sci Rep* **2013**, *3*, 1891. doi:10.1038/srep01891
360. Yen, M.-Y.; Hsiao, M.-C.; Liao, S.-H.; Liu, P.-I.; Tsai, H.-M.; Ma, C.-C. M.; Pu, N.-W.; Ger, M.-D. *Carbon* **2011**, *49* (11), 3597–3606. doi:10.1016/j.carbon.2011.04.062
361. Yang, S.-Y.; Chang, K.-H.; Lee, Y.-F.; Ma, C.-C. M.; Hu, C.-C. *Electrochem. Commun.* **2010**, *12* (9), 1206–1209. doi:10.1016/j.elecom.2010.06.020
362. Wang, G.; Zhang, L.; Zhang, J. *Chem. Soc. Rev.* **2012**, *41* (2), 797–828. doi:10.1039/c1cs15060j
363. Liu, C.; Li, F.; Ma, L.-P.; Cheng, H.-M. *Adv. Mater. Weinheim* **2010**, *22* (8), E28-62. doi:10.1002/adma.200903328
364. Jun Lee, W.; Narayan Maiti, U.; Min Lee, J.; Joonwon Lim; Hee Han, T.; Ouk Kim, S. *Chem. Commun.* **2014**, *50* (52), 6818–6830. doi:10.1039/C4CC00146J
365. Xiehong Cao; Zongyou Yin; Hua Zhang. *Energy Environ. Sci.* **2014**, *7* (6), 1850–1865. doi:10.1039/C4EE00050A
366. Fan, L.-Z.; Qiao, S.; Song, W.; Wu, M.; He, X.; Qu, X. *Electrochim. Acta* **2013**, *105*, 299–304. doi:10.1016/j.electacta.2013.04.137
367. Kim, W.; Joo, J. B.; Kim, N.; Oh, S.; Kim, P.; Yi, J. *Carbon* **2009**, *47* (5), 1407–1411. doi:10.1016/j.carbon.2009.01.043
368. Fernández, J. A.; Arulepp, M.; Leis, J.; Stoeckli, F.; Centeno, T. A. *Electrochim. Acta* **2008**, *53* (24), 7111–7116. doi:10.1016/j.electacta.2008.05.028
369. Raut, A. S.; Parker, C. B.; Stoner, B. R.; Glass, J. T. *Electrochem. Commun.* **2012**, *19*, 138–141. doi:10.1016/j.elecom.2012.03.021
370. Xu, Y.; Lin, Z.; Huang, X.; Wang, Y.; Huang, Y.; Duan, X. *Adv. Mater.* **2013**, *25* (40), 5779–5784. doi:10.1002/adma.201301928
371. Hao Jiang; See Lee, P.; Li, C. *Energy Environ. Sci.* **2013**, *6* (1), 41–53. doi:10.1039/C2EE23284G
372. Chen, H.; Li, Y.; Feng, Y.; Lv, P.; Zhang, P.; Feng, W. *Electrochim. Acta* **2012**, *60*, 449–455. doi:10.1016/j.electacta.2011.11.101
373. Lv, P.; Zhang, P.; Li, F.; Li, Y.; Feng, Y.; Feng, W. *Synth. Met.* **2012**, *162* (13–14), 1090–1096. doi:10.1016/j.synthmet.2012.04.029
374. Hsieh, C.-T.; Chen, W.-Y.; Lin, J.-H. *Micropor. Mesopor. Mat.* **2009**, *122* (1-3), 155–159. doi:10.1016/j.micromeso.2009.02.028
375. Hsieh, C.-T.; Teng, H.; Chen, W.-Y.; Cheng, Y.-S. *Carbon* **2010**, *48* (15), 4219–4229. doi:10.1016/j.carbon.2010.07.021

376. Hsieh, C.-T.; Chen, W.-Y.; Cheng, Y.-S. *Electrochim. Acta* **2010**, *55* (19), 5294–5300. doi:10.1016/j.electacta.2010.04.085
377. Kim, B.; Chung, H.; Kim, W. *J. Phys. Chem. C* **2010**, *114* (35), 15223–15227. doi:10.1021/jp105498d
378. Subramanian, V.; Zhu, H.; Wei, B. *J. Power Sources* **2006**, *159* (1), 361–364. doi:10.1016/j.jpowsour.2006.04.012
379. Zhang, X.; Shi, W.; Zhu, J.; Zhao, W.; Ma, J.; Mhaisalkar, S.; Maria, T. L.; Yang, Y.; Zhang, H.; Hng, H. H.; Yan, Q. *Nano Res.* **2010**, *3* (9), 643–652. doi:10.1007/s12274-010-0024-6
380. Lei, Y.; Daffos, B.; Taberna, P. L.; Simon, P.; Favier, F. *Electrochim. Acta* **2010**, *55* (25), 7454–7459. doi:10.1016/j.electacta.2010.03.012
381. Jurewicz, K.; Delpeux, S.; Bertagna, V.; Béguin, F.; Frackowiak, E. *Chem. Phys. Lett.* **2001**, *347* (1-3), 36–40. doi:10.1016/S0009-2614(01)01037-5
382. Ryu, K. S.; Kim, K. M.; Park, N.-G.; Park, Y. J.; Chang, S. H. *J. Power Sources* **2002**, *103* (2), 305–309. doi:10.1016/S0378-7753(01)00862-X
383. Wang, H.; Lin, J.; Shen, Z. X. *J. Sci.: Adv. Mater. Devices* **2016**, *1* (3), 225–255. doi:10.1016/j.jsamd.2016.08.001
384. Yan, J.; Fan, Z.; Wei, T.; Cheng, J.; Shao, B.; Wang, K.; Song, L.; Zhang, M. *J. Power Sources* **2009**, *194* (2), 1202–1207. doi:10.1016/j.jpowsour.2009.06.006
385. Chen, S.; Zhu, J.; Wu, X.; Han, Q.; Wang, X. *ACS nano* **2010**, *4* (5), 2822–2830. doi:10.1021/nn901311t
386. Wang, H.; Casalongue, H. S.; Liang, Y.; Dai, H. *J. Am. Chem. Soc.* **2010**, *132* (21), 7472–7477. doi:10.1021/ja102267j
387. Horng, Y.-Y.; Lu, Y.-C.; Hsu, Y.-K.; Chen, C.-C.; Chen, L.-C.; Chen, K.-H. *J. Power Sources* **2010**, *195* (13), 4418–4422. doi:10.1016/j.jpowsour.2010.01.046
388. S.L.d.S.e. Lucato. *Lince Softwarein*; Department of Material Science, Darmstadt, Germany, **1999**.
389. Hu, C.-C.; Lin, J.-Y. *Electrochim. Acta* **2002**, *47* (25), 4055–4067. doi:10.1016/S0013-4686(02)00411-5
390. MacDiarmid, A.G.; Yang, L.S.; Huang, W.S.; Humphrey, B.D. *Synth. Met.* **1987**, *18* (1-3), 393–398. doi:10.1016/0379-6779(87)90911-8
391. Padwal, P. M.; Kadam, S. L.; Mane, S. M.; Kulkarni, S. B. *J Mater Sci* **2016**, *51* (23), 10499–10505. doi:10.1007/s10853-016-0270-4
392. Futaba, D. N.; Hata, K.; Yamada, T.; Hiraoka, T.; Hayamizu, Y.; Kakudate, Y.; Tanaike, O.; Hatori, H.; Yumura, M.; Iijima, S. *Nat. Mater.* **2006**, *5* (12), 987–994. doi:10.1038/nmat1782
393. Yuan, C.; Shen, L.; Li, D.; Zhang, F.; Lu, X.; Zhang, X. *Appl. Surf. Sci.* **2010**, *257* (2), 440–445. doi:10.1016/j.apsusc.2010.07.008
394. Yu, D.; Dai, L. *J. Phys. Chem. Lett.* **2010**, *1* (2), 467–470. doi:10.1021/jz9003137

395. Yan, J.; Wei, T.; Shao, B.; Fan, Z.; Qian, W.; Zhang, M.; Wei, F. *Carbon* **2010**, *48* (2), 487–493. doi:10.1016/j.carbon.2009.09.066
396. Wang, Y.-G.; Li, H.-Q.; Xia, Y.-Y. *Adv. Mater.* **2006**, *18* (19), 2619–2623.
397. Liu, J.; Zhou, M.; Fan, L.-Z.; Li, P.; Qu, X. *Electrocatalysis: From Theory to Industrial Applications* **2010**, *55* (20), 5819–5822. doi:10.1016/j.electacta.2010.05.030
398. Wang, H.; Lin, J.; Shen, Z. X. *J. Sci.: Adv. Mater. Devices* **2016**, *1* (3), 225–255. doi:10.1016/j.jsamd.2016.08.001
399. Hughes, M.; Chen, G. Z.; Shaffer, M. S. P.; Fray, D. J.; Windle, A. H. *Chem. Mater.* **2002**, *14* (4), 1610–1613. doi:10.1021/cm010744r
400. Zahran, E. M.; Bhattacharyya, D.; Bachas, L. G. *J. Mater. Chem.* **2011**, *21* (28), 10454. doi:10.1039/c1jm11435b
401. Li, W.; Liang, C.; Zhou, W.; Qiu, J.; Zhou; Sun, G.; Xin, Q. *J. Phys. Chem. B* **2003**, *107* (26), 6292–6299. doi:10.1021/jp022505c
402. Smith, E.; Dent, G. *Modern Raman Spectroscopy, a Practical Approach*; Chichester: Wiley **2005**.
403. Long, D. A. *Raman Spectroscopy*; McGraw-Hill, New York **1977**.
404. Langford, J. I.; Wilson, A. J.C. *J. appl. crystallogr.* **1978**, *11* (2), 102–113.
405. Hammond, C. *The basics of cristallography and diffraction*; Oxford, **2001**.
406. Mayrhofer, K.J.J.; Strmcnik, D.; Blizanac, B. B.; Stamenkovic, V.; Arenz, M.; Markovic, N. M. *Electrochim. Acta* **2008**, *53* (7), 3181–3188. doi:10.1016/j.electacta.2007.11.057
407. Stejskal, J.; Sapurina, I.; Trchová, M. *Prog. Polym. Sci.* **2010**, *35* (12), 1420–1481. doi:10.1016/j.progpolymsci.2010.07.006
408. Guo, S.; Dong, S.; Wang, E. *Small* **2009**, *5* (16), 1869–1876. doi:10.1002/smll.200900190

# Appendices

---

## Abbreviations

3D	Three dimension
AFCs	Alkaline fuel cells
CC	Carbon cloth
CE	Counter electrode
CNTs	Carbon nanotubes
CR	Cathodic reaction
CV	Cyclic voltammetry
DFT	Density functional theory
DMFCs	Direct methanol fuel cells
DPD	Double pulse deposition
ECSA	Electrochemically available active surface area
EG	Ethylene glycol
FWHM	Full width at half maximum
GC	Glassy carbon
GDL	Gas diffusion layer
GO	Graphene oxide
HER	Hydrogen electrode Reaction
HOR	Hydrogen oxidation reaction
HWP	Half-wave potential

## Abbreviations

---

ICP-OES	Inductively coupled plasma optical emission spectroscopy
LSV	Linear sweep voltammogram
MCFCs	Molten carbonate fuel cells
MEA	Membrane electrode assembly
MWCNTs	Multi-walled carbon nanotubes
NCNTs	Nitrogen doped carbon nanotubes
OCNTs	Oxidized carbon nanotubes
ORR	Oxygen reduction reaction
PAFCs	Phosphoric acid fuel cell
PANI	Polyaniline
PANI <sub>ED</sub>	Polyaniline prepared by electrodeposition
PANI <sub>WI</sub>	Polyaniline prepared by wet impregnation
PEMFCs	Proton exchange fuel cells
	Polymer Electrolyte Membrane fuel cells
RDE	Rotating disk electrode
RGO	Reduced graphene oxide
RHE	Reversible hydrogen electrode
RPM	Revolution per minute
SCNTs	Secondary carbon nanotubes
SWCNTs	Single wall carbon nanotubes
SEM	Scanning electron microscopy
SOFC	Solid oxide fuel cell
TEM	Transmission electron microscopy
WE	Working electrode
UPD	Underpotential deposition
XRD	X-ray diffraction

## Symbols

Å	Angstrom	Å
B	Levich constant	
B <sub>2θ</sub>	Full wave half maximum	
C	Concentration	mol L <sup>-1</sup> (M)
CO <sub>2</sub>	Concentration of dissolved O <sub>2</sub> in electrolyte	mol L <sup>-1</sup>
DO <sub>2</sub>	Diffusion coefficient of oxygen	cm <sup>2</sup> s <sup>-1</sup>
e <sup>-</sup>	Electron	
E <sup>0</sup>	Standard potential for half-cell reaction	V
F	Faraday constant	C mol <sup>-1</sup>
h	Hour	
H <sub>ads/des</sub>	Hydrogen adsorption/desorption	
H <sup>+</sup>	Proton	
H <sub>upd</sub>	Underpotential deposited hydrogen	
j	Current density	mA cm <sup>-2</sup>
j <sub>d</sub>	Diffusion-limited current density	mA cm <sup>-2</sup>
j <sub>k</sub>	Kinetic current density	mA cm <sup>-2</sup>
L	Crytallite size of polycrystallized Pt	nm
L <sub>Pt</sub>	Pt loading in the catalyst	mg
n	Number of transferred electrons in oxygen reduction reaction	
nm	Nanometre	nm
ω	Rotation speed of rotating disk electrode	rpm
Q <sub>CO</sub>	Columbic charge consumed by oxidation of adsorbed CO	mC
Q <sub>H</sub>	Columbic charge of the underpotential deposited hydrogen	mC
T	Temperature	°C
μm	micrometre	μm

V	Cell voltage	V
W	Watt	
wt. %	Weight. %	
$\theta$	The diffraction angle	$^{\circ}$
$\lambda$	The wavelength	nm
$\nu$	Kinematic viscosity	$\text{cm}^2 \text{s}^{-1}$

## List of Tabela

<b>Table 2.1.</b> Types of fuel cells, their reactions at anode and cathode, electrolyte and operating temperatures.....	11
<b>Table 3.1.1.</b> Elemental analysis of nitrogen and carbon content in primary CNTs and 3D CNTs.....	35
<b>Table 3.1.2.</b> ECSA values determined by $H_{\text{upd}}$ and $\text{CO}_{\text{ad}}$ for Pt on 3D CNTs, primary CNTs and C.....	42
<b>Table 3.1.3.</b> Pt mass-specific- and surface-specific activities $i_m$ and $i_s$ of ORR for Pt-3D CNTs, Pt-primary CNTs and Pt-C at $E = 0.9 \text{ V}$ vs. RHE. ....	44
<b>Table S3.1.1.</b> Yield ratios and N contents for CNTs grown at different temperature via CVD. ....	50
<b>Table 3.2.1.</b> Pt masse on the different supports and corresponding electrochemically active surface area (ECSA) determined by $H_{\text{upd}}$ and $\text{CO}_{\text{ads}}$ . ....	61
<b>Table S3.4.1.</b> Capacitance values determined before and after 1000 cycles long-term test for CNTs/CC, CNTs/CNTs/CC, CNTs/RGO/CC, $\text{PANI}_{\text{Wf}}$ /CNTs/CC.....	110



## List of Figures

<b>Figure 1.1.</b> Typical polarization curve of a PEM fuel cell, reprinted from [30, 31] with permission.....	6
<b>Figure 2.1.</b> Schematic representation of PEMFCs and DMFCs. ....	12
<b>Figure 2.2.</b> The mechanism of the oxygen reduction on Pt. [48, 60].....	14
<b>Figure 2.3.</b> Possible configurations of O <sub>2</sub> on the metal surface. ....	15
<b>Figure 2.4.</b> Schematic representation of the reaction paths and possible intermediates, green arrows indicate the indirect mechanism to CO <sub>2</sub> formation, reprinted from [70] with permission.....	17
<b>Figure 2.5.</b> ORR volcano plot: ORR activity plotted as a function of oxygen binding energy, reprinted from [63] with permission.....	18
<b>Figure 2.6.</b> Schematic diagram of (a) single wall carbon nanotube, (b) multi-wall carbon nanotube, reprinted from [199] with permission; and (c) graphene, reprinted from [237] with permission.....	24
<b>Figure 2.7.</b> Schematic diagram of thermal CVD technique setup. ....	24
<b>Figure 2.8.</b> CNT growth mechanisms [206]: (a) tip-growth model and (b) base-growth model. ....	26
<b>Figure 2.9.</b> Schematic representation of the preparation of reduced graphene oxide (RGO) from graphite; reprinted from [258] with permission. ....	27
<b>Figure 3.1.1.</b> Schematic representation of the preparation of 3D CNTs network. ....	33
<b>Figure 3.1.2.</b> TEM images of (a) primary CNTs and (b) Fe-primary CNTs and (c) 3D-CNTs via secondary CNTs grown onto primary CNTs. ....	34
<b>Figure 3.1.3.</b> The Raman spectroscopy of primary CNTs, 3D CNTs and NCNTs exposing the different graphitization degree/defect degree of carbon system.....	35
<b>Figure 3.1.4.</b> Nitrogen physisorption at 77 K for primary CNTs and 3D CNTs.....	36
<b>Figure 3.1.5.</b> Cyclic voltammograms of primary CNTs and 3D CNTs on glassy carbon electrodes recorded at a scan rate of 100 mV s <sup>-1</sup> at room temperature in 0.5 M H <sub>2</sub> SO <sub>4</sub> aqueous electrolyte solution purged with N <sub>2</sub> . ....	36
<b>Figure 3.1.6.</b> TEM images and particles size distribution of Pt nanoparticles supported on (a) primary CNTs and (b) 3D CNTs. ....	38
<b>Figure 3.1.7.</b> X-ray diffraction profile of the Pt-primary CNTs and Pt-3D CNTs (determined by Dr. Benedikt Peter).....	39
<b>Figure 3.1.8.</b> Cyclic voltammograms measured at 100 mV s <sup>-1</sup> scan rate in aqueous 0.1 M HClO <sub>4</sub> electrolyte solution for Pt-3D CNTs, Pt-primary CNTs and Pt-C. The double layer charging subtracted for ECSA determination is indicated by the dashed line.....	40
<b>Figure 3.1.9.</b> CO <sub>ad</sub> stripping voltammogram recorded at 20 mV s <sup>-1</sup> scan rate in aqueous 0.1M HClO <sub>4</sub> electrolyte solution for Pt-3D CNTs, Pt-primary CNTs and Pt-C.....	41

- Figure 3.1.10.** ORR polarization curves of Pt-3D CNTs, Pt-primary CNTs and Pt-C measured in oxygen saturated 0.1 M HClO<sub>4</sub> at 1600 rpm with a scan rate of 5 mV s<sup>-1</sup> in the potential range between 0.05-1.1 V vs. RHE, and (b) their Koutecky-Levich plots for ORR at 0.4 V vs. RHE, determined by Koutecky-Levich equation.....43
- Figure 3.1.11.** Cyclic voltammograms for (a) Pt-3D CNTs, (b) Pt-primary CNTs and (c) Pt-C recorded at a scan rate of 100 mV s<sup>-1</sup> in the potential range 0.05-1.2 V vs. RHE in N<sub>2</sub> saturated 0.1 M HClO<sub>4</sub> before and after each oxygen stress test. Each aging stress test was performed by cyclic voltammetry for 500 cycles at a scan rate of 1000 mV s<sup>-1</sup> in the potential range 0.05-1.2 V vs. RHE in O<sub>2</sub> saturated 0.1 M HClO<sub>4</sub> and was repeated 4 times. ....45
- Figure 3.1.12.** ORR polarization curves of (a) Pt-3D CNTs, (b) Pt-primary CNTs and (c) Pt-C measured in oxygen saturated 0.1 M HClO<sub>4</sub> at 1600 rpm with a scan rate of 5 mV s<sup>-1</sup> in the potential range between 0.05-1.1 V vs. RHE before and after each oxygen aging stress test. Each aging stress test was performed by cyclic voltammetry for 500 cycles at a scan rate of 1000 mV s<sup>-1</sup> in the potential range 0.05-1.2 V vs. RHE in O<sub>2</sub> saturated 0.1 M HClO<sub>4</sub> and was repeated 4 times.....46
- Figure S3.1.1.** SEM images of 20% Fe as catalyst of CNT growth deposited onto SiO<sub>2</sub>. ....49
- Figure S3.1.2.** SEM images of CNT growth onto SiO<sub>2</sub> using Fe as catalyst via CVD in 3 L h<sup>-1</sup>/3 L h<sup>-1</sup> Ar/H<sub>2</sub> purged acetonitrile atmosphere for 120 min at (a) 750 °C, (b) 850 °C, (c) 950 °C and (d) 1050 °C, respectively.....49
- Figure S3.1.3.** Koutecky-Levich plots of Pt deposited onto 3D CNTs, primary CNTs and C at different potentials determined by Koutecky-Levich equation. ....50
- Figure S3.1.4.** (a) Schema of multilayered MEA; (b) polarization curves of (a) multilayered MEAs assembled by Pt-3D and Pt-PANI; (b) Polarization curves of the Pt-3D CNTs-PANI-LBL, Pt-primary CNTs-PANI-LBL and Pt-C tested at 70 °C; (c) The long-term stability test of the as-prepared Pt catalysts for 7 days.....51
- Figure 3.2.1.** Scheme of the preparation of hierarchically nanostructured electrodes: (a) electrochemical deposition of Fe nanoparticles onto oxidized GC; (b) CNT growth onto GC through CVD; (c) Deposition of Fe nanoparticles onto CNTs and GC; and (d) growth of secondary CNTs on primary CNTs.....54
- Figure 3.2.2.** (a) SEM image and (b) particle size distribution of Fe nanoparticles electrochemically deposited onto GC. ....55
- Figure 3.2.3.** (a) SEM images of CNTs deposited onto GC by CVD at 750 °C using cyclohexane and a gas flow rate of 1.7 L h<sup>-1</sup> for 120 min with an H<sub>2</sub>/Ar ratio of 1.8 (1.1 L h<sup>-1</sup>/0.6 L h<sup>-1</sup>). (b) CNTs grown under the same conditions but with an increase total gas flow rate of 3.9 L h<sup>-1</sup>. ....56
- Figure 3.2.4.** SEM images of (a) Fe nanoparticles electrodeposited onto primary CNTs and GC (8 s of deposition time) and (b) secondary CNTs grown at 750°C for 120 min with a H<sub>2</sub>/Ar ratio of 2.4 (1.2 L h<sup>-1</sup>/0.5 L h<sup>-1</sup>). ....59
- Figure 3.2.5.** Raman spectra of CNTs/GC and CNTs/CNTs/GC electrodes. The spectra are normalized with respect to the intensity of the D-band, and horizontal lines indicate the height of the G-band. ....60

- Figure 3.2.6.** SEM und BSE images of Pt nanoparticles deposited in a aqueous 0.005 M  $\text{Pt}(\text{NO}_3)_2$  and 0.1 M  $\text{NaNO}_3$  solution via single-sweep voltammetry from 0 to -0.9 V vs.  $\text{Ag}|\text{AgCl}|\text{KCl}_{\text{sat}}$ . at a scan rate of  $5 \text{ mV s}^{-1}$  onto CNTs/CNTs/GC. ....62
- Figure 3.2.7.** Cyclic voltammograms of GC, oxidized GC, CNTs/GC and CNTs/CNTs/GC recorded at a scan rate of  $100 \text{ mV s}^{-1}$  in  $\text{N}_2$ -saturated 0.5 M  $\text{H}_2\text{SO}_4$  aqueous electrolyte solution at room temperature.....63
- Figure 3.2.8.** Cyclic voltammograms of Pt onto GC, CNTs/GC and CNTs/CNTs/GC electrodes recorded at a scan rate of  $100 \text{ mV s}^{-1}$  at room temperature in a  $\text{N}_2$ -purged aqueous 0.5 M  $\text{H}_2\text{SO}_4$  electrolyte solution. ....63
- Figure 3.2.9.**  $\text{CO}_{\text{ad}}$  stripping voltammograms of Pt-CNTs/GC and Pt-CNTs/CNTs/GC monitored at  $20 \text{ mV s}^{-1}$  in  $\text{CO}$ -purged and subsequently  $\text{N}_2$ -purged 0.1 M  $\text{HClO}_4$  solution. The vertical dashed lines are intended as a guide for the eye. ....65
- Figure 3.2.10.** Cyclic voltammograms of Pt-CNTs/GC and Pt-CNTs/CNTs/GC in  $\text{N}_2$  saturated 1 M  $\text{CH}_3\text{OH}$  and 0.5 M  $\text{H}_2\text{SO}_4$  electrolyte solution recorded at a scan rate of  $5 \text{ mV s}^{-1}$  normalized to (a) Pt masse and (b) Pt-ECSA evaluated by  $\text{CO}_{\text{ads}}$  stripping. The vertical dashed lines are intended as a guide for the eye.....67
- Figure S3.2.1.** Single sweep voltammogram of iron deposition on oxidized GC recorded in the potential range between -0.5 V and -1.75 V vs.  $\text{Ag}|\text{AgCl}|\text{KCl}_{\text{sat}}$ . with a scan rate  $5 \text{ mV s}^{-1}$  in  $\text{N}_2$  purged 0.005 M  $\text{FeSO}_4 \cdot 7\text{H}_2\text{O}$  and 0.5 M  $\text{MgSO}_4 \cdot 7\text{H}_2\text{O}$  aqueous solution. The respective potentials for double-pulse deposition are indicated. ....71
- Figure S3.2.2.** SEM images of CNTs grown at  $750^\circ\text{C}$  using cyclohexane as carbon source through CVD with an  $\text{H}_2/\text{Ar}$  ratio of 1.8: (a) for 30 min and (b) for 60 min using  $1.7 \text{ L h}^{-1}$  as total gas flow rate; (c) with  $6.7 \text{ L h}^{-1}$  as total gas flow rate and (d)  $12.1 \text{ L h}^{-1}$  as flow rate for 120 min; as well as with a gas flow rate of  $1.7 \text{ L h}^{-1}$  for 120min with different  $\text{H}_2/\text{Ar}$  ratios: (e) 1.4 ( $1.0 \text{ L h}^{-1}/0.7 \text{ L h}^{-1}$ ), (f) 2.4 ( $1.2 \text{ L h}^{-1}/0.5 \text{ L h}^{-1}$ ), (g) optical images of GC before and after CNT growth for 120 min. ....72
- Figure S3.2.3.** SEM and BSE images of Fe nanoparticles deposited onto primary CNTs on GC via the above mentioned electrochemical deposition with different deposition times: (a) 12 s and (b) 6 s. ....72
- Figure S3.2.4.** SEM image of secondary CNT growth at  $750^\circ\text{C}$  for 120 min with optimized  $\text{H}_2/\text{Ar}$  ratio: 1.8 ( $1.1 \text{ L h}^{-1}/0.6 \text{ L h}^{-1}$ ). ....73
- Figure S3.2.5.** SEM and BSE images of (a) electrodeposited secondary Fe nanoparticles onto thicker CNTs and GC with 6 s deposition time as well as (b) secondary CNTs grown via optimized growth condition. (The CNTs with increased diameter were grown at bigger primary Fe nanoparticles created by longer deposition time.).....73
- Figure S3.2.6.** SEM images of CNTs (a) before and (b) after secondary CNT growth under acetonitrile as carbon source at  $750^\circ\text{C}$  for 120 min. ....74
- Figure S3.2.7.** Linear sweep voltammogram for Pt deposition recorded at a scan rate of  $5 \text{ mV s}^{-1}$  from 0 to -0.9 V vs.  $\text{Ag}|\text{AgCl}|\text{KCl}_{\text{sat}}$ . in a 0.005 M  $\text{Pt}(\text{NO}_3)_2$  and 0.1 M  $\text{NaNO}_3$  solution. ....74

- Figure S3.2.8.** SEM images of Pt nanoparticles deposited onto CNTs/CNTs/Pt in a 0.005 M  $\text{Pt}(\text{NO}_3)_2$  and 0.1 M  $\text{NaNO}_3$  aqueous solution via linear-sweep voltammetry from 0 to -0.9 V vs.  $\text{Ag}|\text{AgCl}|\text{KCl}_{\text{sat}}$ . at  $5 \text{ mV s}^{-1}$  scan rate. .... 74
- Figure S3.2.9.** SEM und BSE images of Pt nanoparticles deposited in a aqueous 0.005 M  $\text{Pt}(\text{NO}_3)_2$  and 0.1 M  $\text{NaNO}_3$  solution via single-sweep voltammetry from 0 to -0.9 V vs.  $\text{Ag}|\text{AgCl}|\text{KCl}_{\text{sat}}$ . at  $5 \text{ mV s}^{-1}$  scan rate onto: (a) oxidized GC, (b) CNTs/GC and (c) CNTs/CNTs/GC. .... 75
- Figure S3.2.10.** Cyclic voltammograms of N-CNTs/GC and N-CNTs/N-CNTs/GC electrodes measured at a  $100 \text{ mV s}^{-1}$  scan rate in 0.5 M  $\text{H}_2\text{SO}_4$  aqueous solution purged with  $\text{N}_2$  at room temperature. .... 76
- Figure S3.2.11.** Cyclic voltammograms of Pt-GC, Pt-CNTs/GC and Pt-CNTs/CNTs/GC recorded at a scan rate of  $5 \text{ mV s}^{-1}$  respectively normalized to Pt-ECSA evaluated by  $H_{\text{ads/des}}$  and Pt mass in the potential range from -0.2 V–1.0 V vs.  $\text{Ag}|\text{AgCl}|\text{KCl}_{\text{sat}}$  in  $\text{N}_2$  purged 1 M  $\text{CH}_3\text{OH}$  and 0.5 M  $\text{H}_2\text{SO}_4$  solution (a, b) as shown in potential range of -0.9 V-0.4 V in 1 M  $\text{CH}_3\text{OH}$  and 0.5 M  $\text{KOH}$  solution (c, d). .... 76
- Figure S3.2.12.** SEM images of CNT growth over Ni particles onto GC via CVD using (a) cyclohexane and (b) acetonitrile as carbon sources at  $750^\circ$ . .... 77
- Figure S3.2.13.** SEM images of (a) and (b) Fe deposited on primary CNTs on CC in different scales, (c) secondary CNT growth over Fe particles via CVD in  $3 \text{ L h}^{-1}/3 \text{ L h}^{-1}$   $\text{Ar}/\text{H}_2$  purged acetonitrile atmosphere for 120 min at  $750^\circ$ . .... 77
- Figure S3.2.14.** Linear-sweep voltammograms of the prepared electrodes (with Pt) recorded in  $\text{O}_2$  saturated 0.5 M  $\text{H}_2\text{SO}_4$  at a scan rate of  $5 \text{ mV s}^{-1}$  for ORR measurements. .... 78
- Figure 3.3.1.** Schematic representation of the preparation of nanostructured electrodes: (a) homogeneous deposition of graphene oxide onto carbon cloth (CC) by dip-coating, (b) reduction of GO through heat-treatment at  $380^\circ\text{C}$  in  $\text{Ar}/\text{H}_2$  atmosphere, (c) electrodeposition of Fe nanoparticles onto RGO/CC, (d) growth of NCNTs on RGO/CC via CVD, (e) electrochemical leaching of Fe particles followed by electrodeposition of Pt nanoparticles to form Pt-NCNTs/RGO/CC. .... 81
- Figure 3.3.2.** SEM images of (a) CC, (c) GO decorated on CC, (e) reduced GO/CC; optical images of (b) CC, (d) GO/CC and (f) RGO/CC. .... 82
- Figure 3.3.3.** X-ray diffraction profiles of (a) graphite, GO, RGO; (b) CC, GO/CC, RGO/CC and NCNTs/RGO/CC; (c) Raman spectra of commercial graphite, CC, GO/CC and RGO/CC showing the shift in the G band. 532 nm laser as excitation. Dashed lines are intended as a help for the eye. .... 83
- Figure 3.3.4.** SEM images of (a) Fe nanoparticles on RGO/CC obtained by electrodeposition; (b) NCNTs grown on the RGO/CC from acetonitrile catalyzed by Fe nanoparticles at  $750^\circ\text{C}$  via CVD; Pt nanoparticles electrodeposited on (c) NCNTs/CC and (d) NCNTs/RGO/CC. .... 85
- Figure 3.3.5.** Cyclic voltammograms of Pt-NCNTs/CC and Pt-NCNTs/RGO/CC electrodes recorded at a scan rate of  $100 \text{ mV s}^{-1}$  at room temperature in 0.1 M  $\text{HClO}_4$  aqueous electrolyte solution purged with  $\text{N}_2$  after MOR measurements. Dashed lines are intended as a help for the eye. .... 88

- Figure 3.3.6.**  $\text{CO}_{\text{ad}}$  stripping voltammograms for Pt on (a) NCNTs/CC and (b) NCNTs/RGO/CC recorded at  $20 \text{ mV s}^{-1}$  in aqueous  $0.1 \text{ M HClO}_4$  electrolyte solution after MOR measurement. Dashed lines are intended as a help for the eye. ....89
- Figure 3.3.7.** Cyclic voltammograms of Pt-NCNTs/CC and Pt-NCNTs/RGO/CC in  $\text{N}_2$  purged  $1 \text{ M CH}_3\text{OH}$  in  $0.5 \text{ M H}_2\text{SO}_4$  electrolyte solution recorded at a scan rate of  $5 \text{ mV s}^{-1}$  normalized to (a) Pt-ECSA evaluated by  $\text{CO}_{\text{ad}}$  stripping and (b) Pt mass loading. Dashed lines are intended as a help for the eye. ....90
- Figure S3.3.1.** SEM images of (a) CC, (c) GO decorated on CC, (e) reduced GO/CC; optical images of (b) CC, (d) GO/CC and (f) RGO/CC. ....94
- Figure S3.3.3.** TEM images and particles size distributions for (a) Pt-NCNTs/CC and (b) Pt-NCNTs/RGO/CC .....95
- Figure S3.3.2:** Raman spectra of commercial CC, NCNTs/CC and NCNTs/RGO/CC measured by  $532 \text{ nm}$  laser as excitation. Dashed lines are intended as a help for the eye...95
- Figure S3.3.4.** Chronoamperometric curves of methanol oxidation for Pt-NCNTs/RGO/CC and Pt-NCNTs/CC in  $\text{N}_2$  purged  $1 \text{ M CH}_3\text{OH}$  and  $0.5 \text{ M H}_2\text{SO}_4$  at a fixed potential of  $0.6 \text{ V}$  vs.  $\text{Ag|AgCl|KCl}_{\text{sat.}}$ . The currents were normalized by the mass of Pt. ....96
- Figure S3.3.5.** ORR polarization curves of Pt-NCNTs/RGO/CC and Pt-NCNTs/CC in  $\text{O}_2$  purged  $0.1 \text{ M HClO}_4$  with a scan rate of  $5 \text{ mV s}^{-1}$  in the potential range between  $-0.15$ - $0.9 \text{ V}$  vs.  $\text{Ag|AgCl|KCl}_{\text{sat.}}$ . ....96
- Figure S3.3.6.** SEM images of Fe nanoparticles on CC obtained via double pulse electrodeposition with nucleation potential  $-1.75 \text{ V}$  and growth pulse potential vs.  $\text{Ag|AgCl|KCl}_{\text{sat.}}$  (a)  $-1.2 \text{ V}$ ,  $15 \text{ s}$  ( $\approx 82 \text{ nm}$  diameter); (b)  $-1.2 \text{ V}$ ,  $20 \text{ s}$ ; (c) and (e)  $-1.1 \text{ V}$ ,  $15 \text{ s}$  in different scale; (d)  $-1.1 \text{ V}$ ,  $20 \text{ s}$ ; (f) CC without Fe deposition as reference electrode. ....97
- Figure S3.3.7.** SEM images of NCNT growth over Fe particles onto CC via CVD in  $3 \text{ L h}^{-1}/3 \text{ L h}^{-1} \text{ H}_2/\text{Ar}$  purged acetonitrile atmosphere for  $120 \text{ min}$  at (a)  $650^\circ$  and (b)  $750^\circ$ . (c) and (d) NCNT growth were repeated in the same conditions at  $650^\circ$  and  $750^\circ$ , respectively. ....98
- Figure S3.3.8.** SEM images of NCNT growth over the electrodeposited bigger Fe particles onto CC via CVD in  $3 \text{ L h}^{-1}/3 \text{ L h}^{-1} \text{ H}_2/\text{Ar}$  purged acetonitrile atmosphere for  $120 \text{ min}$  at  $750^\circ$ . ....98
- Figure 3.4.1.** Scheme of the preparation of hierarchical PANI/CNTs/CC electrodes: (a) electrochemical deposition of Fe nanoparticles onto CC, (b) CNT growth onto CC over Fe particles via CVD, (c) deposition of PANI film onto CNTs/CC by wet impregnation, (d) Electrochemical deposition of PANI film onto CNTs/CC. .... 100
- Figure 3.4.2.** SEM images of (a) CNTs/CC and (b)  $\text{PANI}_{\text{Wt}}/\text{CNTs}/\text{CC}$  prepared by wet impregnation in low and high resolution. .... 101
- Figure 3.4.3.** SEM images of PANI electrodeposited on (a) CC and (b) CNTs/CC surface via cyclic voltammetry at a scan rate of  $100 \text{ mV s}^{-1}$  in a potential range of  $-0.4$ – $1.0 \text{ V}$  vs.  $\text{Ag|AgCl|KCl}_{\text{sat.}}$  in a  $\text{N}_2$  purged  $0.25 \text{ M}$  aniline and  $0.5 \text{ M H}_2\text{SO}_4$  solution for 20 cycles; (c) PANI coated CNTs/CC by CV for 10 cycles in low and high resolution. .... 102
- Figure 3.4.4.** Cyclic voltammograms of (a) CNTs/CC, (b) CNTs/CNTs/CC, (c)  $\text{PANI}_{\text{Wt}}/\text{CNTs}/\text{CC}$ , (d) CNTs/RGO/CC electrodes recorded at different scan rates of  $5, 25, 50, 100 \text{ mV s}^{-1}$  in  $\text{N}_2$  purged  $0.5 \text{ M H}_2\text{SO}_4$  at room temperature. .... 103

- Figure 3.4.5.** (a) Cyclic voltammograms of CNTs/CC, CNTs/CNTs/CC, PANI<sub>wi</sub>/CNTs/CC and CNTs/RGO/CC electrodes recorded at a scan rate of 100 mV s<sup>-1</sup> in 0.5 M H<sub>2</sub>SO<sub>4</sub> aqueous electrolyte solution purged with N<sub>2</sub> at room temperature and (b) their capacitances calculated through CV at different scan rates. .... 104
- Figure 3.4.6.** Galvanostatic charge-discharge curves of (a) CNTs/CC, (b) CNTs/CNTs/CC, (c) PANI<sub>wi</sub>/CNTs/CC, (d) CNTs/RGO/CC electrodes measured at different current densities of 5, 10, 20, 30 mA cm<sup>-2</sup> in N<sub>2</sub>-purged 0.5 M H<sub>2</sub>SO<sub>4</sub>. .... 106
- Figure 3.4.7.** (a) Galvanostatic charge-discharge curves of CNTs/CC, CNTs/CNTs/CC, PANI<sub>wi</sub>/CNTs/CC and CNTs/RGO/CC electrodes recorded at a current density of 10 mA cm<sup>-2</sup> in N<sub>2</sub> purged 0.5 M H<sub>2</sub>SO<sub>4</sub> aqueous electrolyte solution and (b) plot of their capacitances calculated via galvanostatic charge-discharge curves at different current densities. .... 107
- Figure 3.4.8.** Relative capacitance of CNTs/CC, CNTs/CNTs/CC, CNTs/RGO/CC, PANI<sub>wi</sub>/CNTs/CC after each 100 cycles of charge-discharge curves at a current density of 10 mA cm<sup>-2</sup>. .... 107
- Figure S3.4.1.** SEM images of PANI decorated onto CNTs/CC via wet impregnation (chemical oxidative polymerization) in (a) 0.1 M aniline + 1 M HClO<sub>4</sub> solution and (b) 0.1 M aniline + 0.1 M HClO<sub>4</sub> solution for 24 h, respectively. .... 110
- Figure S3.4.2.** Nyquist plots measured in the frequency range of 10<sup>5</sup>-0.01 Hz with 5 mV amplitude of (a) CNTs/CC, CNTs/CNTs/CC and PANI<sub>wi</sub>/CNTs/CC; (b) CNTs/CNTs/CC and (c) PANI<sub>wi</sub>/CNTs/CC before and after long-term test. .... 110

## Publications and Conference Contributions

### Research Articles

1. Pei Wang, Titula Kottakkat and Michael Bron, Pt supported on nanostructured NCNTs/RGO composite electrodes for methanol electrooxidation, *ChemElectroChem*, 2015, 2, 1396-1402.
2. Pei Wang, Katarzyna Kulp and Michael Bron, Hierarchically structured 3D carbon nanotube electrodes for electrocatalytic applications, *Beilstein J. Nanotechnol.*, 2019, 10, 1475-1487.
3. Pei Wang, Benedikt Peter, Titus Lendenberg, Christina Roth and Michael Bron, Preparation of hierarchically structured 3D CNTs as a catalyst support for a proton exchange membrane fuel cell. (*to be submitted*)
4. Pei Wang, Michael Bron, CNT-based hierarchically structured 3D electrodes for supercapacitors. (*to be submitted*)
5. Katarzyna Kulp, Christin Kulp, Pei Wang and Michael Bron, Carbon nanotubes and nitrogen-doped carbon nanotubes grown on carbon cloth for electrocatalytic oxygen reduction. (*to be submitted*)

### Conference Contributions

1. Pei Wang, Katarzyna Kulp, Christin Kulp and Michael Bron, poster-presentation: "Synthesis of hierarchical CNT-CNT composites as catalyst support for applications in electrocatalysis", 67th Annual Meeting of the International Society of Electrochemistry, Aug. 2016, The Hague, Netherland.
2. Pei Wang, Mathias Kühhirt, Katarzyna Piekalska and Michael Bron, oral presentation: "A bottom-up approach to synthesize hierarchically structured electrodes", *Electrochemistry 2014 (GDCh)*, Sep. 2014, Mainz, Germany.
3. Pei Wang and Michael Bron, poster-presentation: "Pt supported on nanostructured CNT- and RGO-based electrodes for methanol electrooxidation", 65th Annual Meeting of the International Society of Electrochemistry, Aug. 2014, Lausanne, Switzerland.
4. Pei Wang and Michael Bron, poster-presentation: "Hierarchically structured electrodes based on CNT", *ChemOnTubes 2014*, Mar. 2014, Riva del Garda, Italy.





# Curriculum Vitae

## Personal Details

Date of Birth: 13.04.1984  
Birthplace: Shandong, China  
Nationality: Chinese  
Marital status: Married



---

## Fields of Interest:

renewable energy, energy conversion and storage (fuel cell, lithium ion battery, redox flow battery, lead acid battery, super capacitors), nanostructured materials, electrocatalyst, polymer.

## Summary

Extensive knowledge in the field of electrochemistry and electrochemical technologies; capable of developing new processes with acquired knowledge; motivated to take on new challenges and learn

## Education

### University Education

- 10/2011–03/2017      **Martin-Luther-University Halle-Wittenberg**  
**Doctoral Studies** (nanostructured electrodes)  
Prof. Dr. Bron's research group  
**Main field of research:** preparation and characterization of novel hierarchically nanostructured electrodes for fuel cell and super capacitor.  
Methodologies: chemical vapor deposition, electrochemical methods, scanning electron microscopy, Raman spectroscopy, thermal gravimetric analysis and mass spectrometry.
- 10/2007–11/2010      **Technical University Clausthal**  
**Master's Studies** in applied chemistry  
Prof. Dr Schmidt's research group

**Major:** macromolecules

Master's thesis: "Radical co-polymerization of donor/acceptor monomers with neutral monomers"

10/2002–07/2006

**Qingdao University of Science and Technology**

**Bachelor's Studies** in applied chemistry

Bachelor's thesis: "Electrosynthesis and Characterization of High Quality Poly (9-fluorone) Films"

*Award as "Outstanding Graduate"*

### **School Education**

09/1999–07/2002

**Laixi No. 2 Middle School of Shandong Province**

*China*

Acquisition of university qualification

Specialization subjects: chemistry, physics, biology

---

### **Internship & Work Experience**

2012-2016

Supervision of bachelor and master students' internships /thesis in technical chemistry, *Halle*

03/2012

Symposium (MDKL) "Mitteldeutschen Katalyse-Lehrverbundes", Leipzig

05/2005–06/2005

Internship in a chemical company (PVC-producer), *Qingdao*

2003–2006

Student chemical laboratory assistant, *Qingdao*

### **Project Experience**

10/2011 – 03/2016

DFG Project of novel electrodes for fuel cell (BR 2244/7-1)

08/2009 – 11/2010

Project for the polymerization of the fuel cell membranes

04/2009 – 07/2009

### **Skills**

Languages: German (good), English (good), Chinese (mother language)

IT-Knowledge: Origin 8, Citavi, Nova, Lince, ChemDraw, Microsoft

Volunteer Work: Vice Chairman of student council at chemistry college (2004-2005, *Qingdao*); Event Organizer at the Chinese student council (2015, *Halle/Saale*)

---

